

# Investigations of Secondary Organic Aerosol Formation in Laboratory Chambers

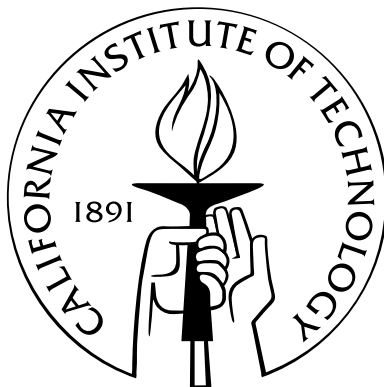
Thesis by

Christine Lauren Loza

In Partial Fulfillment of the Requirements

for the Degree of

Doctor of Philosophy



California Institute of Technology

Pasadena, California

2013

(Defended May 17, 2013)

© 2013

Christine Lauren Loza

All Rights Reserved

*To my parents, Rosemary and Roman Loza*

# Acknowledgements

I am extremely grateful for all the help, guidance, mentoring, support, and friendship that I have received over the course of my PhD. Without it, my thesis would have been impossible to complete.

First, I thank my adviser, John Seinfeld, for welcoming me into his group and sending me up to the roof to work in one of the best-equipped chamber facilities in the world. John gave me the right amount of advising throughout my PhD career, outlining my projects initially and then allowing me to do my own project and experiment design as I gained experience. I appreciate the freedom that John gives the chamber crew to design our experiments and set our day-to-day schedule and that he always made time to talk with me about experiments and papers or to give me advice. Not only did John ensure that I had everything I needed to be successful in my graduate career, he also laid the foundation for future career in industry.

I also thank my adviser Rick Flagan for giving me advice whenever I asked for it, ensuring that I leave Caltech with a good knowledge of fugacity and equilibrium, and for hosting many lovely group barbecues. I thank Paul Wennberg for serving on both my candidacy and PhD committees, for his instrument troubleshooting and data analysis suggestions, and for looking out for the chamber lab during the design of and move to Linde-Robinson. I thank Stan Sander for serving on my PhD committee and for giving me a warm reception into the Caltech concert band clarinet section.

I have worked with many wonderful scientists at Caltech throughout my PhD, many of whom are listed below but all of whom deserve thanks. Upon entering the roof lab, I was apprenticed to Arthur Chan. Not only is he a fantastic mentor, he is also a great friend. After Arthur graduated, he still answered my chamber questions and offered useful advice for experiments and papers. I benefitted from working with many other older graduate students and postdocs in the roof lab: Jason Surratt,



Puneet Chhabra, Beth Katuzman, Scott Hersey, ManNin Chan, Alan Kwan, Nathan Eddingsaas, Jason St. Clair, Melinda Beaver, and John Crounse. Jill Craven, Lindsay Yee, and I all joined the Seinfeld lab in the same year, and I have enjoyed having them as friends and colleagues these past five years. I have had the pleasure of working with grad students and post docs who joined the lab since I started: Xuan Zhang, Matt Coggon, Kate Schilling, Becky Schwantes, and Tran Nguyen. I thank the modelers in the group for stimulating discussions and company at the lunch table: Havala Pye, Andi Zuend, Manabu Shiraiwa, Joey Ensberg, and Renee McVay. I thank Xerxes Lopez-Yglesias for electronics advice, Jason Gamba for construction advice, and Andy Downard for keeping the Notre Dame spirit alive at Caltech. A large thanks goes to our summer student, Jim Wood, for his help setting up the new lab. I also thank Nathan Dalleska for his help with the GC and for his assistance with Linde-Robinson planning.

During my time in the roof lab, I have benefitted from meeting and working with collaborators from other institutions. I got to know Frank Keutsch and Melissa Galloway well through three rounds of glyoxal experiments. During the alkanes project I enjoyed working with Reddy Yatavelli, Manjula Canagaratna, Lynn Russell, Paul Ziemann, and Aiko Matsunaga. One of the best parts of doing aerosol research at Caltech is connecting with Caltech alumni in the aerosol community. Every year, they welcome the current grad students at the AAAR Caltech dinner and are always happy to share their experiences and lend advice. The same can be said of the AMS community. I especially thank Rob Griffin and Yu Jun Leong for lending us part of their AMS and Barbara Wyslouzil for encouraging me to go to Caltech and to work for John. I have also benefitted greatly from having Sally Ng as a mentor, especially in setting up the chamber in Linde-Robinson.

The support staff at Caltech are fantastic, and they have made sure that I can always focus on research while they take care of the details. I owe much thanks to Yvette Grant for handling countless orders for the roof lab. I also thank Nora Oshima and Megan Schmid for patiently addressing our concerns in Linde-Robinson, and Fran Matzen and Joan Sullivan for helping place work orders in Keck. I thank all of ChE secretaries for keeping track of my mail and for stepping in when Yvette, Fran, or Joan were unavailable. I thank Mike Vondrus for sharing the tools in his machine shop,

Mike Roy and Mike Gerfen for machining the parts that we needed for the new lab, and Rick Gerhart for fixing our broken glassware. I thank Rick Germond and the staff at central warehouse for lugging gas cylinders and liquid nitrogen tanks to the roof. Although he is not from Caltech, I also thank Rick Radtke from EGC for his help in starting up the Linde-Robinson chambers that was above and beyond his job description.

In addition to those who helped me in my research, there are others, whom I met during grad school, to thank for all they have given me over the course of my PhD. I enjoyed the camaraderie of the incoming class of 2008, and being there for each other through first year classes and quals. I thank my lunch group from ChE, ESE, and GPS, affectionately known as the ChEESE(G)PSers, for great memories at the lunch table, on the softball field, and at potlucks and parties, and for following college football and marching band (the latter only applies to Jeff). I thank Bill Bing, Lynne Snyder, and the Caltech Concert Band and Clarinet Choir for giving me a place to play my clarinet throughout grad school, and I especially thank Tom Ruchti for being the best stand partner ever. I thank Artemis Ailianou, my roommate for my entire grad student career, for her loyalty and friendship and for inviting me visit her at home in Cyprus. I also thank my friends from St. Philip who have looked out for me since I started at Caltech.

I thank all who have contributed to my education. I thank my professors at Notre Dame for their instruction which prepared me so well for grad school and for help with grad school and fellowship applications. I especially thank my undergrad research adviser, Paul Bohn for introducing me to life in a research group and for continuing to mentor me throughout my graduate career. Finally, I thank Eric Saurer, my former clarinet section leader and fellow cheg, who has been my mentor since I arrived at Notre Dame.

Lastly, I have received much love and support during my PhD. I thank Andrew Metcalf, not only for his help with DMAs, electronics, and everything computer-related, but also for his companionship, for his unwavering belief that I would always “figure it out,” and for his pot roasts and rhubarb pies. I thank my brother Andrew for stimulating discussions about anything science-related. I thank my grandma, babcia, and aunt Tess for their cards and packages that brought a little bit of Buffalo

to California and for patiently waiting for my next visit. Finally I thank my parents for encouraging my interest in science from a young age and suggesting that I become a chemical engineer. Having once been grad students themselves, they understood much of what I was going through, which sometimes led to some tough love, but they were always willing to listen to my problems and offer advice, especially when the GC was broken or when I was designing the new chambers. I am very grateful for all that they have done for my brother and me and hope that they will enjoy having a few more doctors in the family.

# Abstract

Secondary organic aerosol (SOA) is produced in the atmosphere by oxidation of volatile organic compounds. Laboratory chambers are used to understand the formation mechanisms and evolution of SOA formed under controlled conditions. This thesis presents studies of SOA formed from anthropogenic and biogenic precursors and discusses the effects of chamber walls on suspended vapors and particles.

During a chamber experiment, suspended vapors and particles can interact with the chamber walls. Particle wall loss is relatively well-understood, but vapor wall losses have received little study. Vapor wall loss of 2,3-epoxy-1,4-butanediol (BEPOX) and glyoxal was identified, quantified, and found to depend on chamber age and relative humidity.

Particles reside in the atmosphere for a week or more and can evolve chemically during that time period, a process termed aging. Simulating aging in laboratory chambers has proven to be challenging. A protocol was developed to extend the duration of a chamber experiment to 36 h of oxidation and was used to evaluate aging of SOA produced from *m*-xylene. Total SOA mass concentration increased and then decreased with increasing photooxidation suggesting a transition from functionalization to fragmentation chemistry driven by photochemical processes. SOA oxidation, measured as the bulk particle elemental oxygen-to-carbon ratio and fraction of organic mass at  $m/z$  44, increased continuously starting after 5 h of photooxidation.

The physical state and chemical composition of an organic aerosol affect the mixing of aerosol components and its interactions with condensing species. A laboratory chamber protocol was developed to evaluate the mixing of SOA produced sequentially from two different sources by heating the chamber to induce particle evaporation. Using this protocol, SOA produced from toluene was found to be less volatile than that produced from  $\alpha$ -pinene. When the two types of SOA were formed sequentially, the evaporation behavior most closely represented that of SOA from the second parent hydrocarbon, suggesting that the structure of the mixed SOA particles resembles a core of SOA from the first precursor coated by a layer of SOA from the second precursor, indicative of limiting mixing.

# Contents

<b>Acknowledgements</b>	<b>iv</b>
<b>Abstract</b>	<b>viii</b>
<b>1 Introduction</b>	<b>1</b>
<b>2 Characterization of Vapor Wall Loss in Laboratory Chambers</b>	<b>13</b>
2.1 Abstract . . . . .	14
2.2 Introduction . . . . .	14
2.3 Experimental Section . . . . .	16
2.4 Results and Discussion . . . . .	17
2.4.1 Vapor Wall Loss . . . . .	17
2.4.2 Model Description . . . . .	18
2.4.3 Model Predictions . . . . .	20
2.5 Implications for Chamber Experiments . . . . .	22
2.6 Acknowledgements . . . . .	23
<b>3 Chemical Aging of <i>m</i>-Xylene Secondary Organic Aerosol: Laboratory Chamber Study</b>	<b>31</b>
3.1 Abstract . . . . .	32
3.2 Introduction . . . . .	33
3.3 Materials and Methods . . . . .	36
3.3.1 Experimental Setup . . . . .	36

3.3.2	Aging Experiment Protocols . . . . .	37
3.3.3	Total SOA Formation . . . . .	38
3.4	Results and Discussion . . . . .	42
3.4.1	SOA Formation . . . . .	42
3.4.2	SOA Composition . . . . .	43
3.4.3	Fate of SOA After Peak Growth . . . . .	46
3.4.4	Role of Organic-to-Sulfate Ratio in Particle Wall Loss Corrections . . . . .	51
3.4.5	Acidic Seed Effects . . . . .	53
3.5	Conclusions . . . . .	54
3.6	Appendix A: Photochemical Model . . . . .	55
3.7	Acknowledgements . . . . .	56
<b>4</b>	<b>On the Mixing and Evaporation of Secondary Organic Aerosol Components</b>	<b>77</b>
4.1	Abstract . . . . .	78
4.2	Introduction . . . . .	78
4.3	Experimental . . . . .	80
4.4	Results and Discussion . . . . .	83
4.4.1	Aerosol Size Distribution Evolution . . . . .	83
4.4.2	Aerosol Chemical Composition . . . . .	89
4.5	Acknowledgements . . . . .	91
<b>5</b>	<b>Future Work</b>	<b>103</b>
<b>A</b>	<b>Analysis of Photochemical and Dark Glyoxal Uptake: Implications for SOA Formation</b>	<b>107</b>
<b>B</b>	<b><math>\alpha</math>-Pinene Photooxidation Under Controlled Chemical Conditions - Part 1: Gas-Phase Composition in Low- and High-NO<sub>x</sub> Environments</b>	<b>113</b>

<b>C</b>	<b><math>\alpha</math>-Pinene Photooxidation Under Controlled Chemical Conditions - Part 2: SOA Yield and Composition in Low- and High-NO<sub>x</sub> Environments</b>	<b>130</b>
<b>D</b>	<b>Secondary Organic Aerosol Coating Formation and Evaporation: Chamber Studies Using Black Carbon Seed Aerosol and the Single-Particle Soot Photometer</b>	<b>146</b>



# List of Tables

2.1	BEPOX wall loss coefficients as a function of chamber age. . . . .	27
2.2	Wall loss cases for vapors and particles. . . . .	27
3.1	Experiment sampling conditions and instrument sampling protocol. . . . .	65
3.2	Experimental conditions and results. . . . .	66
3.3	Rate constants for the photochemical model. . . . .	67
3.4	Compounds represented in the photochemical model. . . . .	68
4.1	Experimental details. . . . .	99

# List of Figures

2.1	Sinks for a vapor-phase species in a laboratory chamber. . . . .	28
2.2	First-order wall loss of BEPOX. . . . .	28
2.3	First-order wall loss of glyoxal. . . . .	28
2.4	Reversibility of BEPOX and glyoxal wall loss upon chamber dilution with clean air. .	29
2.5	Model comparison with data from a BEPOX uptake experiment. . . . .	29
2.6	Predictions for total BEPOX sinks after injection during an uptake experiment. . . .	30
2.7	Observed and predicted BEPOX uptake, $\Delta\text{VOC}$ , and aerosol mass growth during an uptake experiment. . . . .	30
3.1	Particle wall loss rate constants. . . . .	69
3.2	SOA mass and <i>m</i> -xylene concentration. . . . .	69
3.3	SOA mass and elemental composition. . . . .	70
3.4	Correlation of O:C with $f_{44}$ . . . . .	70
3.5	Evolution of SOA $f_{43}$ , $f_{44}$ , and O:C. . . . .	71
3.6	Average AMS organic mass spectra. . . . .	71
3.7	Time dependency of AMS ions and suspended particle size distribution peak diameter. .	72
3.8	Sources and sinks of a semivolatile vapor in a chamber . . . . .	72
3.9	Time dependency of SOA and <i>m</i> -xylene concentration during and after photooxidation. .	73
3.10	Evolution of $f_{43}$ , $f_{44}$ , and O:C of <i>m</i> -xylene SOA after photooxidation. . . . .	73
3.11	Time evolution of products formed during <i>m</i> -xylene oxidation detected by the CIMS. .	74
3.12	Initial organic and sulfate mass distributions used in simulations. . . . .	75
3.13	Effect of 24 h of wall loss on the mass distributions in Fig. 3.12. . . . .	76

3.14	Elemental ratios of <i>m</i> -xylene aerosol condensed onto neutral and acidic seed particles.	76
4.1	Evolution of the suspended particle size distribution of single-precursor SOA during heating of the chamber enclosure. The data shown are averaged over 1-h intervals. Abbreviations correspond to toluene (tol.) and $\alpha$ -pinene ( $\alpha$ -pin.). The final aerosol size distribution for Experiment 2 is not reported due to inadvertent chamber irradiation (see Table 4.1). The inset in panel b shows the change in particle size distribution for pure wall loss observed in Experiment 7 (Table 4.1). The initial size distribution after dilution is in gray, and the final size distribution after 9 h is in black. . . . .	100
4.2	Experiment profile for SOA formation and evaporation when $\alpha$ -pinene and toluene were injected sequentially (Experiment 4). The suspended particle volume concentration, $\alpha$ -pinene ( $\alpha$ -pin.), toluene (tol.), and cyclohexane (cyc.) concentrations (when above the limit of detection), and the chamber temperature are shown. Periods of irradiation, dilution, and heating are highlighted, and the toluene injection is denoted by the vertical, black line. . . . .	101
4.3	Evolution of the suspended particle size distribution of SOA from sequentially or simultaneously injected precursors during heating of the chamber enclosure. The data shown are averaged over 1-h intervals. Abbreviations correspond to toluene (tol.) and $\alpha$ -pinene ( $\alpha$ -pin.). . . . .	101
4.4	Evolution of aerosol oxidation state during formation (panel a) and dilution and heating (panel b). The error bars in panel a represent the uncertainty values for $\overline{OS}_C$ , calculated from those for H:C and O:C, 10 % and 31 %, respectively (Aiken et al., 2008), at the end of the formation period. The rate of change of $\overline{OS}_C$ as a function of temperature for each experiment is listed in panel b. Abbreviations correspond to toluene (tol.) and $\alpha$ -pinene ( $\alpha$ -pin.). . . . .	102

## Chapter 1

# Introduction

Atmospheric aerosols affect climate, visibility, and human health, but much remains to be understood about the effects aerosols have on these systems. A large fraction of submicron particle mass is comprised of organic aerosols (OA) (Zhang et al., 2007). OA can be categorized as primary organic aerosol (POA), which are directly emitted as particles, or secondary organic aerosol (SOA), which form from semivolatile organic compounds (SVOCs) produced from reaction of volatile organic compounds (VOCs). Understanding SOA formation processes is essential to identifying SOA sources and predicting SOA production in the atmosphere.

VOCs are trace constituents of ambient air; however, they are prominent in tropospheric chemistry. Over 10,000 VOCs have been measured in ambient air, and it is estimated that over a million different VOCs may exist (Goldstein and Galbally, 2007). A single source may emit a variety of different compounds; for example, gasoline and diesel emissions contain aromatics, cycloalkanes, and straight and branched alkanes with 8-25 carbon atoms (Gentner et al., 2012), and multiple monoterpenes, carboxylic acids, and carbonyl compounds have been sampled in ponderosa pine forests (Villanueva-Fierro et al., 2004; Lee et al., 2005). While ambient sampling is essential to identifying SOA sources, the variety of co-emitted VOCs and meteorology at a site preclude specific conclusions of SOA formation mechanisms.

Once SOA precursor molecules have been identified, study of these molecules in laboratory chambers can elucidate chemical reaction and SOA formation mechanisms and quantify the SOA produced from a single source (Hallquist et al., 2009). Laboratory chambers provide a controlled environment in which a single parent VOC can be oxidized with a specific oxidant under defined  $\text{NO}_x$  conditions at one temperature and relative humidity. Various chamber facilities with reactor volume  $\geq 4 \text{ m}^3$  exist around the world (e.g. Cocker et al., 2001; Saathoff et al., 2003; Rohrer et al., 2005; Paulsen et al., 2005; Presto et al., 2005; Carter et al., 2005; King et al., 2007; Nakao et al., 2011; Lee et al., 2004; Siese et al., 2001; Lim and Ziemann, 2009; Liu et al., 2012; Wang et al., 2011; Bernard et al., 2010). Chambers are most commonly constructed out of FEP Teflon film but are also built of aluminum or stainless steel. Oxidation occurs in the dark (e.g. ozonolysis) or is initiated with blacklights, Xenon arc lamps, or natural sunlight. Most indoor chambers are enclosed

in temperature-controlled structures. Chamber experiments typically involve combining a known concentration of a single VOC and oxidant in clean air, initiating oxidation, and measuring the formation of vapor-phase oxidation products and SOA amount and chemical composition with a suite of gas- and particle-phase instrumentation. To prevent contamination between experiments, chambers are cleaned using a variety of techniques including flushing with clean air, baking, irradiating, and oxidizing with  $O_3$ .

Although chambers provide an excellent means of investigating oxidation mechanisms of a single VOC, they also have limitations. Particles deposit to chamber walls by diffusion or gravitational settling (Crump and Seinfeld, 1981); and these particle wall losses can be affected by charging on the walls and particles (McMurry and Rader, 1985). In quantifying SOA production for calculation of SOA yield (mass concentration of SOA formed divided mass concentration of parent VOC reacted), particle wall losses must be taken into account through determination of size-dependent particle wall loss rate constants in separate experiments (Keywood et al., 2004; Ng et al., 2007), by measurement of particle decay before or after SOA growth (Hildebrandt et al., 2009), or through dynamic modeling of a particle size distribution (Pierce et al., 2008). Vapors can also deposit to the walls, either onto particles deposited to the walls during an experiment (Weitkamp et al., 2007; Hildebrandt et al., 2009, 2011) or to the chamber walls directly. The effect of vapor wall loss is difficult to distinguish from condensation to suspended particles in SOA growth experiments and must be examined in dedicated vapor wall loss experiments. Vapor wall losses have been observed in Tedlar sampling bags (McGarvey and Shorten, 2000) and Teflon chambers (Grosjean, 1985; McMurry and Grosjean, 1985; Maddalena et al., 2002; Matsunaga and Ziemann, 2010). The extent of vapor wall loss was found to depend on compound vapor pressure and structure (Matsunaga and Ziemann, 2010). Chapter 2 presents a study of vapor wall loss in laboratory chambers. Two compounds, glyoxal and 2,3-epoxy-1,4-butanediol (BEPOX), are found to reversibly partition to chamber walls, and the extent of partitioning is influenced by chamber age and relative humidity. Once vapor wall loss rate constants are determined, a model is used to assess the competition among uptake to suspended particles, deposited particles, and chamber walls.

A disparity exists between the time that a particle spends in the atmosphere and the duration of chamber experiments. Particles can reside in the atmosphere for approximately one week, whereas the duration of chamber experiments rarely exceeds 18 h. Particles in the atmosphere undergo continuous chemical and physical processing, commonly called aging (Rudich et al., 2007). Measurements of bulk aerosol chemical composition using aerosol mass spectrometry have correlated an increase in particle oxygen content, reported as oxygen-to-carbon ratio, fraction of organic mass at  $m/z$  44, or average carbon oxidation state, with aging (Heald et al., 2010; Ng et al., 2010, 2011; Kroll et al., 2011). The extent of aging in ambient particles is greater than that observed in chamber experiments, and the discrepancy has been attributed to higher SVOC concentrations and shorter oxidation timescales in chamber experiments (Ng et al., 2010). SOA aging has been studied in flow reactors using OH exposures equivalent to 1-20 days of atmospheric oxidation and particle chemical composition was found to follow the same trend in increasing oxygen content as that of ambient OA (Kroll et al., 2009; Lambe et al., 2011). Chapter 3 describes a protocol to extend to 36 h the duration of a chamber experiment and characterizes the chemical aging of SOA formed from *m*-xylene using this protocol. The gas- and particle-phase chemical compositions and SOA mass concentration produced are evaluated to infer aging mechanisms.

Although only a single parent VOC is studied in a chamber experiment, it can be instructive to study SOA from multiple parent VOCs when considering the interactions between SOA produced from multiple sources in the atmosphere. Recent studies suggest that atmospheric OA may exist in an amorphous semi-solid or amorphous solid (glassy) state (e.g. Virtanen et al., 2010; Vaden et al., 2010; Cappa and Wilson, 2011; Shiraiwa et al., 2011; Vaden et al., 2011; Kuwata and Martin, 2012; Perraud et al., 2012; Saukko et al., 2012; Abramson et al., 2013). The physical state of a particle affects its interaction with water and condensing organic compounds and its behavior upon heating or cooling (Koop et al., 2011). Most SOA growth models assume pseudo-ideal mixing, i.e. condensing species quickly diffuse throughout the entire organic particle mass (Odum et al., 1996; Bowman et al., 1997; Odum et al., 1997; Strader et al., 1999). One recent study showed that SOA from  $\alpha$ -pinene ozonolysis and toluene photooxidation was consistent with pseudo-ideal mixing (Hildebrandt et al.,

2011), whereas another study showed that mixed dioctyl phthalane and  $\alpha$ -pinene ozonolysis SOA formed two distinct phases (Vaden et al., 2010). Chapter 4 presents a laboratory chamber protocol designed to probe the mixing state of OA by forming SOA sequentially from two different sources and observing their evaporation behavior upon heating. Using this protocol, SOA from toluene and  $\alpha$ -pinene photooxidation exhibited limited mixing.

## Bibliography

- Abramson, E., Imre, D., Beranek, J., Wilson, J., and Zelenyuk, A.: Experimental determination of chemical diffusion within secondary organic aerosol particles, *Phys. Chem. Chem. Phys.*, 15, 2983–2991, doi:10.1039/C2CP44013J, 2013. 4
- Bernard, F., Eyglunet, G., Daele, V., and Mellouki, A.: Kinetics and products of gas-phase reactions of ozone with methyl methacrylate, methyl acrylate, and ethyl acrylate, *J. Phys. Chem. A*, 114, 8376–8383, doi:10.1021/jp104451v, 2010. 2
- Bowman, F. M., Odum, J. R., Seinfeld, J. H., and Pandis, S. N.: Mathematical model for gas-particle partitioning of secondary organic aerosols, *Atmos. Environ.*, 31, 3921 – 3931, doi:10.1016/S1352-2310(97)00245-8, 1997. 4
- Cappa, C. D. and Wilson, K. R.: Evolution of organic aerosol mass spectra upon heating: implications for OA phase and partitioning behavior, *Atmos. Chem. Phys.*, 11, 1895–1911, doi:10.5194/acp-11-1895-2011, 2011. 4
- Carter, W. P. L., Cocker, D. R., Fitz, D. R., Malkina, I. L., Bumiller, K., Sauer, C. G., Pisano, J. T., Bufalino, C., and Song, C.: A new environmental chamber for evaluation of gas-phase chemical mechanisms and secondary aerosol formation, *Atmos. Environ.*, 39, 7768–7788, doi:10.1016/j.atmosenv.2005.08.040, 2005. 2
- Cocker, D. R., Flagan, R. C., and Seinfeld, J. H.: State-of-the-art chamber facility for studying at-



mospheric aerosol chemistry, *Environ. Sci. Technol.*, 35, 2594–2601, doi:10.1021/es0019169, 2001.

2

Crump, J. G. and Seinfeld, J. H.: Turbulent deposition and gravitational sedimentation of an aerosol in a vessel of arbitrary shape, *J. Aerosol Sci.*, 12, 405–415, doi:10.1016/0021-8502(81)90036-7, 1981. 3

Gentner, D. R., Isaacman, G., Worton, D. R., Chan, A. W. H., Dallmann, T. R., Davis, L., Liu, S., Day, D. A., Russell, L. M., Wilson, K. R., Weber, R., Guha, A., Harley, R. A., and Goldstein, A. H.: Elucidating secondary organic aerosol from diesel and gasoline vehicles through detailed characterization of organic carbon emissions, *P. Natl. Acad. Sci. U.S.A.*, 109, 18 318–18 323, doi:10.1073/pnas.1212272109, 2012. 2

Goldstein, A. H. and Galbally, I. E.: Known and unexplored organic constituents in the earth’s atmosphere, *Environ. Sci. Technol.*, 41, 1514–1521, doi:10.1021/es072476p, 2007. 2

Grosjean, D.: Wall loss of gaseous pollutants in outdoor Teflon chambers, *Environ. Sci. Technol.*, 19, 1059–1065, doi:10.1021/es00141a006, 1985. 3

Hallquist, M., Wenger, J. C., Baltensperger, U., Rudich, Y., Simpson, D., Claeys, M., Dommen, J., Donahue, N. M., George, C., Goldstein, A. H., Hamilton, J. F., Herrmann, H., Hoffmann, T., Iinuma, Y., Jang, M., Jenkin, M. E., Jimenez, J. L., Kiendler-Scharr, A., Maenhaut, W., McFiggans, G., Mentel, T. F., Monod, A., Prévôt, A. S. H., Seinfeld, J. H., Surratt, J. D., Szmigielski, R., and Wildt, J.: The formation, properties and impact of secondary organic aerosol: current and emerging issues, *Atmos. Chem. Phys.*, 9, 5155–5236, doi:10.5194/acp-9-5155-2009, 2009. 2

Heald, C. L., Kroll, J. H., Jimenez, J. L., Docherty, K. S., DeCarlo, P. F., Aiken, A. C., Chen, Q., Martin, S. T., Farmer, D. K., and Artaxo, P.: A simplified description of the evolution of organic aerosol composition in the atmosphere, *Geophys. Res. Lett.*, 37, L08 803, doi:10.1029/2010GL042737, 2010. 4

- Hildebrandt, L., Donahue, N. M., and Pandis, S. N.: High formation of secondary organic aerosol from the photo-oxidation of toluene, *Atmos. Chem. Phys.*, 9, 2973–2986, doi:10.5194/acp-9-2973-2009, 2009. 3
- Hildebrandt, L., Henry, K. M., Kroll, J. H., Worsnop, D. R., Pandis, S. N., and Donahue, N. M.: Evaluating the mixing of organic aerosol components using high-resolution aerosol mass spectrometry, *Environ. Sci. Technol.*, 45, 6329–6335, doi:10.1021/es200825g, 2011. 3, 4
- Keywood, M. D., Varutbangkul, V., Bahreini, R., Flagan, R. C., and Seinfeld, J. H.: Secondary organic aerosol formation from the ozonolysis of cycloalkenes and related compounds, *Environ. Sci. Technol.*, 38, 4157–4164, doi:10.1021/es035363o, 2004. 3
- King, S. M., Rosenoern, T., Shilling, J. E., Chen, Q., and Martin, S. T.: Cloud condensation nucleus activity of secondary organic aerosol particles mixed with sulfate, *Geophys. Res. Lett.*, 34, L24 806, doi:10.1029/2007GL030390, 2007. 2
- Koop, T., Bookhold, J., Shiraiwa, M., and Pöschl, U.: Glass transition and phase state of organic compounds: dependency on molecular properties and implications for secondary organic aerosols in the atmosphere, *Phys. Chem. Chem. Phys.*, 13, 19 238–19 255, doi:10.1039/c1cp22617g, 2011. 4
- Kroll, J. H., Smith, J. D., Che, D. L., Kessler, S. H., Worsnop, D. R., and Wilson, K. R.: Measurement of fragmentation and functionalization pathways in the heterogeneous oxidation of oxidized organic aerosol, *Phys. Chem. Chem. Phys.*, 11, 8005–8014, doi:10.1039/b905289e, 2009. 4
- Kroll, J. H., Donahue, N. M., Jimenez, J. L., Kessler, S. H., Canagaratna, M. R., Wilson, K. R., Altieri, K. E., Mazzoleni, L. R., Wozniak, A. S., Bluhm, H., Mysak, E. R., Smith, J. D., Kolb, C. E., and Worsnop, D. R.: Carbon oxidation state as a metric for describing the chemistry of atmospheric organic aerosol, *Nature Chem.*, 3, 133–139, doi:10.1038/NCHEM.948, 2011. 4
- Kuwata, M. and Martin, S. T.: Phase of atmospheric secondary organic material affects its reactivity, *P. Natl. Acad. Sci. U.S.A.*, 109, 17 354–17 359, doi:10.1073/pnas.1209071109, 2012. 4

- Lambe, A. T., Onasch, T. B., Massoli, P., Croasdale, D. R., Wright, J. P., Ahern, A. T., Williams, L. R., Worsnop, D. R., Brune, W. H., and Davidovits, P.: Laboratory studies of the chemical composition and cloud condensation nuclei (CCN) activity of secondary organic aerosol (SOA) and oxidized primary organic aerosol (OPOA), *Atmos. Chem. Phys.*, 11, 8913–8928, doi:10.5194/acp-11-8913-2011, 2011. 4
- Lee, A., Schade, G. W., Holzinger, R., and Goldstein, A. H.: A comparison of new measurements of total monoterpene flux with improved measurements of speciated monoterpene flux, *Atmos. Chem. Phys.*, 5, 505–513, doi:10.5194/acp-5-505-2005, 2005. 2
- Lee, S., Jang, M., and Kamens, R.: SOA formation from the photooxidation of alpha-pinene in the presence of freshly emitted diesel soot exhaust, *Atmos. Environ.*, 38, 2597–2605, doi:10.1016/j.atmosenv.2003.12.041, 2004. 2
- Lim, Y. B. and Ziemann, P. J.: Effects of molecular structure on aerosol yields from OH radical-initiated reactions of linear, branched, and cyclic alkanes in the presence of NO<sub>x</sub>, *Environ. Sci. Technol.*, 43, 2328–2334, doi:10.1021/es803389s, 2009. 2
- Liu, S., Shilling, J. E., Song, C., Hiranuma, N., Zaveri, R. A., and Russell, L. M.: Hydrolysis of organonitrate functional groups in aerosol particles, *Aerosol Sci. Tech.*, 46, 1359–1369, doi:10.1080/02786826.2012.716175, 2012. 2
- Maddalena, R. L., McKone, T. E., and Kado, N. Y.: Exposure chamber measurements of mass transfer and partitioning at the plant/air interface, *Environ. Sci. Technol.*, 36, 3577–3585, doi:10.1021/es0255554, 2002. 3
- Matsunaga, A. and Ziemann, P. J.: Gas-wall partitioning of organic compounds in a Teflon film chamber and potential effects on reaction product and aerosol yield measurements, *Aerosol Sci. Tech.*, 44, 881–892, doi:10.1080/02786826.2010.501044, 2010. 3
- McGarvey, L. J. and Shorten, C. V.: The effects of adsorption on the reusability of Tedlar® air sampling bags, *Am. Ind. Hyg. Assoc. J.*, 61, 375–380, doi:10.1080/15298660008984546, 2000. 3

- McMurry, P. H. and Grosjean, D.: Gas and aerosol wall losses in Teflon film smog chambers, *Environ. Sci. Technol.*, 19, 1176–1182, doi:10.1021/es00142a006, 1985. 3
- McMurry, P. H. and Rader, D. J.: Aerosol wall losses in electrically charged chambers, *Aerosol Sci. Tech.*, 4, 249–268, doi:10.1080/02786828508959054, 1985. 3
- Nakao, S., Shrivastava, M., Nguyen, A., Jung, H., and Cocker, III, D.: Interpretation of secondary organic aerosol formation from diesel exhaust photooxidation in an environmental chamber, *Aerosol Sci. Tech.*, 45, doi:10.1080/02786826.2011.573510, 2011. 2
- Ng, N. L., Kroll, J. H., Chan, A. W. H., Chhabra, P. S., Flagan, R. C., and Seinfeld, J. H.: Secondary organic aerosol formation from m-xylene, toluene, and benzene, *Atmos. Chem. Phys.*, 7, 3909–3922, doi:10.5194/acp-7-3909-2007, 2007. 3
- Ng, N. L., Canagaratna, M. R., Zhang, Q., Jimenez, J. L., Tian, J., Ulbrich, I. M., Kroll, J. H., Docherty, K. S., Chhabra, P. S., Bahreini, R., Murphy, S. M., Seinfeld, J. H., Hildebrandt, L., Donahue, N. M., DeCarlo, P. F., Lanz, V. A., Prévôt, A. S. H., Dinar, E., Rudich, Y., and Worsnop, D. R.: Organic aerosol components observed in Northern Hemispheric datasets from Aerosol Mass Spectrometry, *Atmos. Chem. Phys.*, 10, 4625–4641, doi:10.5194/acp-10-4625-2010, 2010. 4
- Ng, N. L., Canagaratna, M. R., Jimenez, J. L., Chhabra, P. S., Seinfeld, J. H., and Worsnop, D. R.: Changes in organic aerosol composition with aging inferred from aerosol mass spectra, *Aerosol Sci. Tech.*, 11, 6465–6474, doi:10.5194/acp-11-6465-2011, 2011. 4
- Odum, J. R., Hoffmann, T., Bowman, F., Collins, D., Flagan, R. C., and Seinfeld, J. H.: Gas/particle partitioning and secondary organic aerosol yields, *Environ. Sci. Technol.*, 30, 2580–2585, doi:10.1021/es950943+, 1996. 4
- Odum, J. R., Jungkamp, T. P. W., Griffin, R. J., Flagan, R. C., and Seinfeld, J. H.: The atmospheric aerosol-forming potential of whole gasoline vapor, *Science*, 276, 96–99, doi:10.1126/science.276.5309.96, 1997. 4

- Paulsen, D., Dommen, J., Kalberer, M., Prévôt, A. S. H., Richter, R., Sax, M., Steinbacher, M., Weingartner, E., and Baltensperger, U.: Secondary organic aerosol formation by irradiation of 1,3,5-trimethylbenzene-NO<sub>x</sub>-H<sub>2</sub>O in a new reaction chamber for atmospheric chemistry and physics, *Environ. Sci. Technol.*, 39, 2668–2678, doi:10.1021/es0489137, 2005. 2
- Perraud, V., Bruns, E. A., Ezell, M. J., Johnson, S. N., Yu, Y., Alexander, M. L., Zelenyuk, A., Imre, D., Chang, W. L., Dabdub, D., Pankow, J. F., and Finlayson-Pitts, B. J.: Nonequilibrium atmospheric secondary organic aerosol formation and growth, *P. Natl. Acad. Sci. U.S.A.*, 109, 2836–2841, doi:10.1073/pnas.1119909109, 2012. 4
- Pierce, J. R., Engelhart, G. J., Hildebrandt, L., Weitkamp, E. A., Pathak, R. K., Donahue, N. M., Robinson, A. L., Adams, P. J., and Pandis, S. N.: Constraining particle evolution from wall losses, coagulation, and condensation-evaporation in smog-chamber experiments: Optimal estimation based on size distribution measurements, *Aerosol Sci. Tech.*, 42, 1001–1015, doi:10.1080/02786820802389251, 2008. 3
- Presto, A. A., Hartz, K. E. H., and Donahue, N. M.: Secondary organic aerosol production from terpene ozonolysis. 1. Effect of UV radiation, *Environ. Sci. Technol.*, 39, 7036–7045, doi:10.1021/es050174m, 2005. 2
- Rohrer, F., Bohn, B., Brauers, T., Brüning, D., Johnen, F.-J., Wahner, A., and Kleffmann, J.: Characterisation of the photolytic HONO-source in the atmosphere simulation chamber SAPHIR, *Atmos. Chem. Phys.*, 5, 2189–2201, doi:10.5194/acp-5-2189-2005, 2005. 2
- Rudich, Y., Donahue, N. M., and Mentel, T. F.: Aging of organic aerosol: Bridging the gap between laboratory and field studies, *Annu. Rev. Phys. Chem.*, 58, 321–352, doi:10.1146/annurev.physchem.58.032806.104432, 2007. 4
- Saathoff, H., Mohler, O., Schurath, U., Kamm, S., Dippel, B., and Mihelcic, D.: The AIDA soot aerosol characterisation campaign 1999, *J. Aerosol Sci.*, 34, 1277–1296, doi:10.1016/S0021-8502(03)00363-X, 2003. 2

- Saukko, E., Lambe, A. T., Massoli, P., Koop, T., Wright, J. P., Croasdale, D. R., Pedernera, D. A., Onasch, T. B., Laaksonen, A., Davidovits, P., Worsnop, D. R., and Virtanen, A.: Humidity-dependent phase state of SOA particles from biogenic and anthropogenic precursors, *Atmos. Chem. Phys.*, 12, 7517–7529, doi:10.5194/acp-12-7517-2012, 2012. 4
- Shiraiwa, M., Ammann, M., Koop, T., and Pöschl, U.: Gas uptake and chemical aging of semisolid organic aerosol particles, *P. Natl. Acad. Sci. U.S.A.*, 108, 11 003–11 008, doi:10.1073/pnas.1103045108, 2011. 4
- Siese, M., Becker, K. H., Brockmann, K. J., Geiger, H., Hofzumahaus, A., Holland, F., Mihelcic, D., and Wirtz, K.: Direct measurement of OH radicals from ozonolysis of selected alkenes: A EU-PHORE simulation chamber study, *Environ. Sci. Technol.*, 35, 4660–4667, doi:10.1021/es010150p, 2001. 2
- Strader, R., Lurmann, F., and Pandis, S. N.: Evaluation of secondary organic aerosol formation in winter, *Atmos. Environ.*, 33, 4849–4863, doi:10.1016/S1352-2310(99)00310-6, 1999. 4
- Vaden, T. D., Song, C., Zaveri, R. A., Imre, D., and Zelenyuk, A.: Morphology of mixed primary and secondary organic particles and the adsorption of spectator organic gases during aerosol formation, *P. Natl. Acad. Sci. U.S.A.*, 107, 6658–6663, doi:10.1073/pnas.0911206107, 2010. 4, 5
- Vaden, T. D., Imre, D., Beránek, J., Shrivastava, M., and Zelenyuk, A.: Evaporation kinetics and phase of laboratory and ambient secondary organic aerosol, *P. Natl. Acad. Sci. U.S.A.*, 108, 2190–2195, doi:10.1073/pnas.1013391108, 2011. 4
- Villanueva-Fierro, I., Popp, C. J., and Martin, R. S.: Biogenic emissions and ambient concentrations of hydrocarbons, carbonyl compounds and organic acids from ponderosa pine and cottonwood trees at rural and forested sites in Central New Mexico, *Atmos. Environ.*, 38, 249–260, doi:10.1016/j.atmosenv.2003.09.051, 2004. 2
- Virtanen, A., Joutsensaari, J., Koop, T., Kannosto, J., Yli-Pirila, P., Leskinen, J., Makela, J. M., Holopainen, J. K., Pöschl, U., Kulmala, M., Worsnop, D. R., and Laaksonen, A.: An amorphous

solid state of biogenic secondary organic aerosol particles, *Nature*, 467, 824–827, doi:10.1038/nature09455, 2010. 4

Wang, J., Doussin, J. F., Perrier, S., Perraudin, E., Katrib, Y., Pangu, E., and Picquet-Varraut, B.: Design of a new multi-phase experimental simulation chamber for atmospheric photosmog, aerosol and cloud chemistry research, *Atmos. Meas. Tech.*, 4, 2465–2494, doi:10.5194/amt-4-2465-2011, 2011. 2

Weitkamp, E. A., Sage, A. M., Pierce, J. R., Donahue, N. M., and Robinson, A. L.: Organic aerosol formation from photochemical oxidation of diesel exhaust in a smog chamber, *Environ. Sci. Technol.*, 41, 6969–6975, doi:10.1021/es070193r, 2007. 3

## Chapter 2

# Characterization of Vapor Wall Loss in Laboratory Chambers\*

---

\*Reproduced with permission from “Characterization of vapor wall loss in laboratory chambers” by C. L. Loza, A. W. H. Chan, M. M. Galloway, F. N. Keutsch, R. C. Flagan, and J. H. Seinfeld, *Environmental Science & Technology*, 44, 5074-5078, doi:10.1021/es100727v. Copyright 2010 by the American Chemical Society.



## 2.1 Abstract

Laboratory chambers used to study atmospheric chemistry and aerosol formation are subject to wall loss of vapors and particles that must be accounted for in calculating aerosol yields. While particle wall loss in chambers is relatively well-understood and routinely accounted for, that of vapor is less so. Here we address experimental measurement and modeling of vapor losses in environmental chambers. We identify two compounds that exhibit wall loss: 2,3-epoxy-1,4-butanediol (BEPOX), an analog of an important isoprene oxidation product; and glyoxal, a common volatile organic compound oxidation product. Dilution experiments show that BEPOX wall loss is irreversible on short time scales but is reversible on long time scales, and glyoxal wall loss is reversible for all time scales. BEPOX exhibits minimal uptake onto clean chamber walls under dry conditions, with increasing rates of uptake over the life of an in-use chamber. By performing periodic BEPOX wall loss experiments, it is possible to assess quantitatively the aging of chamber walls.

## 2.2 Introduction

Laboratory chambers are used to elucidate atmospheric chemical mechanisms and secondary organic aerosol (SOA) formation (Hallquist et al., 2009). In experiments performed to measure volatile organic compound (VOC) oxidation products and SOA yields, VOC is oxidized, typically in the presence of seed particles, and particle- and gas-phase concentrations and composition are monitored. Such data allow calculation of the aerosol yield or mass fraction, defined as the ratio of the mass of aerosol formed to the mass of VOC reacted. Throughout an experiment, particles and vapors are inevitably lost to the chamber walls. Neglecting to account for these wall losses can lead to underestimation of SOA yields.

The mechanisms of particle wall loss in chambers are relatively well understood. Crump and Seinfeld (1981) developed the general theory of particle deposition to the walls of a chamber. Later, McMurry and Rader (1985) extended the Crump-Seinfeld theory to include charging effects, and recently, Pierce et al. (2008) have implemented a dynamic model of particle behavior in a vessel.

Physically, particles from the well-mixed core of the chamber are transported through a boundary layer adjacent to the wall by diffusion, gravitational settling, and electrostatic forces. The degree of mixing in the chamber governs the rate that particles move from the bulk of the chamber to the boundary layer. Because it is difficult to describe chamber mixing theoretically, experimental measurements are used to determine the chamber mixing characteristics. An effective method of experimentally characterizing particle wall loss involves measuring the decay rate of a population of polydisperse particles injected into the chamber. The decay of particle concentrations in each size range is subsequently fitted to a first-order loss model in terms of a wall loss coefficient,  $\beta$ , as a function of particle size,  $D_p$  (Keywood et al., 2004; Ng et al., 2007).

Vapor molecules present in a chamber can also deposit on the walls, with a rate that depends on the molecular diffusivity of the species, the thickness of the boundary layer adjacent to the wall, and the concentration gradient in the boundary layer. Whereas it is generally assumed that, upon contact, particles adhere to the wall, not every vapor molecule sticks to the chamber wall with unit efficiency. Vapor molecules may also undergo reactions at the chamber wall, influencing the rate of uptake. These processes are depicted in Fig. 2.1.

Relatively few studies exist devoted to measuring vapor-phase wall uptake in environmental chambers. Chamber walls, typically made of Teflon, have usually been assumed to be clean and inert such that no vapor-phase uptake occurs (e.g. Bowman et al., 1997); nevertheless, vapor uptake may occur on particles that have deposited to the walls during a particular experiment (Hildebrandt et al., 2009). Deposited particles and other species may also remain on the chamber walls after continued use, despite repeated baking and flushing. For example, McGarvey and Shorten (2000) found that some organic compounds adsorbed to Tedlar sampling bags could not be removed completely by flushing and heating. Maddalena et al. (2002) observed semivolatile compounds partitioned to Teflon exposure chamber walls and experimentally determined an effective volume, combining the chamber air and wall volumes, to correct for wall loss. Because little is known about species-wall interactions for most compounds, it is necessary to calibrate wall loss on a case-by-case basis, similar to that for particle wall loss.

We present here an experimental protocol to determine the nature of wall loss of VOCs in laboratory chambers. We study two compounds, both of which partition to the walls but re-partition to the gas phase on different time scales. Wall loss coefficients for each compound are determined experimentally and are found to depend on humidity and chamber aging characteristics. The derived wall loss coefficient is then used to examine simultaneous uptake of a VOC by seed particles and chamber walls to assess the magnitudes of each process. By comparison with experimental data, an uptake coefficient can be determined for the VOC onto seed particles. The studies presented here suggest a protocol to characterize the state of chamber walls over the lifetime of a chamber.

## 2.3 Experimental Section

The experiments reported here were performed in the Caltech indoor, dual 28 m<sup>3</sup> Teflon environmental chambers, details of which are given elsewhere (Cocker et al., 2001; Keywood et al., 2004). For these experiments, the temperature of the chambers was held at 20 ( $\pm$ 1) °C.

Two compounds were selected for study: (1) 2,3-epoxy-1,4-butanediol (BEPOX) is the butadiene derivative of an epoxydiol of isoprene (IEPOX), an important product of isoprene photooxidation and one characteristic, more generally, of products of VOC oxidation that lead to SOA (Paulot et al., 2009; Surratt et al., 2010); and (2) glyoxal, a key atmospheric VOC oxidation product (Fu et al., 2008; Myriokefalitakis et al., 2008). BEPOX and glyoxal have been found to partition to chamber walls on a time scale comparable to those of photooxidation and aerosol uptake. BEPOX was synthesized following methods detailed in Paulot et al. (2009) and injected into the chamber by flowing clean air over a heated sample. BEPOX concentration was monitored with chemical ionization mass spectrometry (CIMS) in negative mode using CF<sub>3</sub>O<sup>-</sup> as a reagent ion. Glyoxal was synthesized following methods detailed in Galloway et al. (2009) and injected into the chamber in the gas phase. Glyoxal was detected using the Madison Laser-Induced Phosphorescence (LIP) Instrument (Huisman et al., 2008).

To determine wall loss coefficients for BEPOX and glyoxal, the compound was injected into a dark, clean chamber, and its concentration was monitored over time. To study wall loss reversibility,

after BEPOX or glyoxal equilibrated with the chamber walls, the chamber contents were diluted by flushing with clean air. Isoprene exhibits negligible wall loss (when isoprene was injected into a clean chamber, its concentration remained constant for 15 h) and was added as a dilution tracer. To detect isoprene, chamber air was drawn through a 10 mL sample loop before injection onto a HP-Plot-Q 15 m x 0.15 mmID x 40  $\mu$ m thickness column installed on a gas chromatograph equipped with a flame ionization detector (GC/FID, Agilent 6890N). The GC response was calibrated by vaporizing a known volume of isoprene into a 55 L chamber.

In experiments to study BEPOX interactions with the chamber walls and particles, acidic ammonium sulfate seed particles were added before BEPOX injection by atomizing a 0.1 M ammonium sulfate with 0.1 M sulfuric acid (AS+SA) solution. The aerosol size distribution and number concentration were measured continuously using a differential mobility analyzer (DMA, TSI, Inc., 3081) coupled to a condensation particle counter (CPC, TSI, Inc., 3760).

## 2.4 Results and Discussion

### 2.4.1 Vapor Wall Loss

Figure 2.2 shows first-order wall loss for BEPOX as a function of RH measured in chambers that had been in use for approximately two years. The first-order BEPOX wall loss coefficient,  $k_w$ , was found to vary linearly with RH (see inset in Fig. 2.2). After new chambers were installed in May 2009, wall loss greatly decreased (Table 2.1). For dry conditions (RH < 10 %), no wall loss was seen immediately after installing the new chambers. Over the next five months, wall loss increased but remained less than that for the previous chambers. Glyoxal wall loss, measured in chambers that had been in use for approximately one year, is shown in Fig. 2.3. Under dry conditions, glyoxal wall loss was minimal, with  $k_w = 9.6 \times 10^{-7} \text{ s}^{-1}$ . However, at 61 % RH,  $k_w$  for glyoxal was calculated as  $4.7 \times 10^{-5} \text{ s}^{-1}$ .

Different wall loss mechanisms were observed when comparing dilution experiments for BEPOX and glyoxal. After injection, both compounds underwent deposition to the chamber walls. As the

chamber was diluted, the BEPOX concentration continued to decrease (see top panel of Fig. 2.4). Initially, the BEPOX concentration is lower than the predicted concentration for dilution as the only sink; however, it is greater than the predicted concentration with both dilution and wall loss (calculated from the pre-dilution period shown in the inset of the top panel). It is possible that the wall loss rate decreased with the onset of dilution, which could be a result of wall saturation. As shown in the inset, BEPOX wall loss followed a first-order decay until dilution began. The lack of non-linearity suggests that the walls were not saturated with BEPOX before dilution; it is unlikely that the onset of dilution would cause the walls to become saturated with BEPOX and change the wall loss rate substantially. After approximately 7 h, the rate of BEPOX decay decreased to a rate less than the dilution rate. At this time, BEPOX began to re-partition to the gas phase suggesting that the walls may have become saturated and henceforth acted as a BEPOX source. Upon dilution, the glyoxal concentration remained constant for the first 7 h before decreasing slightly (see bottom panel of Fig. 2.4). The constant glyoxal concentration during dilution reflects re-partitioning from the walls to the vapor phase. Because the walls were saturated with glyoxal before dilution began, re-partitioning commenced immediately upon dilution. After 7 h of dilution, it is likely that most of the glyoxal deposited to the walls had already re-partitioned to the vapor phase and been removed by flushing, and glyoxal concentration decreased as dilution continued. We conclude that under timescales relevant to chamber experiments, glyoxal wall loss can be considered reversible whereas BEPOX wall loss is irreversible; however, it should be noted that BEPOX wall loss is also reversible on longer time scales.

### 2.4.2 Model Description

Interactions among BEPOX, AS+SA seed particles, and chamber walls were considered in developing a general model for the dynamics of a vapor that irreversibly deposits on particles and walls. Assuming a constant chamber volume, the time rate of change of vapor-phase concentration,  $c_A$  (molecules  $\text{cm}^{-3}$ ), is

$$\frac{dc_A}{dt} = - \sum_{i=1}^m C_{i,s} N_{i,s} - \sum_{j=1}^m C_{j,w} N_{j,w} - k_w c_A \quad (2.1)$$

where  $t$  is time (s),  $m$  is the total number of particle size bins,  $C_{i,s}$  are the condensation coefficients to suspended particles (molecules  $\text{s}^{-1}$ ),  $N_{i,s}$  are the number densities of suspended particles (particles  $\text{cm}^{-3}$ ),  $C_{j,w}$  are the condensation coefficients to deposited particles (molecules  $\text{s}^{-1}$ ), and  $N_{j,w}$  are the number densities of deposited particles (particles  $\text{cm}^{-3}$ );  $k_w$  has units of  $\text{s}^{-1}$ .

The condensation coefficients describe the flux of gas-phase species to a particle surface. For a compound partitioning to a spherical particle with a diameter,  $D_p$  (cm), Bowman et al. (1997) employed the following condensation coefficient:

$$C = \frac{2\pi D_p \lambda \bar{c} (c_A - c_{A,e})}{1 + \frac{8\lambda}{\alpha D_p}} \quad (2.2)$$

where  $\alpha$ , the accommodation coefficient for uptake onto seed particles, represents the fraction of collisions that result in a vapor molecule sticking to a particle surface. Fitting model predictions to experimental data allows estimation of the value of  $\alpha$  specific to a particular vapor compound. In addition,  $\lambda$  is the mean free path of air (cm),  $\bar{c}$  is the mean molecular speed of the compound ( $\text{cm s}^{-1}$ ), and  $c_{A,e}$  is the equilibrium concentration of the compound adjacent to the particle surface ( $\text{molecules cm}^{-3}$ ). Particles deposited on the chamber walls are assumed to be characterized by the same size-dependent condensation coefficients as those suspended when taking into account condensation to deposited particles.

The rate of change of the particle number distribution is affected by condensation and wall loss. Particle concentrations are sufficiently small such that coagulation is neglected for the timescale of the model; at a number concentration of  $1.2 \times 10^4 \text{ cm}^{-3}$ , the characteristic time for coagulation is 1.3 days (Cocker et al., 2001). New particle formation by nucleation is neglected as the vapor concentration is relatively low. Size-dependent particle wall loss is parameterized by  $\beta_i(D_p)$  ( $\text{s}^{-1}$ ). Accounting for these processes in the aerosol general dynamic equation gives the change in number distribution,  $n(D_p, t)$  (particles  $\text{cm}^{-3} \text{ cm}^{-1}$ ) (Seinfeld and Pandis, 2006):

$$\frac{\partial n(D_p, t)}{\partial t} = -\frac{\partial}{\partial D_p} [I_D(D_p, t) n(D_p, t)] \pm \beta(D_p) n(D_p, t) \quad (2.3)$$

where  $I_D(D_p, t)$  ( $\text{cm s}^{-1}$ ) is the rate of change of particle diameter as a result of condensation. For suspended particles, the  $\beta(D_p)n(D_p, t)$  term is a sink and for particles deposited to the wall, the  $\beta(D_p)n(D_p, t)$  term is a source. Assuming spherical particles,

$$I_D(D_p, t) = \frac{dD_p}{dt} = \frac{2C_m}{\pi D_p^2 \rho_p} \quad (2.4)$$

where  $C_m$  is a mass condensation coefficient ( $\text{g s}^{-1}$ ) of the same form as  $C$ , and  $\rho_p$  is the aerosol density ( $\text{g cm}^{-3}$ ).

In applying the model, initial concentrations for BEPOX and particles were taken from those measured immediately following BEPOX injection. No particles are assumed to be present initially on the walls. The seed particles were divided into 111 size bins, the same resolution as that of the DMA, with diameters from 15 nm to 802 nm. The density of the organic matter in the particle is taken as 1.25, that of low- $\text{NO}_x$  isoprene SOA (Kroll et al., 2006). The density used in the particle number balance is 1.60, a weighted average of the densities of AS+SA particles and organic matter. For BEPOX, wall uptake was governed by the experimentally-determined  $k_w$  *v.* RH relationship. For particle wall loss,  $\beta(D_p)$  was calculated from particle wall loss calibration experiments.

### 2.4.3 Model Predictions

Figure 2.5 shows the simulation of a BEPOX uptake experiment with AS+SA seed particles. A value of  $\alpha = 6 \times 10^{-4}$  was found to produce the best fit of both vapor- and particle-phase processes. After the injection period, BEPOX partitions to particles and the chamber walls. The predicted BEPOX concentration matches that observed ( $R^2 = 0.979$ ). Prediction of suspended particle volume concentration without particle wall loss corrections also matches chamber observations. Any particle growth due to BEPOX condensation is offset by particle loss to the chamber walls; thus the suspended aerosol volume appears to decrease.

The decrease in BEPOX concentration is the result of two main processes: wall loss and condensation to suspended particles. Condensation to particles deposited on the wall is predicted to

be much less than either wall loss or condensation to suspended particles; however, in chambers exhibiting more prominent particle wall loss, this may be a larger factor because a greater proportion of the original particles are deposited to the walls throughout the experiment. Figure 2.6 shows the predicted contribution of each process. In this case, wall uptake limits the amount of BEPOX available to partition to particles. It should be noted that the fate of particles, once deposited to the walls, is unknown. If the walls are coated with material accumulated from previous experiments not removed by baking and flushing procedures, deposited particles may combine with this material and interact with vapors no longer as individual particles but as part of the coating on the walls. In this case, the deposited particles do not act as a separate sink for BEPOX and are part of the wall loss sink.

To accurately quantify processes occurring in the chamber, suspended aerosol number distributions and volume concentrations and vapor-phase concentrations can be corrected for wall loss. The effects of wall loss correction methods on predicted BEPOX consumed,  $\Delta\text{VOC}$ , and aerosol growth,  $\Delta M_o$ , were examined using two cases for VOC and two cases for particles. Cases (a) and (b) are vapor-phase assumptions in calculating  $\Delta\text{VOC}$ , and cases (c) and (d) are particle-phase assumptions in calculating  $\Delta M_o$ ; case (c) represents a lower bound estimate and case (d) represents an upper bound estimate for vapor condensation to deposited particles, as suggested by Hildebrandt et al. (2009). The equations governing these cases are presented in Table 2.2. A comparison of the vapor and particle wall loss correction cases with experimental data is shown in Fig. 2.7. Although experimental data are corrected for wall loss with cases (a) and (c), they do not match the corresponding model predictions. From Fig. 2.5, the predicted particle volume is slightly less than the average experimental volume, thus the experiment  $\Delta M_o$  will be larger than the predicted  $\Delta M_o$ , and the experimental data have a steeper slope than predicted case (a,c).

BEPOX wall loss is substantial such that vapor-particle mass conservation cannot be established without determining the amount of BEPOX deposited to the wall, as seen when comparing cases (a) and (b). The  $\Delta\text{VOC}$  in case (b) is significantly less than that in case (a). BEPOX uptake onto deposited particles increases throughout the experiment as more particles deposit to the wall;



if corrections for this uptake are not made, i.e. case (c), a nonlinear trend is observed between  $\Delta M_o$  and  $\Delta \text{VOC}$  that leads to a smaller final  $\Delta M_o$  than case (d). After the 4 h simulated,  $\Delta M_o$  for case (c) was 8.5 % lower than that for case (d). This difference could increase for chambers exhibiting more particle wall loss and over the course of longer experiments. Theoretically, during an uptake experiment, a plot of  $\Delta M_o$  v.  $\Delta \text{VOC}$  should be linear because the mass lost from the vapor phase is proportional to the mass gained by the particles, taking into account the possibility of co-condensing species or further particle-phase reactions. Incorrect wall loss assumptions could result in nonlinearities. To obtain accurate particle wall loss corrections, it is necessary to establish the nature of the interactions of deposited particles with vapors in the chamber bulk; however, without this knowledge, it is still possible to obtain upper- and lower-bound estimates to quantify the error associated with wall loss corrections.

## 2.5 Implications for Chamber Experiments

To properly understand gas-particle partitioning of a compound in a laboratory chamber, it is necessary to determine the extent of its interactions with the chamber walls and account for this in designing experiments and analyzing data. Wall losses of certain vapor compounds can be significant, depending on the system: history of chamber walls, RH, etc. Because all chemical species do not exhibit similar wall losses, it is probable that wall loss is dependent on the compound’s molecular structure, suggesting reactive uptake at the walls in addition to diffusion. As a result, it may be possible to predict the tendency for a compound to deposit on walls based on its chemical structure.

During chamber experiments with a compound, such as glyoxal, that exhibits reversible wall deposition, the walls may become saturated with VOC before all relevant vapor-phase reactions have been completed. In this case, the walls may serve as a source of the vapor. As the compound reacts or partitions to particles, some of it will re-partition from the walls to replenish what has been lost from the vapor phase.

Further complications arise in correcting for wall loss for a compound that is a first- or second-generation oxidation product. Wall loss may be more difficult to detect and separate from the

kinetics of further oxidation reactions or reactions in the aerosol phase. Identifying the importance of wall loss in later-generation oxidation products underscores the need to understand the chemical mechanism of hydrocarbon oxidation leading to SOA formation. With a mechanism, it is possible to identify compounds that are structurally similar to other compounds with substantial wall loss, the extent to which those compounds contribute to SOA, and the relative rates of subsequent reactions and wall loss processes.

## 2.6 Acknowledgements

This work was supported by the Office of Science (Biological and Environmental Research), Electric Power Research Institute, U.S. Department of Energy Grant DE-FG02-05ER63983, and U.S. Environmental Protection Agency (EPA) STAR agreement RD-833749. The CIMS instrument was purchased as part of a major research instrumentation grant from the National Science Foundation (Grant ATM-0619783); assembly and testing was supported by the Davidow Discovery Fund. Development of the Madison-LIP instrument was supported by the National Science Foundation (Grant ATM-0724912) and a Dreyfus New Faculty award. We thank John D. Crounse and Nathan C. Eddingsaas for synthesizing and characterizing (with H-NMR) the BEPOX. Christine Loza was supported by a National Science Foundation Graduate Research Fellowship.

## Bibliography

- Bowman, F. M., Odum, J. R., Seinfeld, J. H., and Pandis, S. N.: Mathematical model for gas-particle partitioning of secondary organic aerosols, *Atmos. Environ.*, 31, 3921 – 3931, doi:10.1016/S1352-2310(97)00245-8, 1997. 15, 19
- Cocker, D. R., Flagan, R. C., and Seinfeld, J. H.: State-of-the-art chamber facility for studying atmospheric aerosol chemistry, *Environ. Sci. Technol.*, 35, 2594–2601, doi:10.1021/es0019169, 2001. 16, 19

- Crump, J. G. and Seinfeld, J. H.: Turbulent deposition and gravitational sedimentation of an aerosol in a vessel of arbitrary shape, *J. Aerosol Sci.*, 12, 405–415, 1981. 14
- Fu, T. M., Jacob, D. J., Wittrock, F., Burrows, J. P., Vrekoussis, M., and Henze, D. K.: Global budgets of atmospheric glyoxal and methylglyoxal, and implications for formation of secondary organic aerosols, *J. Geophys. Res-Atmos.*, 113, D15 303, doi:10.1029/2007JD009505, 2008. 16
- Galloway, M. M., Chhabra, P. S., Chan, A. W. H., Surratt, J. D., Flagan, R. C., Seinfeld, J. H., and Keutsch, F. N.: Glyoxal uptake on ammonium sulphate seed aerosol: reaction products and reversibility of uptake under dark and irradiated conditions, *Atmos. Chem. Phys.*, 9, 3331–3345, 2009. 16
- Hallquist, M., Wenger, J. C., Baltensperger, U., Rudich, Y., Simpson, D., Claeys, M., Dommen, J., Donahue, N. M., George, C., Goldstein, A. H., Hamilton, J. F., Herrmann, H., Hoffmann, T., Iinuma, Y., Jang, M., Jenkin, M. E., Jimenez, J. L., Kiendler-Scharr, A., Maenhaut, W., McFiggans, G., Mentel, T. F., Monod, A., Prevot, A. S. H., Seinfeld, J. H., Surratt, J. D., Szmigielski, R., and Wildt, J.: The formation, properties and impact of secondary organic aerosol: current and emerging issues, *Atmos. Chem. Phys.*, 9, 5155–5236, 2009. 14
- Hildebrandt, L., Donahue, N. M., and Pandis, S. N.: High formation of secondary organic aerosol from the photo-oxidation of toluene, *Atmos. Chem. Phys.*, 9, 2973–2986, doi:10.5194/acp-9-2973-2009, 2009. 15, 21
- Huisman, A. J., Hottle, J. R., Coens, K. L., DiGangi, J. P., Galloway, M. M., Kammrath, A., and Keutsch, F. N.: Laser-induced phosphorescence for the in situ detection of glyoxal at part per trillion mixing ratios, *Anal. Chem.*, 80, 5884–5891, doi:10.1021/ac800407b, 2008. 16
- Keywood, M. D., Varutbangkul, V., Bahreini, R., Flagan, R. C., and Seinfeld, J. H.: Secondary organic aerosol formation from the ozonolysis of cycloalkenes and related compounds, *Environ. Sci. Technol.*, 38, 4157–4164, doi:10.1021/es.035363o, 2004. 15, 16
- Kroll, J. H., Ng, N. L., Murphy, S. M., Flagan, R. C., and Seinfeld, J. H.: Secondary organic

- aerosol formation from isoprene photooxidation, *Environ. Sci. Technol.*, 40, 1869–1877, doi:10.1021/es0524301, 2006. 20
- Maddalena, R. L., McKone, T. E., and Kado, N. Y.: Exposure chamber measurements of mass transfer and partitioning at the plant/air interface, *Environ. Sci. Technol.*, 36, 3577–3585, 2002. 15
- McGarvey, L. J. and Shorten, C. V.: The effects of adsorption on the reusability of Tedlar <sup>®</sup>air sampling bags, *Am. Ind. Hyg. Assoc. J.*, 61, 375–380, 2000. 15
- McMurry, P. H. and Rader, D. J.: Aerosol wall losses in electrically charged chambers, *Aerosol Sci. Tech.*, 4, 249–268, 1985. 14
- Myriokefalitakis, S., Vrekoussis, M., Tsigaridis, K., Wittrock, F., Richter, A., Bruhl, C., Volkamer, R., Burrows, J. P., and Kanakidou, M.: The influence of natural and anthropogenic secondary sources on the glyoxal global distribution, *Atmos. Chem. Phys.*, 8, 4965–4981, 2008. 16
- Ng, N. L., Kroll, J. H., Chan, A. W. H., Chhabra, P. S., Flagan, R. C., and Seinfeld, J. H.: Secondary organic aerosol formation from *m*-xylene, toluene, and benzene, *Atmos. Chem. Phys.*, 7, 3909–3922, 2007. 15
- Paulot, F., Crounse, J. D., Kjaergaard, H. G., Kurten, A., St Clair, J. M., Seinfeld, J. H., and Wennberg, P. O.: Unexpected epoxide formation in the gas-phase photooxidation of isoprene, *Science*, 325, 730–733, doi:10.1126/science.1172910, 2009. 16
- Pierce, J. R., Engelhart, G. J., Hildebrandt, L., Weitkamp, E. A., Pathak, R. K., Donahue, N. M., Robinson, A. L., Adams, P. J., and Pandis, S. N.: Constraining particle evolution from wall losses, coagulation, and condensation-evaporation in smog-chamber experiments: Optimal estimation based on size distribution measurements, *Aerosol Sci. Tech.*, 42, 1001–1015, doi:10.1080/02786820802389251, 2008. 14
- Seinfeld, J. H. and Pandis, S. N.: *Atmospheric Chemistry and Physics*, John Wiley and Sons, Inc., Hoboken, N.J., 2 edn., 2006. 19

Surratt, J. D., Chan, A. W. H., Eddingsaas, N. C., Chan, M., Loza, C. L., Kwan, A. J., Hersey, S. P., Flagan, R. C., Wennberg, P. O., and Seinfeld, J. H.: Reactive intermediates revealed in secondary organic aerosol formation from isoprene, *P. Natl. Acad. Sci. U.S.A.*, 107, 6640–6645, 2010. 16

**Table 2.1:** BEPOX wall loss coefficients,  $k_w$ , as a function of chamber age.

Date (2009)	RH (%)	$k_w$ ( $s^{-1}$ )	Age <sup>a</sup>
03/07	10.0	$3.68 \times 10^{-5}$	110
05/14	11.5	$\approx 0$	0
09/08	8.0	$1.55 \times 10^{-5}$	28
10/01	8.4	$3.11 \times 10^{-5}$	36

<sup>a</sup> Age is measured in number of experiments previously performed in the chamber.

**Table 2.2:** Wall loss cases for vapors and particles<sup>a</sup>

Case	Calculation
(a)	$\Delta VOC(t) = VOC_{sus}(0) - VOC_{sus}(t)$
(b)	$\Delta VOC(t) = VOC_{sus}(0) - VOC_{sus}(t) - VOC_w(t)$
(c)	$\Delta M_o(t) = M_{sus}(t) + M_w(t) - M_{sus}(0)$
(d)	$\Delta M_o(t) = M_{sus}(t) + M_{w+cond}(t) - M_{sus}(0)$

<sup>a</sup>  $VOC_{sus}$  is the suspended VOC concentration,  $VOC_w$  is the VOC concentration deposited to the walls since time 0,  $M_{sus}$  is suspended particle concentration,  $M_w$  is the total concentration of particles deposited to the walls since time 0 with no condensation to deposited particles, and  $M_{w+cond}$  is the total concentration of particles deposited to the walls since time zero allowing for condensation to deposited particles at the same rate as condensation to suspended particles.

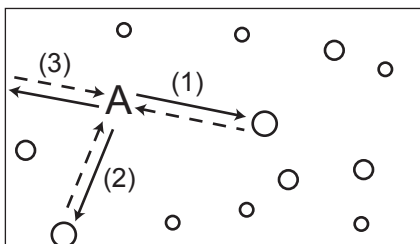


**Figure 2.1:** Sinks for a vapor-phase species, A, in a laboratory chamber. The vapor can condense on suspended particles (1), particles deposited on the chamber walls (2), and the surface of the chamber walls (3). These processes may be reversible or irreversible, as indicated by the dashed arrows.

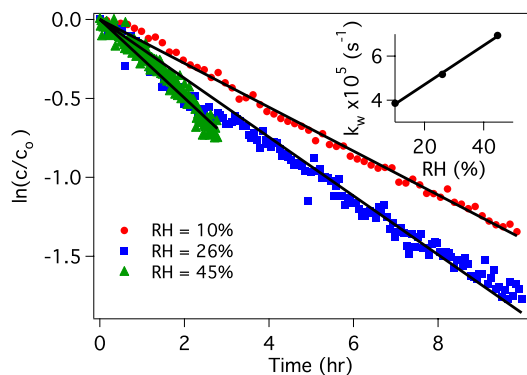


**Figure 2.2:** First-order wall loss of BEPOX. The slope of the lines fitted through each data set is the first-order wall loss coefficient,  $k_w$ . The inset shows the trend for BEPOX  $k_w$  as a function of RH.

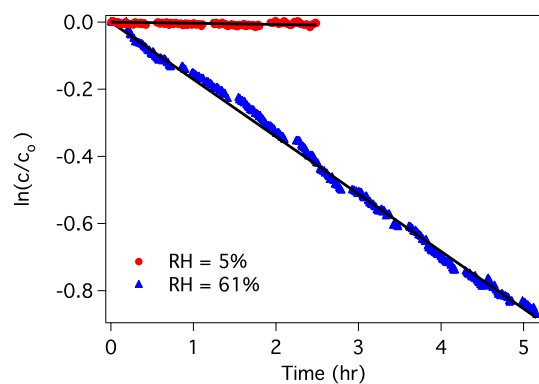


**Figure 2.3:** First-order wall loss of glyoxal under dry and humid conditions. The slope of the lines fitted through each data set is the first-order wall loss coefficient,  $k_w$ .

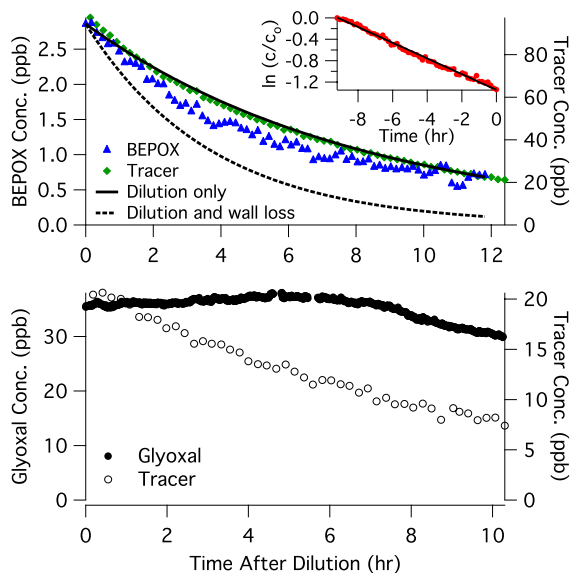


**Figure 2.4:** Reversibility of BEPOX and glyoxal wall loss upon chamber dilution with clean air. The top panel shows experimental and calculated BEPOX concentrations using dilution alone or wall loss (measured before the onset of dilution as shown in the inset) and dilution as sinks. BEPOX concentration decreases initially and begins to level off after approximately 10 h. BEPOX wall loss is irreversible on short time scales but becomes reversible on longer time scales. In the bottom panel, glyoxal concentration remains constant after dilution starts, showing that glyoxal wall loss is reversible for all time scales. Glyoxal concentration eventually begins to decrease as the dilution progresses, indicating that the walls are no longer serving as a significant glyoxal reservoir. In both panels, the tracer compound (isoprene) tracks the progress of the dilution.

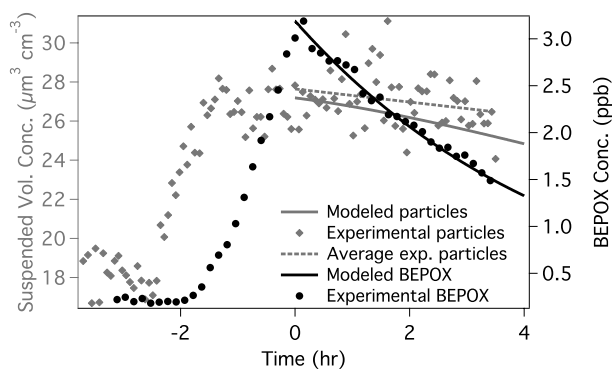


**Figure 2.5:** Model comparison with data from a BEPOX uptake experiment. The model is initialized using experimental conditions after the BEPOX injection is complete and BEPOX concentration reaches a maximum.



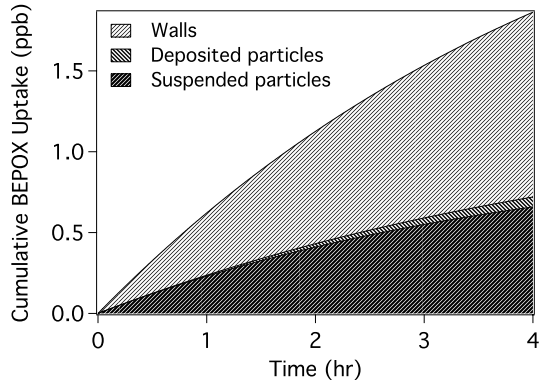


**Figure 2.6:** Predictions for total BEPOX sinks after injection during an uptake experiment with AS+SA seed, showing contributions of the three different mechanisms. Wall loss is the largest BEPOX sink for the chosen model parameters, whereas the effect of uptake on deposited aerosol is small.

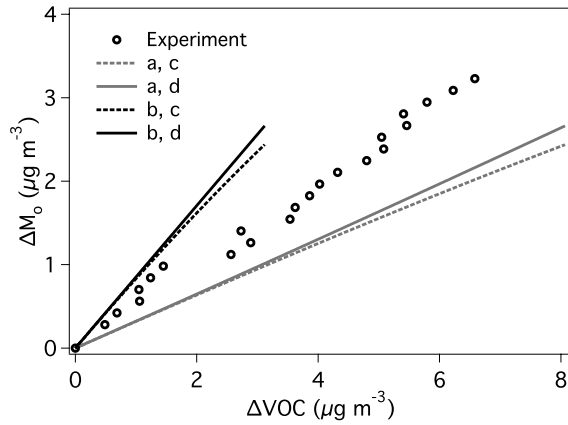


**Figure 2.7:** Observed and predicted BEPOX uptake,  $\Delta\text{VOC}$ , and aerosol mass growth,  $\Delta M_o$ , during an uptake experiment with AS+SA seed. Wall loss cases (a) - (d) are defined in 2.2.

## Chapter 3

# Chemical Aging of *m*-Xylene Secondary Organic Aerosol: Laboratory Chamber Study\*

---

\*Reproduced with permission from “Chemical aging of *m*-xylene secondary organic aerosol: laboratory chamber study” by C. L. Loza, P. S. Chhabra, L. D. Yee, J. S. Craven, R. C. Flagan, and J. H. Seinfeld, *Atmospheric Chemistry and Physics*, 12, 151-167, doi:10.5194/acp-12-151-2012. Copyright 2012 by Authors.

### 3.1 Abstract

Secondary organic aerosol (SOA) can reside in the atmosphere for a week or more. While its initial formation from the gas-phase oxidation of volatile organic compounds tends to take place in the first few hours after emission, SOA can continue to evolve chemically over its atmospheric lifetime. Simulating this chemical aging over an extended time in the laboratory has proven to be challenging. We present here a procedure for studying SOA aging in laboratory chambers that is applied to achieve 36 h of oxidation. The formation and evolution of SOA from the photooxidation of *m*-xylene under low-NO<sub>x</sub> conditions and in the presence of either neutral or acidic seed particles is studied. In SOA aging, increasing molecular functionalization leads to less-volatile products and an increase in SOA mass, whereas gas- or particle-phase fragmentation chemistry results in more-volatile products and a loss of SOA. The challenge is to discern from measured chamber variables the extent to which these processes are important for a given SOA system. In the experiments conducted, *m*-xylene SOA mass, calculated under the assumption of size-invariant particle composition, increased over the initial 12-13 h of photooxidation and decreased beyond that time, suggesting the existence of fragmentation chemistry. The oxidation of the SOA, as manifested in the O:C elemental ratio and fraction of organic ion detected at  $m/z$  44 measured by the Aerodyne aerosol mass spectrometer, increased continuously starting after 5 h of irradiation until the 36 h termination. This behavior is consistent with an initial period in which, as the mass of SOA increases, products of higher volatility partition to the aerosol phase, followed by an aging period in which gas- and particle-phase reaction products become increasingly more oxidized. When irradiation is stopped 12.4 h into one experiment, and OH generation ceases, minimal loss of SOA is observed, indicating that the loss of SOA is either light- or OH-induced. Chemical ionization mass spectrometry measurements of low-volatility *m*-xylene oxidation products exhibit behavior indicative of continuous photooxidation chemistry. A condensed chemical mechanism of *m*-xylene oxidation under low-NO<sub>x</sub> conditions is capable of reproducing the general behavior of gas-phase evolution observed here. Moreover, order of magnitude analysis of the mechanism suggests that gas-phase OH reaction of low volatility SOA precursors is the dominant pathway of aging in the *m*-xylene system although OH reaction with

particle surfaces cannot be ruled out. Finally, the effect of size-dependent particle composition and size-dependent particle wall loss rates on different particle wall loss correction methods is discussed.

## 3.2 Introduction

Organic aerosol (OA) constitutes 20-90% of all submicron particles in the atmosphere, and up to 80% of this is classified as secondary organic aerosol (SOA) (Zhang et al., 2007; Murphy et al., 2006). Aerosol particles in the atmosphere can have lifetimes of 5-12 days (Balkanski et al., 1993), during which they can undergo continuous physical and chemical processing, commonly called aging (Rudich et al., 2007). Laboratory experiments designed to study SOA formation typically have a duration of up to 1 day, during which all processes that cause ambient particle aging may not be captured. Chemical aging of SOA can affect gas-particle partitioning through processes such as vapor-phase oxidation of semivolatiles, heterogeneous oxidation, and reactions within the particle phase, e.g. oligomerization, that take place on a fairly long timescale (Kroll and Seinfeld, 2008; Hallquist et al., 2009).

Given the potentially large number of organic species in ambient particles, bulk chemical measurements are useful to describe the extent of oxidative aging of SOA. Using aerosol mass spectrometry, changes in O:C (elemental oxygen to carbon ratio) and H:C (elemental hydrogen to carbon ratio) from high-resolution data and  $f_{44}$  (ratio of mass-to-charge ( $m/z$ ) 44 to total signal in the organic component mass spectrum) and  $f_{43}$  (ratio of  $m/z$  43 to total signal in the organic component mass spectrum) have been reported for ambient and laboratory-generated particles. The dominant organic ion at  $m/z$  43 is  $\text{C}_2\text{H}_3\text{O}^+$ , and the dominant organic ion at  $m/z$  44 is  $\text{CO}_2^+$ . Ng et al. (2010) evaluated a number of aerosol oxidation data sets in the  $f_{44}$ - $f_{43}$  space and found that data for ambient OA tend to occupy a triangular region. As the OA becomes more oxidized, it tends to move from a region of lower  $f_{44}$  and a wider range of  $f_{43}$  at the base of the triangle toward the apex with higher  $f_{44}$  and less variable  $f_{43}$ . Heald et al. (2010) used the Van Krevelen diagram to show that the H:C and O:C of total ambient OA tend to fall along a line with a slope of  $-1$ , suggesting, on average, equal additions of carbonyl and alcohol moieties. More recently, Ng et al. (2011) determined

a correlation between  $f_{43}$  and H:C and, combined with a correlation between  $f_{44}$  and O:C (Aiken et al., 2008), mapped the triangular region in  $f_{44}$ - $f_{43}$  space onto the Van Krevelen diagram. They found that for ambient OA classified as oxygenated OA (OOA) and laboratory chamber-generated SOA the H:C and O:C evolution toward the apex of the triangle tends to fall along a line with a slope of  $-0.5$  on a Van Krevelen diagram. This difference in slope between the two studies was attributed to the inclusion of primary OA in the study of Heald et al. The evolution of ambient OA can also be represented in terms of saturation concentration ( $C^*$ ) and O:C (Jimenez et al., 2009). As the OA becomes more oxidized,  $C^*$  decreases and O:C increases. In all three of these frameworks, the oxygen content of the organic aerosol increases upon aging.

Laboratory studies have been conducted to probe the mechanisms of chemical aging of SOA. In flow reactor experiments, which have much shorter residence times than chamber experiments, OH concentrations a few orders of magnitude higher than ambient concentrations are used to attain OH exposure similar to that of multiple days of atmospheric processing. Using a flow reactor, Kroll et al. (2009) found that for oxidation of squalane ( $C_{30}H_{36}$ ) particles, functionalization reactions (addition of polar functional groups) dominated at low OH exposure, and fragmentation reactions (scission of C-C bonds in the carbon skeleton) dominated as OH exposure increased. They observed an O:C ratio of 0.45 after 35.8 squalene OH oxidation lifetimes. Lambe et al. (2011) also used a flow reactor to attain OH exposures equivalent to 1-20 days of atmospheric aging. Using a range of anthropogenic and biogenic SOA and oxidized primary organic aerosol (OPOA) precursors, they found that as OH exposure increased, the SOA and OPOA followed and extended the progression of ambient SOA in  $f_{44}$ - $f_{43}$  space, attaining values of  $f_{44}$  higher than ambient SOA. The Van Krevelen diagram slope of the SOA and OPOA was indicative of carboxylic acid formation and carbon-carbon bond fragmentation. In chamber experiments of 16 h oxidant exposure, Qi et al. (2010) found that, starting after 2 h of OH exposure, the volatility of SOA generated from *m*-xylene and  $\alpha$ -pinene under high- $NO_x$  conditions decreased slowly for the remainder of the experiment. After this initial 2-h period the O:C ratio for *m*-xylene SOA increased at a rate of  $0.007\text{ h}^{-1}$ ; however, for  $\alpha$ -pinene SOA, the O:C ratio decreased at a rate of  $0.003\text{ h}^{-1}$ . Chhabra et al. (2010) observed increasing

O:C for SOA formed from toluene, *m*-xylene, and naphthalene for irradiation times up to 12 h. The most rapid increase in O:C occurred during the first hour of low-NO<sub>x</sub> toluene and *m*-xylene experiments and the first 4 h of low-NO<sub>x</sub> naphthalene experiments. Similarly to the results of Qi et al. (2010) that SOA from some precursors exhibits minute aging behavior, no change in O:C was observed for SOA from isoprene photooxidation or  $\alpha$ -pinene ozonolysis after initial SOA formation. Chhabra et al. (2011) extended the analysis of the SOA formed from the compounds studied in Chhabra et al. (2010) to assess their behavior in both  $f_{44}$ - $f_{43}$  space and Van Krevelen diagram representations. Although the SOA formed from the various precursors occupied different regions in each representation, most systems exhibited a progression similar to aging of ambient SOA.

In this work, we develop and apply to *m*-xylene SOA a procedure to extend to 36 h the experimental duration of a laboratory chamber operated as a batch reactor. Aromatic hydrocarbon emissions are an important contribution ( $\sim 20-30\%$ ) to the total volatile organic compounds in the urban atmosphere (Calvert et al., 2002). *m*-Xylene SOA yields (ratio of mass concentration of SOA formed to mass concentration of parent hydrocarbon reacted) have been measured previously for initial *m*-xylene concentrations of 10 to 180 ppb and experimental durations up to 10 h (Ng et al., 2007; Song et al., 2007). SOA yields for low-NO<sub>x</sub> conditions were found to be higher than those for high-NO<sub>x</sub> conditions. In addition, Chhabra et al. (2010) and Qi et al. (2010) observed changes in SOA chemical composition for up to 16 h of oxidation, indicating the potential of aging of *m*-xylene SOA over longer timescales. For a long duration experiment, the initial *m*-xylene concentration can be chosen to produce a sufficient amount of SOA to sample for the duration of the experiment yet remaining close to atmospherically relevant loadings, typically  $0.1-20 \mu\text{g m}^{-3}$  (Shilling et al., 2009). In the present work, the total amount of SOA formed, its chemical composition, and the composition of the gas phase over 36 h of irradiation are evaluated to infer mechanisms of chemical aging of *m*-xylene SOA. For the first time, the effects of size-dependent particle composition on particle wall loss correction methods are discussed.

### 3.3 Materials and Methods

#### 3.3.1 Experimental setup

Experiments were conducted in the Caltech dual 28-m<sup>3</sup> Teflon chambers. Details of the facilities are given elsewhere (Cocker et al., 2001; Keywood et al., 2004). Before each experiment, the chambers were flushed with dried, purified air for > 24 h until the particle number concentration < 50 cm<sup>-3</sup> and the volume concentration < 0.1  $\mu\text{m}^3\text{cm}^{-3}$ . Experiments were run under low-NO<sub>x</sub> conditions using hydrogen peroxide (H<sub>2</sub>O<sub>2</sub>) as the OH source. With H<sub>2</sub>O<sub>2</sub> it is possible to achieve a constant OH concentration for the duration of the experiments. H<sub>2</sub>O<sub>2</sub> was injected into the chamber by evaporating 280  $\mu\text{L}$  of 50% wt aqueous solution into the chamber with 5 L min<sup>-1</sup> of purified air. Seed particles were injected by atomizing a 0.015 M aqueous ammonium sulfate (AS) solution for neutral seed and a 0.03 M aqueous magnesium sulfate with 0.03 M sulfuric acid (MS+SA) solution for acidic seed. *m*-Xylene (Sigma Aldrich, 99+ %) was introduced into the chamber by injecting the volume of the liquid hydrocarbon required to obtain a concentration of 30 ppb into a glass bulb, and the vapor was carried into the chamber with 5 L min<sup>-1</sup> of purified air. The chamber contents were allowed to mix for 1 h before beginning irradiation.

A suite of instruments was used to study the evolution of the gas and particle phases. *m*-Xylene was measured using a gas chromatograph with flame ionization detector (GC/FID, Agilent 6890N), equipped with a HP-5 column (15 m×0.53 mm ID×1.5 $\mu\text{m}$  thickness, Hewlett Packard). Reactive intermediates and H<sub>2</sub>O<sub>2</sub> were continuously monitored using a custom-modified Varian 1200 triple-quadrupole chemical ionization mass spectrometer (CIMS). Details of operation can be found elsewhere (Crounse et al., 2006; Paulot et al., 2009; St.Ćclair et al., 2010). The CIMS was operated in negative mode in which CF<sub>3</sub>O<sup>-</sup> is used as the reagent ion. CF<sub>3</sub>O<sup>-</sup> clusters with the analyte, forming ions at  $m/z$  MW+85 (R·CF<sub>3</sub>O<sup>-</sup>), or, with more acidic species, at  $m/z$  MW+19 (HF·R<sub>-H</sub><sup>-</sup>). Relative humidity (RH), temperature, NO, NO<sub>x</sub>, and O<sub>3</sub> were continuously monitored. The RH of the chamber was < 5%. The initial chamber temperature was  $\sim$  19 °C; however, heating from the blacklights caused a rise in temperature of approximately 5 °C. NO and NO<sub>x</sub> concentrations were

below the 2 ppb detection limit of the instrument, and initial  $\text{O}_3$  concentration was 2 ppb.

Aerosol size distribution and number concentration were measured continuously using a differential mobility analyzer (DMA, TSI, 3081) coupled to a condensation particle counter (CPC, TSI, 3760), henceforth referred to as the DMA. Real-time particle mass spectra were collected continuously by an Aerodyne High Resolution Time-of-Flight Aerosol Mass Spectrometer (DeCarlo et al., 2006; Canagaratna et al., 2007), henceforth referred to as the AMS. The AMS switched once every minute between the high resolution “W-mode” and the lower resolution, higher sensitivity “V-mode”. “V-mode” data were analyzed using a fragmentation table to separate sulfate, ammonium, and organic spectra and to time-trace specific  $m/z$  ratios. “V-mode” and “W-mode” data were analyzed using a separate high-resolution spectra toolbox known as PIKA to determine the chemical formulas contributing to distinct  $m/z$  ratios (DeCarlo et al., 2006). The signals of organic ions below  $m/z$  119 were used to calculate elemental ratios. The ratio of particle-phase  $\text{CO}^+$  to  $\text{CO}_2^+$  was approximately equal to 1, and the contribution of  $\text{CO}^+$  to the organic signal was estimated to equal that of particle-phase  $\text{CO}_2^+$ . The intensities of water-derived ions ( $\text{H}_2\text{O}^+$ ,  $\text{OH}^+$ , and  $\text{O}^+$ ) were estimated from particle phase  $\text{CO}_2^+$  using the correlation suggested by Aiken et al. (2008). A relative ionization intensity of 1.4 was applied to organic ion signals. AMS data reported in this work are averaged over 10-min intervals.

### 3.3.2 [

**Aging experiment protocols** The volume of the reactor limits the duration of experiments in a chamber operated in batch mode; when sampling with all instruments, nearly half of the chamber volume is depleted in 18 h, at which point it is preferable to cease sampling due to deflation of the chamber. To achieve longer OH exposure times with all instruments sampling, sets of experiments were conducted with increasing duration and staggered instrument sampling. Instruments were grouped into two categories based upon their sampling schedule. Group I includes the AMS and a RH and temperature probe. Group II includes the DMA, the CIMS, the GC/FID, the  $\text{O}_3$  analyzer, and the  $\text{NO}_x$  analyzer. All instruments were operated during initial injections before the onset of



irradiation. Experimental time began at the onset of irradiation. First, two 18 h experiments were conducted with Group I and II instruments sampling for the entire duration to establish consistency in the gas and particle phases during separate experiments. Subsequent experiments of 24 h, 30 h, and 36 h were conducted to achieve longer OH exposure. The instrument sampling schedule for all experiments is given in Table 3.1. The entire set of 5 experiments was conducted in the same chamber to avoid any differences between chamber conditions that may arise between the dual chambers. For each of the Group II instruments, the data from all experiments were combined to track the evolution of species for the entire 36 h of OH exposure.

### 3.3.3 Total SOA formation

To determine the total SOA mass concentration in the chamber,  $\Delta M_o$ , particle wall losses must be taken into account. The extent of interactions between particles deposited on the chamber walls and vapors in the chamber has not been determined completely; therefore, two limiting assumptions are used to bound this interaction. These limits have been described and applied to chamber experiments by Weitkamp et al. (2007) and Hildebrandt et al. (2009, 2011). In one limit, particles deposited on the wall are assumed to cease interaction with suspended vapors after deposition. In this case, the amount of organic material in the deposited particles does not change after deposition, and these particles remain at the same size at which they deposited for the remainder of the experiment. In the other limit, particles on the wall are assumed to interact with vapors in the chamber after deposition as if they had remained suspended. Thus, in this case, the amount of organic material in the particles after deposition changes at the same rate as the amount of organic material in the suspended particles, and the deposited particles continue to change size throughout the remainder of the experiment. This limit is analogous in theory to that of a chamber without walls. In either limit, the material on the walls is added to that which remains suspended to obtain the total amount of SOA formed.

During particle growth, the organic mass fraction of the suspended particles increases. In the first limit, the organic mass fraction of deposited particles does not increase after deposition; therefore,

this case produces a lower limit for  $\Delta M_o$ . In the second limit, deposited particles are assumed to continue growing; therefore, this case is an upper limit for  $\Delta M_o$ . These two limits of wall loss corrected  $\Delta M_o$  will subsequently be referred to as the lower bound and upper bound, respectively.

The lower bound limit on  $\Delta M_o$  is calculated from the DMA suspended particle number distribution. For each size bin  $i$  at each time step  $j$  the particle number distribution deposited to the wall,  $n_{w,ij}$  is calculated using size-dependent wall loss rates,  $\beta_i$ :

$$n_{w,ij} = n_{s,ij} \exp(\beta_i \Delta t) \quad (3.1)$$

where  $n_{s,ij}$  is the suspended particle number distribution in size bin  $i$  at time step  $j$ , and  $\Delta t$  is the difference between time step  $j$  and time step  $j + 1$ . Wall loss rates were determined from calibration experiments performed prior to the start of the aging experiments (methods detailed in Keywood et al. (2004); Ng et al. (2007)). The deposited particle number distribution is added to the suspended particle number distribution to give a wall-loss corrected number distribution,  $n_{tot,ij}$ , which is then converted to a volume concentration,  $V_{tot,j}$ , assuming spherical particles,

$$n_{tot,ij} = n_{s,ij} + n_{w,ij} \quad (3.2)$$

$$V_{tot,j} = \sum_{i=1}^m \frac{n_{tot,ij}}{D_{p,i} \ln 10} \times (D_{p,i+} - D_{p,i-}) \times \frac{\pi}{6} D_{p,i}^3 \quad (3.3)$$

where  $m$  is the total number of size bins,  $D_{p,i+}$  is the upper limit diameter for size bin  $i$ , and  $D_{p,i-}$  is the lower limit diameter for size bin  $i$ . A factor of  $\ln 10$  is necessary to convert from a log normal distribution. The initial seed volume concentration,  $V_{seed}$ , is subtracted from the wall-loss corrected volume concentration to give the volume concentration of SOA,  $V_{o,j}$ . To convert to SOA mass,  $\Delta M_{o,j}$ , the SOA volume concentration is multiplied by the SOA density,  $\rho_{org}$ ,

$$\Delta M_{o,j} = \rho_{org} (V_{o,j} - V_{seed}) . \quad (3.4)$$

For low- $\text{NO}_x$  *m*-xylene SOA,  $\rho_{org} = 1.33 \text{ g cm}^{-3}$  (Ng et al., 2007). It is possible that  $\rho_{org}$  changes as

particle age increases, but it was assumed to be constant for the present study, which is consistent with the findings of Qi et al. (2010).

Calculating the lower bound wall-loss corrected mass relies on having continuous number distributions, which were not available for the 24-h, 30-h, and 36-h experiments. To obtain a continuous number distribution, the number distributions for all experiments were combined. The DMA sampling schedule was designed to allow a 2-h overlap period between shorter and longer experiments (i.e. sampling for the 24-h experiment began at 16 h, 2 h prior to the endpoint of the 18-h experiment) to facilitate the comparison of data between shorter and longer experiments. The number distributions from each experiment were combined sequentially. During periods of overlap between two experiments, a weighted average of the number distribution in each size bin was taken giving higher weight to the shorter experiment at the beginning of the overlap period and higher weight to the longer experiment at the end of the overlap period.

Both the number distribution of the seed particles and the initial concentration of *m*-xylene affect the number distribution of the aerosol. In the 24-h experiment, the seed volume was lower than that for the other AS seed experiments (Table 3.2). Assuming that the SOA produced in this experiment was comparable to that in the other experiments, the suspended particle volume would be lower than that of the other AS seed experiments, and the number distribution would be too small to combine with those of the other AS experiments to obtain a continuous number distribution. Without the data from the 24-h experiment, no number distribution data were available between hours 18 and 22. Number distributions during those 4 h were calculated from the 18- and 30-h experiments by fitting an exponential function to the number distribution in each size bin during hours 16-18 of the 18-h experiment and hours 22-24 of the 30-h experiment and using the function to interpolate a number distribution at 4-min increments.

Throughout an experiment, the volume of the chamber decreases due to sampling, but the surface area of the walls remains the same. It is possible that the increasing surface-area-to-volume ratio will increase the particle wall loss rates. The duration of a typical wall loss experiment is 18-24 h, shorter than that of the longest aging experiments. The aging experiments were designed to

minimize the amount of air sampled from the chamber. Although more instruments sample from the chamber during an aging experiment than during a wall loss calibration experiment, the volume of air removed during an aging experiment is comparable to that of a wall loss calibration experiment (Table 3.1).

To confirm that wall loss rates do not vary significantly as chamber volume decreases, an additional wall loss calibration experiment was performed in each chamber. These calibration experiments were conducted following the same protocols as a typical wall loss calibration; however, before AS seed aerosol was injected, approximately 8 m<sup>3</sup> of air was removed from the chambers to simulate conditions found at the end of an 18 h experiment. The wall loss rates determined from these low-volume experiments were within the range of wall loss rates observed in the chambers since they were installed in 2009 (Fig. 3.1). Therefore, time-dependence of the wall loss rate constants was assumed to be negligible during these aging experiments.

The upper bound limit on  $\Delta M_o$  is calculated by combining the AMS and DMA data. The experiments in the present work use seed particles containing sulfate, and the only process that decreases sulfate concentration in the suspended phase is wall loss. The initial sulfate concentration is calculated from the DMA seed volume concentration. There is more uncertainty for the collection efficiency of seed particles in the AMS than in the DMA. Collection efficiency in the AMS increases as organic content of the particles increases, and because the seed particles do not contain organic material, they are more susceptible to bounce in the instrument and have a collection efficiency that is less than unity (Matthew et al., 2008). To calculate the mass of sulfate in the seed,  $m_{\text{SO}_4}$ , the following equation is used:

$$m_{\text{SO}_4} = V_{\text{seed}} \rho_{\text{seed}} \frac{MW_{\text{SO}_4}}{MW_{\text{seed}}} \quad (3.5)$$

where  $\rho_{\text{seed}}$  is the density of the seed particles,  $MW_{\text{SO}_4}$  is the molecular weight of sulfate, and  $MW_{\text{seed}}$  is the molecular weight of the seed particles. For dry AS seed,  $\rho_{\text{seed}}$  is 1.77 g cm<sup>-3</sup>. In the upper bound limit, both suspended and deposited particles gain or lose organic material at the same rate; therefore, the organic-to-sulfate ratio of all particles of the same size is the same, and this ratio is determined from unit mass resolution AMS data. High-resolution analysis of the dominant sulfate

ions,  $m/z$  48 and 64, showed less than 1% contribution of organic signal to the total ion signal; therefore, organic contribution to the unit mass resolution sulfate signal was negligible. Differences in the organic-to-sulfate ratio,  $r_{OS}$ , between unit mass resolution and high resolution data are less than 5%, except during the first 2 h of growth when they are more variable at lower organic loading. To obtain the SOA mass,  $r_{OS}$  is multiplied by the initial mass of sulfate in the seed particles,

$$\Delta M_o = m_{\text{SO}_4} r_{OS}. \quad (3.6)$$

This equation is valid if the organic-to-sulfate ratio does not vary with particle size or if particle wall loss rates are constant over the particle size range of interest. In the Caltech chambers, particle wall loss rates depend on particle size so the latter assumption is not valid. Depending on the condensation behavior of the SOA,  $r_{OS}$  may depend on particle size (Hildebrandt et al., 2009; Riipinen et al., 2011). For the present experiments, data were not available to determine the size dependence of  $r_{OS}$  of the particles. For the purpose of calculating the upper bound wall loss corrected organic mass, it is assumed that  $r_{OS}$  does not vary with particle size. The implications of this assumption will be discussed in Sect. 3.4.4.

## 3.4 Results and Discussion

### 3.4.1 SOA formation

Two experiments with the same initial conditions and 18 h of irradiation were performed to assess the reproducibility of initial conditions and SOA production (Table 3.2). For both AS seed and MS+SA seed, similar concentrations of  $m$ -xylene reacted and  $\Delta M_o$  formed after 18 h of irradiation were achieved. Given the consistency between matched experiments, it was not necessary to sample for the entire duration of longer experiments. It was assumed that data collected during previous, shorter experiments are adequate to describe the same time period during longer experiments.

Figure 3.2 shows decay of  $m$ -xylene and  $\Delta M_o$  corrected for wall loss for both the upper and lower

bound cases over 36 h of irradiation. The lower bound  $\Delta M_o$  and *m*-xylene data are a compilation of the 18-, 30-, and 36-h AS seed experiments (the 24-h experiment was omitted as noted earlier due to low seed particle volume), but the upper bound  $\Delta M_o$  data are from only the 36-h experiment because continuous data were available. The variation in the lower bound wall loss corrected mass concentration after peak growth is likely due to differences in number distributions during the 18-, 30-, and 36-h experiments. The peak in SOA formation occurs before all of the *m*-xylene has been reacted. For the lower bound case,  $\Delta M_o$  remains relatively stable after its peak, decreasing only slightly over 20 h of irradiation. For the upper bound case,  $\Delta M_o$  peaks at approximately the same time as in the lower bound case; however, there is a pronounced decay of  $\Delta M_o$  after the maximum is reached. Wall losses result in 43% of the total volume concentration of particles deposited on the wall for the lower bound case and 56% of  $\Delta M_o$  deposited on the wall for the upper bound case after 36 h. The behavior of  $\Delta M_o$  after peak growth will be discussed in Sect. 3.4.3.

Throughout each experiment, the OH concentration was approximately  $2.5 \times 10^6 \text{ cm}^{-3}$ , as estimated from the decay of *m*-xylene and simulated by a photochemical model (see Appendix A). After 36 h of irradiation, 40% of the initial 4 ppm of  $\text{H}_2\text{O}_2$  injected into the chamber remained unreacted.

### 3.4.2 SOA composition

Figure 3.3 shows the evolution in the elemental oxygen-to-carbon ratio (O:C) of the suspended particles for all 5 of the AS seeded experiments. O:C values overlap for all of the experiments with different irradiation durations. O:C decreases during the first 5 h of irradiation in all but the 36-h experiment. During the 36-h experiment, the sensitivity of the AMS sampling in W-mode was lower than that in the other aging experiments, which hindered the detection of initially-formed SOA. The O:C calculated using V-mode data (not shown) decreases during the first 5 h of irradiation for all 5 of the aging experiments. The dominant trend in O:C begins after 5 h. After this time, O:C gradually increases at an average rate of  $0.0019 \text{ h}^{-1}$  for the remainder of the irradiation period. The minimum in O:C occurs before the maximum  $\Delta M_o$  is reached.

The mass spectral parameter  $f_{44}$  is commonly used to characterize SOA chemical composition.

Aiken et al. (2008) determined a relationship between O:C and  $f_{44}$  for ambient aerosol in Mexico City:  $\text{O} : \text{C} = (3.82 \pm 0.05) \times f_{44} + (0.0794 \pm 0.0070)$  for  $f_{44}$  ranging from 0 to 0.25. The SOA in the current set of experiments does not follow the same trend as the Mexico City SOA, and exhibits trendline of  $\text{O} : \text{C} = (1.42 \pm 0.04) \times f_{44} + (0.439 \pm 0.005)$  over a range of 0.10 to 0.14 of  $f_{44}$ . Although the data for *m*-xylene SOA do not follow the same trendline as the Mexico City data, they lie within the scatter of the Mexico City data (Fig. 3.4). Using the same AMS instrument, Chhabra et al. (2010) found that the O:C and  $f_{44}$  of SOA from aromatics, isoprene, and glyoxal did not lie along the trendline reported in Aiken et al., but the O:C and  $f_{44}$  of SOA from  $\alpha$ -pinene and naphthalene did. In general, if  $\text{CO}_2^+$  contributed most of the oxygen signal in the spectra, then the O:C and  $f_{44}$  of the SOA more closely matched those predicted by the trendline from the Mexico City data. The correlation between O:C and  $f_{44}$  for *m*-xylene SOA in the present work differs from that of Lambe et al. (2011), who observed that *m*-xylene SOA follows the same trendline as the Mexico City data. The range of  $f_{44}$  values observed by Lambe et al. is much larger than that in the present work, initial hydrocarbon loadings are higher, and OH exposure is 2-3 times greater than the maximum OH exposure achieved in the present work ( $3.2 \times 10^{11} \text{ cm}^{-3} \text{ s}$ ). Any of these factors could contribute to the different correlations between O:C and  $f_{44}$ . The factor most likely to explain the discrepancy between the correlation in the present work and that in Lambe et al. is the difference in OH exposure. At higher OH exposure, the SOA is likely to be more oxidized, and  $\text{CO}_2^+$  is likely to be a major contributor to the oxygen signal in the spectra.

The evolution of *m*-xylene SOA is also represented in  $f_{44}$ - $f_{43}$  space (Fig. 3.5). The change in O:C, derived from the correlation specific to *m*-xylene, is also shown. The marker size is a function of the concentration of suspended organics, normalized to suspended sulfate concentration to account for wall losses. Overall, low- $\text{NO}_x$  *m*-xylene SOA exhibits higher  $f_{43}$  than the typical range of ambient SOA observed by Ng et al. (2010) and lies to the right of the triangular region derived for ambient SOA. At the beginning of irradiation when the organic mass loading is small, the SOA has a higher  $f_{44}$  and a lower  $f_{43}$ . As SOA continues to form,  $f_{44}$  decreases and  $f_{43}$  increases until approximately 5 h of irradiation, at which time the trends reverse. For the remaining duration of irradiation,  $f_{44}$

increases and  $f_{43}$  decreases, resulting in a progression of the SOA characteristic of the behavior of more-aged ambient SOA. The time at which the path reversal in  $f_{44}$ - $f_{43}$  space occurs is the same as that at which the minimum in O:C occurs. Curvature in  $f_{44}$ - $f_{43}$  space has been observed in other studies (Kroll et al., 2009; Ng et al., 2010; Chhabra et al., 2011; Lee et al., 2011; Lambe et al., 2011). Lambe et al. did not observe curvature in  $f_{44}$ - $f_{43}$  space for *m*-xylene SOA, and the curvature observed in the present study occurred for lower OH exposures than the lowest value attained by Lambe et al.. It is possible that the OH exposure levels used to form *m*-xylene SOA in Lambe et al. were too large to observe the curvature.

The high-resolution AMS mass spectra provide clues to the trends in O:C,  $f_{44}$ , and  $f_{43}$ . The average mass spectra at peak organic growth and at the end of the 36-h aging experiment are shown in Fig. 3.6. Figure 3.7 shows the time trends of the 4 dominant organic ions ( $\text{CH}_3^+$ ,  $\text{CHO}^+$ ,  $\text{C}_2\text{H}_3\text{O}^+$ , and  $\text{CO}_2^+$ ) in the aerosol mass spectra and the maximum of the suspended particle size distribution throughout 36 h of oxidation. Excluding  $\text{CO}_2^+$ , these ions account for 30-35% of the total organic signal throughout the experiment. When organic  $\text{CO}_2^+$  and the ions whose organic contributions are assumed to correlate with it ( $\text{CO}^+$ ,  $\text{H}_2\text{O}^+$ ,  $\text{OH}^+$ , and  $\text{O}^+$ ) are included, the mass fraction of the organic signal is approximately 52%. In the top panel of Fig. 3.7, the time trends of the normalized, wall-loss corrected ion signals are shown. To obtain this, the ion signal was divided by the sulfate signal to correct for wall losses. The sulfate-normalized ion signal was then scaled by its average value at the peak concentration. In the middle panel, the fractional contribution of each ion to the total organic signal is shown. The bottom panel shows the particle diameter ( $D_p$ ) of the maximum of the suspended particle size distribution. The most rapid change in  $D_p$  occurs during the first 5 h of irradiation. The amount of each of the 4 ions in the particles increases during this time (top panel). After 5 h,  $D_p$  changes more slowly, and the contribution of each ion to the spectra begins to peak.  $\text{CHO}^+$  reaches a maximum most quickly, followed by  $\text{CH}_3^+$  and  $\text{C}_2\text{H}_3\text{O}^+$ .  $\text{CO}_2^+$  peaks later than the other ions. After most of the ions peak, their contribution to the spectra decreases for the remainder of the experiment; however, the amount of  $\text{CO}_2^+$  shows much less of a decrease, suggesting that compounds that contribute to the  $\text{CO}_2^+$  signal have a lower tendency to be removed



from the particles than those that contribute to the other ion signals.

Shortly after the onset of irradiation,  $\text{CO}_2^+$  constitutes the largest fraction of the organic signal, likely from the condensation of low-volatility organics. As irradiation continues, the  $\text{CO}_2^+$  fraction of the organic signal decreases as semivolatile material represented by the other ions, especially  $\text{C}_2\text{H}_3\text{O}^+$ , begins to partition to the particles. Once the rate of particle growth slows, the fraction of  $\text{CO}_2^+$  increases because the contribution of  $\text{CO}_2^+$  to the mass spectra is still increasing, whereas the amounts of the other ions are beginning to stabilize and then decrease. The increase in the organic fraction of  $\text{CO}_2^+$  continues throughout the duration of the experiment caused by a larger decrease in the amounts of the other ions in the particle mass spectra than  $\text{CO}_2^+$ .

### 3.4.3 Fate of SOA after peak growth

After peak growth, a decrease in most of the major organic ions and the total organic mass is observed (Fig. 3.2 and 3.7). The magnitude of the decrease in  $\Delta M_o$  is much greater for the upper bound wall loss correction than that for the lower bound wall loss correction, suggesting that either the process causing the decrease in  $\Delta M_o$  has a larger effect on the upper bound wall loss case or that an incorrect assumption was made for one of the wall loss corrections. For the upper bound wall loss correction,  $r_{OS}$  was assumed to be constant such that the  $r_{OS}$  of the suspended particles was equivalent to that of the deposited particles. If this is not the case, the mass lost to the walls may be over- or under-estimated. Implications of the size-dependence of  $r_{OS}$  on the upper and lower bound wall loss correction and its effects on the conclusions of the present section will be discussed in Sect. 3.4.4.

If the organic mass lost to the wall was correctly calculated for both upper and lower bound cases, a possible explanation for the decrease in  $\Delta M_o$  after peak growth is repartitioning of semivolatiles to the gas phase. As irradiation continues, semivolatiles in the gas phase can undergo reaction with OH or photolysis to form higher-volatility products, or they may be lost to the walls. As the concentration of a semivolatile in the gas phase decreases from fragmentation reactions or wall loss, repartitioning can occur to maintain gas-particle equilibrium. OH can also react with the particle

surface, forming higher volatility fragmentation products that evaporate and decrease the particle organic mass. These processes are summarized in Fig. 3.8. Evaporation of semivolatiles is expected to have a greater effect on  $\Delta M_o$  in the upper bound limit because all particles are assumed to undergo gas-particle partitioning, as opposed to only the suspended particles in the lower bound limit, thus a higher decrease in  $\Delta M_o$  should be expected in the upper bound limit.

Semivolatile species are expected to repartition from the particle phase more easily than low volatility species. This behavior is observed with the organic ions  $\text{C}_2\text{H}_3\text{O}^+$ , characteristic of semivolatile oxygenated organic aerosol (SV-OOA), and  $\text{CO}_2^+$ , characteristic of low volatility oxygenated organic aerosol (LV-OOA). The amount of  $\text{C}_2\text{H}_3\text{O}^+$  in the particle mass spectra increases faster than  $\text{CO}_2^+$  and shows a much greater decrease than  $\text{CO}_2^+$  as the experiment progresses. There is a slight decrease in  $\text{CO}_2^+$  at longer irradiation times, and it is possible that the uptake of low volatility species is not completely irreversible, allowing for some evaporation.

Evaporation of particles is characterized by a shift of the  $D_p$  at the maximum of the size distribution to smaller size. This shift was not observed in the aging experiments, as shown in the bottom panel of Fig. 3.7 where  $D_p$  increased slightly after the peak organic loading was attained around 12 h. The two main processes affecting the particle size distribution in chamber experiments are gas-particle partitioning and wall loss. In the Caltech chambers, wall loss rates are at a minimum for particles of diameters between 200 and 300 nm (Fig. 3.1). During the aging experiments, the  $D_p$  at the size distribution maximum is below the 200-300 nm minimum in wall loss. If evaporation is occurring, the rate of wall loss will increase as particles get smaller. As a result, the greater loss of small particles will cause size distribution, characterized by the  $D_p$  at its maximum, to shift slightly toward the 200-300 nm minimum in wall loss rate. Both the evaporation and wall loss processes are slow; therefore, the two processes will tend to counteract each other with respect to their effects on the dynamics of the aerosol size distribution, and no change in  $D_p$  at the maximum of the size distribution is observed. It is also possible that the upper bound wall loss correction over-predicts the amount of evaporation occurring (see Sect. 3.4.4). In this case, the  $D_p$  at the size distribution maximum would only be expected to increase slightly toward the 200-300 nm minimum in wall loss

rate.

To determine the extent to which photochemical processes are affecting the aerosol after peak growth, an experiment was performed in which the lights were turned off after 12.4 h of irradiation (Fig. 3.9). Production of OH ceases, and shortly thereafter, OH is no longer present in the chambers. The *m*-xylene concentration stabilizes after lights are turned off, and the substantial decrease in the upper bound  $\Delta M_o$  is not observed with the lights off. The lower bound  $\Delta M_o$  increases after lights are turned off to result in a 5% change in mass after 8 h. This increase could be the result of uncertainty induced by the wall loss correction or condensation of vapors as the chamber cooled after irradiation stopped from 24 °C to 19 °C during hours 12.4 to 16. The latter process is not observed in the upper bound  $\Delta M_o$ , but condensation could be masked by uncertainty in the wall loss correction method, discussed in Sect. 3.4.4. Despite the potential uncertainties of the wall loss correction and the cooling of the chamber, the decrease observed in the lower bound  $\Delta M_o$  in the 36 h aging experiment is not observed after irradiation ceases. After the lights are turned off, the chemical composition of the particles also stops changing significantly. This is shown in  $f_{44}$ - $f_{43}$  space in Fig. 3.10. While the aerosol forms,  $f_{43}$  decreases and  $f_{44}$  increases; however, after the lights are turned off, the rates of change of both  $f_{43}$  and  $f_{44}$  decrease substantially. In the absence of irradiation, a semivolatile species in the gas phase,  $A^g$ , can partition to and from particles or be lost to the walls (Fig. 3.8). After irradiation stops, the rate of change in the amount and composition of the particles decreases substantially; therefore, no significant repartitioning is occurring. Under these conditions, only vapor phase wall loss is expected to cause repartitioning; therefore, vapor phase wall loss is not significant in this system. If no repartitioning is observed without irradiation, and if there are no substantial vapor phase wall losses, then repartitioning must be driven by photochemical processes that affect the chemical composition of the gases and SOA.

It was not possible to distinguish among the photochemical process occurring: reaction of OH with semivolatiles; reaction of OH with particles; and photolysis of semivolatiles. The photochemical model described in Appendix A was used to estimate lifetimes for OH against reaction with particles, OH against reaction with semivolatiles, semivolatiles against reaction with OH, and semivolatiles

against photolysis. The lifetime of OH against reaction with gas-phase species A<sup>g</sup>,  $\tau_{\text{OH+A}}$  (s), is

$$\tau_{\text{OH+A}} = \frac{1}{k_{\text{A+OH}}c_{\text{A}}} \quad (3.7)$$

where  $k_{\text{A+OH}}$  ( $\text{cm}^3\text{s}^{-1}$ ) is the reaction rate constant and  $c_{\text{A}}$  ( $\text{cm}^{-3}$ ) is the gas-phase concentration of A. Using the combined concentrations of species ROOH, ROHOH, ROHOOH, and EPOXOOH and an average rate constant  $k_{\text{OH}} = 1 \times 10^{-10} \text{ cm}^3 \text{ s}^{-1}$  (Table 3.3),  $\tau_{\text{OH+A}} \cong 0.2 \text{ s}$ . The heterogeneous reaction of OH with a particle surface is assumed to be pseudo-first order in terms of OH (Seinfeld and Pandis, 2006). The characteristic time for this process,  $\tau_{\text{OH+P}}$  (s), can be calculated by,

$$\tau_{\text{OH+P}} = \frac{1}{\frac{1}{4}\gamma\overline{c_{\text{OH}}}A_p} \quad (3.8)$$

where  $\gamma$  is an uptake coefficient, here assumed to be 1,  $A_p$  ( $\text{cm}^2 \text{ cm}^{-3}$ ) is the surface area concentration of the particles, and  $\overline{c_{\text{OH}}}$  ( $\text{cm s}^{-1}$ ) is given by

$$\overline{c_{\text{OH}}} = \left( \frac{8RT}{\pi MW_{\text{OH}}} \right)^{\frac{1}{2}} \quad (3.9)$$

where  $T$  (K) is temperature and  $MW_{\text{OH}}$  ( $\text{kg mol}^{-1}$ ) is the molecular weight of OH. The particle surface area was calculated from measured particle number distributions. Based on the upper and lower bound wall loss corrections,  $\tau_{\text{OH+P}}$  ranges from 6-13.5 s, corresponding to particle surface areas of  $(0.47 - 1.1) \times 10^{-5} \text{ cm}^2 \text{ cm}^{-3}$ .

Some of the semivolatile species used to determine  $\tau_{\text{OH+A}}$  can also photolyze. The lifetimes of these species, ROOH, ROHOOH, and EPOXOOH, against OH reaction and photolysis were also calculated to determine if photolysis is expected to be a large sink of gas-phase species. The lifetime of these species against reaction with OH,  $\tau_{\text{A+OH}}$  (s), is

$$\tau_{\text{A+OH}} = \frac{1}{k_{\text{A+OH}}c_{\text{OH}}} \quad (3.10)$$

where  $c_{\text{OH}}$  ( $\text{cm}^{-3}$ ) is the OH concentration, which was estimated to be  $2.5 \times 10^6 \text{ cm}^{-3}$  from the measured *m*-xylene decay. Under this condition,  $\tau_{\text{A}+\text{OH}} = 4.0 \times 10^4 \text{ s}$ . The lifetime of these species against photolysis,  $\tau_{\text{A}+h\nu}$ , is calculated by,

$$\tau_{\text{A}+h\nu} = \frac{1}{j_{\text{ROOH}}} \quad (3.11)$$

where  $j_{\text{ROOH}}$  is the photolysis rate constant of an organic peroxide, as described in Appendix A. The characteristic lifetime against photolysis is estimated as  $4.7 \times 10^5 \text{ s}$ . Photolysis is an order of magnitude slower than reaction with OH, and photolysis is not expected to be a major sink of gas-phase species. Changes in particle composition are likely driven by continued oxidation of the gas phase, although OH reaction with particle surfaces cannot be categorically dismissed.

The continued oxidation of semivolatile species is apparent upon examination of possible gas-phase *m*-xylene oxidation products using the CIMS (Fig. 3.11). The top panel shows the time trace of  $m/z$  207, which has the same  $m/z$  as the predicted reagent ion clustering of first-generation oxidation products ROH (MW+85) and ROOH (MW+19) in the model (Table 3.4). This  $m/z$  signal increases rapidly and peaks at 3-4 h of irradiation. When lights are turned off during the experiment, the decay slows significantly. The middle panel shows the time trace of  $m/z$  223, which has the same  $m/z$  as the predicted reagent ion clustering of second-generation oxidation products ROHOH (MW+85), ROHOOH (MW+19), and EPOXOOH (MW+19). Again, this  $m/z$  signal increases rapidly and peaks slightly later at 4-5 h irradiation. When the lights are turned off, the signal stabilizes. The photochemical model predicts the peak of the first generation product concentrations to occur about an hour before that of the second generation product concentrations, and the time difference between the peak of the CIMS signals at  $m/z$  207 and  $m/z$  223 is consistent with the model output. The bottom panel shows the time trace of  $m/z$  271, which has the same  $m/z$  as the predicted reagent ion clustering of third-generation oxidation product (MW+85) formed by the EPOXOOH + OH reaction ( $prod_{\text{EPOXOOH}+\text{OH}}$  in the model). From model predictions, this compound with predicted reagent ion clustering at  $m/z$  271 should form more slowly. The signal at  $m/z$  271 peaks at 13-14

h of irradiation and does not decrease after irradiation ceases. The behavior of these signals is consistent with multiple generations of oxidation. The changes are clearly photochemically driven. Vapor-phase wall loss is not a significant sink of compounds contributing to these signals, indicated by the absence of decay after the lights are turned off.

### 3.4.4 Role of organic-to-sulfate ratio in particle wall loss corrections

The partitioning behavior of SOA precursors affects how these species condense onto a particle size distribution (Riipinen et al., 2011). If condensation is limited by diffusion, which is typically the case for essentially non-volatile compounds, the rate of condensation depends on the surface area of the particle size distribution (Seinfeld and Pandis, 2006); in that case the organic growth tends to occur on particles with smaller  $D_p$  as this is the particle size regime where the surface area is greatest. For organics exhibiting diffusion-limited behavior, organic condensation on AS seed particles tends to form organic and sulfate mass distributions such that mean  $D_p$  of the organic mass distribution is smaller than that of the sulfate distribution. If condensation is controlled by gas-particle partitioning equilibrium, which is typically the case for semi-volatile compounds, these species will tend to condense preferentially into the particle size range where the mass concentration is greatest, i.e. a majority of the organic growth will occur on particles with larger  $D_p$  (Zhang et al., 2012). In this case, the organic mass distribution will peak at a larger  $D_p$  than the sulfate mass distribution. Because information about the organic and sulfate mass distributions was not available for the present experiments, a simulation was performed to assess the effects of different shapes of organic and sulfate mass distributions on the upper bound wall loss correction method.

Three different pairs of organic and sulfate mass distributions consistent with the measured number distribution and  $r_{OS}$  were created from the suspended particle number distribution averaged between hours 12 and 12.5 of irradiation from the combined 36 h aging experiment in order to determine the uncertainty in the upper bound wall loss correction induced by size-dependent  $r_{OS}$  (Fig. 3.12). The peak of the measured aerosol number distribution occurs at a  $D_p$  smaller than that at which the wall loss rate is at its minimum, and the wall loss rate increases moving from lower

$D_p$  to higher  $D_p$  across the measured number distribution (not shown). Each of the distributions in Fig. 3.12 is characterized by the same total particle number distribution, an organic-to-sulfate ratio of 2.00, and an organic mass concentration of 22.7-22.8  $\mu\text{g m}^{-3}$ . Case I represents condensation resulting from equilibrium gas-particle partitioning, and Case III represents condensation resulting from diffusion-limited growth. In Case II all particles have the same  $r_{OS}$ .

The aerosol size distribution was subjected to 24 h of wall loss at the rates applied to the experimental number distributions, ignoring condensation (growth and evaporation are assumed to cease) and coagulation. For each of the cases,  $r_{OS}$  of the suspended particles and the upper bound wall-loss corrected mass concentration were calculated as a function of time (Fig. 3.13). In Case I,  $r_{OS}$  of suspended particles increased by about 10% over 24 h as particles with a lower  $r_{OS}$  were preferentially lost to the walls. Because  $r_{OS}$  of suspended particles is higher than that of deposited particles, using  $r_{OS}$  of suspended particles to represent deposited particles leads to an over-estimation of organic mass lost to the walls. The over-prediction of wall loss corrected organic mass concentration is about 10%. In Case II,  $r_{OS}$  of suspended and deposited particles are the same by definition, and the predicted wall loss corrected organic mass was estimated properly. In Case III  $r_{OS}$  of deposited particles is greater than that of suspended particles, and  $r_{OS}$  of suspended particles decreased by about 10% over 24 h because particles with a higher  $r_{OS}$  were preferentially lost to the walls. This resulted in an under-prediction of wall loss corrected organic mass concentration by about 10%.

Organic and sulfate mass distributions have been reported for toluene SOA condensed onto AS seed and are indicative of diffusion-limited condensation (Hildebrandt et al., 2009). If *m*-xylene SOA formation occurs by processes similar to those of toluene, the mass distributions during the present experiments will most closely resemble Case III, and increasing under-prediction of the upper bound wall-loss corrected organic mass concentration may occur with time. During the 36 h combined aging experiments, the measured  $r_{OS}$  of suspended particles decreased from 2.1 to 1.9 between hours 12.4 and 20 and continued to decrease linearly to 1.4 at 36 h. Between hours 12.4 and 20, the wall-loss corrected organic mass concentration decreased from 32.8 to 30  $\mu\text{g m}^{-3}$ . By hour 36, it

had decreased to  $22.3 \mu\text{g m}^{-3}$ . The changes in  $r_{OS}$  and mass loss can be compared to those in the experiment in which irradiation ceased after 12 h and in which only particle wall loss occurred after that time. Between hours 12.4 and 20,  $r_{OS}$  decreased from 1.50 to 1.42, and the wall-loss corrected mass concentration decreased from 20.5 to  $19.2 \mu\text{g m}^{-3}$ . The decrease in both organic-to-sulfate ratio and wall-loss corrected mass concentration in the 12-h irradiation experiment are indicative of wall loss of an aerosol size distribution characterized by diffusion-limited growth. The experimental conditions of the 36-h experiment were similar to the 12-h irradiation experiment; however, both the initial *m*-xylene concentration and the seed volume concentration in the 12-h irradiation experiment were lower than those in the combined 36-h aging experiments, and  $r_{OS}$  is expected to differ as a result. Despite the differences, it is expected that the size distribution of the suspended particles in hours 12.4-20 during the 36-h experiment should behave similarly to the size distribution of particles during hours 12.4-20 of the 12-h irradiation experiment if only particle wall loss is occurring. The fractional decrease in  $r_{OS}$  during hours 12.4-20 of the 36-h irradiation experiment is approximately double that of the 12-h irradiation experiment, suggesting that an additional process besides particle wall loss, such as gas-particle repartitioning due to evaporation, affected the suspended particle  $r_{OS}$ . The magnitude of evaporation, however, may not be as large as originally thought due to uncertainty in the upper bound wall loss correction method.

The lower bound wall loss correction should be unaffected by size-dependent  $r_{OS}$  distributions. The number and size of deposited particles is calculated independently of particle composition and is added back to the number distribution of suspended particles to calculate the total volume of particles. In obtaining the total volume of organics, the volume of seed or other background particles is subtracted from the total volume. This calculation assumes that the seed or background particle volume does not change during an experiment.

### 3.4.5 Acidic seed effects

Aging experiments were also performed using acidic MS+SA seed to determine the extent to which particle acidity affects chemical aging of *m*-xylene SOA. Figure 3.14 shows the elemental ratios for



both AS and MS+SA seeded experiments. No difference between the acidic and neutral seeds for *m*-xylene-derived SOA is observed. Ng et al. (2007) did not observe a difference in yields for low- $\text{NO}_x$  *m*-xylene SOA with neutral and acidic seed particles; therefore, it is plausible that the chemical composition of the aerosol condensed onto the two types of seed particles is similar.

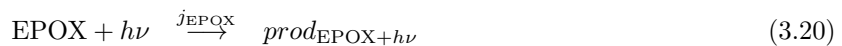
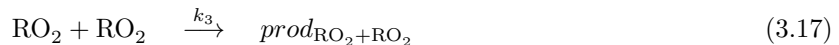
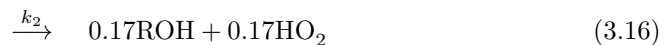
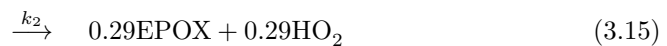
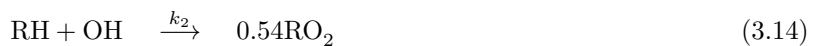
### 3.5 Conclusions

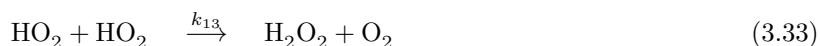
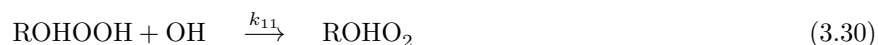
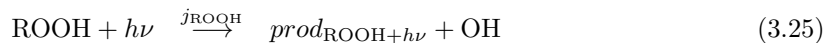
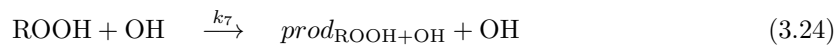
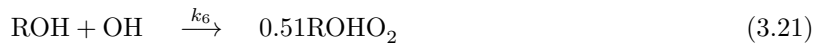
Laboratory chamber studies provide fundamental information on the mechanisms of formation of SOA. The duration of chamber experiments is limited by several factors, including wall loss of particles and vapors and depletion of chamber air through instrument sampling. Laboratory experiments attempt to approach durations of OH radical exposure corresponding to those of particles in the atmosphere, the order of a week, through enhanced OH radical levels. In the present work we extend the duration of chamber experiments by sampling protocols that minimize the amount of chamber air removed over the course of the experiment. The protocol developed here allows experiments up to 36 h duration. Hydroxyl radical levels in the experiments reported here are roughly at atmospheric levels. We address SOA formation from the photooxidation of *m*-xylene, an important anthropogenic precursor to organic aerosol. The extended duration experiments provide a view into the multi-generational chemistry involved in *m*-xylene SOA formation that can be expected to be occurring in the atmosphere. Although the current work studies only low- $\text{NO}_x$  chemistry, the *m*-xylene oxidation mechanism leading to SOA formation under high- $\text{NO}_x$  conditions is also expected to follow multi-generational chemistry (Kwok et al., 1997; Zhao et al., 2005; Ng et al., 2007; Song et al., 2007; Noda et al., 2009; Birdsall et al., 2010). The generations of oxidation of a precursor volatile organic compound can lead to functionalized products of ever decreasing volatility, characterized by increasing elemental O:C ratio, as well as to products of higher volatility that do not contribute to SOA. Based on CIMS measurements, there is strong evidence of gas-phase loss of higher generation products. That this process involves photooxidation or photolysis is confirmed by the absence of changes in total aerosol amount when irradiation is stopped. Wall loss of vapor can be excluded as the cause of this behavior. Estimates of reaction timescales suggest that gas-phase processes are

most likely involved in this latter stage of aging, although direct OH reaction with the surface of the particles cannot be ruled out. Finally, the present work offers a protocol for laboratory chamber experiments to attain times approaching more closely those of atmospheric aerosol residence times.

### 3.6 Appendix A: Photochemical Model

To estimate both OH concentration and the importance of OH reaction with later-generation oxidation products, a photochemical model (reactions 3.12-3.34 below) was constructed. Products through three generations of oxidation are included. Primary oxidation products are those suggested by Birdsall et al. (2010) and Zhao et al. (2005) with product yields and further oxidative pathways as derived from the MCM (Jenkin et al., 2003; Bloss et al., 2005). Values of rate constants are listed in Table 3.3, and compounds represented in the model are given in Table 3.4. Photolysis rate constants are calculated using the irradiance spectrum measured for the chamber lights and absorption cross section values and quantum yields from Sander et al. (2011). The following reactions are included:





Neither gas-particle partitioning nor vapor-phase wall loss was included in the model because there is not sufficient information about either process to accurately represent it in the model. Vapor-phase wall loss is assumed to be minor (Fig. 3.11) and should not have a large effect on gas species concentrations.

### 3.7 Acknowledgements

This work was supported by the Office of Science (Biological and Environmental Research), U.S. Department of Energy Grant DE-SC 0006626, and National Science Foundation Grant AGS-1057183. The CIMS instrument was purchased as part of a major research instrumentation grant from the National Science Foundation (Grant ATM-0619783); assembly and testing was supported by the

Davidow Discovery Fund. We thank Katherine Schilling and ManNin Chan for experimental assistance and Arthur Chan for helpful discussion. We thank the reviewers for useful feedback on the discussions paper. Christine Loza, Lindsay Yee, and Jill Craven were supported by National Science Foundation Graduate Research Fellowships.

## Bibliography

- Aiken, A. C., DeCarlo, P. F., Kroll, J. H., Worsnop, D. R., Huffman, J. A., Docherty, K. S., Ulbrich, I. M., Mohr, C., Kimmel, J. R., Sueper, D., Sun, Y., Zhang, Q., Trimborn, A., Northway, M., Ziemann, P. J., Canagaratna, M. R., Onasch, T. B., Alfarra, M. R., Prevot, A. S. H., Dommen, J., Duplissy, J., Metzger, A., Baltensperger, U., and Jimenez, J. L.: O/C and OM/OC ratios of primary, secondary, and ambient organic aerosols with high-resolution time-of-flight aerosol mass spectrometry, *Environ. Sci. Technol.*, 42, 4478–4485, doi:10.1021/es703009q, 2008. 34, 37, 44, 70
- Balkanski, Y. J., Jacob, D. J., D. J., Gardner, G. M., Graustein, W. C., and Turekian, K. K.: Transport and residence times of tropospheric aerosols inferred from a global 3-dimensional simulation of PB-210, *J. Geophys. Res–Atmos.*, 98, 20 573–20 586, doi:10.1029/93JD02456, 1993. 33
- Birdsall, A. W., Andreoni, J. F., and Elrod, M. J.: Investigation of the role of bicyclic peroxy radicals in the oxidation mechanism of toluene, *J. Phys. Chem. A*, 114, 10 655–10 663, doi:10.1021/jp105467e, 2010. 54, 55, 67
- Bloss, C., Wagner, V., Jenkin, M. E., Volkamer, R., Bloss, W. J., Lee, J. D., Heard, D. E., Wirtz, K., Martin-Reviejo, M., Rea, G., Wenger, J. C., and Pilling, M. J.: Development of a detailed chemical mechanism (MCMv3.1) for the atmospheric oxidation of aromatic hydrocarbons, *Atmos. Chem. Phys.*, 5, 641–664, doi:10.5194/acp-5-641-2005, 2005. 55, 67
- Calvert, J. G., Atkinson, R., Becker, K. H., Kamens, R. M., Seinfeld, J. H., Wallington, T. J., and Yarwood, G.: *The Mechanisms of Atmospheric Oxidation of Aromatic Hydrocarbons*, Oxford University Press, New York, 2002. 35, 67

- Canagaratna, M. R., Jayne, J. T., Jimenez, J. L., Allan, J. D., Alfarra, M. R., Zhang, Q., Onasch, T. B., Drewnick, F., Coe, H., Middlebrook, A., Delia, A., Williams, L. R., Trimborn, A. M., Northway, M. J., DeCarlo, P. F., Kolb, C. E., Davidovits, P., and Worsnop, D. R.: Chemical and microphysical characterization of ambient aerosols with the Aerodyne aerosol mass spectrometer, *Mass Spectrom. Rev.*, 26, 185–222, doi:10.1002/mas.20115, 2007. 37
- Chhabra, P. S., Flagan, R. C., and Seinfeld, J. H.: Elemental analysis of chamber organic aerosol using an Aerodyne high-resolution aerosol mass spectrometer, *Atmos. Chem. Phys.*, 10, 4111–4131, doi:10.5194/acp-10-4111-2010, 2010. 34, 35, 44
- Chhabra, P. S., Ng, N. L., Canagaratna, M. R., Corrigan, A. L., Russell, L. M., Worsnop, D. R., Flagan, R. C., and Seinfeld, J. H.: Elemental composition and oxidation of chamber organic aerosol, *Atmos. Chem. Phys. Discuss.*, 11, 10 305–10 342, doi:10.5194/acpd-11-10305-2011, 2011. 35, 45
- Cocker, D. R., Flagan, R. C., and Seinfeld, J. H.: State-of-the-art chamber facility for studying atmospheric aerosol chemistry, *Environ. Sci. Technol.*, 35, 2594–2601, doi:10.1021/es0019169, 2001. 36
- Crounse, J. D., McKinney, K. A., Kwan, A. J., and Wennberg, P. O.: Measurement of gas-phase hydroperoxides by chemical ionization mass spectrometry, *Anal. Chem.*, 78, 6726–6732, doi:10.1021/ac0604235, 2006. 36
- DeCarlo, P. F., Kimmel, J. R., Trimborn, A., Northway, M. J., Jayne, J. T., Aiken, A. C., Gonin, M., Fuhrer, K., Horvath, T., Docherty, K. S., Worsnop, D. R., and Jimenez, J. L.: Field-deployable, high-resolution, time-of-flight aerosol mass spectrometer, *Anal. Chem.*, 78, 8281–8289, doi:10.1021/ac061249n, 2006. 37
- Hallquist, M., Wenger, J. C., Baltensperger, U., Rudich, Y., Simpson, D., Claeys, M., Dommen, J., Donahue, N. M., George, C., Goldstein, A. H., Hamilton, J. F., Herrmann, H., Hoffmann, T., Iinuma, Y., Jang, M., Jenkin, M. E., Jimenez, J. L., Kiendler-Scharr, A., Maenhaut, W.,

- McFiggans, G., Mentel, T. F., Monod, A., Prevot, A. S. H., Seinfeld, J. H., Surratt, J. D., Szmigielski, R., and Wildt, J.: The formation, properties and impact of secondary organic aerosol: current and emerging issues, *Atmos. Chem. Phys.*, 9, 5155–5236, 2009. 33
- Heald, C. L., Kroll, J. H., Jimenez, J. L., Docherty, K. S., DeCarlo, P. F., Aiken, A. C., Chen, Q., Martin, S. T., Farmer, D. K., and Artaxo, P.: A simplified description of the evolution of organic aerosol composition in the atmosphere, *Geophys. Res. Lett.*, 37, doi:10.1029/2010GL042737, 2010. 33
- Hildebrandt, L., Donahue, N. M., and Pandis, S. N.: High formation of secondary organic aerosol from the photo-oxidation of toluene, *Atmos. Chem. Phys.*, 9, 2973–2986, doi:10.5194/acp-9-2973-2009, 2009. 38, 42, 52
- Hildebrandt, L., Henry, K. M., Kroll, J. H., Worsnop, D. R., Pandis, S. N., and Donahue, N. M.: Evaluating the mixing of organic aerosol components using high-resolution aerosol mass spectrometry, *Environ. Sci. Technol.*, 45, 6329–6335, doi:10.1021/es200825g, 2011. 38
- Jenkin, M. E., Saunders, S. M., Wagner, V., and Pilling, M. J.: Protocol for the development of the Master Chemical Mechanism, MCM v3 (Part B): Tropospheric degradation of aromatic volatile organic compounds, *Atmos. Chem. Phys.*, 3, 181–193, doi:10.5194/acp-3-181-2003, 2003. 55, 67
- Jimenez, J. L., Canagaratna, M. R., Donahue, N. M., Prevot, A. S. H., Zhang, Q., Kroll, J. H., DeCarlo, P. F., Allan, J. D., Coe, H., Ng, N. L., Aiken, A. C., Docherty, K. S., Ulbrich, I. M., Grieshop, A. P., Robinson, A. L., Duplissy, J., Smith, J. D., Wilson, K. R., Lanz, V. A., Hueglin, C., Sun, Y. L., Tian, J., Laaksonen, A., Raatikainen, T., Rautiainen, J., Vaattovaara, P., Ehn, M., Kulmala, M., Tomlinson, J. M., Collins, D. R., Cubison, M. J., Dunlea, E. J., Huffman, J. A., Onasch, T. B., Alfarra, M. R., Williams, P. I., Bower, K., Kondo, Y., Schneider, J., Drewnick, F., Borrmann, S., Weimer, S., Demerjian, K., Salcedo, D., Cottrell, L., Griffin, R., Takami, A., Miyoshi, T., Hatakeyama, S., Shimono, A., Sun, J. Y., Zhang, Y. M., Dzepina, K., Kimmel, J. R., Sueper, D., Jayne, J. T., Herndon, S. C., Trimborn, A. M., Williams, L. R., Wood, E. C.,

- Middlebrook, A. M., Kolb, C. E., Baltensperger, U., and Worsnop, D. R.: Evolution of organic aerosols in the atmosphere, *Science*, 326, 1525–1529, doi:10.1126/science.1180353, 2009. 34
- Keywood, M. D., Varutbangkul, V., Bahreini, R., Flagan, R. C., and Seinfeld, J. H.: Secondary organic aerosol formation from the ozonolysis of cycloalkenes and related compounds, *Environ. Sci. Technol.*, 38, 4157–4164, doi:10.1021/es035363o, 2004. 36, 39
- Kroll, J. and Seinfeld, J.: Chemistry of secondary organic aerosol: Formation and evolution of low-volatility organics in the atmosphere, *Atmos. Environ.*, 42, 3593–3624, doi:10.1016/j.atmosenv.2008.01.003, 2008. 33
- Kroll, J. H., Smith, J. D., Che, D. L., Kessler, S. H., Worsnop, D. R., and Wilson, K. R.: Measurement of fragmentation and functionalization pathways in the heterogeneous oxidation of oxidized organic aerosol, *Phys. Chem. Chem. Phys.*, 11, 8005–8014, doi:10.1039/b905289e, 2009. 34, 45
- Kwok, E., Aschmann, S., Atkinson, R., and Arey, J.: Products of the gas-phase reactions of *o*-, *m*- and *p*-xylene with the OH radical in the presence and absence of NO<sub>x</sub>, *J. Chem. Soc., Faraday Trans.*, 93, 2847–2854, 1997. 54
- Lambe, A. T., Onasch, T. B., Massoli, P., Croasdale, D. R., Wright, J. P., Ahern, A. T., Williams, L. R., Worsnop, D. R., Brune, W. H., and Davidovits, P.: Laboratory studies of the chemical composition and cloud condensation nuclei (CCN) activity of secondary organic aerosol (SOA) and oxidized primary organic aerosol (OPOA), *Atmos. Chem. Phys.*, 11, 8913–8928, doi:10.5194/acp-11-8913-2011, 2011. 34, 44, 45
- Lee, A. K. Y., Herckes, P., Leaitch, W. R., Macdonald, A. M., and Abbatt, J. P. D.: Aqueous OH oxidation of ambient organic aerosol and cloud water organics: Formation of highly oxidized products, *Geophys. Res. Lett.*, 38, L11 805, doi:10.1029/2011GL047439, 2011. 45
- Matthew, B. M., Middlebrook, A. M., and Onasch, T. B.: Collection efficiencies in an Aerodyne aerosol mass spectrometer as a function of particle phase for laboratory generated aerosols, *Aerosol Sci. Tech.*, 42, 884–898, doi:10.1080/02786820802356797, 2008. 41

- Murphy, D. M., Cziczo, D. J., Froyd, K. D., Hudson, P. K., Matthew, B. M., Middlebrook, A. M., Peltier, R. E., Sullivan, A., Thomson, D. S., and Weber, R. J.: Single-particle mass spectrometry of tropospheric aerosol particles, *J. Geophys. Res–Atmos.*, 111, doi:10.1029/2006JD007340, 2006. 33
- Ng, N. L., Kroll, J. H., Chan, A. W. H., Chhabra, P. S., Flagan, R. C., and Seinfeld, J. H.: Secondary organic aerosol formation from *m*-xylene, toluene, and benzene, *Atmos. Chem. Phys.*, 7, 3909–3922, 2007. 35, 39, 54
- Ng, N. L., Canagaratna, M. R., Zhang, Q., Jimenez, J. L., Tian, J., Ulbrich, I. M., Kroll, J. H., Docherty, K. S., Chhabra, P. S., Bahreini, R., Murphy, S. M., Seinfeld, J. H., Hildebrandt, L., Donahue, N. M., DeCarlo, P. F., Lanz, V. A., Prevot, A. S. H., Dinar, E., Rudich, Y., and Worsnop, D. R.: Organic aerosol components observed in Northern Hemispheric datasets from aerosol mass spectrometry, *Atmos. Chem. Phys.*, 10, 4625–4641, doi:10.5194/acp-10-4625-2010, 2010. 33, 44, 45, 71, 73
- Ng, N. L., Canagaratna, M. R., Jimenez, J. L., Chhabra, P. S., Seinfeld, J. H., and Worsnop, D. R.: Changes in organic aerosol composition with aging inferred from aerosol mass spectra, *Aerosol Sci. Tech.*, 11, 6465–6474, doi:10.5194/acp-11-6465-2011, 2011. 33
- Noda, J., Volkamer, R., and Molina, M. J.: Dealkylation of alkylbenzenes: A significant pathway in the toluene, *o*-, *m*-, *p*-xylene + OH reaction, *J. Phys. Chem. A*, 113, 9658–9666, doi:10.1021/jp901529k, 2009. 54
- Paulot, F., Crounse, J. D., Kjaergaard, H. G., Kurten, A., St Clair, J. M., Seinfeld, J. H., and Wennberg, P. O.: Unexpected epoxide formation in the gas-phase photooxidation of isoprene, *Science*, 325, 730–733, doi:10.1126/science.1172910, 2009. 36
- Qi, L., Nakao, S., Malloy, Q., Warren, B., and Cocker, D. R.: Can secondary organic aerosol formed in an atmospheric simulation chamber continuously age?, *Atmos. Environ.*, 44, 2990–2996, doi:10.1016/j.atmosenv.2010.05.020, 2010. 34, 35, 40



- Riipinen, I., Pierce, J. R., Yli-Juuti, T., Nieminen, T., Häkkinen, S., Ehn, M., Junninen, H., Lehtipalo, K., Petäjä, T., Slowik, J., Chang, R., Shantz, N. C., Abbatt, J., Leaitch, W., Kerminen, V. M., Worsnop, D. R., Pandis, S. N., Donahue, N. M., and Kulmala, M.: Organic condensation: a vital link connecting aerosol formation to cloud condensation nuclei (CCN) concentration, *Atmos. Chem. Phys.*, 11, 3865–3878, doi:10.5194/acp-11-3865-2011, 2011. 42, 51
- Rudich, Y., Donahue, N. M., and Mentel, T. F.: Aging of organic aerosol: Bridging the gap between laboratory and field studies, *Annu. Rev. Phys. Chem.*, 58, 321–352, doi:10.1146/annurev.physchem.58.032806.104432, 2007. 33
- Sander, S. P., Abbatt, J., Barker, J. R., Burkholder, J. B., Friedl, R. R., Golden, D. M., Huie, R. E., Kolb, C. E., Kurylo, M. J., Moortgat, G. K., Orkin, V. L., and Wine, P. H.: Chemical kinetics and photochemical data for use in atmospheric studies, Evaluation No. 17. JPL Publication 10-6, Jet Propulsion Laboratory, Pasadena, URL <http://jpldataeval.jpl.nasa.gov>, 2011. 55, 67
- Seinfeld, J. H. and Pandis, S. N.: *Atmospheric Chemistry and Physics*, John Wiley and Sons, Inc., Hoboken, N.J., second edn., 2006. 49, 51
- Shilling, J. E., Chen, Q., King, S. M., Rosenoern, T., Kroll, J. H., Worsnop, D. R., DeCarlo, P. F., Aiken, A. C., Sueper, D., Jimenez, J. L., and Martin, S. T.: Loading-dependent elemental composition of  $\alpha$ -pinene SOA particles, *Atmos. Chem. Phys.*, 9, 771–782, doi:10.5194/acp-9-771-2009, 2009. 35
- Shiraiwa, M., Ammann, M., Koop, T., and Pöschl, U.: Gas uptake and chemical aging of semisolid organic aerosol particles, *Proc. Natl. Acad. Sci. U.S.A.*, 108, 11 003–11 008, doi:10.1073/pnas.1103045108, 2011. 72
- Song, C., Na, K., Warren, B., Malloy, Q., and Cocker, D. R.: Secondary organic aerosol formation from *m*-xylene in the absence of  $\text{NO}_x$ , *Environ. Sci. Technol.*, 41, 7409–7416, doi:10.1021/es070429r, 2007. 35, 54
- St.Ćclair, J. M., McCabe, D. C., Crounse, J. D., Steiner, U., and Wennberg, P. O.: Chemical

- ionization tandem mass spectrometer for the in situ measurement of methyl hydrogen peroxide, *Rev. Sci. Instrum.*, 81, 094 102–094 102–6, doi:10.1063/1.3480552, 2010. 36
- Vaden, T. D., Song, C., Zaveri, R. A., Imre, D., and Zelenyuk, A.: Morphology of mixed primary and secondary organic particles and the adsorption of spectator organic gases during aerosol formation, *Proc. Natl. Acad. Sci. U.S.A.*, 107, 6658–6663, doi:10.1073/pnas.0911206107, 2010. 72
- Vaden, T. D., Imre, D., Beránek, J., Shrivastava, M., and Zelenyuk, A.: Evaporation kinetics and phase of laboratory and ambient secondary organic aerosol, *Proc. Natl. Acad. Sci. U.S.A.*, 108, 2190–2195, doi:10.1073/pnas.1013391108, 2011. 72
- Virtanen, A., Joutsensaari, J., Koop, T., Kannosto, J., Yli-Pirilä, P., Leskinen, J., Mäkelä, J. M., Holopainen, J. K., Pöschl, U., Kulmala, M., Worsnop, D. R., and Laaksonen, A.: An amorphous solid state of biogenic secondary organic aerosol particles, *Nature*, 467, 824–827, doi:10.1038/nature09455, 2010. 72
- Weitkamp, E. A., Sage, A. M., Pierce, J. R., Donahue, N. M., and Robinson, A. L.: Organic Aerosol Formation from Photochemical Oxidation of Diesel Exhaust in a Smog Chamber, *Environ. Sci. Technol.*, 41, 6969–6975, doi:10.1021/es070193r, 2007. 38
- Zhang, Q., Jimenez, J. L., Canagaratna, M. R., Allan, J. D., Coe, H., Ulbrich, I., Alfarra, M. R., Takami, A., Middlebrook, A. M., Sun, Y. L., Dzepina, K., Dunlea, E., Docherty, K., DeCarlo, P. F., Salcedo, D., Onasch, T., Jayne, J. T., Miyoshi, T., Shimonono, A., Hatakeyama, S., Takegawa, N., Kondo, Y., Schneider, J., Drewnick, F., Borrmann, S., Weimer, S., Demerjian, K., Williams, P., Bower, K., Bahreini, R., Cottrell, L., Griffin, R. J., Rautiainen, J., Sun, J. Y., Zhang, Y. M., and Worsnop, D. R.: Ubiquity and dominance of oxygenated species in organic aerosols in anthropogenically-influenced Northern Hemisphere midlatitudes, *Geophys. Res. Lett.*, 34, doi:10.1029/2007GL029979, 2007. 33
- Zhang, X., Pandis, S. N., and Seinfeld, J. H.: Diffusion-Limited Versus Quasi-Equilibrium Aerosol Growth, *Aerosol Sci. Tech.*, 46, 874–885, doi:10.1080/02786826.2012.679344, 2012. 51

Zhao, J., Zhang, R., Misawa, K., and Shibuya, K.: Experimental product study of the OH-initiated oxidation of *m*-xylene, J. Photoch. Photobio. A, 176, 199–207, doi:10.1016/j.jphotochem.2005.07.013, 2005. 54, 55

**Table 3.1:** Experiment sampling conditions and instrument sampling protocol.

Experiment Type	Duration (h)	Volume Removed (m <sup>3</sup> )	Sampling hours	
			Group I <sup>a</sup>	Group II <sup>b</sup>
Wall loss	23	6.14	N/A <sup>c</sup>	N/A
18 h aging	18	7.92	0-18	0-18
24 h aging	24	3.60	0-24	16-24
30 h aging	30	3.63	0-30	22-30
36 h aging	36	3.66	0-36	28-36

<sup>a</sup>Group I instruments: AMS, RH and temperature probe (total volumetric flow rate = 0.084 L min<sup>-1</sup>).

<sup>b</sup>Group II instruments: DMA, CIMS, GC/FID, O<sub>3</sub> analyzer, NO<sub>x</sub> analyzer (total volumetric flow rate = 7.25 L min<sup>-1</sup>).

<sup>c</sup>Instruments sampling: DMA, O<sub>3</sub> analyzer, NO<sub>x</sub> analyzer, RH and temperature probe (total volumetric flow rate = 4.45 L min<sup>-1</sup>).

**Table 3.2:** Experimental conditions and results.

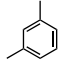
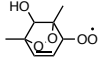
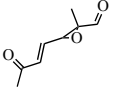
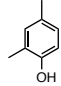
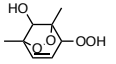
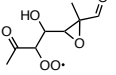
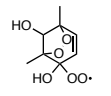
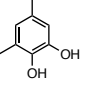
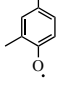
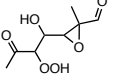
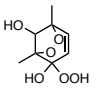
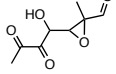
Seed	Duration (h)	Initial <i>m</i> -xylene (ppb)	Seed vol. ( $\mu\text{m}^3 \text{cm}^{-3}$ )	Final <i>m</i> -xylene (ppb)	Final $\Delta M_o^a$ ( $\mu\text{g m}^{-3}$ )
AS	18	$32.2 \pm 0.7$	$11.1 \pm 0.3$	$2.46 \pm 0.66$	$21.9 \pm 1.7$
AS	18	$31.8 \pm 0.7$	$12.3 \pm 0.3$	$0.84 \pm 0.66$	$24.7 \pm 1.9$
AS	24	$29.2 \pm 0.7$	$9.10 \pm 0.2$	$< 0.5$	N/A
AS	30	$29.1 \pm 0.7$	$12.3 \pm 0.4$	$< 0.5$	N/A
AS	36	$28.7 \pm 0.7$	$13.1 \pm 0.2$	$< 0.5$	N/A
AS	12+8 <sup>b</sup>	$25.0 \pm 0.6$	$10.5 \pm 0.3$	$2.1 \pm 0.6$	$20.0 \pm 1.0$
MS+SA	18	$32.9 \pm 0.7$	$10.5 \pm 0.4$	$1.94 \pm 0.66$	$22.5 \pm 1.8$
MS+SA	18	$32.4 \pm 0.7$	$10.8 \pm 0.4$	$1.15 \pm 0.66$	$21.7 \pm 1.7$
MS+SA	24	$32.5 \pm 0.7$	$10.6 \pm 0.3$	$< 0.5$	N/A
MS+SA	30	$29.6 \pm 0.7$	$10.6 \pm 0.3$	$< 0.5$	N/A
MS+SA	36	$30.0 \pm 0.7$	$10.8 \pm 0.4$	$< 0.5$	N/A

<sup>a</sup>Lower bound limit<sup>b</sup>12.4 h irradiated + 8 h dark

**Table 3.3:** Rate constants for the photochemical model.

Rate constant ( $\text{cm}^3 \text{s}^{-1}$ )	Source
$j_{\text{H}_2\text{O}_2} = 2.9 \times 10^{-6} \text{ (s}^{-1}\text{)}$	Sander et al. (2011)
$k_1 = 1.8 \times 10^{-12}$	Sander et al. (2011)
$k_2 = 2.31 \times 10^{-11}$	Calvert et al. (2002)
$k_3 = 9.8 \times 10^{-13}$	Birdsall et al. (2010)
$k_4 = 1.96 \times 10^{-11}$	MCM (Jenkin et al., 2003; Bloss et al., 2005)
$k_5 = 8.02 \times 10^{-11}$	MCM
$j_{\text{EPOX}} = 1.24 \times 10^{-4} \text{ (s}^{-1}\text{)}$	MCM and Sander et al. (2011)
$k_6 = 9.1 \times 10^{-11}$	MCM
$k_7 = 1.17 \times 10^{-10}$	MCM
$j_{\text{ROOH}} = 2.1 \times 10^{-6} \text{ (s}^{-1}\text{)}$	Sander et al. (2011)
$k_8 = 1.96 \times 10^{-11}$	MCM
$k_9 = 7.41 \times 10^{-11}$	MCM
$k_{10} = 1.96 \times 10^{-11}$	MCM
$k_{11} = 1.13 \times 10^{-10}$	MCM
$k_{12} = 2.05 \times 10^{-10}$	MCM
$k_{13} = 1.4 \times 10^{-12}$	Sander et al. (2011)
$k_{14} = 1.1 \times 10^{-10}$	Sander et al. (2011)

**Table 3.4:** Compounds represented in the photochemical model.

Compound	Structure	Formula
RH		$C_8H_{12}$
RO <sub>2</sub>		$C_8H_{11}O_5$
EPOX		$C_8H_{10}O_3$
ROH		$C_8H_{10}O$
ROOH		$C_8H_{12}O_5$
EPOXO <sub>2</sub>		$C_8H_{11}O_6$
ROHO <sub>2</sub>		$C_8H_{11}O_6$
ROHOH		$C_8H_{10}O_2$
RO		$C_8H_9O$
EPOXOOH		$C_8H_{12}O_6$
ROHOOH		$C_8H_{12}O_6$
<i>prod</i> <sub>EPOXOOH+OH</sub>	e.g. 	$C_8H_{12}O_5$

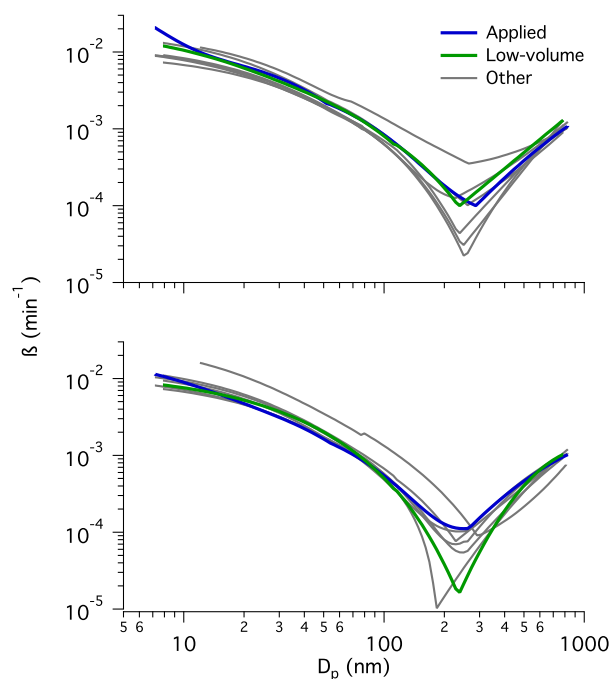


**Figure 3.1:** Particle wall loss rate constants,  $\beta$ , measured in both chambers from September 2009 to August 2011. The top panel corresponds to near chamber, and the bottom panel corresponds to far chamber. The wall loss rates labeled “applied” were applied to the experiments reported in this manuscript. The wall loss rates labeled “low-volume” were calculated during a wall loss calibration experiment in which the initial chamber volume was decreased by 8 m<sup>3</sup> to simulate conditions achieved after 18 h of sampling. The wall loss rates labeled “other” are those calculated from quarterly calibration experiments.

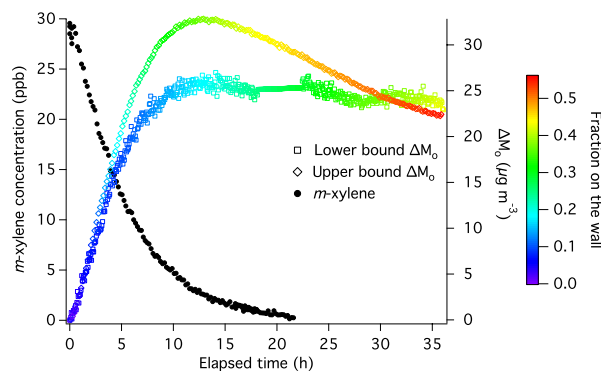


**Figure 3.2:** SOA mass (right axis), corrected for particle wall losses, and *m*-xylene (left axis) for 36 h of OH exposure using AS seed. The lower bound  $\Delta M_o$  is calculated assuming that, once deposited, particles on the walls do not interact with gases in the chamber. The upper bound  $\Delta M_o$  assumes that, once deposited, particles continue to exhibit the same gas-particle partitioning behavior as suspended particles. The fraction on the wall for the lower bound is the ratio of particle volume on the wall to total particle volume, both suspended and deposited, and includes seed volume. The fraction on the wall for the upper bound is the ratio of organic mass concentration on the wall to the total organic mass concentration.



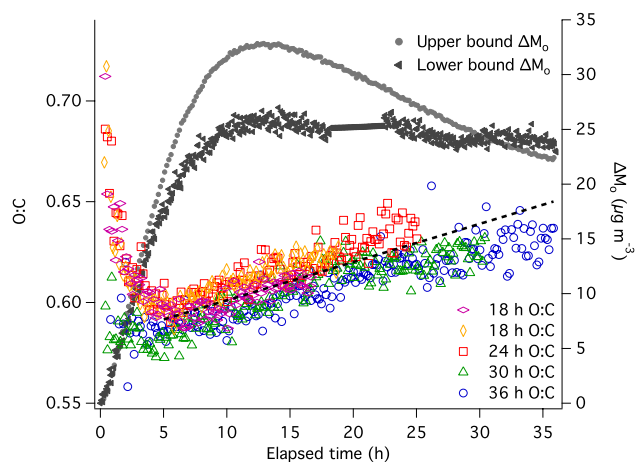


**Figure 3.3:** SOA mass (right axis) and O:C elemental composition (left axis) over 36 h of OH exposure using AS seed. After hour 5, the O:C increases at an average rate of  $0.0019 \text{ h}^{-1}$  (dashed line).

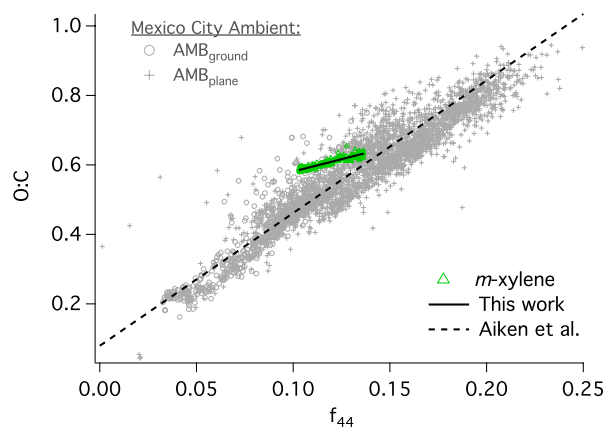


**Figure 3.4:** Correlation of O:C with  $f_{44}$  for SOA from *m*-xylene in the present study and Mexico City ambient aerosol from Aiken et al. (2008).

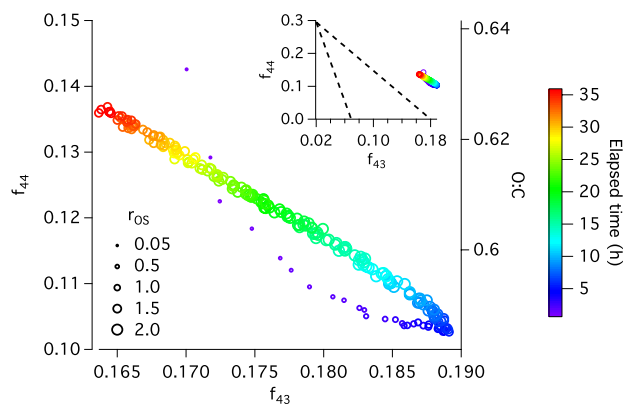


**Figure 3.5:** Evolution of  $f_{43}$ ,  $f_{44}$ , and O:C for 36 h of OH exposure. This system lies to the right of the triangular region in which typical ambient aerosol resides, as shown by the dashed lines in the inset (Ng et al., 2010). Marker size denotes the organic-to-sulfate ratio,  $r_{OS}$ , of suspended particles.

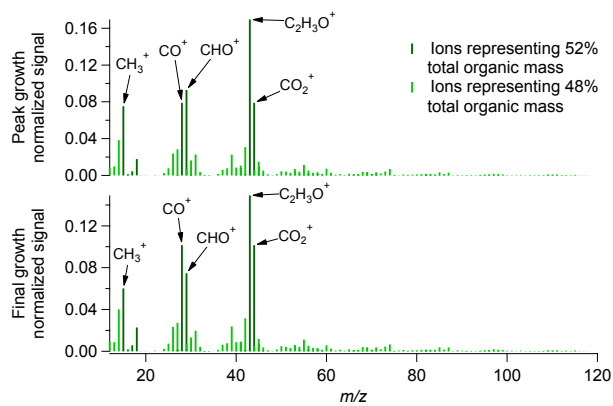


**Figure 3.6:** Average AMS high-resolution organic mass spectra at the time of peak growth and at the end of the experiment (final growth) for the 36-h aging experiment. Prominent peaks are identified. The mass of  $\text{CO}^+$  is estimated to equal that of  $\text{CO}_2^+$ .

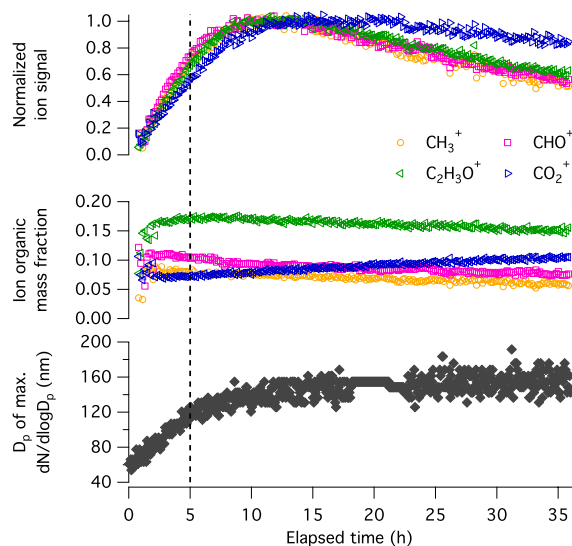


**Figure 3.7:** Evolution of SOA chemical composition from high-resolution AMS measurements and diameter of the maximum number distribution of suspended particles. In the top panel, the ion signal is normalized by sulfate to account for particle wall losses. The sulfate-normalized ion signal is then scaled by the average value at the peak concentration. The middle panel shows the fractional contribution of each ion to the total organic mass signal. A relative ionization efficiency of 1.4 is used when calculating the organic ion concentration. The dashed line at 5 h corresponds to the reversal in trend of O:C.

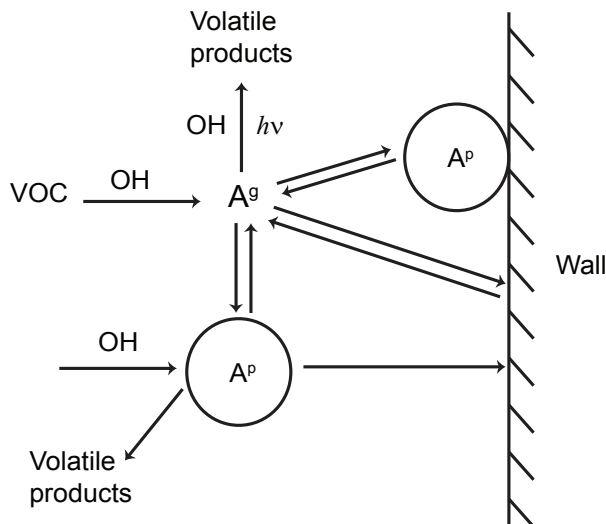


**Figure 3.8:** Sources and sinks of a semivolatile gas-phase species,  $A^g$ , and particles containing the condensed semivolatile species,  $A^p$ , during SOA aging. We do not explicitly indicate in the sketch processes by which the particle-phase  $A^p$  attains a semisolid state, greatly affecting continued exchange with the gas phase (Virtanen et al., 2010; Vaden et al., 2010, 2011; Shiraiwa et al., 2011).

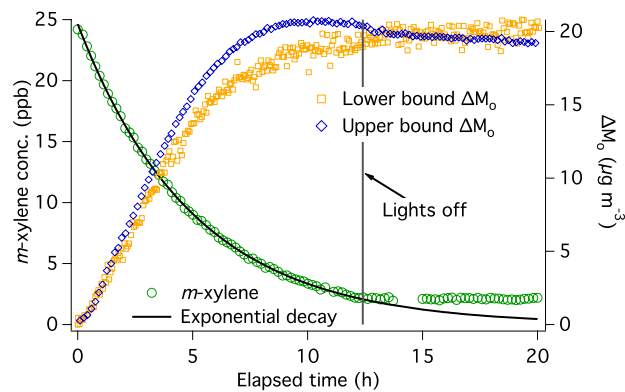


**Figure 3.9:** Trends in  $m$ -xylene concentration (left axis) and  $\Delta M_o$  (right axis) when irradiation is stopped once peak  $\Delta M_o$  is attained.

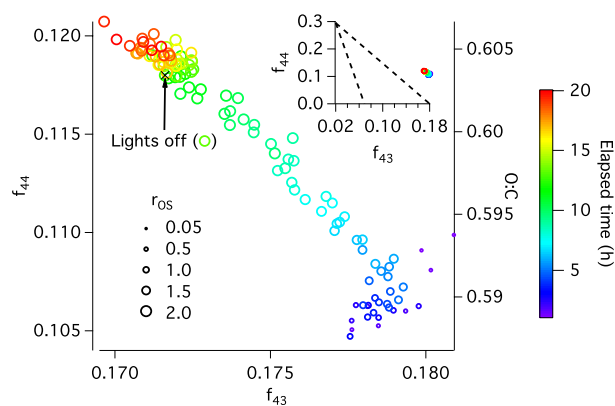


**Figure 3.10:** Evolution of  $f_{43}$ ,  $f_{44}$ , and O:C of  $m$ -xylene SOA. Irradiation was stopped after 12.4 hours, corresponding to the peak of  $\Delta M_o$ . This point is denoted by the “x”. Marker size denotes the organic-to-sulfate ratio,  $r_{OS}$ , of suspended particles. After irradiation stops, the chemical composition of the SOA does not change significantly. The inset shows the position of the data with respect to the triangular region characteristic of ambient SOA bounded by the dashed lines, as defined by Ng et al. (2010)

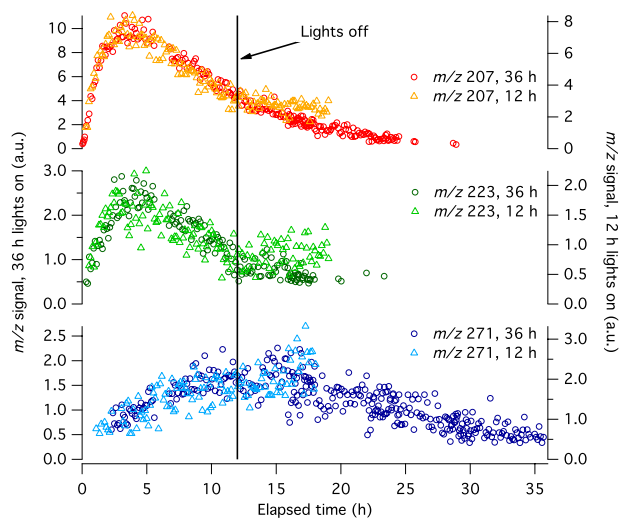


**Figure 3.11:** Time evolution of products formed during *m*-xylene oxidation detected by the CIMS. The signals labeled 36 h were recorded during the set of experiments in which the chamber contents were irradiated for 36 h. The signals labeled 12 h were recorded during the experiment in which the lights were turned off after 12.4 h of irradiation and remained off for the remainder of the experiment.

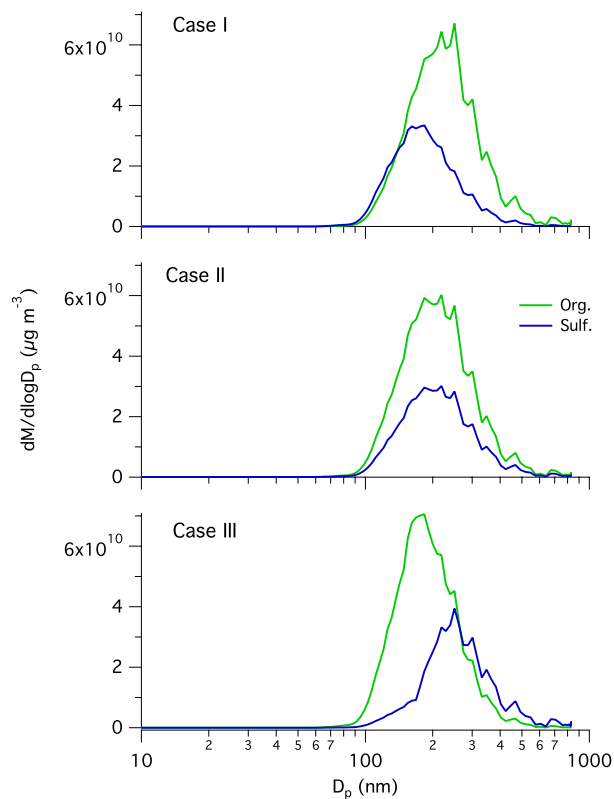


**Figure 3.12:** Organic and sulfate mass distributions used in a simulation to assess the effect of size-dependent  $r_{OS}$  on the upper bound organic mass wall loss correction. All mass distributions are derived from the same observed particle number distribution and have  $r_{OS}$  of 2.00 and an organic mass concentration of  $22.7\text{--}22.8 \mu\text{g m}^{-3}$ . Case I is representative of condensation governed by gas-particle equilibrium partitioning (see text), and Case III is representative of condensation governed by diffusion-limited growth (see text). In Case II,  $r_{OS}$  is constant for all  $D_p$ .

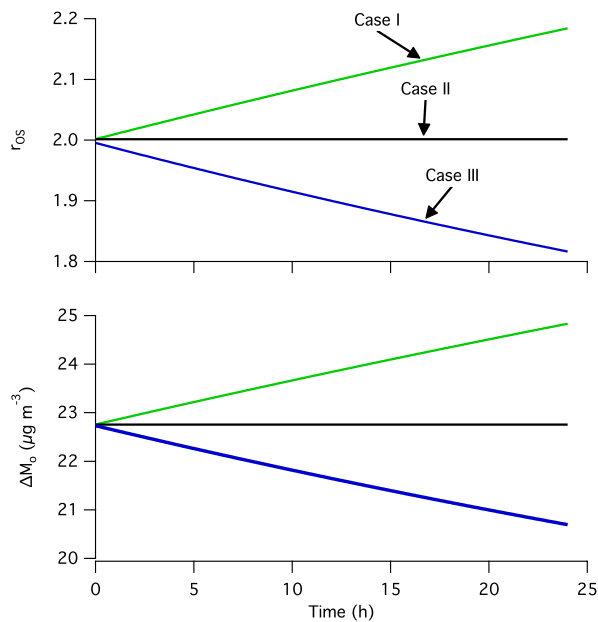


**Figure 3.13:** Effect of 24 h of wall loss on the mass distributions in Fig. 3.12. The top panel shows the suspended particle organic-to-sulfate ratio,  $r_{OS}$ , as a function of time for each case, and the bottom panel shows the upper bound wall-loss corrected organic mass concentration as a function of time for each case.

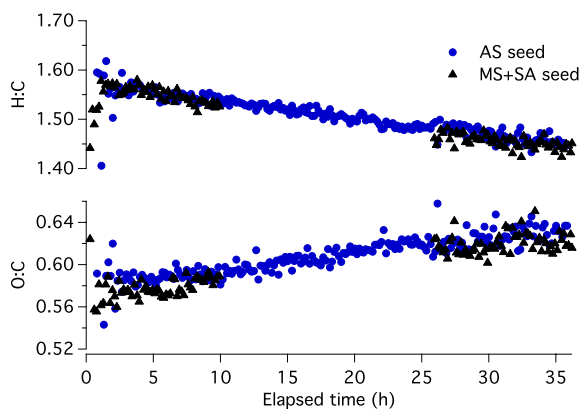


**Figure 3.14:** Elemental ratios of *m*-xylene aerosol condensed onto neutral (AS) and acidic (MS+SA) seed particles.

## Chapter 4

# On the Mixing and Evaporation of Secondary Organic Aerosol Components\*

---

\*Reproduced with permission from “On the Mixing and Evaporation of Secondary Organic Aerosol Components” by C. L. Loza, M. M. Coggon, T. B. Nguyen, A. Zuend, R. C. Flagan, and J. H. Seinfeld *Environmental Science & Technology*, doi:10.1021/es400979k. Copyright 2013 by the American Chemical Society.



## 4.1 Abstract

The physical state and chemical composition of an organic aerosol affect its degree of mixing and its interactions with condensing species. We present here a laboratory chamber procedure for studying the effect of the mixing of organic aerosol components on particle evaporation. The procedure is applied to the formation of secondary organic aerosol (SOA) from  $\alpha$ -pinene and toluene photooxidation. SOA evaporation is induced by heating the chamber aerosol from room temperature (25 °C) to 42 °C over 7 h and detected by a shift in the peak diameter of the SOA size distribution. With this protocol,  $\alpha$ -pinene SOA is found to be more volatile than toluene SOA. When SOA is formed from the two precursors sequentially, the evaporation behavior of the SOA most closely resembles that of SOA from the second parent hydrocarbon, suggesting that the structure of the mixed SOA resembles a core of SOA from the initial precursor coated by a layer of SOA from the second precursor. Such a core-and-shell configuration of the organic aerosol phases implies limited mixing of the SOA from the two precursors on the timescale of the experiments, consistent with a high viscosity of at least one of the phases.

## 4.2 Introduction

Recent studies suggest that atmospheric organic aerosols may exist in an amorphous semi-solid or amorphous solid (glassy) state (Virtanen et al., 2010; Vaden et al., 2010; Cappa and Wilson, 2011; Shiraiwa et al., 2011; Vaden et al., 2011; Kuwata and Martin, 2012; Perraud et al., 2012; Saukko et al., 2012; Abramson et al., 2013). The physical state of a particle affects its interaction with water and condensing organic compounds and its behavior upon heating or cooling (Koop et al., 2011). It is difficult to observe the physical state of submicrometer particles directly; therefore, a number of indirect techniques have been used to probe the physical state of aerosols, typically at room temperature and low relative humidity (RH). Bounce of secondary organic aerosol (SOA) particles in an impactor was taken as indicative of a solid state (Virtanen et al., 2010; Saukko et al., 2012). Another study employed an amorphous protein substrate as a proxy for an amorphous,

semi-solid aerosol and showed that a model with finite, condensed-phase diffusion was necessary to reproduce ozone uptake by the substrate (Shiraiwa et al., 2011). That the uptake of organic nitrates by  $\alpha$ -pinene ozonolysis SOA did not follow absorptive equilibrium partitioning theory was taken, in another study, as indicative of non-liquid-like behavior (Perraud et al., 2012). Ammonia uptake of  $\alpha$ -pinene ozonolysis SOA was larger under humid conditions ( $\text{RH} > 94\%$ ) than under dry conditions ( $\text{RH} < 5\%$ ), suggesting a transition from semi-solid to liquid particles for increasing RH (Kuwata and Martin, 2012). In other studies,  $\alpha$ -pinene ozonolysis SOA exhibited slower evaporation kinetics than those expected for liquid droplets (Vaden et al., 2011), and pyrene evaporation from  $\alpha$ -pinene ozonolysis SOA indicated a particle viscosity of approximately  $10^8$  Pa s, much greater than typical liquid viscosities of  $10^{-2}$ - $10^3$  Pa s (Abramson et al., 2013). Based on the observation that  $\alpha$ -pinene ozonolysis SOA partially evaporated in a thermodenuder without a change in particle chemical composition, it was concluded that particle-phase diffusional limitations prevented higher volatility compounds from evaporating preferentially (Cappa and Wilson, 2011). The primary inference in each of these studies is that the retarded diffusion of compounds within the condensed phase can be attributed to highly viscous particle-phase behavior.

Others have studied particle mixing using controlled aerosol generation from two different sources. Laser ablation single-particle mass spectrometry data suggest that dioctyl phthalate and  $\alpha$ -pinene ozonolysis SOA formed two separate phases when one type of aerosol was coated with the other type (Vaden et al., 2010). In another study (Hildebrandt et al., 2011), SOA mass yields (ratio of mass of SOA formed to mass of parent hydrocarbon reacted) of sequentially formed  $\alpha$ -pinene ozonolysis and labeled toluene photooxidation SOA showed that the SOA yield of the second precursor was consistent with partitioning to the combined SOA mass from the first and second precursors (pseudo-ideal mixing, Odum et al., 1996; Bowman et al., 1997; Odum et al., 1997; Strader et al., 1999) rather than partitioning to the SOA mass formed solely by the second precursor.

In this work, we present an experimental protocol designed to probe the mixing state of organic aerosols by observing the evaporation behavior of SOA formed sequentially from two different precursors in an environmental chamber. While oxidation products from the first precursor are present

in the chamber throughout the experiment and can partition into the particle phase as more organic particle mass is formed from the second precursor, the second period of SOA formation is likely dominated by oxidation products from the second precursor. It is hypothesized that particle evaporation reflects the nature of SOA mixing. If a particle is well mixed, i.e. molecular diffusion timescales within the particle are the same order of magnitude or faster than evaporation timescales (Shiraiwa and Seinfeld, 2012), then volatile SOA components have essentially immediate access to the particle surface for evaporation. If diffusion timescales within the particle are much longer than evaporation timescales, evaporation of volatile components is inhibited.

Evaporation is induced by heating the chamber, run as a batch reactor, rather than using a thermodenuder, which is limited in the study of potential particle-phase mass transfer limitations due to its characteristic residence time (2 to 30 s, An et al., 2007; Tritscher et al., 2011). Two drawbacks exist, however, to using chamber heating as a basis to infer aerosol evaporation behavior. First, the maximum chamber temperature, in the present case 50 °C, is substantially lower than that achieved in thermodenuders,  $\sim 400$  °C. Second, condensable organic vapors are difficult to remove from a batch reactor without also removing the particles themselves. In a thermodenuder, the sample flows over a bed of activated carbon to remove vapors immediately after heating. Here, we dilute the chamber contents before heating to decrease the concentration of vapor-phase components and promote particle evaporation. Other studies have used chamber heating or dilution separately to evaluate the yield, volatility, reversibility of SOA formed from  $\alpha$ -pinene ozonolysis (Grieshop et al., 2007; Stanier et al., 2007; Warren et al., 2009) and *m*-xylene photooxidation (Qi et al., 2010); we combine these procedures to study the mixing state of SOA.

### 4.3 Experimental

Experiments were performed in the Caltech indoor, dual 24-m<sup>3</sup> Teflon chambers. Prior to an experiment, the chamber was cleaned by flushing with air passed through beds of activated carbon, silica gel, Purafil SP Blend Media, and molecular sieves and a particle filter to achieve a particle background of  $< 10$  cm<sup>-3</sup> and a relative humidity of  $< 7$  %. The experiments were conducted under

conditions of  $\leq 5$  ppbv  $\text{NO}_x$  and  $< 7\%$  relative humidity. Initial  $\text{O}_3$  concentration was  $< 5$  ppbv, the instrument lower detection limit. While some  $\text{O}_3$  formed during photooxidation, the major sink of both SOA precursors was reaction with OH. The temperature of the chamber enclosure was maintained initially at  $25 \pm 1$  °C. Hydrogen peroxide ( $\text{H}_2\text{O}_2$ , 50 % wt., Sigma Aldrich) was used as the OH radical source and was injected into the chamber by flowing purified air at 5 LPM over 280  $\mu\text{L}$  of  $\text{H}_2\text{O}_2$  in a glass bulb immersed in a 35 °C water bath. Photolysis of  $\text{H}_2\text{O}_2$  by 350 nm-centered UV broadband lamps (40 W Sylvania 350BL,  $j_{\text{NO}_2} \sim 6 \times 10^{-3} \text{ s}^{-1}$ ) provided a constant source of OH radicals during the irradiation period at a concentration of about  $3 \times 10^6 \text{ molec cm}^{-3}$ , as inferred from the decrease in parent hydrocarbon concentration. Ammonium sulfate seed particles were added to the chamber by atomizing an aqueous solution of 0.015 M ammonium sulfate; particles dried upon contact with the dry air in the chamber. Toluene (99.8 % purity, Sigma Aldrich) and/or  $\alpha$ -pinene (99+ % purity, Sigma Aldrich) were added to the chamber by flowing purified air at 5 LPM over a measured liquid volume. After injections, the chamber contents were allowed to mix for 1 h before irradiation.

During sequential precursor experiments, the second precursor was added in the same manner as the first after SOA growth from the first precursor stabilized. After 17-24 h, the irradiation period ended, the lights were turned off, halting OH production, which was confirmed by a leveling of the concentration of unreacted toluene. Approximately 100 ppbv of cyclohexane, used as a dilution tracer, was added to the chamber using the same method as the hydrocarbon injections. Once the cyclohexane concentration stabilized, the chamber contents were diluted by a factor of 2-3 with purified air. After dilution, the temperature of the dark chamber enclosure was ramped linearly over 7 h from 25 °C to 45 °C to achieve a maximum chamber temperature of 40-42 °C. The chamber was maintained at the maximum temperature for 7 h.

A suite of instruments was used to study the evolution of the gas and particle phases. Toluene,  $\alpha$ -pinene, and cyclohexane were measured using a gas chromatograph equipped with a flame ionization detector (GC/FID, Agilent, 6890N). Samples were collected by drawing chamber air through a 10 mL sample loop and were analyzed using a HP-5 column (15 m $\times$ 0.53 mm ID $\times$ 1.5  $\mu\text{m}$  thickness, Agilent).

The sample was injected onto the 60 °C column; after 1 min, the oven temperature was ramped at 40 °C min<sup>-1</sup> to 250 °C, and then held at 250 °C for 3 min. Relative humidity and temperature, NO and NO<sub>x</sub>, and O<sub>3</sub> were continuously monitored using a Vaisala HMP 233, a chemiluminescence NO<sub>x</sub> monitor (T200, Teledyne), and an O<sub>3</sub> monitor (APOA-360, Horiba), respectively.

The suspended aerosol size distribution and number concentration were measured continuously using a custom-built scanning mobility particle sizer consisting of a differential mobility analyzer (DMA, TSI, 3081) coupled to a condensation particle counter (CPC, TSI, 3010), henceforth referred to as the DMA. The DMA was operated in a closed-loop configuration with a recirculating sheath and excess flow of 2.67 L min<sup>-1</sup> and a 5.4:1 ratio of sheath to aerosol flow rates, and column voltage was scanned from 15 to 9850 V over 45 s. DMA mobility (diameter) resolution,  $R$ , is defined as (Zhang and Flagan, 1996)

$$R = \frac{Z_p^*}{\Delta Z_p} \quad (4.1)$$

where  $Z_p^*$  is the mobility corresponding to the peak of the transfer function and  $\Delta Z_p$  is the full width of the transfer function at half maximum. The resolution was calculated for each of the 106 mobility (diameter) bins using the transfer function given in Stolzenburg (1988). Because size distribution data are binned, a well-resolved change in mobility is deemed one in which a particle with any mobility in the first bin is resolved from a particle with any mobility in the second bin. At the DMA operating conditions in the present work, the DMA can resolve a 15-25 % change in particle diameter. Here, particle diameter shifts are reported using the size bin median diameter. Real-time particle mass spectra were collected by an Aerodyne high-resolution time-of-flight aerosol mass spectrometer (AMS, DeCarlo et al., 2006; Canagaratna et al., 2007). The AMS switched among the higher sensitivity, lower resolution “V-mode,” Particle Time-of-Flight (PToF) mode, and the lower sensitivity, higher resolution “W-mode.” AMS data were processed using “Squirrel,” the ToF-AMS Unit Resolution Analysis Toolkit (<http://cires.colorado.edu/jimenez-group/ToFAMSResources/ToFSoftware/index.html>), in Igor Pro Version 6.22A (Wavemetrics, Lake Oswego, OR). “V-mode” and PToF data were analyzed using a fragmentation table to separate sulfate, ammonium, and organic spectra and to time-trace specific  $m/z$  ratios (Allan et al., 2004).

“V-mode” and “W-mode” data were analyzed using a separate high-resolution spectra toolbox PIKA (Peak Integration by Key Analysis) to determine the chemical formulas contributing to distinct  $m/z$  ratios (DeCarlo et al., 2006). The signals of organic ions below  $m/z$  141 were used to calculate elemental ratios. The ratio of particle-phase  $\text{CO}^+$  to  $\text{CO}_2^+$  was approximately equal to 1, and in “V-mode,” the contribution of  $\text{CO}^+$  to the organic signal was equated to that of particle-phase  $\text{CO}_2^+$ . The intensities of water-derived ions ( $\text{H}_2\text{O}^+$ ,  $\text{OH}^+$ , and  $\text{O}^+$ ) were calculated from particle-phase  $\text{CO}_2^+$  (Aiken et al., 2008). A relative ionization efficiency of 1.4 was applied to organic ion signals. AMS data reported in this work are averaged over 1-h intervals.

## 4.4 Results and Discussion

### 4.4.1 Aerosol Size Distribution Evolution

Both evaporation and particle wall losses affect suspended particle size distributions in this study (Figure 4.1). Partial particle evaporation decreases particle size but does not affect the number concentration, whereas particle wall loss decreases the number concentration but does not change particle size. Particle wall loss rate constants in the Caltech chambers are size-dependent with a minimum occurring between 200 and 300 nm. Particle wall losses potentially change the shape of the size distribution as particles of certain diameters are lost faster than others. The inset of Figure 4.1b shows the evolution of a SOA size distribution generated from sequential photooxidation of toluene and then  $\alpha$ -pinene in which the chamber contents were diluted but not heated (Table 4.1, Experiment 7), and only particle wall losses were observed. The diameter of the size distribution peak remained within the same size bin (300-319 nm) over 9 h of wall loss. In the size range of the present experiments, wall loss is not expected to affect the diameter of the size distribution peak, only its magnitude. Evaporation can shift the size distribution peak diameter to lower diameters and, due to the Kelvin effect, broaden the size distribution as vapors evaporating from smaller diameter particles condense onto larger diameter particles, a process known as Ostwald ripening (Marqusee and Ross, 1984). For particle diameters in the present study ( $\geq 200$  nm), the Kelvin

effect is not expected to be significant, but the effect is admittedly difficult to isolate in the behavior of the particle size distributions.

SOA evaporation also can be observed as a decrease in bulk particle mass and volume; however, particle wall losses, in addition to evaporation, affect the bulk particle mass and volume and must be corrected for prior to assessing possible particle evaporation. One large uncertainty associated with particle wall loss corrections is the extent of gas-particle partitioning of deposited particles. SOA mass, calculated using the two gas-particle partitioning limiting assumptions (deposited particles undergo no gas-particle partitioning or the same gas-particle partitioning as suspended particles), can differ by almost 100 % when comparing the lower and higher limits (Hildebrandt et al., 2009). There are also uncertainties associated with quantifying particle wall loss rates necessary to wall-loss correct the DMA data, and AMS PToF data show that the organic-to-sulfate ratio is not constant across the mass distribution in the present experiments, which would necessitate the use of size-dependent wall loss rates to quantify particle wall losses for AMS data (Loza et al., 2012). Given the uncertainties associated with particle wall loss corrections, it is advantageous to detect partial SOA evaporation as a shift in the size distribution peak diameter.

The evaporation of toluene and  $\alpha$ -pinene SOA was first assessed individually (Experiments 1 and 2, see Table 4.1). SOA was photochemically formed and aged for 17-19.5 h before dark dilution and heating, and no particle nucleation was observed. In Experiment 1, all  $\alpha$ -pinene was consumed before dilution, and in Experiment 2, 70 % of the toluene reacted before dilution. Figure 4.1 shows the evolution of the hourly averaged, suspended particle size distributions during the 7-h heating period after dilution. Particle evaporation is characterized by a significant shift, as determined by the DMA resolution, in the size distribution peak diameter to smaller diameters, behavior that is observed for  $\alpha$ -pinene (Figure 4.1a) but not for toluene (Figure 4.1b). After the heating period,  $\alpha$ -pinene SOA continued to evaporate while the chamber enclosure was held at an elevated temperature, indicated by the black size distribution in Figure 4.1a. For the initial  $\alpha$ -pinene SOA size distribution, a shift in peak diameter of 36 nm was deemed significant, and a 47 nm peak shift was observed; the 9 nm peak shift observed for the toluene SOA size distribution was not considered significant. These

observations suggest that  $\alpha$ -pinene SOA is more volatile than toluene SOA. Previous studies have measured the volatility of SOA from  $\alpha$ -pinene or toluene photooxidation using a thermodenuder and found that both types of SOA evaporated to some extent (Lambe et al., 2011; Hildebrandt et al., 2009; Emanuelsson et al., 2012). Notably, 55 % of toluene SOA evaporated at 39 °C and 16.5 s residence time (Hildebrandt et al., 2009). In that study, however, the SOA was produced at 11 °C. In the present study, SOA was produced at 27 °C. SOA yields increase as temperature decreases (Hildebrandt et al., 2009; Warren et al., 2009; Qi et al., 2010), as partitioning of semivolatile species to the particle phase is facilitated at lower temperatures. SOA produced from a specific precursor at higher temperatures is expected to contain a higher fraction of low volatility components than that produced at lower temperatures.

The results from Experiments 1 and 2 show that  $\alpha$ -pinene SOA evaporates partially whereas toluene SOA does not evaporate significantly. By observing the evaporation behavior of combinations of  $\alpha$ -pinene and toluene SOA, it is possible to determine whether particle-phase diffusion is rapid (i.e. evaporation of SOA components, presumably from  $\alpha$ -pinene photooxidation, occurs regardless of the SOA formation sequence) or not.

Figure 4.2 shows irradiation, dilution, and heating stages and the evolution of the chamber contents during Experiment 4 in which SOA was produced sequentially, first from  $\alpha$ -pinene and then from toluene. Similar particle growth, hydrocarbon decay, and temperature changes were observed for Experiments 3 and 5. In Experiment 6, both  $\alpha$ -pinene and toluene were injected before irradiation, and the evolution of the chamber contents resembled that in Experiment 4, excluding the second SOA growth period (commencing at the black, vertical line). During Experiments 3-5, SOA growth from the first precursor stabilized before the second precursor was added;  $\alpha$ -pinene and toluene growth stabilized after 8 and 17 h of irradiation, respectively. Although some toluene remained after 17 h, the next part of the experiment was begun at this point due to constraints imposed by particle wall losses. Particle nucleation was not observed in Experiments 3-6.

The evolution of the hourly averaged suspended particle size distributions during the heating period for Experiments 3-6 is shown in Figure 4.3. A significant shift of the size distribution peak



diameter is observed only in Experiment 5 (panel c), in which toluene oxidation was followed by  $\alpha$ -pinene oxidation. The peak shift observed was 98 nm, and a shift of at least 77 nm was deemed significant. Experiments 3 and 4 (panels a and b), in which SOA was produced in the reverse order, did not show significant changes in particle diameter due to heating. A significant shift in the peak diameter was considered to be at least 45 nm, but the peak diameter shifted 0 nm and 31 nm in Experiments 3 and 4, respectively. The size distribution behavior in Experiment 6, in which both precursors are present initially, is similar to that observed in Experiments 3 and 4. In Experiment 6, the diameter change of the peak, 33 nm, was also deemed insignificant (48 nm shift required). Because  $\alpha$ -pinene reacts more rapidly with OH than does toluene (the OH reaction rate constants at 298 K are  $5.3 \times 10^{-11} \text{ cm}^3\text{molec}^{-1}\text{s}^{-1}$  (Atkinson et al., 2006) and  $5.6 \times 10^{-12} \text{ cm}^3\text{molec}^{-1}\text{s}^{-1}$  (Atkinson and Arey, 2003), respectively), SOA formed initially in Experiment 6 likely was composed of  $\alpha$ -pinene photooxidation products; toluene photooxidation products condensed later in the experiment, which resulted in SOA that was more similar to that in Experiments 3 and 4 than to that in Experiment 5.

The evaporation behavior in Experiments 3-6 suggests the extent of particle mixing. In Experiments 3-6, the evaporative behavior of the SOA most closely represents that of the SOA from the second parent hydrocarbon. This behavior suggests that the particle structure more closely resembles that of a core of SOA from the initial precursor coated by a layer of SOA from the second precursor rather than a single, homogeneous particle phase (aside from the solid ammonium sulfate seed). The evaporation behavior of particles in the present experiments is consistent with observations by Emanuelsson et al. (2012), who measured the volatility of mixed anthropogenic (toluene or *p*-xylene) and biogenic ( $\alpha$ -pinene and limonene) SOA using a thermodenuder. The anthropogenic SOA was less volatile than the biogenic SOA. When anthropogenic SOA was formed on biogenic SOA particles, the volatility of the particles decreased, whereas when biogenic SOA was formed on anthropogenic SOA particles, the volatility of the particles increased. The proposed core-and-shell SOA configuration is inconsistent with results obtained by Hildebrandt et al. (2011), who found that SOA yields of  $\alpha$ -pinene and toluene SOA indicated pseudo-ideal particle mixing. Uncertainties

in the SOA mass calculations prevented the authors from making definitive conclusions about SOA mixing thermodynamic ideality. It is possible that the SOA in the present experiments does not exist as a strict core and shell but that long diffusion times cause SOA at the gas-particle interface to be poorly mixed with that in the particle interior.

For Experiments 3 and 4, in which SOA from  $\alpha$ -pinene was coated with that of toluene and for which no evaporation was observed, it is possible to estimate the thickness of SOA from toluene condensed onto that from  $\alpha$ -pinene and to obtain an upper bound on the diffusion coefficient for SOA components from  $\alpha$ -pinene photooxidation in a matrix of those from toluene photooxidation, assuming that diffusional limitations prevented evaporation of SOA formed from  $\alpha$ -pinene. The characteristic diffusion time in spherical coordinates,  $\tau$  (s), is (Seinfeld and Pandis, 2006)

$$\tau = \frac{R_p^2}{\pi^2 D} \quad (4.2)$$

where  $R_p$  is distance in the radial direction (cm) and  $D$  is the diffusion coefficient ( $\text{cm}^2\text{s}^{-1}$ ). Toluene SOA coating thicknesses in Experiments 3 and 4 were  $2.2 \times 10^{-6}$  and  $2.9 \times 10^{-6}$  cm, respectively, and significant evaporation was not observed in a 14-h period, providing a upper estimate of  $D = 1 \times 10^{-17} \text{ cm}^2\text{s}^{-1}$ , that of a semi-solid (Shiraiwa et al., 2011).

The initial concentrations of  $\alpha$ -pinene and toluene differed among Experiments 1-6 by  $\sim 25$  ppbv (Table 4.1). In Experiment 5, the initial concentration of  $\alpha$ -pinene, 81 ppbv, was the highest of all experiments in the present work. Partial SOA evaporation was observed in this case; however, partial evaporation was also observed in Experiment 1, in which SOA was formed from 67 ppbv  $\alpha$ -pinene. This result indicates that within the range of  $\alpha$ -pinene concentrations in the present work, no bias towards evaporation should be expected of SOA formed from higher initial  $\alpha$ -pinene concentrations.

Because of the sequential protocol in Experiments 3-6, the second precursor and its photooxidation products were present in the chamber for less time than the first precursor and thus experienced lower OH exposure. SOA that partially evaporated (Experiment 5) contained products formed from

8 h of  $\alpha$ -pinene photooxidation, whereas SOA that did not evaporate significantly (Experiments 3, 4, and 6) contained products formed from 23 h of  $\alpha$ -pinene photooxidation. To investigate if increased oxidative aging affected particle evaporation, dilution and heating of solely  $\alpha$ -pinene SOA (Experiment 1) was begun after 19.5 h of irradiation. The SOA partially evaporated (Figure 4.1) after experiencing OH exposures slightly less, i.e. shorter photooxidation time, than in experiments that did not show significant SOA evaporation (Experiments 3, 4, and 6). Similar results were observed by Lambe et al. (2012), who found that  $\alpha$ -pinene photooxidation SOA evaporated partially in a thermodenuder regardless of the OH exposure used to produce it. It is unlikely that increased OH exposure under these laboratory settings would produce  $\alpha$ -pinene SOA that is essentially non-volatile.

Experiments 3 and 4 were conducted in the same manner, but different amounts of  $\alpha$ -pinene and toluene were used to generate SOA in each experiment (Table 4.1). Although the size distribution peak diameter shifts were not significant upon heating in either experiment (0 and 31 nm for Experiments 3 and 4, respectively), a larger shift was observed in Experiment 4 than in Experiment 3. The initial  $\alpha$ -pinene concentration in Experiment 4 was higher than that in Experiment 3, and the concentration of toluene added in Experiment 4 was lower than that in Experiment 3. At the end of the  $\alpha$ -pinene SOA growth period, the size distribution peak diameters were similar for both experiments, but after toluene addition, the peak diameter of the size distribution in Experiment 3 increased by 43-73 nm, whereas the peak diameter increased by 14-43 nm in Experiment 4. If SOA from the second precursor coats the existing SOA from the first precursor, then the observed increase in size distribution peak diameter suggests that particles in Experiment 3 were more thickly coated with toluene SOA than those in Experiment 4. It is possible that a thicker toluene SOA coating would hinder evaporation of an  $\alpha$ -pinene SOA core more than a thinner coating because species must diffuse farther through a thicker coating than through a thinner coating to reach the particle surface; however, this effect was not clearly detected in the present study with a 14-h evaporation period.

#### 4.4.2 Aerosol Chemical Composition

One may expect to find a correlation between evaporation behavior and SOA chemical composition. If compounds with a range of volatilities exist within a particle and if mass transfer limitations do not exist, then species of higher volatility should evaporate before species of lower volatility. However, mass transfer limitations within a particle will impede evaporation of high volatility compounds. The extent to which such trends exist was evaluated using average carbon oxidation state,  $\overline{OS}_C$  calculated from oxygen-to-carbon and hydrogen-to-carbon ratios (O:C, H:C) measured by the AMS (Kroll et al., 2011). It is important to note that the AMS measures bulk particle chemical composition even if the SOA exists as a core-and-shell configuration. For example, as  $\alpha$ -pinene SOA condenses onto toluene SOA, the bulk chemical composition of the particles may change; however, the condensing  $\alpha$ -pinene SOA may not greatly affect the chemical composition of the pre-existing toluene SOA core. With the exception of small molecules and oligomers, volatility of a compound decreases with increasing O:C (Jimenez et al., 2009), and thus  $\overline{OS}_C$ . Upon evaporation of higher volatility components,  $\overline{OS}_C$  should increase in the remaining SOA.

The bulk chemical composition of SOA formed during all experiments is shown in Figure 4.4. During the SOA formation period (Figure 4.4a),  $\overline{OS}_C$  increases, a trend generally observed during SOA growth (Ng et al., 2010; Chhabra et al., 2011; Lambe et al., 2011), with the exception of Experiment 5. In Experiment 5, the expected trend is observed during the initial formation of SOA from toluene, but once  $\alpha$ -pinene is injected and  $\alpha$ -pinene SOA condenses onto the toluene SOA,  $\overline{OS}_C$  decreases abruptly. As  $\alpha$ -pinene SOA continues to condense, the expected trend is repeated. SOA from  $\alpha$ -pinene has lower  $\overline{OS}_C$  than that from toluene, as observed in Experiments 1 and 2 and by others, reported separately as O:C and H:C (Chhabra et al., 2011; Lambe et al., 2011). The aromatic ring of toluene provides more sites for OH attack than does the structure of  $\alpha$ -pinene, which contains only a single alkene functionality, and has a greater potential for producing highly oxygenated species. The vapor pressure of  $\alpha$ -pinene is a factor of 10 lower than that of toluene (Hawkins and Armstrong, 1954; Pitzer and Scott, 1943), and less oxygenation of  $\alpha$ -pinene than of toluene is needed to produce condensable products. Because toluene contains fewer carbons than

$\alpha$ -pinene, the addition of each oxygen atom to the molecule preferentially increases the O:C, and thus  $\overline{OS}_C$ , for toluene products more than for  $\alpha$ -pinene products. SOA condenses within 30 min of  $\alpha$ -pinene photooxidation, and because its chemical composition differs from that of toluene SOA, a sudden change in SOA chemical composition when  $\alpha$ -pinene SOA condenses onto toluene SOA is not unexpected. A rough estimation of the volume fractions of SOA from  $\alpha$ -pinene and toluene in Experiments 5 can be obtained from the change in size distribution peak diameter upon SOA condensation. Peak diameters for the seed, seed and SOA from toluene, and seed and SOA from toluene and  $\alpha$ -pinene are 69, 162, and 482 nm, respectively. The ratio of SOA from  $\alpha$ -pinene to that from toluene is approximately 25:1, and bulk SOA chemical composition is expected to reflect primarily  $\alpha$ -pinene, even upon evaporation.

Bulk SOA chemical composition did not change drastically upon dilution and heating (Figure 4.4 b).  $\overline{OS}_C$  increased upon heating linearly with temperature, as shown in Figure 4.4b with the rate-of-change of  $\overline{OS}_C$ ,  $r_{\overline{OS}_C}$ , listed for each experiment on the right side of the panel. The largest  $r_{\overline{OS}_C}$  was observed for SOA from toluene coated with that from  $\alpha$ -pinene (Experiment 5), and the smallest  $r_{\overline{OS}_C}$  was observed for SOA from toluene only (Experiment 2). All changes in  $\overline{OS}_C$  during the heating period were small relative to the change in  $\overline{OS}_C$  upon SOA formation and the differences in  $\overline{OS}_C$  amongst SOA generated in the different experiments. The lack of substantial chemical change during evaporation is consistent with results obtained by Cappa and Wilson (2011) and Huffman et al. (2009) when measuring the bulk chemical composition of thermodenuded  $\alpha$ -pinene ozonolysis SOA. However, in other studies of  $\alpha$ -pinene ozonolysis SOA evaporation, using either a thermodenuder or diluting particles suspended in a chamber, chemical changes were observed in the SOA upon evaporation (Docherty et al., 2005; Grieshop et al., 2007; Kostenidou et al., 2009). The differences in the studies that lead to the contrasting results remain to be identified.

Correlations between bulk chemical composition and evaporation behavior were assessed using data collected immediately before the dilution and heating period, those with the largest elapsed time in Figure 4.4a. The data show that the SOA formed spans a range of  $\overline{OS}_C$  values. A clear correlation of chemical composition with volatility is observed for the solely toluene SOA and the

solely  $\alpha$ -pinene SOA experiments. Toluene SOA, which has the highest  $\overline{OS}_C$  of the systems studied, did not evaporate significantly.  $\alpha$ -Pinene SOA exhibited lower  $\overline{OS}_C$  than the toluene SOA and partially evaporated. From these two observations, it is possible to conclude that a transition from volatile to essentially non-volatile SOA occurs in the range of average  $\overline{OS}_C$  observed in the present work for  $\alpha$ -pinene and toluene SOA. However, for the combined  $\alpha$ -pinene and toluene SOA, no distinct correlation between bulk chemical composition and evaporation behavior is observed. The bulk chemical composition of the two-precursor SOA more closely resembled that of  $\alpha$ -pinene SOA than toluene SOA. SOA with lower  $\overline{OS}_C$  than solely  $\alpha$ -pinene SOA (formed from toluene then  $\alpha$ -pinene) partially evaporated whereas SOA with higher  $\overline{OS}_C$  than solely  $\alpha$ -pinene SOA (formed from  $\alpha$ -pinene then toluene or  $\alpha$ -pinene and toluene) did not significantly evaporate. However, the variance in the data for these SOA types, excluding solely toluene SOA, lies within the uncertainty of the measurements, represented by the error bars in Figure 4.4a. Even if SOA exists in a core-and-shell configuration, the bulk elemental composition reflects a combination of SOA from the two precursors and will not be indicative necessarily of the elemental composition of the phase at the gas-particle interface. While bulk chemical composition data correlate with volatility for SOA from a single parent hydrocarbon, the same correlation does not apply to SOA formed from multiple precursors. The present experiments suggest that both particle composition and history can play a role in its physiochemical behavior.

## 4.5 Acknowledgements

This work was supported by the Office of Science (Biological and Environmental Research), US Department of Energy Grant DE-SC 0006626. We thank Jill Craven, Rebecca Schwantes, Lindsay Yee, and Xuan Zhang for experimental assistance, Andrew Metcalf and Manabu Shiraiwa for helpful discussion, and Yu Jun Leong and Robert Griffin for lending us their AMS power supply.

## Bibliography

- Abramson, E., Imre, D., Beranek, J., Wilson, J., and Zelenyuk, A.: Experimental determination of chemical diffusion within secondary organic aerosol particles, *Phys. Chem. Chem. Phys.*, 15, 2983–2991, doi:10.1039/C2CP44013J, 2013. 78, 79
- Aiken, A. C., DeCarlo, P. F., Kroll, J. H., Worsnop, D. R., Huffman, J. A., Docherty, K. S., Ulbrich, I. M., Mohr, C., Kimmel, J. R., Sueper, D., Sun, Y., Zhang, Q., Trimborn, A., Northway, M., Ziemann, P. J., Canagaratna, M. R., Onasch, T. B., Alfarra, M. R., Prévôt, A. S. H., Dommen, J., Duplissy, J., Metzger, A., Baltensperger, U., and Jimenez, J. L.: O/C and OM/OC ratios of primary, secondary, and ambient organic aerosols with high-resolution time-of-flight aerosol mass spectrometry, *Environ. Sci. Technol.*, 42, 4478–4485, doi:10.1021/es703009q, 2008. xv, 83, 102
- Allan, J. D., Delia, A. E., Coe, H., Bower, K. N., Alfarra, M. R., Jimenez, J. L., Middlebrook, A. M., Drewnick, F., Onasch, T. B., Canagaratna, M. R., Jayne, J. T., and Worsnop, D. R.: A generalised method for the extraction of chemically resolved mass spectra from Aerodyne aerosol mass spectrometer data, *J. Aerosol Sci.*, 35, 909–922, doi:10.1016/j.jaerosci.2004.02.007, 2004. 82
- An, W. J., Pathak, R. K., Lee, B.-H., and Pandis, S. N.: Aerosol volatility measurement using an improved thermodenuder: Application to secondary organic aerosol, *J. Aerosol Sci.*, 38, 305–314, doi:10.1016/j.jaerosci.2006.12.002, 2007. 80
- Atkinson, R. and Arey, J.: Atmospheric degradation of volatile organic compounds, *Chem. Rev.*, 103, 4605–4638, doi:10.1021/cr0206420, 2003. 86
- Atkinson, R., Baulch, D. L., Cox, R. A., Crowley, J. N., Hampson, R. F., Hynes, R. G., Jenkin, M. E., Rossi, M. J., Troe, J., and IUPAC Subcommittee: Evaluated kinetic and photochemical data for atmospheric chemistry: Volume II - gas phase reactions of organic species, *Atmos. Chem. Phys.*, 6, 3625–4055, doi:10.5194/acp-6-3625-2006, 2006. 86
- Bowman, F. M., Odum, J. R., Seinfeld, J. H., and Pandis, S. N.: Mathematical model for gas-particle partitioning of secondary organic aerosols, *Atmos. Environ.*, 31, 3921 – 3931, 1997. 79

- Canagaratna, M. R., Jayne, J. T., Jimenez, J. L., Allan, J. D., Alfarra, M. R., Zhang, Q., Onasch, T. B., Drewnick, F., Coe, H., Middlebrook, A., Delia, A., Williams, L. R., Trimborn, A. M., Northway, M. J., DeCarlo, P. F., Kolb, C. E., Davidovits, P., and Worsnop, D. R.: Chemical and microphysical characterization of ambient aerosols with the aerodyne aerosol mass spectrometer, *Mass Spectrom. Rev.*, 26, 185–222, doi:10.1002/mas.20115, 2007. 82
- Cappa, C. D. and Wilson, K. R.: Evolution of organic aerosol mass spectra upon heating: Implications for OA phase and partitioning behavior, *Atmos. Chem. Phys.*, 11, 1895–1911, doi:10.5194/acp-11-1895-2011, 2011. 78, 79, 90
- Chhabra, P. S., Ng, N. L., Canagaratna, M. R., Corrigan, A. L., Russell, L. M., Worsnop, D. R., Flagan, R. C., and Seinfeld, J. H.: Elemental composition and oxidation of chamber organic aerosol, *Atmos. Chem. Phys.*, 11, 8827–8845, doi:10.5194/acp-11-8827-2011, 2011. 89
- DeCarlo, P. F., Kimmel, J. R., Trimborn, A., Northway, M. J., Jayne, J. T., Aiken, A. C., Gonin, M., Fuhrer, K., Horvath, T., Docherty, K. S., Worsnop, D. R., and Jimenez, J. L.: Field-deployable, high-resolution, time-of-flight aerosol mass spectrometer, *Anal. Chem.*, 78, 8281–8289, doi:10.1021/ac061249n, 2006. 82, 83
- Docherty, K. S., Wu, W., Lim, Y. B., and Ziemann, P. J.: Contributions of organic peroxides to secondary aerosol formed from reactions of monoterpenes with  $O_3$ , *Environ. Sci. Technol.*, 39, 4049–4059, doi:10.1021/es050228s, 2005. 90
- Emanuelsson, E. U., Hallquist, M., Kristensen, K., Glasius, M., Bohn, B., Fuchs, H., Kammer, B., Kiendler-Scharr, A., Nehr, S., Rubach, F., Tillmann, R., Wahner, A., Wu, H.-C., and Mentel, T. F.: Formation of anthropogenic secondary organic aerosol (SOA) and its influence on biogenic SOA properties, *Atmos. Chem. Phys. Discuss.*, 12, 20311–20350, doi:10.5194/acpd-12-20311-2012, 2012. 85, 86
- Grieshop, A. P., Donahue, N. M., and Robinson, A. L.: Is the gas-particle partitioning in alpha-pinene secondary organic aerosol reversible?, *Geophys. Res. Lett.*, 34, L14810, doi:10.1029/2007GL029987, 2007. 80, 90



- Hawkins, J. and Armstrong, G.: Physical and thermodynamic properties of terpenes. III. The vapor pressures of  $\alpha$ -pinene and  $\beta$ -pinene, *J. Am. Chem. Soc.*, 76, 3756–3758, doi:10.1021/ja01643a051, 1954. 89
- Hildebrandt, L., Donahue, N. M., and Pandis, S. N.: High formation of secondary organic aerosol from the photo-oxidation of toluene, *Atmos. Chem. Phys.*, 9, 2973–2986, 2009. 84, 85
- Hildebrandt, L., Henry, K. M., Kroll, J. H., Worsnop, D. R., Pandis, S. N., and Donahue, N. M.: Evaluating the mixing of organic aerosol components using high-resolution aerosol mass spectrometry, *Environ. Sci. Technol.*, 45, 6329–6335, doi:10.1021/es200825g, 2011. 79, 86
- Huffman, J. A., Docherty, K. S., Mohr, C., Cubison, M. J., Ulbrich, I. M., Ziemann, P. J., Onasch, T. B., and Jimenez, J. L.: Chemically-resolved volatility measurements of organic aerosol from different sources, *Environ. Sci. Technol.*, 43, 5351–5357, doi:10.1021/es803539d, 2009. 90
- Jimenez, J. L., Canagaratna, M. R., Donahue, N. M., Prévôt, A. S. H., Zhang, Q., Kroll, J. H., DeCarlo, P. F., Allan, J. D., Coe, H., Ng, N. L., Aiken, A. C., Docherty, K. S., Ulbrich, I. M., Grieshop, A. P., Robinson, A. L., Duplissy, J., Smith, J. D., Wilson, K. R., Lanz, V. A., Hueglin, C., Sun, Y. L., Tian, J., Laaksonen, A., Raatikainen, T., Rautiainen, J., Vaattovaara, P., Ehn, M., Kulmala, M., Tomlinson, J. M., Collins, D. R., Cubison, M. J., Dunlea, E. J., Huffman, J. A., Onasch, T. B., Alfarra, M. R., Williams, P. I., Bower, K., Kondo, Y., Schneider, J., Drewnick, F., Borrmann, S., Weimer, S., Demerjian, K., Salcedo, D., Cottrell, L., Griffin, R., Takami, A., Miyoshi, T., Hatakeyama, S., Shimono, A., Sun, J. Y., Zhang, Y. M., Dzepina, K., Kimmel, J. R., Sueper, D., Jayne, J. T., Herndon, S. C., Trimborn, A. M., Williams, L. R., Wood, E. C., Middlebrook, A. M., Kolb, C. E., Baltensperger, U., and Worsnop, D. R.: Evolution of organic aerosols in the atmosphere, *Science*, 326, 1525–1529, doi:10.1126/science.1180353, 2009. 89
- Koop, T., Bookhold, J., Shiraiwa, M., and Pöschl, U.: Glass transition and phase state of organic compounds: Dependency on molecular properties and implications for secondary organic aerosols in the atmosphere, *Phys. Chem. Chem. Phys.*, 13, 19 238–19 255, doi:10.1039/c1cp22617g, 2011.

- Kostenidou, E., Lee, B.-H., Engelhart, G. J., Pierce, J. R., and Pandis, S. N.: Mass spectra deconvolution of low, medium, and high volatility biogenic secondary organic aerosol, *Environ. Sci. Technol.*, 43, 4884–4889, doi:10.1021/es803676g, 2009. 90
- Kroll, J. H., Donahue, N. M., Jimenez, J. L., Kessler, S. H., Canagaratna, M. R., Wilson, K. R., Altieri, K. E., Mazzoleni, L. R., Wozniak, A. S., Bluhm, H., Mysak, E. R., Smith, J. D., Kolb, C. E., and Worsnop, D. R.: Carbon oxidation state as a metric for describing the chemistry of atmospheric organic aerosol, *Nat. Chem.*, 3, 133–139, doi:10.1038/NCHEM.948, 2011. 89
- Kuwata, M. and Martin, S. T.: Phase of atmospheric secondary organic material affects its reactivity, *P. Natl. Acad. Sci. U.S.A.*, 109, 17 354–17 359, doi:10.1073/pnas.1209071109, 2012. 78, 79
- Lambe, A. T., Onasch, T. B., Massoli, P., Croasdale, D. R., Wright, J. P., Ahern, A. T., Williams, L. R., Worsnop, D. R., Brune, W. H., and Davidovits, P.: Laboratory studies of the chemical composition and cloud condensation nuclei (CCN) activity of secondary organic aerosol (SOA) and oxidized primary organic aerosol (OPOA), *Atmos. Chem. Phys.*, 11, 8913–8928, doi:10.5194/acp-11-8913-2011, 2011. 85, 89
- Lambe, A. T., Onasch, T. B., Croasdale, D. R., Wright, J. P., Martin, A. T., Franklin, J. P., Massoli, P., Kroll, J. H., Canagaratna, M. R., Brune, W. H., Worsnop, D. R., and Davidovits, P.: Transitions from functionalization to fragmentation reactions of laboratory secondary organic aerosol (SOA) generated from the OH oxidation of alkane precursors, *Environ. Sci. Technol.*, 46, 5430–5437, doi:10.1021/es300274t, 2012. 88
- Loza, C. L., Chhabra, P. S., Yee, L. D., Craven, J. S., Flagan, R. C., and Seinfeld, J. H.: Chemical aging of *m*-xylene secondary organic aerosol: Laboratory chamber study, *Atmos. Chem. Phys.*, 12, 151–167, doi:10.5194/acp-12-151-2012, 2012. 84
- Marqusee, J. A. and Ross, J.: Theory of Ostwald ripening: Competitive growth and its dependence on volume fraction, *J. Chem. Phys.*, 80, 536–543, doi:10.1063/1.446427, 1984. 83
- Ng, N. L., Canagaratna, M. R., Zhang, Q., Jimenez, J. L., Tian, J., Ulbrich, I. M., Kroll, J. H.,

- Docherty, K. S., Chhabra, P. S., Bahreini, R., Murphy, S. M., Seinfeld, J. H., Hildebrandt, L., Donahue, N. M., DeCarlo, P. F., Lanz, V. A., Prévôt, A. S. H., Dinar, E., Rudich, Y., and Worsnop, D. R.: Organic aerosol components observed in Northern Hemispheric datasets from Aerosol Mass Spectrometry, *Atmos. Chem. Phys.*, 10, 4625–4641, doi:10.5194/acp-10-4625-2010, 2010. 89
- Odum, J. R., Hoffmann, T., Bowman, F., Collins, D., Flagan, R. C., and Seinfeld, J. H.: Gas/particle partitioning and secondary organic aerosol yields, *Environ. Sci. Technol.*, 30, 2580–2585, doi:10.1021/es950943+, 1996. 79
- Odum, J. R., Jungkamp, T. P. W., Griffin, R. J., Flagan, R. C., and Seinfeld, J. H.: The atmospheric aerosol-forming potential of whole gasoline vapor, *Science*, 276, 96–99, doi:10.1126/science.276.5309.96, 1997. 79
- Perraud, V., Bruns, E. A., Ezell, M. J., Johnson, S. N., Yu, Y., Alexander, M. L., Zelenyuk, A., Imre, D., Chang, W. L., Dabdub, D., Pankow, J. F., and Finlayson-Pitts, B. J.: Nonequilibrium atmospheric secondary organic aerosol formation and growth, *P. Natl. Acad. Sci. U.S.A.*, 109, 2836–2841, doi:10.1073/pnas.1119909109, 2012. 78, 79
- Pitzer, K. S. and Scott, D. W.: The thermodynamics and molecular structure of benzene and its methyl derivatives, *J. Am. Chem. Soc.*, 65, 803–829, doi:10.1021/ja01245a019, 1943. 89
- Qi, L., Nakao, S., Tang, P., and Cocker, III, D. R.: Temperature effect on physical and chemical properties of secondary organic aerosol from *m*-xylene photooxidation, *Atmos. Chem. Phys.*, 10, 3847–3854, 2010. 80, 85
- Saukko, E., Lambe, A. T., Massoli, P., Koop, T., Wright, J. P., Croasdale, D. R., Pedernera, D. A., Onasch, T. B., Laaksonen, A., Davidovits, P., Worsnop, D. R., and Virtanen, A.: Humidity-dependent phase state of SOA particles from biogenic and anthropogenic precursors, *Atmos. Chem. Phys.*, 12, 7517–7529, doi:10.5194/acp-12-7517-2012, 2012. 78

- Seinfeld, J. H. and Pandis, S. N.: Atmospheric Chemistry and Physics, John Wiley and Sons, Inc., Hoboken, N.J., 2 edn., 2006. 87
- Shiraiwa, M. and Seinfeld, J. H.: Equilibration timescale of atmospheric secondary organic aerosol partitioning, *Geophys. Res. Lett.*, 39, L24 801, doi:10.1029/2012GL054008, 2012. 80
- Shiraiwa, M., Ammann, M., Koop, T., and Pöschl, U.: Gas uptake and chemical aging of semisolid organic aerosol particles, *P. Natl. Acad. Sci. U.S.A.*, 108, 11 003–11 008, doi:10.1073/pnas.1103045108, 2011. 78, 79, 87
- Stanier, C. O., Pathak, R. K., and Pandis, S. N.: Measurements of the volatility of aerosols from  $\alpha$ -pinene ozonolysis, *Environ. Sci. Technol.*, 41, 2756–2763, doi:10.1021/es0519280, 2007. 80
- Stolzenburg, M. R.: An ultrafine aerosol size distribution measuring system, Ph.D. thesis, University of Minnesota, Minneapolis, MN, 1988. 82
- Strader, R., Lurmann, F., and Pandis, S. N.: Evaluation of secondary organic aerosol formation in winter, *Atmos. Environ.*, 33, 4849–4863, doi:10.1016/S1352-2310(99)00310-6, 1999. 79
- Tritscher, T., Dommen, J., DeCarlo, P. F., Gysel, M., Barmet, P. B., Praplan, A. P., Weingartner, E., Prévôt, A. S. H., Riipinen, I., Donahue, N. M., and Baltensperger, U.: Volatility and hygroscopicity of aging secondary organic aerosol in a smog chamber, *Atmos. Chem. Phys.*, 11, 11 477–11 496, doi:10.5194/acp-11-11477-2011, 2011. 80
- Vaden, T. D., Song, C., Zaveri, R. A., Imre, D., and Zelenyuk, A.: Morphology of mixed primary and secondary organic particles and the adsorption of spectator organic gases during aerosol formation, *P. Natl. Acad. Sci. U.S.A.*, 107, 6658–6663, doi:10.1073/pnas.0911206107, 2010. 78, 79
- Vaden, T. D., Imre, D., Beránek, J., Shrivastava, M., and Zelenyuk, A.: Evaporation kinetics and phase of laboratory and ambient secondary organic aerosol, *P. Natl. Acad. Sci. U.S.A.*, 108, 2190–2195, doi:10.1073/pnas.1013391108, 2011. 78, 79
- Virtanen, A., Joutsensaari, J., Koop, T., Kannosto, J., Yli-Pirilä, P., Leskinen, J., Mäkelä, J. M., Holopainen, J. K., Pöschl, U., Kulmala, M., Worsnop, D. R., and Laaksonen, A.: An amorphous

solid state of biogenic secondary organic aerosol particles, *Nature*, 467, 824–827, doi:10.1038/nature09455, 2010. 78

Warren, B., Austin, R. L., and Cocker, III, D. R.: Temperature dependence of secondary organic aerosol, *Atmos. Environ.*, 43, 3548–3555, doi:10.1016/j.atmosenv.2009.04.011, 2009. 80, 85

Zhang, S. H. and Flagan, R. C.: Resolution of the radial differential mobility analyzer for ultrafine particles, *J. Aerosol Sci.*, 27, 1179–1200, doi:10.1016/0021-8502(96)00036-5, 1996. 82

**Table 4.1:** Experimental details.

Expt. #	Seed vol. ( $\mu\text{m}^3\text{cm}^{-3}$ )	First precursor <sup>a</sup>	Conc. (ppbv)	Second precursor <sup>a</sup>	Conc. (ppbv)	Dilution ratio <sup>b</sup>	Max Temp. (°C)
1	$23.6 \pm 7.1$	$\alpha$ -pin.	$67.1 \pm 3.8$	-	-	3.0	$41 \pm 2$
2 <sup>c</sup>	$22.7 \pm 6.8$	tol.	$98.8 \pm 6.2$	-	-	1.8	$41 \pm 2$
3	$95.0 \pm 28.5$	$\alpha$ -pin.	$61.0 \pm 3.5$	tol.	$90.4 \pm 5.7$	3.0	$40 \pm 2$
4	$42.8 \pm 12.8$	$\alpha$ -pin.	$74.0 \pm 4.2$	tol.	$75.3 \pm 4.8$	3.7	$40 \pm 2$
5	$34.6 \pm 10.4$	tol.	$76.0 \pm 4.8$	$\alpha$ -pin.	$80.7 \pm 4.6$	3.4	$42 \pm 2$
6	$116 \pm 35$	$\alpha$ -pin. <sup>d</sup>	$58.0 \pm 3.3$	tol. <sup>d</sup>	$100. \pm 6$	3.0	$41 \pm 2$
7	$65.3 \pm 19.6$	tol.	$43.5 \pm 2.8$	$\alpha$ -pin.	$47.0 \pm 2.7$	3.2	$27 \pm 2$

<sup>a</sup> Abbreviations correspond to toluene (tol.) and  $\alpha$ -pinene ( $\alpha$ -pin.).

<sup>b</sup> Ratio of cyclohexane concentration before and after dilution.

<sup>c</sup> During Experiment 2, the chamber was inadvertently irradiated beginning approximately 1 h after the chamber reached 41 °C. The remaining 17 ppbv of toluene reacted with the OH produced, forming a small amount of SOA.

<sup>d</sup> Both  $\alpha$ -pinene and toluene were injected initially.

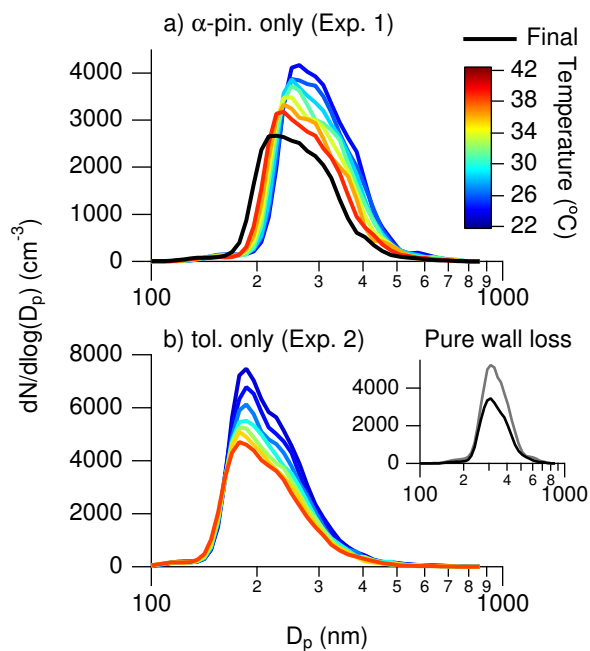


**Figure 4.1:** Evolution of the suspended particle size distribution of single-precursor SOA during heating of the chamber enclosure. The data shown are averaged over 1-h intervals. Abbreviations correspond to toluene (tol.) and  $\alpha$ -pinene ( $\alpha$ -pin.). The final aerosol size distribution for Experiment 2 is not reported due to inadvertent chamber irradiation (see Table 4.1). The inset in panel b shows the change in particle size distribution for pure wall loss observed in Experiment 7 (Table 4.1). The initial size distribution after dilution is in gray, and the final size distribution after 9 h is in black.

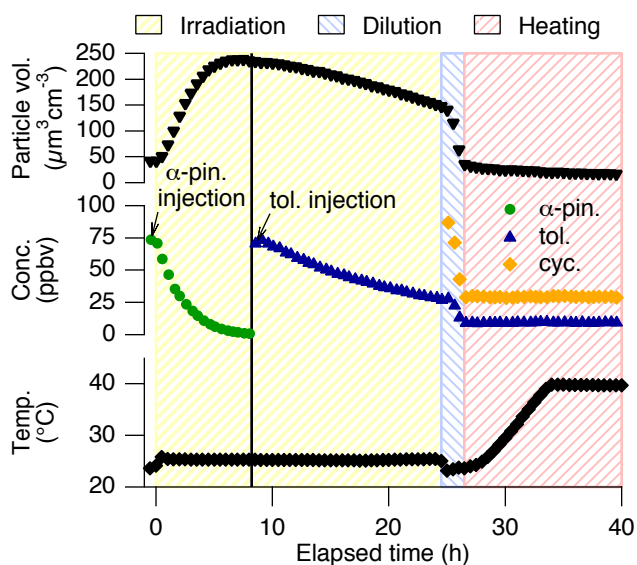


**Figure 4.2:** Experiment profile for SOA formation and evaporation when  $\alpha$ -pinene and toluene were injected sequentially (Experiment 4). The suspended particle volume concentration,  $\alpha$ -pinene ( $\alpha$ -pin.), toluene (tol.), and cyclohexane (cyc.) concentrations (when above the limit of detection), and the chamber temperature are shown. Periods of irradiation, dilution, and heating are highlighted, and the toluene injection is denoted by the vertical, black line.

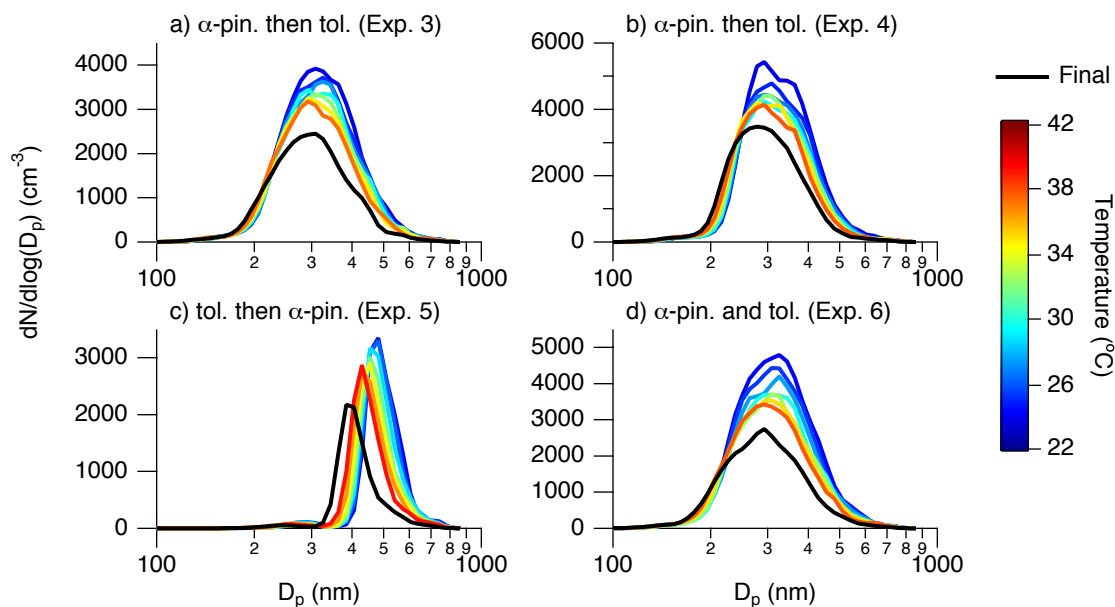


**Figure 4.3:** Evolution of the suspended particle size distribution of SOA from sequentially or simultaneously injected precursors during heating of the chamber enclosure. The data shown are averaged over 1-h intervals. Abbreviations correspond to toluene (tol.) and  $\alpha$ -pinene ( $\alpha$ -pin.).



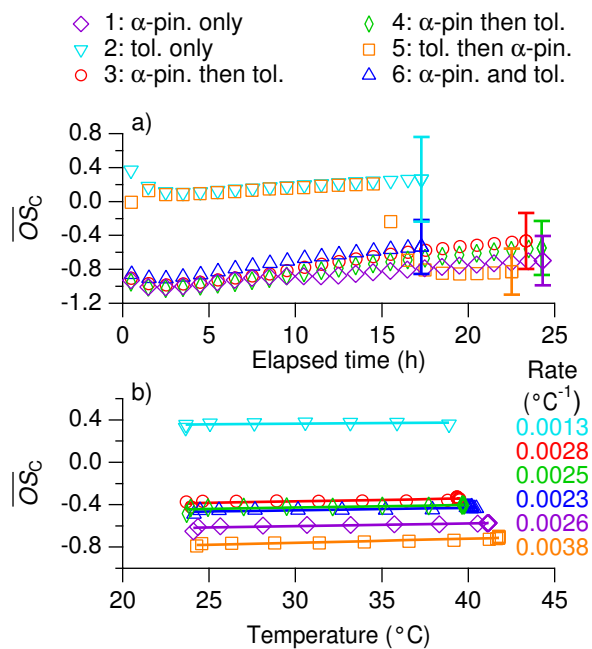


**Figure 4.4:** Evolution of aerosol oxidation state during formation (panel a) and dilution and heating (panel b). The error bars in panel a represent the uncertainty values for  $\overline{OS}_C$ , calculated from those for H:C and O:C, 10 % and 31 %, respectively (Aiken et al., 2008), at the end of the formation period. The rate of change of  $\overline{OS}_C$  as a function of temperature for each experiment is listed in panel b. Abbreviations correspond to toluene (tol.) and  $\alpha$ -pinene ( $\alpha$ -pin.).

## Chapter 5

# Future Work

Laboratory chambers are useful for studying secondary organic aerosol (SOA) formation and evolution from a single or a small number of parent volatile organic compounds (VOCs) under controlled conditions. This thesis presents two such studies and also discusses the ways in which the chamber itself interacts with both gases and particles.

To properly interpret chamber data, it is essential to understand the effect of the walls on suspended particles and condensible vapors. Both 2,3-epoxy-1,4-butanediol (BEPOX) and glyoxal were subject to deposition to chamber walls, but the wall loss rate constant was different for each compound and changed with the age of the chamber and the relative humidity (see Chapter 2). Matsunaga and Ziemann (2010) also have shown that vapor wall losses are a function of molecular structure. Oxidation of a parent VOC produces multiple products having different functionalities. If each of these products deposits to the walls at different rates, it is necessary to measure wall loss rate for each type of compound. Currently, wall loss rate constants have been measured for only a small number of compounds. A broad study of compounds with varied functional groups would be beneficial to establishing correlations between compound structure and wall loss behavior. Vapor wall losses will have the largest effect on the oxidation product distribution in a chamber experiment if the wall losses are irreversible on the timescale of the experiment. Further study of the reversibility of vapor wall losses would aid in quantifying losses throughout an experiment, in which the vapor concentrations change due to condensation to particles and further gas-phase reactions, and in understanding wall sorption mechanisms.

The results of recent studies have challenged the traditional assumption that organic aerosols exist as liquid particles, providing evidence that organic aerosols may be amorphous semi-solid or solid particles. Chapter 4 presented one such example with SOA formed from  $\alpha$ -pinene and toluene. Some degree of particle phase separation was inferred through the evaporative behavior of SOA formed sequentially from the two SOA precursors. The way in which evaporation was characterized, by a shift in the peak size distribution diameter, successfully identified evaporation and showed that toluene SOA condensed onto  $\alpha$ -pinene SOA inhibited  $\alpha$ -pinene SOA evaporation. Due to the effect of particle wall loss on the suspended particle size distribution, it was difficult to quantify

evaporation using the bulk particle measurements available, either particle volume concentration calculated from differential mobility analyzer and condensation particle counter measurements or SOA mass concentration calculated from aerosol mass spectrometer measurements.

Evaporation of SOA produced using the protocols outlined in Chapter 4 could be better quantified with additional instrumentation or by using a different seed particle. If no additional instrumentation is available, using a monodisperse seed particle size distribution would produce a monodisperse SOA size distribution. Mass lost due to evaporation could be calculated from the change in diameter of the monodisperse size distribution, and, assuming that particles do not fully evaporate, wall losses could be quantified from the change in total particle number concentration. If single particle instrumentation, such as the aerosol time-of-flight mass spectrometer (ATOFMS, Gard et al., 1997) or single-particle soot photometer (SP2, Droplet Measurement Technologies, Boulder, CO), are available, SOA can be condensed onto a non-evaporative seed particle, such as ammonium sulfate or black carbon, and evaporation can be detected as a change in organic coating thickness. To speciate molecules present at a particle surface and make inferences on phase separation within particles, particles could be sampled using a mass spectrometer capable of ablating and ionizing molecules at the particle surface, such as the single particle mass spectrometer (SPLATII, Zelenyuk et al., 2009). Data provided by these single-particle instruments would allow for better characterization of evaporation and particle phase separation.

Most studies probing organic aerosol phase were performed at low relative humidity (RH) using a select number of SOA-forming systems, most notably  $\alpha$ -pinene ozonolysis. A large variety of SOA precursors, both from anthropogenic and biogenic sources, exist in the atmosphere, as do a range of RH conditions. The experimental procedures described in Chapter 4 could be used to investigate the mixing behavior of combinations of SOA precursors under dry conditions. Extending the procedures to humid conditions presents some challenges, e.g. maintaining a specific relative humidity as the chamber is heated, but the results of experiments performed under multiple RH conditions would provide much insight into factors affecting the phase behavior of ambient SOA.

## Bibliography

- Gard, E., Mayer, J. E., Morrical, B. D., Dienes, T., Fergenson, D. P., and Prather, K. A.: Real-time analysis of individual atmospheric aerosol particles: Design and performance of a portable ATOFMS, *Anal. Chem.*, 69, 4083–4091, doi:10.1021/ac970540n, 1997. 105
- Matsunaga, A. and Ziemann, P. J.: Gas-wall partitioning of organic compounds in a Teflon film chamber and potential effects on reaction product and aerosol yield measurements, *Aerosol Sci. Tech.*, 44, 881–892, doi:10.1080/02786826.2010.501044, 2010. 104
- Zelenyuk, A., Yang, J., Choi, E., and Imre, D.: SPLAT II: An aircraft compatible, ultra-sensitive, high precision instrument for in-situ characterization of the size and composition of fine and ultrafine particles, *Aerosol Sci. Tech.*, 43, 411–424, doi:10.1080/02786820802709243, 2009. 105

## Appendix A

# Analysis of Photochemical and Dark Glyoxal Uptake: Implications for SOA Formation\*

---

\*Reproduced with permission from “Analysis of photochemical and dark glyoxal uptake: Implications for SOA formation” by M. M. Galloway, C. L. Loza, P. S. Chhabra, A. W. H. Chan, L. D. Yee, J. H. Seinfeld, and F. N. Keutsch, *Geophys. Res. Lett.*, 38, L17811, doi:10.1029/2011GL048514. Copyright 2011 by the American Geophysical Union.

## Analysis of photochemical and dark glyoxal uptake: Implications for SOA formation

M. M. Galloway,<sup>1</sup> C. L. Loza,<sup>2</sup> P. S. Chhabra,<sup>2</sup> A. W. H. Chan,<sup>2,3</sup> L. D. Yee,<sup>4</sup> J. H. Seinfeld,<sup>2,4</sup> and F. N. Keutsch<sup>1</sup>

Received 23 June 2011; revised 15 August 2011; accepted 23 August 2011; published 15 September 2011.

[1] The dependence of glyoxal uptake onto deliquesced ammonium sulfate seed aerosol was studied under photochemical (light + hydroxyl radical (OH)) and dark conditions. In this study, the chemical composition of aerosol formed from glyoxal is identical in the presence or absence of OH. In addition, there was no observed OH dependence on either glyoxal uptake or glyoxal-driven aerosol growth for this study. These findings demonstrate that, for the system used here, glyoxal uptake is not affected by the presence of OH. In combination with previous studies, this shows that the exact nature of the type of seed aerosol, in particular the presence of a coating, has a large influence on fast photochemical uptake of glyoxal. Due to the challenge of relating this seed aerosol dependence to ambient conditions, this work highlights the resulting difficulty in quantitatively including SOA formation from glyoxal in models. **Citation:** Galloway, M. M., C. L. Loza, P. S. Chhabra, A. W. H. Chan, L. D. Yee, J. H. Seinfeld, and F. N. Keutsch (2011), Analysis of photochemical and dark glyoxal uptake: Implications for SOA formation, *Geophys. Res. Lett.*, 38, L17811, doi:10.1029/2011GL048514.

### 1. Introduction

[2] The formation of secondary organic aerosol (SOA) is traditionally explained via uptake of gas-phase species onto aerosol following vapor pressure and partitioning theory [Pankow, 1994a, 1994b; Odum *et al.*, 1996]. Recent work has shown that chemical reactions occurring within the aerosol can increase SOA yields as well as alter both chemical and optical aerosol properties [Carlton *et al.*, 2007; Ervens *et al.*, 2008; Galloway *et al.*, 2009; Nozière *et al.*, 2009; Shapiro *et al.*, 2009; Bones *et al.*, 2010]. Glyoxal has a high effective Henry's Law coefficient, which results in more efficient uptake onto aqueous aerosol droplets than expected for a small carbonyl [Ip *et al.*, 2009]. In the aerosol, glyoxal can react with other species to form acetal oligomers, imidazoles, other high molecular weight compounds, and be oxidized with OH to carboxylic acids [Carlton *et al.*, 2007; De Haan

*et al.*, 2009b; Galloway *et al.*, 2009; Tan *et al.*, 2009]. Due to this potential contribution to SOA, glyoxal has received increasing attention [Kroll *et al.*, 2005; Liggio *et al.*, 2005; Corrigan *et al.*, 2008; Galloway *et al.*, 2009; Volkamer *et al.*, 2009].

[3] Glyoxal uptake onto liquid (deliquesced) aqueous ammonium sulfate (AS) seed aerosol has been studied under dark [Kroll *et al.*, 2005; Liggio *et al.*, 2005; Galloway *et al.*, 2009] and photochemical conditions [Volkamer *et al.*, 2009]. Photochemical conditions will be defined as UV-irradiation with explicit addition of a source of gas-phase OH radicals. Galloway *et al.* [2009] showed that dark uptake is largely reversible except for minor imidazole formation. However, drying of the aerosol results in glyoxal being retained [De Haan *et al.*, 2009a]. Volkamer *et al.* [2009] studied SOA formation from acetylene (C<sub>2</sub>H<sub>2</sub>) via glyoxal in a photochemical system and dark glyoxal uptake onto different types of seed aerosol. Whereas rapid photochemical uptake was observed for pure AS, pure fulvic acid, and mixed AS/fulvic acid seed, no rapid photochemical uptake was observed in mixed AS/fulvic acid seed that also contained sulfuric or amino acids, highlighting the complex dependence of rapid photochemical uptake on seed composition. SOA yields from the fast photochemical uptake are substantially higher than from slow, dark-type uptake [Ervens and Volkamer, 2010], hence a thorough understanding of the seed dependence of fast photochemical glyoxal uptake and the chemical processes responsible for it are central for models of SOA formation.

[4] In the gas-phase, OH oxidizes glyoxal to form CO, CO<sub>2</sub>, and other high volatility species that do not contribute to aerosol growth (Figure 1). Hence, the gas-phase reaction of glyoxal with OH should not form aerosol. The observed rapid photochemical glyoxal uptake strongly indicates condensed-phase reactions with OH [Volkamer *et al.*, 2009]. Carlton *et al.* [2007] observed oxalic acid production in laboratory studies of photochemical oxidation of glyoxal in bulk aqueous, cloud-processing-like systems with a source of condensed-phase OH radicals. In a related study, Tan *et al.* [2009] demonstrated that transition from cloud to aerosol-processing conditions leads to increased concentrations of larger (C<sub>3</sub>–C<sub>4</sub>) carboxylic acids. As the condensed-phase glyoxal-OH reaction produces higher molecular weight compounds, specifically carboxylic acids, any observed increase in aerosol from glyoxal and OH should be a result of carboxylic acid formation within the aerosol. The goals of the work presented here were to investigate these processes within aqueous aerosol and the extent to which photochemical glyoxal uptake affects the chemical composition of the resulting aerosol, in particular

<sup>1</sup>Department of Chemistry, University of Wisconsin-Madison, Madison, Wisconsin, USA.

<sup>2</sup>Division of Chemistry and Chemical Engineering, California Institute of Technology, Pasadena, California, USA.

<sup>3</sup>Now at Department of Environmental Science, Policy and Management, University of California, Berkeley, California, USA.

<sup>4</sup>Division of Engineering and Applied Science, California Institute of Technology, Pasadena, California, USA.

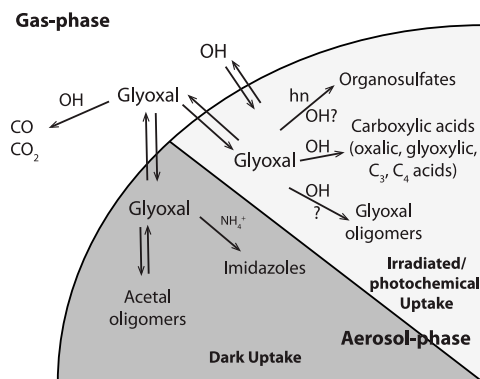


**Figure 1.** Simplified schematic of glyoxal reactions within aqueous AS aerosol. Glyoxal oligomers formed during photochemical uptake refers to any type of higher molecular weight compound. Whereas dark-type reaction products and kinetics have been extensively studied, photochemical reaction products have only been studied in detail for laboratory bulk samples more similar to cloud processing conditions. These studies show that condensed-phase reactions of glyoxal with OH produce carboxylic acids, leading to oxidized organic aerosol.

the presence of carboxylic acids and higher molecular weight compounds.

## 2. Experimental Methods

### 2.1. Preparation and Instrumentation

[5] Experiments were carried out in the Caltech dual 28 m<sup>3</sup> Teflon chambers, described in detail elsewhere [Cocker *et al.*, 2001; Keywood *et al.*, 2004]. The chambers were flushed with clean, humidified air for over 40 hrs before each experiment. AS seed particles (~60–80 nm diameter) were generated by atomization of 0.015 M aqueous AS using a constant rate atomizer. Methyl nitrite (CH<sub>3</sub>ONO) was used as the OH source, and was prepared following the method described by Chan *et al.* [2010], stored at liquid nitrogen temperatures, and allowed to vaporize into a 500 mL glass bulb before injection into the chamber by a dry air stream. The mixing ratio of injected CH<sub>3</sub>ONO was 1 ppm and the initial OH concentration was  $\sim 7 \times 10^7$  molec cm<sup>-3</sup>. Gas-phase glyoxal was prepared from glyoxal trimer dihydrate as described by Galloway *et al.* [2009], vaporized into a 2 L glass bulb, and injected using a dry air stream. Temperature, relative humidity (RH), O<sub>3</sub>, and NO<sub>x</sub> were continuously monitored. Aerosol size distribution, number and volume concentrations were monitored using a differential mobility analyzer (TSI 3081) coupled with a condensation particle counter (TSI 3760). All aerosol volume data are corrected for wall loss, as described by Ng *et al.* [2007]. CH<sub>3</sub>ONO was monitored via a gas chromatograph with flame ionization detector (Agilent 6890N). The Madison Laser-Induced-Phosphorescence instrument monitored gas-phase glyoxal [Huisman *et al.*, 2008].

[6] An Aerodyne HR-ToF-AMS operating in “V-mode” continuously collected real-time particle mass spectra [DeCarlo *et al.*, 2006; Canagaratna *et al.*, 2007]. Data were analyzed using a fragmentation table to separate out sulfate,

ammonium, and organic spectra and to allow for monitoring of specific mass-to-charge ratios (see auxiliary material) [Allan *et al.*, 2004].<sup>1</sup> AMS mass fragments  $m/z$  58 (C<sub>2</sub>H<sub>2</sub>O<sub>2</sub><sup>+</sup>) and  $m/z$  105 (C<sub>3</sub>H<sub>5</sub>O<sub>4</sub><sup>+</sup>) are tracers for glyoxal and its oligomers, respectively, and have been used to monitor non-oxidative glyoxal uptake [Galloway *et al.*, 2009]. Their magnitude is only ~10% of the total organic uptake from glyoxal, but these fragments are useful as tracers of glyoxal uptake into aerosol and oligomer formation. The  $m/z$  44 fragment (CO<sub>2</sub><sup>+</sup>) is typically used as a tracer for oxidized organics in aerosol, especially carboxylic acids [Canagaratna *et al.*, 2007], the glyoxal condensed-phase oxidation products. During these and previous dark (non-oxidative) glyoxal uptake experiments [Galloway *et al.*, 2009], the magnitude of  $m/z$  44 was 8% of  $m/z$  58. In the absence of oxidants, this signal cannot be due to OH-driven oxidation and must be directly from glyoxal. To correct for this contribution, 8% of the  $m/z$  58 signal was subtracted from the  $m/z$  44 signal. The resulting signal corresponds to highly oxidized organics (other than glyoxal but including glyoxal oxidation products, e.g., oxalic acid) and will be referred to as “corrected  $m/z$  44” and used as a tracer of condensed-phase reaction products of glyoxal with OH. All AMS data are normalized to sulfate in order to account for aerosol wall loss and changes in collection efficiency (bounce).

### 2.2. Experimental Procedures

[7] Experimental conditions are summarized in Table 1. AS seed aerosol was injected into the humid chamber and allowed to mix and equilibrate. Then, chamber blacklights were turned on for 2 min to quantify aerosol growth from residual chamber organics without an OH source (1st irradiated period). After this, CH<sub>3</sub>ONO and (usually) NO were added (see Table 1), and blacklights were turned on again to quantify aerosol growth from residual chamber organics with an OH source (2nd irradiated period). After ~15 min, the total and oxidized organic signals on the AMS started to plateau although less than 15% of initial CH<sub>3</sub>ONO had reacted and glyoxal was then injected. After 1 hr, the lights were turned off to allow dark uptake of glyoxal. Blank experiments were run with the same procedures without addition of glyoxal.

## 3. Results

[8] In all experiments, the 1st irradiated period produced no aerosol volume growth and no increase in the total organic or carboxylic acid tracer fraction (corr.  $m/z$  44 to sulfate ratio). At the beginning of the 2nd irradiated period,  $t = 0$  in Figure 2, after CH<sub>3</sub>ONO but before glyoxal injection, a rapid increase in the carboxylic acid tracer (Figure 2c) and aerosol volume were observed at high RH, but not at low RH. This shows that rapid photochemical growth from residual organics can occur under humid conditions, even after extensive cleaning of the chamber. This chamber-background aerosol (OA) was highly oxidized (O/C ratio of 0.95), typical for water-soluble organic carbon (WSOC), high CCN activity, and aqueous processing [Turpin and Lim, 2001; Massoli *et al.*, 2010]. Figures 2a and 2b show that upon injection of gas-phase glyoxal, the aerosol glyoxal-tracer and total OA fractions increased

<sup>1</sup>Auxiliary materials are available in the HTML. doi:10.1029/2011GL048514.



**Table 1.** Experimental Conditions<sup>a</sup>

Experiment	Initial Glyoxal (ppb)	Initial Seed ( $\mu\text{m}^3 \text{cm}^{-3}$ )	$\Delta$ Seed ( $\mu\text{m}^3 \text{cm}^{-3}$ )	NO (ppb)	RH (%)	T (K)	Lights	OH Precursor
1	None	20	5	625	66	293	5%	CH <sub>3</sub> ONO
2	38	37	N/A <sup>b</sup>	768	54	294	50%	CH <sub>3</sub> ONO
3	None	31	-4	278	82	293	50%	CH <sub>3</sub> ONO
4	131	29	33	1	60	293	10%	None
5	38	19	5	93	76	292	10%	CH <sub>3</sub> ONO
6	59	18	5	860	76	291	10%	CH <sub>3</sub> ONO
7	253	19	96	116	67	292	10%	CH <sub>3</sub> ONO

<sup>a</sup> $\Delta$  seed volume is calculated at lights off.<sup>b</sup>Glyoxal was allowed to equilibrate with the walls before seed injection.

rapidly, whereas the carboxylic acid tracer (corr.  $m/z$  44) was not affected and closely resembled the blanks, demonstrating that formation of carboxylic acids from glyoxal, the expected OH-driven aerosol-processing products, is not observed under our photochemical uptake conditions. In summary, Figure 2 highlights that photochemical aerosol-phase reaction/oxidation products are independent of glyoxal, whereas total organic growth during the photochemical experiments clearly depends on glyoxal but this glyoxal-dependent growth in our photochemical experiments closely resembles that of slow, dark-type uptake.

[9] Figure 3 depicts the change in carboxylic acid, glyoxal, and total OA fractions during the photochemical processing period ( $t = 0$  up to vertical lines shown in Figure 2) as a function of gas-phase glyoxal. The glyoxal tracer and the total OA fraction depend on glyoxal, corr.  $m/z$  44 to sulfate ratio is statistically independent of glyoxal concentrations from 0 to 260 ppb. The experimental variability, most readily observed in the difference between the blank experiments

(Figure 3c), does not allow us to fully rule out a small dependence of the carboxylic acid tracer (corr.  $m/z$  44 to sulfate) on glyoxal. However, this contribution must be very small compared to that of the slow, dark-type glyoxal uptake. The fact that no such contribution is observed demonstrates that virtually all uptake from glyoxal can be explained by non-oxidative (dark-type) uptake. Once the blacklights are turned off, OH is quickly depleted. If OH is responsible for an increased glyoxal uptake, the growth in glyoxal and total organic to sulfate ratios should slow down or level off at lights off. This is not the case (Figures 2a and 2b), and glyoxal uptake increases slightly when the blacklights are turned off, likely as a result of the drop in temperature and rise in RH.

#### 4. Discussion

[10] Under all conditions studied here, the observed aerosol growth can be fully explained by slow, dark-type

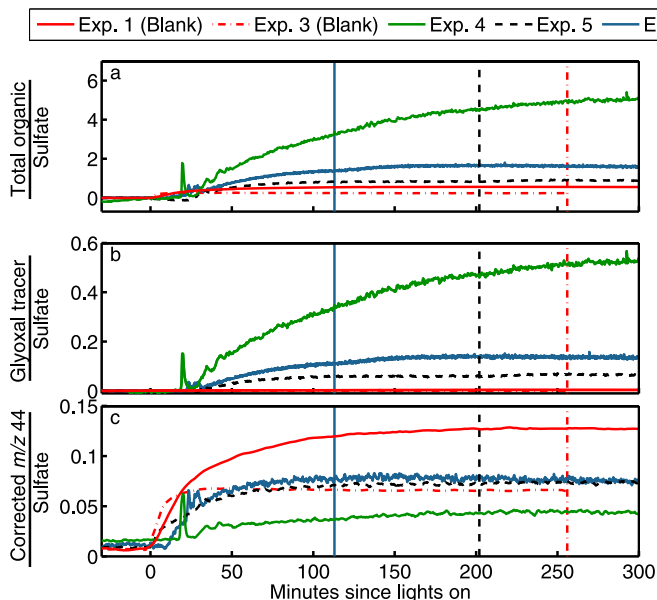


**Figure 2.** (a) Total organic tracer, (b)  $m/z$  58 and (c) carboxylic acid (corr.  $m/z$  44) tracers, all normalized to sulfate. For experiments with gas-phase glyoxal, glyoxal injections occurred at  $\sim 15$  minutes after lights were turned on. Vertical lines indicate when lights were turned off for each experiment to observe glyoxal uptake in the absence of light and OH. After this time, a slight increase in glyoxal and organic tracer can be seen, while there is no increase in oxidized organic tracer. The growth rate of the oxidized organic fraction does not increase upon addition of glyoxal. After initial fluctuations from glyoxal mixing in the chamber, glyoxal uptake rates are very similar for all experiments.

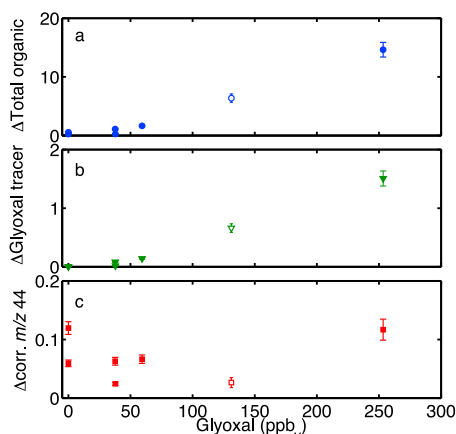


**Figure 3.** Change in (a) total organic fraction, (b) glyoxal-tracer fraction ( $m/z$  58), and (c) the oxidized fraction (corr.  $m/z$  44) of aerosol during time of OH exposure for all experiments. These data are normalized to sulfate. Solid points indicate experiments with OH source present, open points indicate an irradiated experiment with no OH source present. Error bars reflect precision.  $\Delta$ organic and  $\Delta$ glyoxal-tracer increase with increasing glyoxal concentration. The variability in blanks shows that environmental factors and not precision dominate the variability of the corr.  $m/z$  44 to sulfate ratio but not the total organic to sulfate ratio. The trend in oxidized organic with gas-phase glyoxal is statistically not significant, indicating that the contribution to aerosol as a result of oxidized glyoxal uptake is very small.

glyoxal uptake and fast photochemical uptake that results only from residual organics in the chamber. The oxidized OA fraction (carboxylic acids) was not attributable to glyoxal (Figure 3c) in our uptake experiments with glyoxal and a gas-phase OH source. This is in contrast to the laboratory studies of bulk aqueous oxidation of glyoxal by OH with a condensed-phase OH source, which saw photochemical products, specifically carboxylic acids [Carlton *et al.*, 2007; Tan *et al.*, 2009]. The corrected  $m/z$  44 (carboxylic acid) signal indicates the presence of oxidation products, but blank experiments show that this is not a result of glyoxal uptake but from residual chamber organics. With the exception of the oxidized aerosol fraction, which exhibits no dependence on glyoxal, the glyoxal-dependent growth rate and composition of the aerosol as judged by the AMS are identical in the presence and absence of OH. Although the AMS fragments both oligomers and other higher molecular weight compounds, previous experiments have clearly shown that glyoxal oligomers can be detected [Galloway *et al.*, 2009; Liggio *et al.*, 2005]. If OH affected the oxidation or oligomerization chemistry in the aerosol, a shift to higher masses would be evident in the overall AMS mass spectra when compared to dark uptake conditions. Analysis of the  $m/z$  105 to  $m/z$  58 ratio rules out that OH influences the formation of glyoxal (acetal) oligomers. Our analysis also shows that the overall mass spectra of photochemical glyoxal uptake are not shifted to higher molecular weights or do not indicate other changes compared to dark uptake. In addition, analysis with particle-into-liquid-samplers

and analysis of filter extracts of aerosol did not show any higher molecular weight compounds, such as organosulfates or carboxylic acids (see auxiliary material).

[11] The observation of only slow, dark-type uptake in our experiments matches the results for mixed AS/fulvic/amino/sulfuric acid seed particles of Volkamer *et al.* [2009] but disagrees with their AS results that show fast photochemical uptake. This merits further discussion, specifically in the context of the exact nature of the seed, its influence on uptake, and resulting atmospheric implications. The seed introduced into the chamber consisted of pure AS seed aerosol, for which Volkamer *et al.* [2009] saw fast photochemical uptake. However, the seed to which glyoxal was exposed in our study was not pure as it had experienced a small amount of growth from chamber background aerosol, which was unavoidable under humid conditions even after extensive chamber cleaning.

[12] The key question is if and how this small amount of background aerosol or differences in experimental procedure resulted in a barrier for photochemical glyoxal uptake but not dark-type uptake. It was not known if a coating was present on the aerosol, and it is possible that, despite its high O/C ratio, expected high CCN activity, and WSOC-like properties, the chamber-background aerosol formed a coating. This coating may have prevented fast photochemical uptake but not slower dark-type uptake of glyoxal. This could result if dark-type uptake is rate-limited by a bulk-process whereas fast photochemical uptake is rate-limited by surface reactions. It is also possible that direct injection of glyoxal rather than photochemical generation from  $C_2H_2$  could explain the different results. Glyoxal oligomers may have formed in the gas-phase as a result of the high concentrations at the injection port, although it is unclear whether this is a gas-phase or wall/surface process. These oligomers have much lower vapor pressures than glyoxal and should rapidly partition to surfaces, including aerosol, potentially forming a coating. We also conducted experiments in which glyoxal was injected and allowed to equilibrate to the walls before seed was injected and photochemistry initiated (Exp. 2) in which case one might expect the oligomers to rapidly partition to the chamber walls before the seed was present. No fast photochemical uptake was observed, but it is possible that chamber background-aerosol rapidly coated the seed. A coating on our seed from chamber background or glyoxal/glyoxal oligomers could reconcile our results with those of Volkamer *et al.* [2009] if such coatings were not present for the latter experiments.

[13] The atmospheric implications of this work are less dependent on the differences than the similarities between our experimental results for AS and those of Volkamer *et al.* [2009]. Both studies show that fast photochemical uptake does not occur for all types of seed aerosol. The critical question is which type of seed is closest to atmospheric conditions. If the lack of fast photochemical uptake is caused by a coating on the seed, it is important to determine the necessary conditions and types of coatings that are common in the atmosphere to determine when and where ambient aerosol will show fast glyoxal uptake. Answering these questions about ambient aerosol and further elucidating conditions of fast photochemical uptake is required to determine the role of glyoxal in SOA formation from uptake on aerosol. At present, this is unclear and this work high-

lights the difficulty in both quantitatively and accurately including SOA formation from glyoxal in models.

[14] **Acknowledgments.** The authors thank Rainer Volkamer for helpful discussions prior to publication. This work was supported by the National Science Foundation, Division of Atmospheric Sciences, Atmospheric Chemistry Program (grants 1026667, 0852406), US Department of Energy grant DE-FG02-05ER63 983 and US Environmental Protection Agency STAR grant RD-83 374 901. It has not been formally reviewed by the EPA. The views expressed in this document are solely those of the authors and the EPA does not endorse any products in this publication.

[15] The Editor thanks two anonymous reviewers for their assistance in evaluating this paper.

## References

- Allan, J. D., et al. (2004), A generalised method for the extraction of chemically resolved mass spectra from Aerodyne aerosol mass spectrometer data, *J. Aerosol Sci.*, 35(7), 909–922, doi:10.1016/j.jaerosci.2004.02.007.
- Bones, D. L., D. K. Henriksen, S. A. Mang, M. Gonsior, A. P. Bateman, T. B. Nguyen, W. J. Cooper, and S. A. Nizkorodov (2010), Appearance of strong absorbers and fluorophores in limonene-O<sub>3</sub> secondary organic aerosol due to NH<sub>4</sub>-mediated chemical aging over long time scales, *J. Geophys. Res.*, 115, D05203, doi:10.1029/2009JD012864.
- Canagaratna, M. R., et al. (2007), Chemical and microphysical characterization of ambient aerosols with the aerodyne aerosol mass spectrometer, *Mass Spectrom. Rev.*, 26(2), 185–222, doi:10.1002/Mas.20115.
- Carlton, A., B. Turpin, K. Altieri, S. Seitzinger, A. Reff, H. Lim, and B. Ervens (2007), Atmospheric oxalic acid and soa production from glyoxal: Results of aqueous photooxidation experiments, *Atmos. Environ.*, 41(35), 7588–7602, doi:10.1016/j.atmosenv.2007.05.035.
- Chan, A. W. H., et al. (2010), Role of aldehyde chemistry and NO<sub>x</sub> concentrations in secondary organic aerosol formation, *Atmos. Chem. Phys.*, 10(15), 7169–7188, doi:10.5194/acp-10-7169-2010.
- Cocker, D. R., R. C. Flagan, and J. H. Seinfeld (2001), State-of-the-art chamber facility for studying atmospheric aerosol chemistry, *Environ. Sci. Technol.*, 35(12), 2594–2601, doi:10.1021/Es0019169.
- Corrigan, A. L., S. W. Hanley, and D. O. De Haan (2008), Uptake of glyoxal by organic and inorganic aerosol, *Environ. Sci. Technol.*, 42(12), 4428–4433, doi:10.1021/es7032394.
- DeCarlo, P. F., et al. (2006), Field-deployable, high-resolution, time-of-flight aerosol mass spectrometer, *Anal. Chem.*, 78(24), 8281–8289, doi:10.1021/ac061249n.
- De Haan, D. O., A. L. Corrigan, M. A. Tolbert, J. L. Jimenez, S. E. Wood, and J. J. Turley (2009a), Secondary organic aerosol formation by self-reactions of methylglyoxal and glyoxal in evaporating droplets, *Environ. Sci. Technol.*, 43(21), 8184–8190, doi:10.1021/Es902152t.
- De Haan, D. O., et al. (2009b), Secondary organic aerosol-forming reactions of glyoxal with amino acids, *Environ. Sci. Technol.*, 43(8), 2818–2824, doi:10.1021/es803534f.
- Ervens, B., and R. Volkamer (2010), Glyoxal processing by aerosol multiphase chemistry: Towards a kinetic modeling framework of secondary organic aerosol formation in aqueous particles, *Atmos. Chem. Phys.*, 10(17), 8219–8244, doi:10.5194/Acp-10-8219-2010.
- Ervens, B., A. G. Carlton, B. J. Turpin, K. E. Altieri, S. M. Kreidenweis, and G. Feingold (2008), Secondary organic aerosol yields from cloud-processing of isoprene oxidation products, *Geophys. Res. Lett.*, 35, L02816, doi:10.1029/2007GL031828.
- Galloway, M. M., P. S. Chhabra, A. W. H. Chan, J. D. Surratt, R. C. Flagan, J. H. Seinfeld, and F. N. Keutsch (2009), Glyoxal uptake on ammonium sulphate seed aerosol: Reaction products and reversibility of uptake under dark and irradiated conditions, *Atmos. Chem. Phys.*, 9(10), 3331–3345, doi:10.5194/acp-9-3331-2009.
- Huisman, A. J., J. R. Hottle, K. L. Coens, J. P. DiGangi, M. M. Galloway, A. Kamrath, and F. N. Keutsch (2008), Laser-induced phosphorescence for the in situ detection of glyoxal at part per trillion mixing ratios, *Anal. Chem.*, 80(15), 5884–5891, doi:10.1021/ac800407b.
- Ip, H. S. S., X. H. Huang, and J. Z. Yu (2009), Effective Henry's law constants of glyoxal, glyoxylic acid, and glycolic acid, *Geophys. Res. Lett.*, 36, L01802, doi:10.1029/2008GL036212.
- Keywood, M. D., V. Varutbangkul, R. Bahreini, R. C. Flagan, and J. H. Seinfeld (2004), Secondary organic aerosol formation from the ozonolysis of cycloalkenes and related compounds, *Environ. Sci. Technol.*, 38(15), 4157–4164, doi:10.1021/Es.035363o.
- Kroll, J. H., N. L. Ng, S. M. Murphy, V. Varutbangkul, R. C. Flagan, and J. H. Seinfeld (2005), Chamber studies of secondary organic aerosol growth by reactive uptake of simple carbonyl compounds, *J. Geophys. Res.*, 110, D23207, doi:10.1029/2005JD006004.
- Liggio, J., S.-M. Li, and R. McLaren (2005), Reactive uptake of glyoxal by particulate matter, *J. Geophys. Res.*, 110, D10304, doi:10.1029/2004JD005113.
- Massoli, P., et al. (2010), Relationship between aerosol oxidation level and hygroscopic properties of laboratory generated secondary organic aerosol (SOA) particles, *Geophys. Res. Lett.*, 37, L24801, doi:10.1029/2010GL045258.
- Ng, N. L., J. H. Kroll, A. W. H. Chan, P. S. Chhabra, R. C. Flagan, and J. H. Seinfeld (2007), Secondary organic aerosol formation from m-xylene, toluene, and benzene, *Atmos. Chem. Phys.*, 7(14), 3909–3922, doi:10.5194/acp-7-3909-2007.
- Nozière, B., P. Dziedzic, and A. Cordova (2009), Products and kinetics of the liquid-phase reaction of glyoxal catalyzed by ammonium ions (NH<sub>4</sub><sup>+</sup>), *J. Phys. Chem. A*, 113(1), 231–237, doi:10.1021/jp8078293.
- Odum, J. R., T. Hoffmann, F. Bowman, D. Collins, R. C. Flagan, and J. H. Seinfeld (1996), Gas/particle partitioning and secondary organic aerosol yields, *Environ. Sci. Tech.*, 30(8), 2580–2585, doi:10.1021/es950943+.
- Pankow, J. F. (1994a), An absorption-model of gas-particle partitioning of organic-compounds in the atmosphere, *Atmos. Environ.*, 28(2), 185–188, doi:10.1016/1352-2310(94)90093-0.
- Pankow, J. F. (1994b), An absorption-model of the gas aerosol partitioning involved in the formation of secondary organic aerosol, *Atmos. Environ.*, 28(2), 189–193, doi:10.1016/1352-2310(94)90094-9.
- Shapiro, E. L., J. Szprengiel, N. Sareen, C. N. Jen, M. R. Giordano, and V. F. McNeill (2009), Light-absorbing secondary organic material formed by glyoxal in aqueous aerosol mimics, *Atmos. Chem. Phys.*, 9(7), 2289–2300, doi:10.5194/acp-9-2289-2009.
- Tan, Y., M. J. Perri, S. P. Seitzinger, and B. J. Turpin (2009), Effects of precursor concentration and acidic sulfate in aqueous glyoxal-OH radical oxidation and implications for secondary organic aerosol, *Environ. Sci. Technol.*, 43(21), 8105–8112, doi:10.1021/es901742f.
- Turpin, B. J., and H. J. Lim (2001), Species contributions to PM<sub>2.5</sub> mass concentrations: Revisiting common assumptions for estimating organic mass, *Aerosol Sci. Technol.*, 35(1), 602–610, doi:10.1080/02786820119445.
- Volkamer, R., P. J. Ziemann, and M. J. Molina (2009), Secondary organic aerosol formation from acetylene (C<sub>2</sub>H<sub>2</sub>): Seed effect on SOA yields due to organic photochemistry in the aerosol aqueous phase, *Atmos. Chem. Phys.*, 9(6), 1907–1928, doi:10.5194/acp-9-1907-2009.

A. W. H. Chan, Department of Environmental Science, Policy and Management, University of California, 250C Hilgard Hall, Berkeley, CA 94720, USA.

P. S. Chhabra, C. L. Loza, and J. H. Seinfeld, Division of Chemistry and Chemical Engineering, California Institute of Technology, 1200 E. California Blvd., Pasadena, CA 91125, USA.

M. M. Galloway and F. N. Keutsch, Department of Chemistry, University of Wisconsin-Madison, 1101 University Ave., Madison, WI 53706, USA. (keutsch@chem.wisc.edu)

L. D. Yee, Division of Engineering and Applied Science, California Institute of Technology, 1200 E. California Blvd., Pasadena, CA 91125, USA.

## Appendix B

# $\alpha$ -Pinene Photooxidation Under Controlled Chemical Conditions - Part 1: Gas-Phase Composition in Low- and High-NO<sub>x</sub> Environments\*

---

\*Reproduced with permission from “ $\alpha$ -pinene photooxidation under controlled chemical conditions - Part 1: Gas-phase composition in low- and high-NO<sub>x</sub> environments” by N. C. Eddingsaas, C. L. Loza, L. D. Yee, J. H. Seinfeld, and P. O. Wennberg, *Atmos. Chem. Phys.*, 12, 6489-6504, doi:10.5194/acp-12-6489-2012. Copyright 2012 by the Authors. This work is distributed under the Creative Commons Attribution 3.0 License.



## $\alpha$ -pinene photooxidation under controlled chemical conditions – Part 1: Gas-phase composition in low- and high-NO<sub>x</sub> environments

N. C. Eddingsaas<sup>1</sup>, C. L. Loza<sup>1</sup>, L. D. Yee<sup>2</sup>, J. H. Seinfeld<sup>1,2</sup>, and P. O. Wennberg<sup>2,3</sup>

<sup>1</sup>Division of Chemistry and Chemical Engineering, California Institute of Technology, Pasadena, CA, USA

<sup>2</sup>Division of Engineering and Applied Science, California Institute of Technology, Pasadena, CA, USA

<sup>3</sup>Division of Geological and Planetary Sciences, California Institute of Technology, Pasadena, CA, USA

Correspondence to: N. C. Eddingsaas (eddingsa@caltech.edu)

Received: 29 December 2011 – Published in Atmos. Chem. Phys. Discuss.: 1 March 2012

Revised: 21 June 2012 – Accepted: 1 July 2012 – Published: 25 July 2012

**Abstract.** The OH oxidation of  $\alpha$ -pinene under both low- and high-NO<sub>x</sub> environments was studied in the Caltech atmospheric chambers. Ozone was kept low to ensure OH was the oxidant. The initial  $\alpha$ -pinene concentration was 20–50 ppb to ensure that the dominant peroxy radical pathway under low-NO<sub>x</sub> conditions is reaction with HO<sub>2</sub>, produced from reaction of OH with H<sub>2</sub>O<sub>2</sub>, and under high-NO<sub>x</sub> conditions, reactions with NO. Here we present the gas-phase results observed. Under low-NO<sub>x</sub> conditions the main first generation oxidation products are a number of  $\alpha$ -pinene hydroxy hydroperoxides and pinonaldehyde, accounting for over 40 % of the yield. In all, 65–75 % of the carbon can be accounted for in the gas phase; this excludes first-generation products that enter the particle phase. We suggest that pinonaldehyde forms from RO<sub>2</sub> + HO<sub>2</sub> through an alkoxy radical channel that regenerates OH, a mechanism typically associated with acyl peroxy radicals, not alkyl peroxy radicals. The OH oxidation and photolysis of  $\alpha$ -pinene hydroxy hydroperoxides leads to further production of pinonaldehyde, resulting in total pinonaldehyde yield from low-NO<sub>x</sub> OH oxidation of ~33 %. The low-NO<sub>x</sub> OH oxidation of pinonaldehyde produces a number of carboxylic acids and peroxyacids known to be important secondary organic aerosol components. Under high-NO<sub>x</sub> conditions, pinonaldehyde was also found to be the major first-generation OH oxidation product. The high-NO<sub>x</sub> OH oxidation of pinonaldehyde did not produce carboxylic acids and peroxyacids. A number of organonitrates and peroxyacyl nitrates are observed and identified from  $\alpha$ -pinene and pinonaldehyde.

### 1 Introduction

The emissions of biogenic volatile organic compounds (BVOCs) far outnumber those of anthropogenic VOCs (Guenther et al., 1995; Steinbrecher et al., 2009; Monks et al., 2009). Excluding methane, BVOCs are estimated to account for a flux of ~1150 Tg C yr<sup>-1</sup>, while anthropogenic VOCs account for only ~140 Tg C yr<sup>-1</sup> (Guenther et al., 1995; Goldstein and Galbally, 2007). Important BVOCs include isoprene, (flux of ~500 Tg C yr<sup>-1</sup>) and the monoterpenes (~127 Tg C yr<sup>-1</sup>) of which  $\alpha$ -pinene accounts for ~50 Tg C yr<sup>-1</sup> (Guenther et al., 1995; Chung and Seinfeld, 2002). Because they are unsaturated, these compounds are highly reactive towards OH, O<sub>3</sub>, and NO<sub>3</sub> and thus play an important role in tropospheric chemistry. The atmospheric oxidation of BVOCs also results in the formation of secondary organic aerosol (SOA). Monoterpenes are significant sources of SOA due to their large emission rate and high SOA yield (Hoffmann et al., 1997; Pye et al., 2010).

The gas-phase oxidation of simple alkanes and alkenes is well understood and most tropospheric chemical mechanisms use laboratory studies of reactions of these species to inform the parameterization of the atmospheric oxidation of VOCs. Many BVOCs, including isoprene, which has a conjugated double bond system, and  $\alpha$ -pinene which is a bicyclic hydrocarbon with an endocyclic double bond, however, have much more complicated chemistry than the simple alkanes and alkenes. For example, recent experimental and theoretical studies with isoprene have shown that its atmospheric chemistry is not well modeled by the reactions of simple

**Table 1.** Experimental conditions.

Date	Hydrocarbon	Concentration (ppb)	OH Source	Aerosol seed <sup>a</sup>	Length of experiment (hours)
5 May 2010	$\alpha$ -pinene	45	H <sub>2</sub> O <sub>2</sub>	No seed	12
6 May 2010	$\alpha$ -pinene	50	HONO	No seed	10
7 May 2010	$\alpha$ -pinene	48	H <sub>2</sub> O <sub>2</sub>	AS	11
9 May 2010	$\alpha$ -pinene	52	HONO	AS	8
10 May 2010	$\alpha$ -pinene	47	H <sub>2</sub> O <sub>2</sub>	AS+SA	11
11 May 2010	$\alpha$ -pinene	46	HONO	AS+SA	10
12 May 2010	$\alpha$ -pinene	20	H <sub>2</sub> O <sub>2</sub>	No seed	19
13 May 2010	$\alpha$ -pinene	42	CH <sub>3</sub> ONO	No seed	8
14 May 2010	$\alpha$ -pinene	47	H <sub>2</sub> O <sub>2</sub>	AS	12
17 May 2010	$\alpha$ -pinene	48	CH <sub>3</sub> ONO	AS	8
18 May 2010	$\alpha$ -pinene	47	H <sub>2</sub> O <sub>2</sub>	AS+SA	12
19 May 2010	$\alpha$ -pinene	44	CH <sub>3</sub> ONO	AS+SA	8
2 June 2010	$\alpha$ -pinene	45	H <sub>2</sub> O <sub>2</sub>	AS	12
3 June 2010	$\alpha$ -pinene	45	CH <sub>3</sub> ONO	AS	8
4 June 2010	Pinonaldehyde	— <sup>b</sup>	H <sub>2</sub> O <sub>2</sub>	No Seed	9
8 Feb 2011	$\alpha$ -pinene	43	H <sub>2</sub> O <sub>2</sub>	No seed	8
14 Feb 2011	Pinonaldehyde	— <sup>b</sup>	H <sub>2</sub> O <sub>2</sub>	No seed	9
16 Feb 2011	$\alpha$ -pinene	31	CH <sub>3</sub> ONO	No seed	3
17 Feb 2011	Pinonaldehyde	— <sup>b</sup>	CH <sub>3</sub> ONO	No seed	4

<sup>a</sup> AS: ammonium sulfate, AS+SA: ammonium sulfate and sulfuric acid.<sup>b</sup> The initial concentration of pinonaldehyde was not determined.

alkenes, especially under low-NO<sub>x</sub> (NO and NO<sub>2</sub>) conditions (Paulot et al., 2009b; Peeters and Muller, 2010; Crounse et al., 2011).

$\alpha$ -pinene is a ten-carbon bicyclic hydrocarbon with an endocyclic double bond and, therefore, has the potential to react in ways not represented by simple alkenes. In addition,  $\alpha$ -pinene is highly reactive with both O<sub>3</sub> and OH, reacting in the atmosphere with  $\alpha$ -pinene nearly equally, adding to the richness of its atmospheric photochemistry (Capouet et al., 2008). Despite a number of studies of OH oxidation of  $\alpha$ -pinene, large uncertainties in the identity and yields of its reaction products remain. For instance, the reported yield of pinonaldehyde from the photooxidation of  $\alpha$ -pinene ranges from 28 to 87 % in the presence of NO<sub>x</sub> and from 3 to 37 % in the absence of NO<sub>x</sub> (Arey et al., 1990; Hatakeyama et al., 1991; Noziere et al., 1999; Jaoui and Kamens, 2001; Wisthaler et al., 2001; Aschmann et al., 2002; Lee et al., 2006). In addition, the molecular structures of major products identified by mass (e.g. 184 and 200 daltons) are subject to debate (Aschmann et al., 2002; Vereecken et al., 2007). The photooxidation product with molecular mass 184 has been assigned to an unsaturated hydroperoxy carbonyl (Vereecken et al., 2007) or a dihydroxy carbonyl (Aschmann et al., 2002). A better understanding of  $\alpha$ -pinene gas-phase chemistry will increase the accuracy of  $\alpha$ -pinene atmospheric chemistry models and provide insight into atmospheric photooxidation mechanisms in general.

In this study, we isolate the peroxy radical reaction pathways to investigate the photochemistry of  $\alpha$ -pinene. We have

studied these reactions under low-NO<sub>x</sub> conditions similar to those found in the atmosphere, where RO<sub>2</sub> + HO<sub>2</sub> is the dominant peroxy radical reaction, and other reactions are suppressed (RO<sub>2</sub> + RO<sub>2</sub> and reactions with O<sub>3</sub>). We contrast these conditions with results from the gas-phase photooxidation of  $\alpha$ -pinene under high-NO<sub>x</sub> (with varied amounts of NO<sub>2</sub> to study both RO<sub>2</sub> + NO and RO<sub>2</sub> + NO<sub>2</sub>). We focus our analysis on low-NO<sub>x</sub> rather than high-NO<sub>x</sub> chemistry because the low-NO<sub>x</sub> chemistry of  $\alpha$ -pinene is less well-characterized yet it is more atmospherically-relevant (Pye et al., 2010). In a forthcoming paper, SOA yields and composition formed from the controlled chemical conditions described here will be presented.

## 2 Experimental

Photooxidation experiments of  $\alpha$ -pinene were performed in the Caltech dual 28 m<sup>3</sup> Teflon chambers. Details of the chamber facilities have been described elsewhere (Cocker et al., 2001; Keywood et al., 2004). A few photooxidation experiments were performed in a  $\sim$ 1 m<sup>3</sup> bag enclosed in a small, black walled chamber with UV-lights lining one wall, as described by Crounse et al. (2011). 40 W black lights (Sylvania F40/350BL) with emission peak emission at 352 nm were used in both chambers. The light intensity as a function of wavelength (300–800 nm) was measured using a Licor (LI-1800) spectroradiometer. Prior to each run, the chamber was flushed for a minimum of 24 h with dry purified air. While

being flushed, the chamber was irradiated with the chamber lights for a minimum of six hours. The temperature, relative humidity (RH), and concentrations of  $O_3$ , and  $NO_x$  ( $NO$  and  $NO_2$ ) were continuously monitored. In all experiments the RH was kept below 10 %. Aerosol size distribution and number concentration were measured continuously by a differential mobility analyzer (DMA, TSI model 3081) coupled to a condensation nucleus counter (TSI model 3760). Information on aerosol measurements can be found in part 2, where aerosol formation, growth, and composition are discussed. Table 1 shows a list of conditions for all experiments used in this study. Experiments ran for 3 to 19 h. No gas phase losses to the chamber walls of either  $\alpha$ -pinene prior to light irradiation or oxidation products after lights were extinguished was observed.

Experiments were performed under low- and high- $NO_x$  conditions. Under low- $NO_x$  conditions, photolysis of hydrogen peroxide ( $H_2O_2$ ) was the OH source, while for the high- $NO_x$  experiments the photolysis of nitrous acid (HONO) or methyl nitrite ( $CH_3ONO$ ) produced OH. For low- $NO_x$  experiments, 280  $\mu$ L of 50 wt %  $H_2O_2$  was injected into the chamber resulting in an  $H_2O_2$  concentration  $\sim 4$  ppm. The two different OH sources used during the high- $NO_x$  experiments provided the mechanism to vary the  $NO$  to  $NO_2$  ratio, with a higher quantity of  $NO_2$  in the  $CH_3ONO$  experiments. HONO was prepared daily by dropwise addition of 15 mL of 1 wt %  $NaNO_2$  into 30 mL of 10 wt %  $H_2SO_4$  in a glass bulb, and then introduced into the chamber with dry air. This process produces  $NO$  and  $NO_2$  as side products, which are also introduced to the chamber.  $CH_3ONO$  was synthesized, purified, and stored according to the procedure outlined by Taylor et al. (1980).  $CH_3ONO$  was warmed from liquid nitrogen temperatures and vaporized into an evacuated 500 mL glass bulb and introduced into the chamber with an air stream of  $5\text{ L min}^{-1}$ . After addition of  $CH_3ONO$ , 300–400 ppb of  $NO$  was added to the chamber to suppress the formation of  $O_3$ . Determination of exact  $NO$  and  $NO_2$  concentrations using the commercial  $NO_x$  monitor was precluded due to interferences by both HONO and  $CH_3ONO$ . At the start of all high- $NO_x$  experiments the total  $NO_x$  reading ( $NO$ ,  $NO_x$ , and interference from HONO or  $CH_3ONO$ ) was 800 ppb and  $NO$  concentration throughout the experiments was such that the concentration of  $O_3$  never exceeded 5 ppb.

$\alpha$ -pinene was added to the chamber to achieve a concentration of 20–50 ppb by passing dry air through a bulb containing a known volume of  $\alpha$ -pinene. The mixing ratio of  $\alpha$ -pinene was monitored by gas chromatography (Agilent 6890N) coupled with a flame ionization detector (GC-FID). The GC-FID was calibrated using a 55 L Teflon bag containing a known concentration of pure  $\alpha$ -pinene. Gas phase photooxidation products were monitored using triple-quadrupole chemical ionization mass spectrometry (CIMS) (St. Clair et al., 2010).

Details of the operation of the CIMS can be found in a number of previous reports (Crounse et al., 2006; Paulot

et al., 2009a; St. Clair et al., 2010) and therefore only a brief description is presented here. The CIMS was operated in negative ion mode using  $CF_3O^-$  as the reagent ion, and in the positive ion mode using  $H_3O^+$  for proton transfer mass spectrometry (PTR-MS). In negative mode,  $CF_3O^-$  is sensitive to the detection of polar and acidic compounds by either clustering with the analyte (R) resulting in an ion with a mass-to-charge ratio ( $m/z$ )  $MW+85$  ( $R \cdot CF_3O^-$ ) or via fluorine ion transfer resulting in  $m/z$   $MW+19$  ( $HF \cdot R_{-H}^-$ ). The dominant ionization mechanism depends mostly on the acidity of the neutral species; highly acidic species such as nitric acid only form the fluorine transfer ion, while non-acidic species such as methyl hydrogen peroxide form only the cluster ion. This separation aids both in the determination of the structure of a molecule and in the identification of isomers. In negative mode, tandem mass spectrometry (MS/MS) was used to help identify functional groups of an analyte. In brief, a parent ion selected in the first quadrupole is exposed to an elevated pressure of  $N_2$  resulting in collision-induced dissociation (CID) in the second quadrupole, and the resulting fragmentation ions are detected in the third quadrupole. Molecules with different functional groups have been shown to fragment differently by CID and thus the detection of certain fragment ions in quadrupole three can aid in the identification of an analyte. For instance, hydroperoxides form a characteristic fragment at  $m/z$  63 (Paulot et al., 2009b).

Standards are not available for most of the VOCs described here and thus the sensitivity of the CIMS is related to the thermal capture rate and the binding energy of the cluster ( $VOC \cdot CF_3O^-$ ). Details on calculating the sensitivity of the CIMS to a given analyte can be found in previous publications (Paulot et al., 2009a,b).

### 3 Results and discussion

The goal of this study is to determine the gas-phase reaction products and mechanism of the photooxidation of  $\alpha$ -pinene by OH under both low- $NO_x$  and high- $NO_x$  conditions. In both cases, the experiment is designed such that  $\alpha$ -pinene only reacts with OH and that a single peroxy radical reaction is dominant. Under ambient conditions,  $\alpha$ -pinene reacts at an approximately equal rate with  $O_3$  ( $k_{O_3} = 9.0 \times 10^{-17} \text{ cm}^3 \text{ molecules}^{-1} \text{ s}^{-1}$ ) and OH ( $k_{OH} = 5.3 \times 10^{-11} \text{ cm}^3 \text{ molecules}^{-1} \text{ s}^{-1}$ ) (Sander et al., 2006; Atkinson et al., 2006). To isolate the OH chemistry, the formation of  $O_3$  was suppressed.

Under low- $NO_x$  conditions, photolysis of  $H_2O_2$  resulted in steady state OH concentration of  $\sim 2 \times 10^6 \text{ cm}^{-3}$  and an  $HO_2$  concentration  $\sim 1 \times 10^{10} \text{ cm}^{-3}$ . The OH and  $HO_2$  concentrations were determined from a kinetic molecular model of  $\alpha$ -pinene OH reaction which is described in detail in Sect. 3.2 and in the Supplement. In brief, OH is produced by the photolysis of  $H_2O_2$  and is primarily consumed by reactions with VOCs in the chamber and with  $H_2O_2$ . The reaction of OH

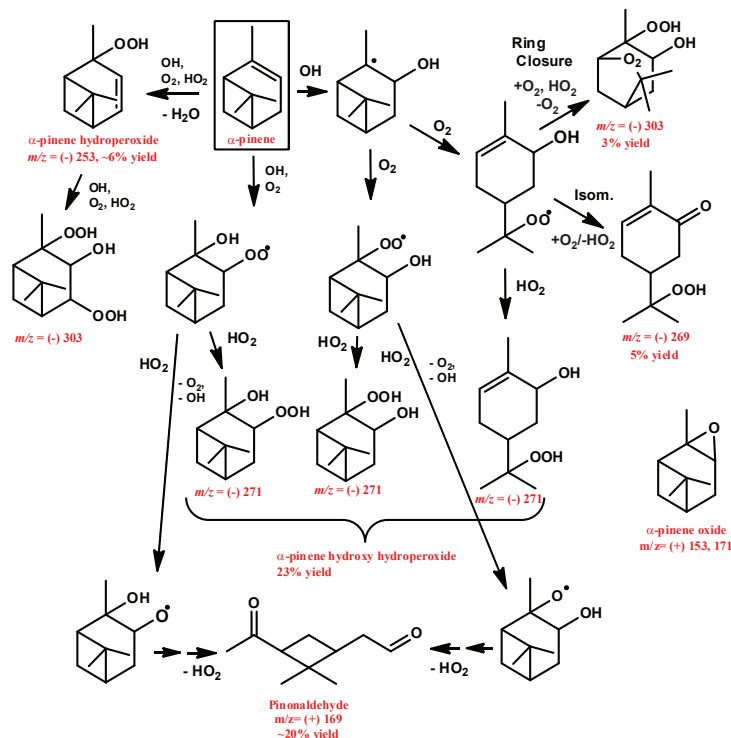


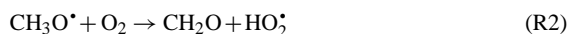
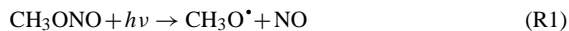
**Fig. 1.** Pathway of photooxidation of  $\alpha$ -pinene under low- $\text{NO}_x$  conditions. Species that were observed are labeled in red. The  $m/z$  of all species observed in the negative mode are of the complex with  $\text{CF}_3\text{O}^-$  (molecular mass + 85). Pinonaldehyde is observed at molecular mass + 1 in the positive mode and  $\alpha$ -pinene oxide is observed at molecular mass + 1 and + 19. The observed percent yield for first-generation products is also indicated.

and  $\text{H}_2\text{O}_2$  produces  $\text{HO}_2$ . The photolysis rate of  $\text{H}_2\text{O}_2$  used in the model and the  $\text{OH}$  concentration determined by the model were confirmed by comparison of the gas-phase concentrations of  $\text{H}_2\text{O}_2$  and  $\alpha$ -pinene from the experiment and the model (Fig. S1). These  $\text{OH}$  concentrations are similar to those observed in the troposphere; however, the  $\text{HO}_2$  concentrations are about an order of magnitude greater than levels typically observed in rural or remote areas (Lelieveld et al., 2008; Ren et al., 2008; Wolfe et al., 2011). The  $\text{O}_3$  concentration at the start of each experiment was  $<4$  ppb and typically did not exceed 12 ppb over the course of an experiment (in one experiment, conducted for 20 h, the  $\text{O}_3$  concentration increased nearly linearly from 4 to 25 ppb). Modeling of these oxidant concentrations indicated that reaction with  $\text{O}_3$  accounted for  $<3\%$  of the  $\alpha$ -pinene loss.

In the oxidation of  $\alpha$ -pinene by  $\text{OH}$ ,  $\text{OH}$  adds predominantly to the endocyclic double bond, followed by addition of  $\text{O}_2$  to the resulting  $\beta$ -hydroxy alkyl radicals producing a number of hydroxy peroxy radicals.  $\text{OH}$  abstraction of a hydrogen from  $\alpha$ -pinene occurs with a yield of  $\sim 12\%$ , resulting in a peroxy radical when  $\text{O}_2$  reacts with the alkyl rad-

ical (Capouet et al., 2004). Under low- $\text{NO}_x$  conditions the peroxy radicals can react with either  $\text{HO}_2$  or with another  $\text{RO}_2$  (self or cross-reactions). Here we seek to emulate atmospheric conditions where  $\text{RO}_2 + \text{HO}_2$  dominates. To confirm that the  $\text{RO}_2 + \text{HO}_2$  pathway dominated in our experiments, a kinetic model was constructed, as described in Sect. 3.2 and the Supplement. For the experimental conditions (with initial concentration of  $\alpha$ -pinene of 20–50 ppb), the kinetic model indicates that less than 1 % of the peroxy radical reactions proceed via  $\text{RO}_2 + \text{RO}_2$ .

For high- $\text{NO}_x$  photooxidation experiments,  $\text{OH}$  is generated from the photolysis of either  $\text{HONO}$  or methyl nitrite. When  $\text{HONO}$  is synthesized,  $\text{NO}$  and  $\text{NO}_2$  are produced as side products, which are also introduced to the chamber when  $\text{HONO}$  is injected. Methyl nitrite is synthesized pure and upon photolysis eventually produces  $\text{OH}$  and  $\text{NO}_2$ :





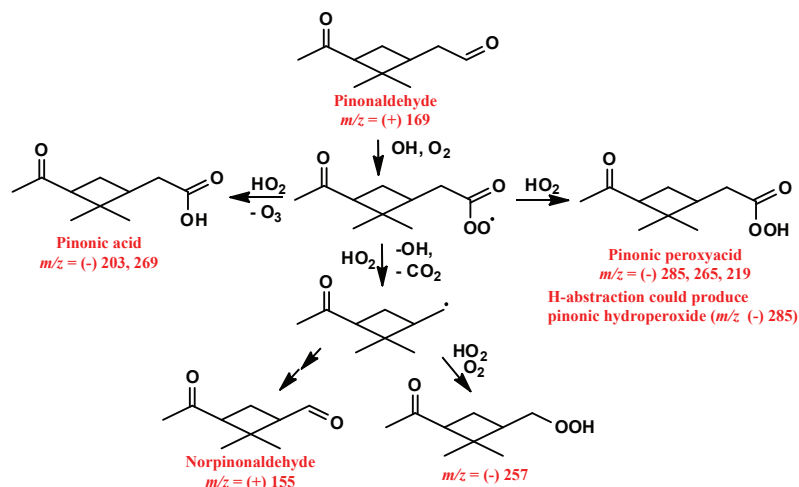


**Fig. 2.** Pathway of photooxidation of pinonaldehyde under low- $\text{NO}_x$  conditions. Species that were observed are labeled in red. Pinonic acid and pinonic peracid were observed in the negative mode as both the transfer ion (molecular mass + 19) and the complex (molecular mass + 85), pinonic peracid is also observed as the complex minus HF (molecular mass + 65), norpinonaldehyde hydroperoxide was observed as the complex ion, pinonaldehyde and norpinonaldehyde are observed in the positive mode at their molecular mass + 1.

When methyl nitrite was used as the OH source, 300 to 400 ppb of NO was added to suppress  $\text{O}_3$  production. Under the conditions used, the peroxy radicals formed from the OH reaction of  $\alpha$ -pinene react with NO and not  $\text{RO}_2$  or  $\text{HO}_2$ . This is confirmed by the lack of  $\text{RO}_2 + \text{HO}_2$  or  $\text{RO}_2 + \text{RO}_2$  reaction products during high- $\text{NO}_x$  photooxidation. The exact ratio of NO to  $\text{NO}_2$  is not known as both HONO and methyl nitrite interfere with the signals from the chemiluminescence  $\text{NO}_x$  instrument; however, it was determined that a higher  $\text{NO}_2$  concentration exists during methyl nitrite photolysis due to the increased production of peroxyacyl nitrates (PANs), as detected by CIMS in the negative mode, which result from the  $\text{RO}_2 + \text{NO}_2$  reaction. More details on the detection of, as well as the specific PANs detected will be discussed in Sect. 3.3.

### 3.1 Gas phase composition from low- $\text{NO}_x$ photooxidation of $\alpha$ -pinene

The principal first-generation oxidation products observed from the low- $\text{NO}_x$  photooxidation of  $\alpha$ -pinene were a number of  $\alpha$ -pinene hydroxy hydroperoxides and pinonaldehyde. Production of  $\alpha$ -pinene hydroperoxide from H-abstraction and  $\alpha$ -pinene oxide are also observed (see Fig. 1 for proposed reaction mechanism for  $\alpha$ -pinene and Fig. 2 for pinonaldehyde). The time traces from the CIMS are shown in Fig. 3 along with those from a number of the minor oxidation products. The identification of each of these signals is discussed below.

The  $\alpha$ -pinene hydroxy hydroperoxides are observed at  $m/z = (-) 271$  (molecular weight +  $\text{CF}_3\text{O}^-$ ) by the CIMS. They

are expected to be a major products of the reaction channel of  $\text{RO}_2 + \text{HO}_2$ . Three different  $\alpha$ -pinene hydroxy hydroperoxide isomers are formed; two  $\beta$ -hydroxy hydroperoxides and one ring opened hydroxy hydroperoxide containing a double bond (see Fig. 1). The subsequent reaction pathways of these three  $\alpha$ -pinene hydroxy hydroperoxides are expected to be different and will lead to distinct reaction products, as discussed in Sect. 3.2. The overall estimated initial yield of the  $\alpha$ -pinene hydroxy hydroperoxides is  $\sim 23\%$ . This estimate accounts for the small yield of pinic acid, which has the same molecular weight as these peroxides (MW = 186). Similar to other carboxylic acids, ionization of pinic acid by  $\text{CF}_3\text{O}^-$  yields approximately equal amounts of signal at  $m/z = (-) 271$  and 205 (MW<sub>-H</sub> + HF). This allows us to use the signal at  $m/z = (-) 205$  to insure that the pinic acid concentration does not significantly impact the hydroperoxide yield estimate.

Pinonaldehyde is neither acidic nor is the complex with  $\text{CF}_3\text{O}^-$  significantly strong to be detected in the negative mode and thus is observed only in the positive mode of the CIMS. Pinonaldehyde was synthesized to directly observe its OH oxidation; however, the synthesized sample was not of sufficient purity to calibrate the CIMS response. While we cannot report an absolute yield for pinonaldehyde, we observe that the yield under low- $\text{NO}_x$  conditions is 2/3 of that under high- $\text{NO}_x$  conditions. As pinonaldehyde is one of the main products of  $\alpha$ -pinene oxidation by any atmospheric oxidant, it has been widely studied. Although the reported yield of pinonaldehyde under high- $\text{NO}_x$  conditions varies widely from 27–87 % (Arey et al., 1990; Hatakeyama et al., 1991; Nozière et al., 1999; Wisthaler et al., 2001; Jaoui and Kamens, 2001; Aschmann et al., 2002; Lee et al., 2006),

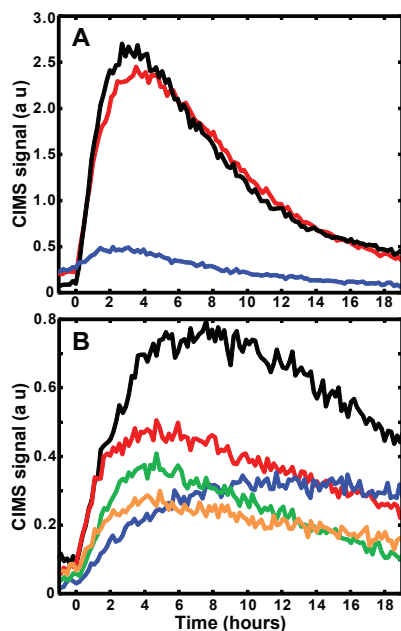
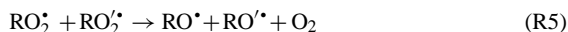
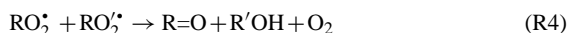


**Fig. 3.** CIMS time traces of a number of important low- $\text{NO}_x$  photooxidation products of  $\alpha$ -pinene. (A) Main first generation products,  $m/z$  (–)271  $\alpha$ -pinene hydroxy hydroperoxide (black),  $m/z$  (+)169 pinonaldehyde (red),  $m/z$  (–)253  $\alpha$ -pinene hydroperoxide (blue) (B) Signals of species that are formed in multiple generations  $m/z$  (–)285 (black),  $m/z$  (–)269 (red),  $m/z$  (–)303 (green),  $m/z$  (–)301 (orange), and purely second-generation  $m/z$  (–)203 pinonic acid (blue). The signal from  $m/z$  (+)169 is the only signal shown from the positive mode and the intensity was divided by 2 for clarity.

most of the measured yields are between 27–35 %. The very high yields were measured by FTIR which may be biased by interference from other carbonyls (Nozière et al., 1999; Hatakeyama et al., 1991). Assuming that under high- $\text{NO}_x$  conditions the pinonaldehyde yield is between 27–35 %, we estimate that the low- $\text{NO}_x$  yield is about 20 %.

Pinonaldehyde has been observed from the low- $\text{NO}_x$  photooxidation of  $\alpha$ -pinene previously; however, it is typically assigned as a product of  $\text{RO}_2 + \text{RO}_2$  chemistry (Nozière et al., 1999; Larsen et al., 2001). In the present set of experiments, the chemistry is overwhelmingly dominated by  $\text{RO}_2 + \text{HO}_2$  (i.e. low  $\alpha$ -pinene concentration and relatively high  $\text{HO}_2$  concentration). This is confirmed by the photooxidation products observed. The two main reaction channels for alkyl peroxy radicals with other  $\text{RO}_2$  are:

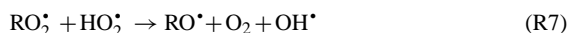


resulting in the formation of alcohols and carbonyls from Reaction (R4) and alkoxy radicals from Reaction (R5). In the case of  $\alpha$ -pinene, these would be  $\beta$ -diols,  $\beta$ -hydroxy carbonyl, and hydroxy alkoxy radicals. The six membered ring of the hydroxy alkoxy radical will then open forming pinonaldehyde. There is no indication of either  $\beta$ -diols or  $\beta$ -hydroxyl carbonyl being formed during the present experiments. In the case of alkyl peroxy radicals reacting with  $\text{HO}_2$ , the main reaction channel is:



which forms hydroperoxides. For  $\alpha$ -pinene, Reaction (R6) will produce the observed  $\alpha$ -pinene hydroxy hydroperoxides. For many small alkyl peroxy radicals it has been shown to be the only channel (Hasson et al., 2004; Raventos-Duran et al., 2007; Noell et al., 2010).

If Reaction (R6) was the only channel, there would be no route to pinonaldehyde production. One possible route to pinonaldehyde is a radical channel (see Fig. 1):



similar to those known to be important for acetyl peroxy radicals (Hasson et al., 2004; Dillon and Crowley, 2008) and possibly for the reaction of OH with toluene (Birdsall et al., 2010). If this is the route to pinonaldehyde formation, an OH recycling channel would also be of importance in the reaction of OH with  $\alpha$ -pinene under low- $\text{NO}_x$  conditions.

$\alpha$ -pinene hydroperoxide and  $\alpha$ -pinene oxide are also observed products of the OH oxidation of  $\alpha$ -pinene under low- $\text{NO}_x$  conditions.  $\alpha$ -pinene hydroperoxide can be formed from H-abstraction by OH, which is estimated to account for about 12 % of the OH reaction with  $\alpha$ -pinene (Capouet et al., 2004). Assuming similar CIMS sensitivity to  $\alpha$ -pinene hydroperoxide and  $\alpha$ -pinene hydroxy hydroperoxide, the yield of  $\alpha$ -pinene hydroperoxide is estimated to be ~6 %. The remainder of the H-abstraction branching ratio cannot be accounted for at this time.  $\alpha$ -pinene oxide is neither acidic nor is the complex with  $\text{CF}_3\text{O}^-$  significantly strong to be detected in the negative mode and thus is observed only in the positive mode at  $m/z$  (+)153 and 171 as confirmed by direct injection of  $\alpha$ -pinene oxide into the chamber. Further evidence of  $\alpha$ -pinene oxide formation is presented in part 2 of this series of paper where SOA composition is discussed.  $\alpha$ -pinene oxide appears to be a minor product, and the mechanism for its formation by OH oxidation is not known. The mechanism for the formation from  $\text{O}_3$  oxidation is known and yields of a few percent have been reported (Alvarado et al., 1998; Berndt et al., 2003); however, in the present experiments  $\text{O}_3$  accounts for less than 3 % of the oxidation of  $\alpha$ -pinene.

The oxidation products of pinonaldehyde have been shown to be important in the formation of SOA from the photooxidation of  $\alpha$ -pinene. Specifically, pinonic acid, 10-hydroxypinonic acid, and pinic acid have been observed in ambient SOA samples (Kavouras et al., 1998, 1999; Yu

et al., 1999; Laaksonen et al., 2008; Zhang et al., 2010) and in laboratory studies of  $\alpha$ -pinene photooxidation (Larsen et al., 2001; Jaoui and Kamens, 2001; Librando and Tringali, 2005). The low- $\text{NO}_x$  photooxidation of pinonaldehyde was carried out to determine the contribution of pinonaldehyde oxidation products to the gas and particle phases of  $\alpha$ -pinene photooxidation.

Photooxidation of pinonaldehyde accounts for a number of the products observed from  $\alpha$ -pinene photooxidation. OH oxidation of pinonaldehyde occurs by H-abstraction, typically from the aldehydic group (59–86 %) (Kwok and Atkinson, 1995; Vereecken and Peeters, 2002) forming an acyl peroxy radical after the addition of  $\text{O}_2$ . The reaction of  $\text{HO}_2$  with an acyl peroxy radical produces carboxylic acids, peroxyacids, and acetoxy radicals that will decompose to produce  $\text{CO}_2$  and an alkyl radical. Hasson et al. (2004) have shown that these three pathways occur in roughly equal yields. The reaction pathways and products from pinonaldehyde are shown in Fig. 2. Pinonic acid is observed by the CIMS mostly by its transfer product ion (ratio of  $m/z$  (–)203 to  $m/z$  (–)269 is  $\sim 9:1$ ), typical of acidic species, while the peroxyacid is observed more by its complex ion (ratio of  $m/z$  (–)219 to  $m/z$  (–)285 is  $\sim 1:4$ ) (Fig. 4). In addition, we have observed, using synthesized peracetic acid, that peroxyacids are also observed in the negative mode as its molecular mass +65 (complex with  $\text{CF}_3\text{O}^- - \text{HF}$ ) at 10–20 % that of the complex ion (+85). A signal at  $m/z$  (–)265,  $\sim 10\%$  the intensity of  $m/z$  (–)285, has been assigned to pinonic peroxyacid providing further evidence of its formation. These two products are formed in roughly equal yields. H-abstraction at carbons other than the aldehydic carbon could also form pinonaldehyde hydroperoxide which would also be detected at  $m/z$  (–)285, as would 10-hydroxy pinonic acid (product found in SOA). A signal at  $m/z$  (–)257 that has nine carbons was observed and has been assigned to the hydroperoxide formed from the alkyl radical formed from the decomposition of the acetoxy radical. The formation of norpinonaldehyde was also detected. Pinic acid was observed in equal amounts at  $m/z$  (–)205 and  $m/z$  (–)271, but is a minor product.

Low- $\text{NO}_x$  photooxidation of  $\alpha$ -pinene also leads to the pinonaldehyde oxidation products (Fig. 4). Ions at  $m/z$  (–)203 and (–)219 assigned to the transfer ions of pinonic acid and pinonic peroxyacid are observed to be second generation products from  $\alpha$ -pinene photooxidation, as would be expected arising from the oxidation of pinonaldehyde. The ion at  $m/z$  (–)257 assigned to the  $\text{C}_9$  hydroperoxide produced from pinonaldehyde photooxidation is also observed to be second generation. Pinonic acid and pinonic peroxyacid are also observed as the complex ion at  $m/z$  (–)269 and (–)285 respectively. The time traces for  $m/z$  (–)269 and  $m/z$  (–)285 from the photooxidation of  $\alpha$ -pinene are not purely from first or second generation products (see Figs. 3 and 4) but a combination of the two. The second generation products observed as these two ions are pinonic acid and pinonic peroxyacid, evident from their transfer ions, while

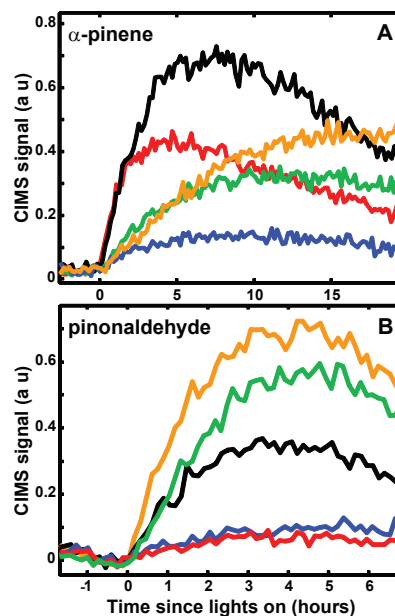


**Fig. 4.** Comparison of CIMS signals from low- $\text{NO}_x$  photooxidation of (A)  $\alpha$ -pinene and (B) pinonaldehyde;  $m/z$  (–)285 (black),  $m/z$  (–)269 (red),  $m/z$  (–)257 (orange),  $m/z$  (–)219 (blue), and  $m/z$  (–)203 (green). Pinonaldehyde photooxidation produces pinonic peroxyacid observed at both  $m/z$  (–)285 and (–)219, pinonic acid observed at both  $m/z$  (–)269 and (–)203, and a  $\text{C}_9$  hydroperoxide observed at  $m/z$  (–)257. The pinonaldehyde photooxidation products are observed from  $\alpha$ -pinene photooxidation along with additional first-generation signals at  $m/z$  (–)269 and (–)285 from first-generation photooxidation products.

the first generation products arise from the photooxidation of  $\alpha$ -pinene. Oxidation products of these molecular mass (184 and 200) have been observed and theoretically proposed from the photooxidation of  $\alpha$ -pinene in the presence of NO (Aschmann et al., 2002; Vereecken et al., 2007). Under high- $\text{NO}_x$  conditions, Aschmann et al. (2002) observed molecules at these masses and assigned them to a dihydroxy carbonyl and a trihydroxy carbonyl that would be formed by a number of isomerization steps as well as multiple reactions of peroxy radicals with NO to form alkoxy radicals. Vereecken et al. (2007) indicate that molecules with these molecular weights could be formed by isomerization reactions after ring opening, while the molecule with  $\text{MW} = 200$  is produced from a reaction of NO with the peroxy radical. In both mechanisms, alkoxy radicals are essential. Alkoxy radicals appear to form from the reaction of the initially formed  $\alpha$ -pinene hydroxy peroxy radical intermediates with  $\text{HO}_2$ , and this is a possible route; however, at this point, the structure of these molecules is unknown. These are, however, clearly polyoxygenated species formed from the primary oxidation

of  $\alpha$ -pinene and their most likely molecular formulas are  $C_{10}H_{16}O_3$  and  $C_{10}H_{16}O_4$ .

Highly oxidized species at  $m/z$  (–)301 and (–)303 are also observed as first generation products (see Fig. 3). Both signals decay similarly to the signals at  $m/z$  (–)269 and (–)285, indicating that they are also formed as later generation products. The most likely structure for the first-generation species at  $m/z$  (–)303 is an  $\alpha$ -pinene hydroxy hydroperoxide with a bridging peroxy group that results from the ring closing channel of the ring opened hydroxy hydroperoxide as shown in Fig. 1. This mechanism has been postulated by Vereecken et al. (2007). The addition of one hydroxyl group and two hydroperoxyl groups decreases the vapor pressure about eight orders of magnitude making this product a likely aerosol phase component (Capouet and Müller, 2006). The photooxidation of  $\alpha$ -pinene hydroperoxide will produce a hydroxy dihydroperoxide that will also be observed at  $m/z$  (–)303 thus accounting for the slow decay of the signal. We do not know the structure of the photooxidation product(s) at  $m/z$  (–)301. Given the molecular weight, the structure potentially includes one carbonyl and two hydroperoxyl groups. Whatever the structure, the vapor pressure will be greatly reduced from that of  $\alpha$ -pinene, once again making it a potential SOA component.

Another route to the formation of the low vapor pressure oxidation products at  $m/z$  (–)301 and (–)303 is peroxy radical isomerization. Peroxy radical isomerization has recently been extensively studied for the isoprene system both theoretically (Peeters et al., 2009; da Silva et al., 2010; Nguyen et al., 2010) as well as experimentally (Crounse et al., 2011). It has been shown that peroxy radical isomerization most often occurs via a six or seven membered intermediate (Perrin et al., 1998; Blin-Simiani et al., 2001; Jorand et al., 2003). When OH adds to the tertiary carbon of the double bond the peroxy radical on the secondary carbon can form a seven membered ring with the hydrogen of either the secondary carbon in the four membered ring or one of primary carbons attached to the four membered ring. After isomerization, reaction with  $O_2$  and  $HO_2$  will result in the formation of  $\alpha$ -pinene hydroxy dihydroperoxide which would be detected at  $m/z$  (–)303. See Fig. S2 in the Supplement for proposed mechanism. When OH adds to the secondary carbon of the double bond, a seven membered intermediate can form with the other tertiary carbon of the four membered ring ultimately forming  $\alpha$ -pinene hydroxy dihydroperoxide. Similarly, the  $\alpha$ -pinene hydroxy hydroperoxide peroxy radical formed from isomerization from the addition of OH to the secondary carbon can form a six membered ring with the hydrogen on the carbon  $\alpha$  to the hydroxyl group. This isomerization would result in the formation of  $\alpha$ -pinene carbonyl dihydroperoxide which would be observed at  $m/z$  (–)301. For the species observed at  $m/z$  (–)301 and (–)303 to be formed via isomerization, the rate of peroxy radical isomerization would have to be competitive with that of  $RO_2 + HO_2$ . In the present experiments  $[HO_2]$  is  $\sim 1 \times 10^{10}$  molecules  $cm^{-3}$  so

the rate of loss of  $\alpha$ -pinene hydroxy peroxy radical by reaction with  $HO_2$  is  $\sim 0.2 s^{-1}$ . In the atmosphere the  $HO_2$  concentration is about an order of magnitude less, so for isomerization to be competitive (10 % of peroxy radical reaction) the rate would have to be  $\sim 0.002 s^{-1}$ . In the isoprene system the isomerization rate has been found to be  $0.002 s^{-1}$  with conformer specific rates being much faster (Crounse et al., 2011). At this time there have been no experimental studies on the isomerization rate in the  $\alpha$ -pinene system so it is unknown what the rate is and therefore its atmospheric relevance. If the rate of isomerization is competitive with reaction with  $HO_2$  in the atmosphere, more low vapor pressure species capable of partitioning into the aerosol will be formed than were observed in this study.

### 3.2 Kinetic model of low- $NO_x$ photooxidation of $\alpha$ -pinene

To gain a better understanding of the low- $NO_x$  photooxidation of  $\alpha$ -pinene, a kinetic model was assembled and compared to the time traces of  $\alpha$ -pinene and the reaction products measured during the photooxidation of 19.8 ppb  $\alpha$ -pinene and 4 ppm  $H_2O_2$ . The kinetic model was constructed using Kintecus modeling software (Ianni, 2002). When available, rate constants from literature were used; however, a majority of the rate constants are not known. In these cases, reaction rates with respect to OH oxidation were estimated using the structural activity relationship derived by Kwok and Atkinson (Kwok and Atkinson, 1995). This method has been shown to predict rate constants to within a factor of two for most species (see Tables S1 and S2 for lists of photooxidation products, reactions, and reaction rates used in this model). The rate constants were then modified slightly to best fit the data. The rate constants for  $RO_2 + HO_2$  and  $RO_2 + RO_2$  were taken from the estimates used for the Master Chemical Mechanism (Saunders et al., 2003). Photolysis was included for hydrogen peroxide, the organic hydroperoxides, and for pinonaldehyde. The photodissociation frequencies ( $j$ ) were determined from the spectral radiance measured from the chamber lights and the absorption cross sections reported in the literature for hydrogen peroxide and pinonaldehyde and estimated for the organic hydroperoxides from reported cross sections of similar hydroperoxides (Atkinson et al., 2006; Sander et al., 2006).

For the model to be accurate, the concentration of OH and  $HO_2$  need to be correct. OH is produced from photolysis of  $H_2O_2$  which initially reacts with hydrocarbons in the chamber as well as  $H_2O_2$ . It is the reaction of OH with  $H_2O_2$  that produces  $HO_2$ . The value of  $j_{H_2O_2}$  was confirmed by comparing the simulated loss of  $H_2O_2$  (photolysis and reaction with OH) to the time trace observed from the CIMS (see SI Fig. S1). The comparison of the simulated loss of  $\alpha$ -pinene, using the recommended rate constant for the reaction of  $\alpha$ -pinene with OH from the IUPAC database (Atkinson et al., 2006), with the the observed loss of  $\alpha$ -pinene also confirms

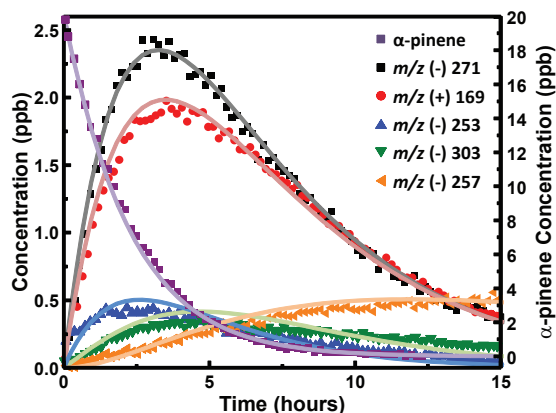


Fig. 5. Time-dependent observed (points) versus simulated (lines) concentrations from the photooxidation of 19.8 ppb of  $\alpha$ -pinene. Represented are  $\alpha$ -pinene (purple),  $\alpha$ -pinene hydroxy hydroperoxide (black), pinonaldehyde (red),  $\alpha$ -pinene hydroperoxide (blue),  $\alpha$ -pinene hydroxy dihydroperoxide (green), and the C<sub>9</sub> hydroperoxide from pinonaldehyde (orange). See the Supplement for structural information and kinetic model.

the simulation produces the correct amount of OH (see Fig. S1 in the Supplement). The modeled OH concentration quickly reaches  $2.2 \times 10^6$  molecules  $\text{cm}^{-3}$  and is approximately constant between  $2.2\text{--}2.5 \times 10^6$  molecules  $\text{cm}^{-3}$  over the course of the experiment, while the HO<sub>2</sub> concentration rapidly plateaus at about  $1 \times 10^{10}$  molecules  $\text{cm}^{-3}$ . In addition, the rate constant of OH with pinonaldehyde was confirmed from the experiment where pinonaldehyde was directly injected into the chamber. Pinonaldehyde is lost by reaction with OH as well as photolysis ( $\sim 10\%$  of overall reaction), and the best fit to the data is achieved with  $k_{\text{pinonaldehyde}+\text{OH}} = 3.7 \times 10^{-11}$   $\text{cm}^3$  molecules $^{-1}$  s $^{-1}$  (Fig. S3 in the Supplement). This rate constant is within the error recommended by the IUPAC database and the latest measurement of this reaction rate by Davis et al. (2007); Atkinson et al. (2006).

Figure 5 shows the time traces of  $\alpha$ -pinene and several of the photooxidation products along with the simulated concentrations from the kinetic model. The oxidation products in Fig. 5 are representative of first-generation products ( $\alpha$ -pinene hydroxy-hydroperoxides, pinonaldehyde, and  $\alpha$ -pinene hydroperoxide) and a second-generation product (C<sub>9</sub> hydroperoxide from pinonaldehyde) (see Table S1 for structural information of each compound). The one exception is the highly oxygenated compound observed at  $m/z$  (–)303 (assigned to hydroxyl dihydroperoxide) that is both a first- and second-generation product, and due to its high degree of oxidation and low volatility is predicted to partition into the particle phase. As noted in Sect. 3.1, pinic acid is a minor second generation product that is observed at  $m/z$  (–)205 and  $m/z$  (–)271 in roughly equal amounts. This small yield was

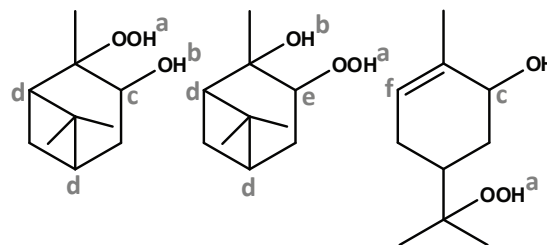


Fig. 6. Structure of the hydroxy hydroperoxides formed from the low-NO<sub>x</sub> photooxidation of  $\alpha$ -pinene, the most likely positions for reaction with OH are also shown; H-abstraction (a–e) and OH addition (f).

accounted for in determining the concentration of  $\alpha$ -pinene hydroxy hydroperoxides. Using the fastest RO<sub>2</sub> + RO<sub>2</sub> rate constant for  $\alpha$ -pinene hydroxy peroxy radicals from MCM, only 0.05 % of the peroxy radical is predicted to react through the RO<sub>2</sub> + RO<sub>2</sub> channel. Including all of the identified first-generation products (these presented here along with the products at  $m/z$  (–)269, 285, and 301), 65–75 % of the carbon can be accounted for, and this does not include compounds that are expected to partition into the aerosol phase.

Pinonaldehyde, in the present set of experiments, is formed from the RO<sub>2</sub> + HO<sub>2</sub> reaction channel of two of the  $\alpha$ -pinene hydroxy peroxy radicals, and the reaction rate with OH has been well characterized. However, based on these formation and loss mechanisms for pinonaldehyde, the simulated pinonaldehyde decays far too quickly; therefore, pinonaldehyde must also be produced as a second-generation oxidation product. Of the first-generation products, the most likely candidates to produce pinonaldehyde from a reaction with OH are the  $\alpha$ -pinene hydroxy hydroperoxides.

There are a number of paths by which the  $\alpha$ -pinene hydroxy hydroperoxides will form pinonaldehyde. First of all, the hydroperoxide will not only react with OH but will also undergo photolysis. Photolysis cleaves the weak O–O bond of the hydroperoxide producing an alkoxy radical that will produce pinonaldehyde. We estimate, however, that photolysis represents  $\sim 3\%$  of the  $\alpha$ -pinene hydroxy hydroperoxide loss and thus does not provide mass closure between the data and the simulation.

Figure 6 shows the three hydroxy hydroperoxides that are formed from low-NO<sub>x</sub> photooxidation of  $\alpha$ -pinene, two  $\beta$ -hydroxy hydroperoxides and a ring-opened one that includes a double bond. The  $\beta$ -hydroxy hydroperoxides have a number of places where OH hydrogen abstraction could occur (Fig. 6), the carbon  $\alpha$  to the alcohol; carbon  $\alpha$  to the hydroperoxyl group; either of the tertiary carbons; the alcoholic hydrogen; or the hydroperoxy hydrogen. Hydrogen abstraction from an alcohol will mostly occur from the  $\alpha$  carbon which has been shown to result in the formation of a

carbonyl and HO<sub>2</sub> (Carter et al., 1979; Atkinson, 1986; Grosjean, 1997). Presumably this would form a hydroperoxy carbonyl, a mass analog of the known second-generation product pinonic acid. As there are first- and second-generation products with  $m/z$  (–)269, it is not clear how important this H-abstraction channel is. There have only been a few hydroperoxides whose H-abstraction reaction rates and product distributions have been studied: methyl, ethyl and tert-butyl (Vaghjiani and Ravishankara, 1989; Niki et al., 1983; Wang and Chen, 2008; Baasandorj et al., 2010). It has been shown that the OO-H bond is fairly labile and H-abstraction from both the hydroperoxide as well as the  $\alpha$ -carbon will occur. H-abstraction from the hydroperoxyl group will result in reformation of the peroxy radical with the same branching ratio of products from the initial reaction forming, among other species, pinonaldehyde and hydroxy hydroperoxide. H-abstraction from the  $\alpha$ -carbon of the hydroperoxy group would presumably form a hydroxy carbonyl, which is a mass analog of  $\alpha$ -pinene hydroperoxide. In the model, the signal associated with  $\alpha$ -pinene hydroperoxide is fit well with a production channel from  $\alpha$ -pinene and a reaction rate with OH that is nearly as fast as  $\alpha$ -pinene itself, suggesting that it is unlikely that there is a second-generation product formed at this mass. It is possible that following hydrogen abstraction, the ring is cleaved, ultimately resulting in the formation of pinonaldehyde. Finally, H-abstraction from either of the tertiary carbons will produce more highly oxygenated species, including a hydroxyl dihydroperoxide ( $m/z$  (–)303). Of these different H-abstraction pathways, those involving the hydroperoxide and carbons  $\alpha$  to the hydroperoxy and hydroxyl groups are expected to dominate. The ring opened hydroxy hydroperoxide has a highly reactive double bond instead of one of the tertiary carbons. After addition of OH to the double bond, the reaction will most likely proceed in one of the following ways: formation of a dihydroxy dihydroperoxide or intermolecular reaction of the alkyl radical with the hydroperoxy group forming a ring with one oxygen and releasing OH. The former product has not been observed in the present experiments; however, this highly oxidized compound has a low vapor pressure and is expected to primarily reside in the particle phase. The later product is a mass analog of the hydroxy hydroperoxide, and the two species are indistinguishable by CIMS.

In the simulation, all the pathways for reaction of the  $\alpha$ -pinene hydroxy hydroperoxides were considered and the contribution of each was varied until the simulation best fit the data based on a least-squares analysis of  $\alpha$ -pinene hydroxy hydroperoxide and pinonaldehyde. The best fit results when 58 % of the reaction produces pinonaldehyde directly while another 25 % reforms the peroxy radical, resulting in a net  $\sim$ 33 % of  $\alpha$ -pinene producing pinonaldehyde from low-NO<sub>x</sub> photooxidation. This is important since the oxidation products of pinonaldehyde are main SOA components. There is need for further studies on the photooxidation of  $\alpha$ -pinene hydroxy hydroperoxides to confirm these reaction pathways

and branching ratios; however, the data and kinetic model strongly indicate that pinonaldehyde is produced from the OH oxidation of  $\alpha$ -pinene hydroxy hydroperoxides under low-NO<sub>x</sub> conditions.

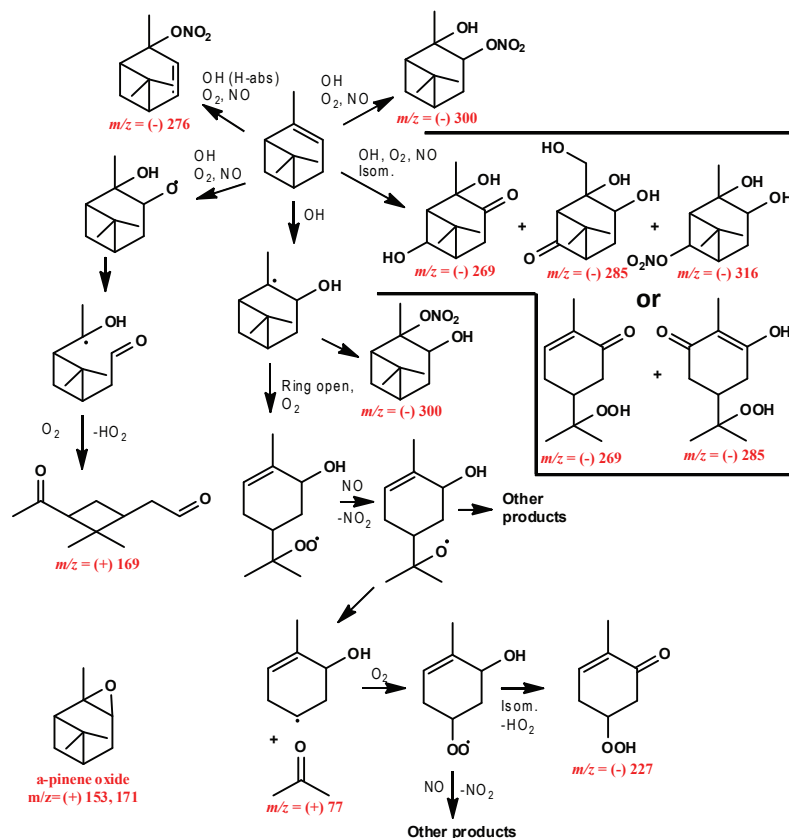
### 3.3 Gas-phase composition from high-NO<sub>x</sub> photooxidation of $\alpha$ -pinene

Figure 7 shows the proposed reaction mechanism of  $\alpha$ -pinene photooxidation under high-NO<sub>x</sub> conditions. This mechanism and the following discussion of the reaction products are not intended to be all-inclusive. The photooxidation of  $\alpha$ -pinene under high-NO<sub>x</sub> conditions produces a large variety of compounds through functionalization and fragmentation reactions. We observe signals at many masses but, for brevity, we only focus on those of the major products of  $\alpha$ -pinene and pinonaldehyde high-NO<sub>x</sub> OH oxidation.

In the presence of NO<sub>x</sub>, the main photooxidation products of  $\alpha$ -pinene are pinonaldehyde, organonitrates, and isomerization products from the alkoxy radical formed from the reaction of NO with the peroxy radical. The yield of pinonaldehyde is 1.5 times that formed in the absence of NO<sub>x</sub>, and, as mentioned above, previous studies show that it is 27–35 %. Capouet et al. (2004) estimates  $\alpha$ -pinene hydroxy nitrate yield to be  $\sim$ 15 %. Alkoxy radical isomerization products are observed at  $m/z$  (–)269 (MW 184) and  $m/z$  (–)285 (MW 200). These isomerization products have been observed previously and have been assigned to either a dihydroxy carbonyl and a trihydroxy carbonyl (Aschmann et al., 2002) or to ring opened substituted hydroperoxides (Vereecken et al., 2007). In the present study, the yield of the isomerization products was found to be less than 20 %. The OH addition to the double bond can also result in prompt ring opening of the four-membered ring. Further reactions of the ring-opened alkyl radical will result in fragmentation producing an alkyl radical and acetone (see Fig. 7). This is a minor pathway, as the total acetone yield observed was less than 10 %, including the production of acetone from the photooxidation of pinonaldehyde. Finally, there is a first-generation species observed at  $m/z$  (–)301, which was also present during low-NO<sub>x</sub> photooxidation. A likely molecular formula is C<sub>10</sub>H<sub>16</sub>O<sub>5</sub>, but the identity of this molecule is unknown. The same oxidation products were observed from high-NO<sub>x</sub> photooxidation, regardless of OH source, HONO or methyl nitrite.

The photooxidation of pinonaldehyde was studied using methyl nitrite as the OH source. Figure 8 shows the proposed mechanism and products of this reaction. There have been two theoretical studies on the H-abstraction of pinonaldehyde (Kwok and Atkinson, 1995; Vereecken and Peeters, 2002). Kwok and Atkinson (1995) indicate that 86 % of the abstraction will occur at the aldehydic hydrogen, while Vereecken and Peeters (2002) determined that 59 % will be of the aldehydic hydrogen, 23 % from the carbon  $\beta$  to the aldehydic carbon, and 14 % from the tertiary carbons. The





**Fig. 7.** Pathways of photooxidation of  $\alpha$ -pinene under high- $\text{NO}_x$  conditions, the structures for  $m/z$  (–)269 and (–)285 (MW 184 and 200) are those proposed by Aschmann et al. (2002) and Vereecken et al. (2007). Ion of compounds detected by CIMS are indicated in red.

products expected, and observed, of the primary channel (H-abstraction of the aldehydic hydrogen) are pinonaldehyde PAN, formed from reaction of the acyl peroxy radical with  $\text{NO}_2$  or norpinonaldehyde, formed from reaction of the acyl peroxy radical with  $\text{NO}$  (see Fig. 8 for structures and mechanisms). H-abstraction from the carbon  $\beta$  to the aldehydic carbon produces either pinonaldehyde nitrate or norpinonaldehyde with the loss of  $\text{CO}$ . Finally, H-abstraction from the tertiary carbons produces pinonaldehyde nitrate or a tertiary alkoxy radical. One potential reaction pathway for the tertiary alkoxy radical is the decomposition to form acetone (see Fig. 8), which is observed in low yield from high- $\text{NO}_x$  photooxidation of pinonaldehyde. Once formed, norpinonaldehyde will be oxidized in similar fashion to pinonaldehyde. The signal for pinonaldehyde PAN is 4–8 times that of pinonaldehyde nitrate (from all high- $\text{NO}_x$  experiments,  $\alpha$ -pinene and pinonaldehyde) depending on the  $\text{NO}_2$  concentration relative to  $\text{NO}$ . The observed signal of the norpinonaldehyde PAN to norpinonaldehyde nitrate from the photooxidation of pinonaldehyde was greater than 14 to 1. Pinonaldehyde PAN

is formed from an acyl peroxy radical while pinonaldehyde nitrate will be formed from an alkyl peroxy radical. The formation of an acyl peroxy radical is favored over the formation of an alkyl peroxy radical from H-abstraction of pinonaldehyde and thus the formation of pinonaldehyde PANs is expected to be formed in higher yield than pinonaldehyde nitrate. A quantitative yield of the PAN is not known because the CIMS has not been calibrated for these compounds. The product distribution from the photooxidation of pinonaldehyde indicates that it does not add much to the total organonitrate yield from the photooxidation of  $\alpha$ -pinene. Pinonic acid and pinic acid were not observed in the gas phase from either  $\alpha$ -pinene or pinonaldehyde photooxidation under high- $\text{NO}_x$  conditions.

An array of organonitrates and PANs are observed from the photooxidation of  $\alpha$ -pinene. In addition to those previously discussed, nitrates were observed at  $m/z$  (–)276, 316, 318, 320, and 332 as well as PANs at  $m/z$  (–)346 and (–)362 (most likely observed as the molecular complex ion MW + 85). The unidentified organonitrates and PANs are

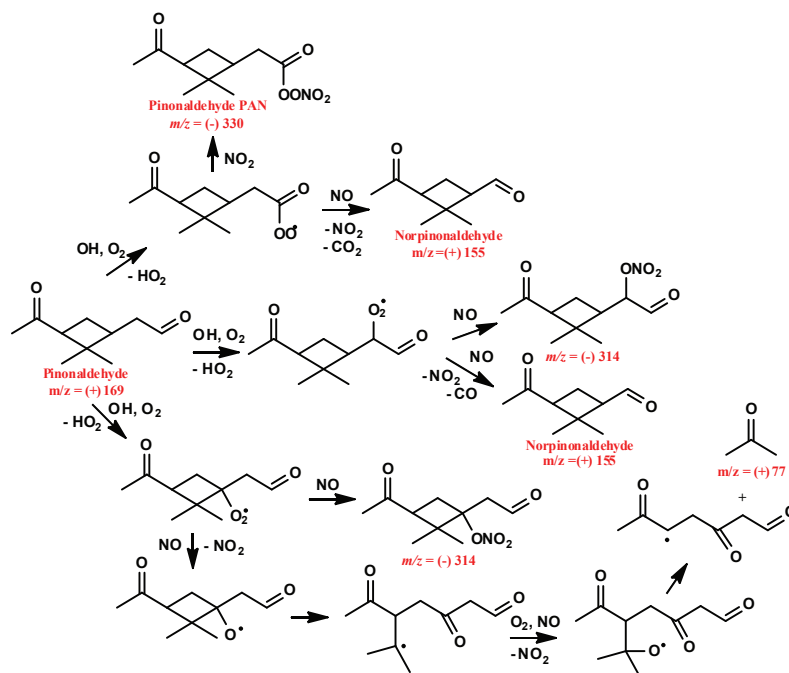


**Fig. 8.** Pathways of photooxidation of pinonaldehyde under high- $\text{NO}_x$  conditions, H-abstraction by OH occurs predominantly at the aldehydic carbon. Ion of compounds detected by CIMS are indicated in red.

formed in much lower yields than those identified earlier. Nitrates and PANs are distinguished from each other by the nature of their decay. PANs thermally decompose so their gas-phase concentration will continue to decrease even after OH is no longer present. Norpinonaldehyde PAN is observed at  $m/z$  (−)316; however, comparing the time traces of this ion from pinonaldehyde photooxidation and  $\alpha$ -pinene photooxidation, there appears to be a product formed from  $\alpha$ -pinene as well. This could be the  $\alpha$ -pinene dihydroxynitrate proposed by Aschmann et al. (2002). One interesting observation is that  $\alpha$ -pinene hydroxy nitrate is lost from the gas phase at nearly an equal rate as pinonaldehyde. This is in contrast to the other organonitrates, whose signals are stable once they are formed.

The products of high- $\text{NO}_x$  photooxidation of  $\alpha$ -pinene are the same regardless of  $\text{NO}_2$  level; however, there are a few differences in concentrations of certain species depending on the level of  $\text{NO}_2$ . The most noticeable difference in the gas-phase composition depending on the  $[\text{NO}_2]$  is the concentration of PANs, which are greater at high  $\text{NO}_2$  (methyl nitrite photolysis). This is expected as the  $\text{NO}_2$  concentration is higher in the methyl nitrite experiments resulting in a greater likelihood of  $\text{NO}_2$  reacting with the acyl peroxy radicals produced from pinonaldehyde and norpinonaldehyde. The concentrations of isomerization products at  $m/z$  (−)269 and (−)285 showed a dependence on seed particle acidity when

HONO was used as the OH source but not when  $\text{CH}_3\text{ONO}$  was used as the OH source. In the case of the HONO source, the isomerization products were observed to be lower in the presence of an acidic seed. A discussion of why the products observed at  $m/z$  (−)269 and (−)285 are dependent on aerosol acidity only for the HONO case will be presented in part 2. The only other observed difference in the gas phase was the concentration of nitric acid, which was 1.5 times greater when methyl nitrite was the OH source than when HONO was the OH source.

#### 4 Atmospheric implications

Under low- $\text{NO}_x$  photooxidation of  $\alpha$ -pinene, pinonaldehyde is produced by  $\text{RO}_2 + \text{HO}_2$  chemistry in high yields.  $\text{RO}_2 + \text{RO}_2$  chemistry is not the source, as is commonly assumed. While the atmospheric concentrations of  $\text{HO}_2$  and  $\text{RO}_2$  are similar, the rate constant of  $\text{RO}_2 + \text{HO}_2$  is typically 1–4 orders of magnitude greater than  $\text{RO}_2 + \text{RO}_2$ . The further OH oxidation of pinonaldehyde produces a number of low volatility carboxylic acids and peroxyacids, which are important SOA components. While the only product with higher yield than pinonaldehyde is  $\alpha$ -pinene hydroxy hydroperoxide, pinonaldehyde is also produced from the photolysis and OH oxidation of  $\alpha$ -pinene hydroxy hydroperoxide. Including



the reaction channels of  $\alpha$ -pinene hydroxy hydroperoxide that form pinonaldehyde (58 %) and assuming 19 % direct yield from  $\alpha$ -pinene, the overall oxidation of  $\alpha$ -pinene by OH under low-NO<sub>x</sub> conditions has a pinonaldehyde yield of ~33 %.

Pinonic acid is an important tracer for SOA formed from  $\alpha$ -pinene oxidation and is believed to be the precursor for other SOA tracers, such as 3-methyl-1,2,3-butanetricarboxylic acid (Szmigielski et al., 2007; Müller et al., 2012). Pinonic acid is not observed from the high-NO<sub>x</sub> photooxidation of  $\alpha$ -pinene, which is not surprising since there is no clear formation mechanism for it in the gas phase. Thus, observation of pinonic acid and the tracers derived from pinonic acid likely point to either low-NO<sub>x</sub> oxidation of  $\alpha$ -pinene by OH or ozonolysis under high-NO<sub>x</sub> conditions. The aerosol-phase composition of these carboxylic acids as well as other carboxylic acids from  $\alpha$ -pinene photooxidation will be discussed in detail in Part 2.

The gas-phase chemistry of  $\alpha$ -pinene and its photooxidation products is complex and not well represented by the reactions of simple alkenes. By isolating the critical peroxy radical reactions, the products and branching ratios of a number of key reactions have been better constrained. Perhaps most importantly, we suggest that the formation of pinonaldehyde from low-NO<sub>x</sub> photooxidation of  $\alpha$ -pinene via RO<sub>2</sub> + HO<sub>2</sub> proceeds by the formation of an alkoxy radical and OH recycling. This reaction scheme has previously been shown to be important only for acyl peroxy radicals and possibly toluene. Unfortunately, the nature of the potential energy surface leading to radical recycling in the reactions of HO<sub>2</sub> with peroxy radicals has not been fully formulated. Is the OH recycling channel available due to the  $\beta$  hydroxyl group withdrawing electron density from the peroxy group, the bicyclic ring structure of  $\alpha$ -pinene, or some other reason all together? To date, most of the detailed work on the reaction of alkyl peroxy radicals with HO<sub>2</sub> has focused on small, unsubstituted peroxy radicals; further work on a broader set of peroxy radicals, including atmospherically relevant VOCs such as monoterpenes and sesquiterpenes, is clearly needed to elucidate the physical chemistry. Finally, we suggest that there is a large secondary pinonaldehyde source from the photooxidation and/or photolysis of the three pinene hydroxy hydroperoxides produced from  $\alpha$ -pinene.

**Supplementary material related to this article is available online at:** <http://www.atmos-chem-phys.net/12/6489/2012/acp-12-6489-2012-supplement.pdf>.

**Acknowledgements.** This work was supported in part by Department of Energy grant DE-SC0006626 and National Science Foundation grant AGS-1057183. N. Eddingsaas was supported by the Camille and Henry Dreyfus Postdoctoral Program in

Environmental Chemistry. C. Loza and L. Yee were supported by National Science Foundation Graduate Research Fellowships. The authors would like to thank John Crounse for helpful discussion.

Edited by: F. Keutsch

## References

- Alvarado, A., Tuazon, E. C., Aschmann, S. M., Atkinson, R., and Arey, J.: Products of the gas-phase reactions of O(<sup>3</sup>P) atoms and O<sub>3</sub> with  $\alpha$ -pinene and 1,2-dimethyl-1-cyclohexene, *J. Geophys. Res.-Atmos.*, 103, 25541–25551, doi:10.1029/98JD00524, 1998.
- Arey, J., Atkinson, R., and Aschmann, S. M.: Product study of the gas-phase reactions of monoterpenes with the OH radical in the presence of NO<sub>x</sub>, *J. Geophys. Res.*, 95, 18539–18546, doi:10.1029/JD095iD11p18539, 1990.
- Aschmann, S. M., Atkinson, R., and Arey, J.: Products of reaction of OH radicals with  $\alpha$ -pinene, *J. Geophys. Res.-Atmos.*, 107, D14, doi:10.1029/2001JD001098, 2002.
- Atkinson, R.: Kinetics and mechanisms of the gas-phase reactions of the hydroxyl radical with organic compounds under atmospheric conditions, *Chem. Rev.*, 86, 69–201, 1986.
- Atkinson, R., Baulch, D. L., Cox, R. A., Crowley, J. N., Hampson, R. F., Hynes, R. G., Jenkin, M. E., Rossi, M. J., Troe, J., and IUPAC Subcommittee: Evaluated kinetic and photochemical data for atmospheric chemistry: Volume II – gas phase reactions of organic species, *Atmos. Chem. Phys.*, 6, 3625–4055, doi:10.5194/acp-6-3625-2006, 2006.
- Baasandorj, M., Papanastasiou, D. K., Talukdar, R. K., Hasson, A. S., and Burkholder, J. B.: (CH<sub>3</sub>)<sub>3</sub>COOH (tert-butyl hydroperoxide): OH reaction rate coefficients between 206 and 375 K and the OH photolysis quantum yield at 248 nm, *Phys. Chem. Chem. Phys.*, 12, 12101–12111, doi:10.1039/C0CP00463D, 2010.
- Berndt, T., Boge, O., and Stratmann, F.: Gas-phase ozonolysis of  $\alpha$ -pinene: gaseous products and particle formation, *Atmos. Environ.*, 37, 3933–3945, 2003.
- Birdsall, A. W., Andreoni, J. F., and Elrod, M. J.: Investigation of the role of bicyclic peroxy radicals in the oxidation mechanism of toluene, *J. Phys. Chem. A*, 114, 10655–10663, 2010.
- Blin-Simiand, N., Jorand, F., Sahetchian, K., Brun, M., Kerhoas, L., Malosse, C., and Einhorn, J.: Hydroperoxides with zero, one, two or more carbonyl groups formed during the oxidation of n-dodecane, *Combust. Flame*, 126, 1524–1532, doi:10.1016/S0010-2180(01)00264-4, 2001.
- Capouet, M. and Müller, J.-F.: A group contribution method for estimating the vapour pressures of  $\alpha$ -pinene oxidation products, *Atmos. Chem. Phys.*, 6, 1455–1467, doi:10.5194/acp-6-1455-2006, 2006.
- Capouet, M., Peeters, J., Nozière, B., and Müller, J.-F.:  $\alpha$ -pinene oxidation by OH: simulations of laboratory experiments, *Atmos. Chem. Phys.*, 4, 2285–2311, doi:10.5194/acp-4-2285-2004, 2004.
- Capouet, M., Mueller, J. F., Ceulemans, K., Compernelle, S., Vereecken, L., and Peeters, J.: Modeling aerosol formation in  $\alpha$ -pinene photo-oxidation experiments, *J. Geophys. Res.-Atmos.*, 113, D02308, doi:10.1029/2007JD008995, 2008.
- Carter, W. P. L., Darnall, K. R., Graham, R. A., Winer, A. M., and Pitts, J. N.: Reactions of C<sub>2</sub> and C<sub>4</sub>  $\alpha$ -hydroxy radicals with

- oxygen, *J. Phys. Chem.*, 83, 2305–2311, 1979.
- Chung, S. H. and Seinfeld, J. H.: Global distribution and climate forcing of carbonaceous aerosols, *J. Geophys. Res.-Atmos.*, 107, doi:10.1029/2001JD001397, 2002.
- Cocker, D. R. I., Flagan, R. C., and Seinfeld, J. H.: State-of-the-art chamber facility for studying atmospheric aerosol chemistry, *Environ. Sci. Technol.*, 35, 2594–2601, 2001.
- Crounse, J. D., McKinney, K. A., Kwan, A. J., and Wennberg, P. O.: Measurement of gas-phase hydroperoxides by chemical ionization mass spectrometry, *Anal. Chem.*, 78, 6726–6732, 2006.
- Crounse, J. D., Paulot, F., Kjaergaard, H. G., and Wennberg, P. O.: Peroxy radical isomerization in the oxidation of isoprene, *Phys. Chem. Chem. Phys.*, 13, 13607–13613, doi:10.1039/C1CP21330J, 2011.
- da Silva, G., Graham, C., and Wang, Z.-F.: Unimolecular beta-Hydroxyperoxy Radical Decomposition with OH Recycling in the Photochemical Oxidation of Isoprene, *Environ. Sci. Technol.*, 44, 250–256, doi:10.1021/es900924d, 2010.
- Davis, M. E., Talukdar, R. K., Notte, G., Ellison, G. B., and Burkholder, J. B.: Rate coefficients for the OH plus pinonaldehyde ( $C_{10}H_{16}O_2$ ) reaction between 297 and 374 K, *Environ. Sci. Technol.*, 41, 3959–3965, 2007.
- Dillon, T. J. and Crowley, J. N.: Direct detection of OH formation in the reactions of  $HO_2$  with  $CH_3C(O)O_2$  and other substituted peroxy radicals, *Atmos. Chem. Phys.*, 8, 4877–4889, doi:10.5194/acp-8-4877-2008, 2008.
- Goldstein, A. H. and Galbally, I. E.: Known and unexplored organic constituents in the Earth's atmosphere, *Environ. Sci. Technol.*, 41, 1514–1521, 2007.
- Grosjean, D.: Atmospheric chemistry of alcohols, *J. Braz. Chem. Soc.*, 8, 433–442, 1997.
- Guenther, A., Hewitt, C. N., Erickson, D., Fall, R., Geron, C., Graedel, T., Harley, P., Klinger, L., Lerdau, M., McKay, W. A., Pierce, T., Scholes, B., Steinbrecher, R., Tallamraju, R., Taylor, J., and Zimmerman, P.: A global model of natural volatile organic compound emissions, *J. Geophys. Res.-Atmos.*, 100, 8873–8892, doi:10.1029/94JD02950, 1995.
- Hasson, A. S., Tyndall, G. S., and Orlando, J. J.: A product yield study of the reaction of  $HO_2$  radicals with ethyl peroxy ( $C_2H_5O_2$ ), acetyl peroxy ( $CH_3C(O)O_2$ ), and acetonyl peroxy ( $CH_3C(O)CH_2O_2$ ) radicals, *J. Phys. Chem. A*, 108, 5979–5989, 2004.
- Hatakeyama, S., Izumi, K., Fukuyama, T., Akimoto, H., and Washida, N.: Reactions of OH with  $\alpha$ -pinene and  $\beta$ -pinene in air – Estimate of global CO production from the atmospheric oxidation of terpenes, *J. Geophys. Res.-Atmos.*, 96, 947–958, 1991.
- Hoffmann, T., Odum, J. R., Bowman, F., Collins, D., Klockow, D., Flagan, R. C., and Seinfeld, J. H.: Formation of organic aerosols from the oxidation of biogenic hydrocarbons, *J. Atmos. Chem.*, 26, 189–222, doi:10.1029/90JD02341, 1997.
- Ianni, J. C.: Kintecus, Window v. 2.80, www.kintecus.com, 2002.
- Jaoui, M. and Kamens, R. M.: Mass balance of gaseous and particulate products analysis from  $\alpha$ -pinene/ $NO_x$ /air in the presence of natural sunlight, *J. Geophys. Res.-Atmos.*, 106, 12541–12558, doi:10.1029/2001JD900005, 2001.
- Jorand, F., Heiss, A., Perrin, O., Sahetchian, K., Kerhoas, L., and Einhorn, J.: Isomeric hexyl-ketohydroperoxides formed by reactions of hexoxy and hexylperoxy radicals in oxygen, *Int. J. Chem. Kinet.*, 35, 354–366, doi:10.1002/kin.10136, 2003.
- Kavouras, I. G., Mihalopoulos, N., and Stephanou, E. G.: Formation of atmospheric particles from organic acids produced by forests, *Nature (London)*, 395, 683–686, 1998.
- Kavouras, I. G., Mihalopoulos, N., and Stephanou, E. G.: Formation and gas/particle partitioning of monoterpenes photo-oxidation products over forests, *Geophys. Res. Lett.*, 26, 55–58, doi:10.1029/1998GL900251, 1999.
- Keywood, M. D., Varutbangkul, V., Bahreini, R., Flagan, R. C., and Seinfeld, J. H.: Secondary organic aerosol formation from the ozonolysis of cycloalkenes and related compounds, *Environ. Sci. Technol.*, 38, 4157–4164, 2004.
- Kwok, E. S. C. and Atkinson, R.: Estimation of hydroxyl radical reaction rate constants for gas-phase organic compounds using a structure-reactivity relationship: an update, *Atmos. Environ.*, 29, 1685–1695, 1995.
- Laaksonen, A., Kulmala, M., O'Dowd, C. D., Joutsensaari, J., Vaattovaara, P., Mikkonen, S., Lehtinen, K. E. J., Sogacheva, L., Dal Maso, M., Aalto, P., Petäjä, T., Sogachev, A., Yoon, Y. J., Lihavainen, H., Nilsson, D., Facchini, M. C., Cavalli, F., Fuzzi, S., Hoffmann, T., Arnold, F., Hanke, M., Sellegri, K., Umann, B., Junkermann, W., Coe, H., Allan, J. D., Alfarra, M. R., Worsnop, D. R., Riekkola, M.-L., Hyötyläinen, T., and Viisanen, Y.: The role of VOC oxidation products in continental new particle formation, *Atmos. Chem. Phys.*, 8, 2657–2665, doi:10.5194/acp-8-2657-2008, 2008.
- Larsen, B. R., Di Bella, D., Glasius, M., Winterhalter, R., Jensen, N. R., and Hjorth, J.: Gas-phase OH oxidation of monoterpenes: Gaseous and particulate products, *J. Atmos. Chem.*, 38, 231–276, 2001.
- Lee, A., Goldstein, A. H., Kroll, J. H., Ng, N. L., Varutbangkul, V., Flagan, R. C., and Seinfeld, J. H.: Gas-phase products and secondary aerosol yields from the photooxidation of 16 different terpenes, *J. Geophys. Res.-Atmos.*, 111, D17305, doi:10.1029/2006JD007050, 2006.
- Lelieveld, J., Butler, T. M., Crowley, J. N., Dillon, T. J., Fischer, H., Ganzeveld, L., Harder, H., Lawrence, M. G., Martinez, M., Taraborrelli, D., and Williams, J.: Atmospheric oxidation capacity sustained by a tropical forest, *Nature*, 452, 737–740, 2008.
- Librando, V. and Tringali, G.: Atmospheric fate of OH initiated oxidation of terpenes. Reaction mechanism of  $\alpha$ -pinene degradation and secondary organic aerosol formation, *J. Environ. Manage.*, 75, 275–282, 2005.
- Monks, P. S., Granier, C., Fuzzi, S., Stohl, A., Williams, M. L., Akimoto, H., Amann, M., Baklanov, A., Baltensperger, U., Bey, I., Blake, N., Blake, R. S., Carslaw, K., Cooper, O. R., Dentener, F., Fowler, D., Fragkou, E., Frost, G. J., Generoso, S., Ginoux, P., Grewe, V., Guenther, A., Hansson, H. C., Henne, S., Hjorth, J., Hofzumahaus, A., Huntrieser, H., Isaksen, I. S. A., Jenkin, M. E., Kaiser, J., Kanakidou, M., Klimont, Z., Kulmala, M., Laj, P., Lawrence, M. G., Lee, J. D., Lioussé, C., Maione, M., McFiggans, G., Metzger, A., Mieville, A., Moussiopoulos, N., Orlando, J. J., O'Dowd, C. D., Palmer, P. I., Parrish, D. D., Petzold, A., Platt, U., Pöschl, U., Prevot, A. S. H., Reeves, C. E., Reimann, S., Rudich, Y., Sellegri, K., Steinbrecher, R., Simpson, D., ten Brink, H., Theloke, J., van der Werf, G. R., Vautard, R., Vestreng, V., Vlachokostas, C., and von Glasow, R.: Atmospheric composition change – global and regional air quality, *Atmos. Environ.*, 43, 5268–5350, 2009.

- Müller, L., Reinnig, M.-C., Naumann, K. H., Saathoff, H., Mentel, T. F., Donahue, N. M., and Hoffmann, T.: Formation of 3-methyl-1,2,3-butanetricarboxylic acid via gas phase oxidation of pinonic acid – a mass spectrometric study of SOA aging, *Atmos. Chem. Phys.*, 12, 1483–1496, doi:10.5194/acp-12-1483-2012, 2012.
- Nguyen, T. L., Vereecken, L., and Peeters, J.: HO<sub>x</sub> Regeneration in the Oxidation of Isoprene III: Theoretical Study of the key Isomerisation of the Z-delta-hydroxyperoxy Isoprene Radicals, *Chem. Phys. Chem.*, 11, 3996–4001, doi:10.1002/cphc.201000480, 2010.
- Niki, H., Maker, P. D., Savage, C. M., and Breitenbach, L. P.: A Fourier transform infrared study of the kinetics and mechanism for the reaction hydroxyl + methyl hydroperoxide, *J. Phys. Chem.*, 87, 2190–2193, 1983.
- Noell, A. C., Alconcel, L. S., Robichaud, D. J., Okumura, M., and Sander, S. P.: Near-Infrared kinetic spectroscopy of the HO<sub>2</sub> and C<sub>2</sub>H<sub>5</sub>O<sub>2</sub> self-reactions and cross reactions, *J. Phys. Chem. A*, 114, 6983–6995, 2010.
- Noziere, B., Barnes, I., and Becker, K.-H.: Product study and mechanisms of the reactions of alpha -pinene and of pinonaldehyde with OH radicals, *J. Geophys. Res.-Atmos.*, 104, 23645–23656, doi:10.1029/1999JD900778, 1999.
- Paulot, F., Crounse, J. D., Kjaergaard, H. G., Kroll, J. H., Seinfeld, J. H., and Wennberg, P. O.: Isoprene photooxidation: new insights into the production of acids and organic nitrates, *Atmos. Chem. Phys.*, 9, 1479–1501, doi:10.5194/acp-9-1479-2009, 2009a.
- Paulot, F., Crounse, J. D., Kjaergaard, H. G., Kurten, A., St. Clair, J. M., Seinfeld, J. H., and Wennberg, P. O.: Unexpected epoxide formation in the gas-phase photooxidation of isoprene, *Science*, 325, 730–733, 2009b.
- Peeters, J. and Müller, J. F.: HO<sub>x</sub> radical regeneration in isoprene oxidation via peroxy radical isomerisations. II: experimental evidence and global impact, *Phys. Chem. Chem. Phys.*, 12, 14227–14235, doi:10.1039/C0CP00811G, 2010.
- Peeters, J., Nguyen, T. L., and Vereecken, L.: HO<sub>x</sub> radical regeneration in the oxidation of isoprene, *Phys. Chem. Chem. Phys.*, 11, 5935–5939, 2009.
- Perrin, O., Heiss, A., Doumenc, F., and Sahetchian, K.: Homogeneous and heterogeneous reactions of the n-C<sub>5</sub>H<sub>11</sub>O, n-C<sub>5</sub>H<sub>10</sub>OH and OOC<sub>5</sub>H<sub>10</sub>OH radicals in oxygen. Analytical-steady state solution by use of the Laplace transform, *J. Chem. Soc. Faraday T*, 94, 2323–2335, doi:10.1039/a803340d, 1998.
- Pye, H. O. T., Chan, A. W. H., Barkley, M. P., and Seinfeld, J. H.: Global modeling of organic aerosol: the importance of reactive nitrogen (NO<sub>x</sub> and NO<sub>3</sub>), *Atmos. Chem. Phys.*, 10, 11261–11276, doi:10.5194/acp-10-11261-2010, 2010.
- Raventós-Duran, M. T., Percival, C. J., McGillen, M. R., Hamer, P. D., and Shallcross, D. E.: Kinetics and branching ratio studies of the reaction of C<sub>2</sub>H<sub>5</sub>O<sub>2</sub> + HO<sub>2</sub> using chemical ionization mass spectrometry, *Phys. Chem. Chem. Phys.*, 9, 4338–4348, doi:10.1039/B703038J, 2007.
- Ren, X., Olson, J. R., Crawford, J. H., Brune, W. H., Mao, J., Long, R. B., Chen, Z., Chen, G., Avery, M. A., Sachse, G. W., Barrick, J. D., Diskin, G. S., Huey, L. G., Fried, A., Cohen, R. C., Heikes, B., Wennberg, P. O., Singh, H. B., Blake, D. R., and Shetter, R. E.: HO<sub>x</sub> chemistry during INTEX-A 2004: observation, model calculation, and comparison with previous studies, *J. Geophys. Res.-Atmos.*, 113, D05310, doi:10.1029/2007JD009166, 2008.
- Sander, S. P., Finlayson-Pitts, B. J., Friedl, R. R., Golden, D. M., Huie, R. E., Kolb, C. E., Kurylo, M. J., Molina, M. J., Moortgat, G. K., Orkin, V. L., and Ravishankara, A. R.: Chemical kinetics and photochemical data for use in atmospheric studies, evaluation number 15, Tech. rep., Jet Propulsion Laboratory, 2006.
- Saunders, S. M., Jenkin, M. E., Derwent, R. G., and Pilling, M. J.: Protocol for the development of the Master Chemical Mechanism, MCM v3 (Part A): tropospheric degradation of non-aromatic volatile organic compounds, *Atmos. Chem. Phys.*, 3, 161–180, doi:10.5194/acp-3-161-2003, 2003.
- St. Clair, J. M., McCabe, D. C., Crounse, J. D., Steiner, U., and Wennberg, P. O.: Chemical ionization tandem mass spectrometer for the in situ measurement of methyl hydrogen peroxide, *Rev. Sci. Instrum.*, 81, 094102, doi:10.1063/1.3480552, 2010.
- Steinbrecher, R., Smiatek, G., Koeble, R., Seufert, G., Theloke, J., Hauff, K., Ciccioli, P., Vautard, R., and Curci, G.: Intra- and inter-annual variability of VOC emissions from natural and semi-natural vegetation in Europe and neighbouring countries, *Atmos. Environ.*, 43, 1380–1391, 2009.
- Szmigielski, R., Surratt, J. D., Gomez-Gonzalez, Y., Van der Veken, P., Kourtchev, I., Vermeylen, R., Blockhuys, F., Jaoui, M., Kleindienst, T. E., Lewandowski, M., Offenberg, J. H., Edney, E. O., Seinfeld, J. H., Maenhaut, W., and Claeys, M.: 3-methyl-1,2,3-butanetricarboxylic acid: an atmospheric tracer for terpene secondary organic aerosol, *Geophys. Res. Lett.*, 34, L24811, doi:10.1029/2007GL031338, 2007.
- Taylor, W. D., Allston, T. D., Moscato, M. J., Fazekas, G. B., Kozlowski, R., and Takacs, G. A.: Atmospheric photo-dissociation lifetimes for nitromethane, methyl nitrite, and methyl nitrate, *Int. J. Chem. Kinet.*, 12, 231–240, doi:10.1002/kin.550120404, 1980.
- Vaghjani, G. L. and Ravishankara, A. R.: Kinetics and mechanism of OH reaction with CH<sub>3</sub>OOH, *J. Phys. Chem.*, 93, 1948–1959, 1989.
- Vereecken, L. and Peeters, J.: Enhanced H-atom abstraction from pinonaldehyde, pinonic acid, pinic acid, and related compounds: theoretical study of C-H bond strengths, *Phys. Chem. Chem. Phys.*, 4, 467–472, doi:10.1039/B109370C, 2002.
- Vereecken, L., Müller, J. F., and Peeters, J.: Low-volatility poly-oxygenates in the OH-initiated atmospheric oxidation of alpha-pinene: impact of non-traditional peroxy radical chemistry, *Phys. Chem. Chem. Phys.*, 9, 5241–5248, doi:10.1039/B708023A, 2007.
- Wang, C. and Chen, Z.: An experimental study for rate constants of the gas phase reactions of CH<sub>3</sub>CH<sub>2</sub>OOH with OH radicals, O<sub>3</sub>, NO<sub>2</sub> and NO, *Atmos. Environ.*, 42, 6614–6619, 2008.
- Wisthaler, A., Jensen, N. R., Winterhalter, R., Lindinger, W., and Hjorth, J.: Measurements of acetone and other gas phase product yields from the OH-initiated oxidation of terpenes by proton-transfer-reaction mass spectrometry (PTR-MS), *Atmos. Environ.*, 35, 6181–6191, 2001.
- Wolfe, G. M., Thornton, J. A., Bouvier-Brown, N. C., Goldstein, A. H., Park, J.-H., McKay, M., Matross, D. M., Mao, J., Brune, W. H., LaFranchi, B. W., Browne, E. C., Min, K.-E., Wooldridge, P. J., Cohen, R. C., Crounse, J. D., Faloona, I. C., Gilman, J. B., Kuster, W. C., de Gouw, J. A., Huisman, A., and Keutsch, F. N.: The Chemistry of Atmosphere-Forest Exchange (CAFE) Model – Part 2: Application to BEARPEX-2007 observations, *Atmos. Chem. Phys.*, 11, 1269–1294, doi:10.5194/acp-11-1269-2011, 2011.

Yu, J., Griffin, R. J., Cocker, David R., I., Flagan, R. C., Seinfeld, J. H., and Blanchard, P.: Observation of gaseous and particulate products of monoterpene oxidation in forest atmospheres, *Geophys. Res. Lett.*, 26, 1145–1148, doi:10.1029/1999GL900169, 1999.

Zhang, Y. Y., Müller, L., Winterhalter, R., Moortgat, G. K., Hoffmann, T., and Pöschl, U.: Seasonal cycle and temperature dependence of pinene oxidation products, dicarboxylic acids and nitrophenols in fine and coarse air particulate matter, *Atmos. Chem. Phys.*, 10, 7859–7873, doi:10.5194/acp-10-7859-2010, 2010.

## Appendix C

# $\alpha$ -Pinene Photooxidation Under Controlled Chemical Conditions - Part 2: SOA Yield and Composition in Low- and High-NO<sub>x</sub> Environments\*

---

\*Reproduced with permission from “ $\alpha$ -pinene photooxidation under controlled chemical conditions - Part 2: SOA yield and composition in low- and high-NO<sub>x</sub> environments” by N. C. Eddingsaas, C. L. Loza, L. D. Yee, M. Chan, K. A. Schilling, P. S. Chhabra, J. H. Seinfeld, and P. O. Wennberg, *Atmos. Chem. Phys.*, 12, 7413-7427, doi:10.5194/acp-12-7413-2012. Copyright 2012 by the Authors. This work is distributed under the Creative Commons Attribution 3.0 License.



## **$\alpha$ -pinene photooxidation under controlled chemical conditions – Part 2: SOA yield and composition in low- and high-NO<sub>x</sub> environments**

N. C. Eddingsaas<sup>1</sup>, C. L. Loza<sup>1</sup>, L. D. Yee<sup>2</sup>, M. Chan<sup>2</sup>, K. A. Schilling<sup>1</sup>, P. S. Chhabra<sup>1,\*</sup>, J. H. Seinfeld<sup>1,2</sup>, and  
 P. O. Wennberg<sup>2,3</sup>

<sup>1</sup>Division of Chemistry and Chemical Engineering, California Institute of Technology, Pasadena, CA, USA

<sup>2</sup>Division of Engineering and Applied Science, California Institute of Technology, Pasadena, CA, USA

<sup>3</sup>Division of Geological and Planetary Sciences, California Institute of Technology, Pasadena, CA, USA

\* now at: Aerodyne Research Inc, Billerica, MA, USA

Correspondence to: N. C. Eddingsaas (eddingsa@caltech.edu)

Received: 2 March 2012 – Published in Atmos. Chem. Phys. Discuss.: 4 April 2012

Revised: 26 July 2012 – Accepted: 30 July 2012 – Published: 16 August 2012

**Abstract.** The gas-phase oxidation of  $\alpha$ -pinene produces a large amount of secondary organic aerosol (SOA) in the atmosphere. A number of carboxylic acids, organosulfates and nitrooxy organosulfates associated with  $\alpha$ -pinene have been found in field samples and some are used as tracers of  $\alpha$ -pinene oxidation.  $\alpha$ -pinene reacts readily with OH and O<sub>3</sub> in the atmosphere followed by reactions with both HO<sub>2</sub> and NO. Due to the large number of potential reaction pathways, it can be difficult to determine what conditions lead to SOA. To better understand the SOA yield and chemical composition from low- and high-NO<sub>x</sub> OH oxidation of  $\alpha$ -pinene, studies were conducted in the Caltech atmospheric chamber under controlled chemical conditions. Experiments used low O<sub>3</sub> concentrations to ensure that OH was the main oxidant and low  $\alpha$ -pinene concentrations such that the peroxy radical (RO<sub>2</sub>) reacted primarily with either HO<sub>2</sub> under low-NO<sub>x</sub> conditions or NO under high-NO<sub>x</sub> conditions. SOA yield was suppressed under conditions of high-NO<sub>x</sub>. SOA yield under high-NO<sub>x</sub> conditions was greater when ammonium sulfate/sulfuric acid seed particles (highly acidic) were present prior to the onset of growth than when ammonium sulfate seed particles (mildly acidic) were present; this dependence was not observed under low-NO<sub>x</sub> conditions. When aerosol seed particles were introduced after OH oxidation, allowing for later generation species to be exposed to fresh inorganic seed particles, a number of low-NO<sub>x</sub> products partitioned to the highly acidic aerosol. This indicates that the effect of

seed acidity and SOA yield might be under-estimated in traditional experiments where aerosol seed particles are introduced prior to oxidation. We also identify the presence of a number of carboxylic acids that are used as tracer compounds of  $\alpha$ -pinene oxidation in the field as well as the formation of organosulfates and nitrooxy organosulfates. A number of the carboxylic acids were observed under all conditions, however, pinic and pinonic acid were only observed under low-NO<sub>x</sub> conditions. Evidence is provided for particle-phase sulfate esterification of multi-functional alcohols.

### **1 Introduction**

Biogenically emitted monoterpenes are important to atmospheric organic aerosol concentration and composition due to their large emission rates and high secondary organic aerosol (SOA) yields (Guenther et al., 1995; Hoffmann et al., 1997; Chung and Seinfeld, 2002; Pye et al., 2010). Of the monoterpenes,  $\alpha$ -pinene is the most abundantly emitted. Many carboxylic acids, organonitrates, and organosulfates associated with  $\alpha$ -pinene have been observed in aerosols both in the field and from laboratory oxidation (Kavouras et al., 1998, 1999; Yu et al., 1999b; Jaoui and Kamens, 2001; Larsen et al., 2001; Librando and Tringali, 2005; Surratt et al., 2007, 2008; Laaksonen et al., 2008; Zhang et al., 2010). A number of carboxylic acids have been used as particle-phase

tracers of  $\alpha$ -pinene oxidation, including pinonic acid, pinic acid, 10-hydroxypinonic acid, terpenylic acid, diaterpenylic acid acetate, and 3-methyl-1,2,3-butanetricarboxylic acid (3-MBTCA). For instance, pinonic and pinic acid have been observed to be in high concentration in aerosols collected in Portugal (accounting for 18–40 % of fine particle mass), in Greece (up to 26 % of fine particle mass), as well as in high yield in Finland (Kavouras et al., 1998, 1999; Anttila et al., 2005).

In the troposphere,  $\alpha$ -pinene is oxidized approximately equally by OH and  $O_3$  during the daytime (Capouet et al., 2008). During the nighttime,  $NO_3$  is the most important oxidant of  $\alpha$ -pinene worldwide and oxidation by  $NO_3$  can be important during the daytime under conditions of elevated  $NO_x$  (Spittler et al., 2006). After reaction with the oxidant, the peroxy radicals that are formed can react with a number of species, including  $HO_2$ , NO,  $NO_2$  and other peroxy radicals ( $RO_2$ ). Depending on the nature of the reactant with the peroxy radical, different oxidation products are produced in the gas phase. This was demonstrated in Part 1 of this series of papers (Eddingsaas et al., 2012). It was determined that pinonaldehyde is an important oxidation product under both low- and high- $NO_x$  conditions. The formation of pinonaldehyde from low- $NO_x$  OH oxidation implies that the reaction of  $\alpha$ -pinene hydroxy hydroperoxy radical and  $HO_2$  has a channel that produces an alkoxy radical and recycles OH. This type of reaction channel has been shown to be important only for acyl peroxy radicals and possibly toluene. In addition, it was demonstrated that number of organic acids formed from low- $NO_x$  OH oxidation, including pinonic acid and pinonic peracid, are not formed from high- $NO_x$  OH oxidation. From a modeling standpoint, it is of interest to understand how the different gas-phase reaction mechanisms influence the particle-phase composition and concentration. This understanding will improve the ability to accurately simulate the amount of aerosol produced in the oxidation of  $\alpha$ -pinene.

In this study, we describe the SOA yield and particle phase composition from the photooxidation of  $\alpha$ -pinene under conditions where the peroxy radical chemistry is known. We focus on OH photooxidation because particle-phase composition from ozonolysis of  $\alpha$ -pinene has been extensively studied (Glasius et al., 1999; Yu et al., 1999a; Iinuma et al., 2005; Presto et al., 2005; Ma et al., 2008; Shilling et al., 2009). The SOA composition from OH photooxidation has been much less studied and there are almost no studies examining low- $NO_x$  conditions (Noziere et al., 1999; Ng et al., 2007a; Claeys et al., 2009). We discuss SOA composition focusing on several carboxylic acids which have been used as tracers of  $\alpha$ -pinene oxidation. The formation of organosulfates and nitrooxy organosulfates formed from  $\alpha$ -pinene photooxidation is also addressed. We compare SOA and gas-phase composition based on different peroxy radical reactants as well as different aerosol seed (i.e. no seed, ammonium sulfate (AS) seed, and ammonium sulfate and sulfuric acid (AS+SA) seed).

## 2 Experimental

Photooxidation experiments of  $\alpha$ -pinene and pinonaldehyde were performed in the Caltech dual 28 m<sup>3</sup> Teflon chambers. Details of the chamber facilities have been described elsewhere (Cocker et al., 2001; Keywood et al., 2004). Prior to each run, the chamber was flushed for a minimum of 24 h with dry purified air. While being flushed, the chamber was irradiated with the chamber lights for a minimum of six hours. The temperature, relative humidity, and concentrations of  $O_3$ , NO, and  $NO_x$  (NO and  $NO_2$ ) were continuously monitored. In all experiments the RH was kept below 10 %. Aerosol size distribution and number concentration were measured continuously by a differential mobility analyzer (DMA, TSI model 3081) coupled to a condensation nucleus counter (TSI model 3760). Aerosol growth data were corrected for size dependent wall-loss (Keywood et al., 2004; Ng et al., 2007b).

Experiments were performed under low- and high- $NO_x$  conditions. Under low- $NO_x$  conditions, photolysis of hydrogen peroxide ( $H_2O_2$ ) was the OH source, while for the high- $NO_x$  experiments the photolysis of nitrous acid (HONO) or methyl nitrite ( $CH_3ONO$ ) produced OH. For low- $NO_x$  experiments, 280  $\mu$ l of 50 wt %  $H_2O_2$  was injected into the chamber, resulting in a concentration  $\sim 4$  ppm. Using HONO and  $CH_3ONO$  allowed the ratio of NO to  $NO_2$  to be varied, with a lower ratio in the  $CH_3ONO$  experiments. For the remainder of this paper, the use of HONO as the OH source will be referred to as high-NO and the use of methyl nitrite will be referred to as high- $NO_2$  to distinguish between the relative importance of NO and  $NO_2$ .

HONO was prepared daily by dropwise addition of 15 ml of 1 wt %  $NaNO_2$  into 30 ml of 10 wt %  $H_2SO_4$  in a glass bulb, and then introduced into the chamber with dry air. This process produces NO and  $NO_2$  as side products, which are also introduced to the chamber.  $CH_3ONO$  was synthesized, purified, and stored according to the procedure outlined by Taylor et al. (1980).  $CH_3ONO$  was warmed from liquid nitrogen temperatures and vaporized into an evacuated 500 ml glass bulb and introduced into the chamber with an air stream of 5 l min<sup>-1</sup>. After addition of  $CH_3ONO$ , 300–400 ppb of NO was added to the chamber to suppress the formation of  $O_3$ . Determination of exact NO and  $NO_2$  concentrations using the commercial  $NO_x$  monitor was precluded due to interferences by both HONO and  $CH_3ONO$ . While the exact NO and  $NO_2$  concentration could not be determined, it was confirmed that greater  $NO_2$  concentration and the ratio of  $NO_2$  to NO is greater in the methyl nitrite experiments due to the increased gas-phase concentration of nitric acid and peroxyacyl nitrates (PANs). The gas-phase concentration of nitric acid and PANs in the methyl nitrite experiments was 1.4–2 times that in similar HONO experiments. At the start of all high- $NO_x$  experiments the total  $NO_x$  reading (NO,  $NO_x$ , and interference from HONO or  $CH_3ONO$ ) was 800 ppb and NO

concentration throughout the experiments was such that the concentration of  $O_3$  never exceeded 5 ppb.

Experiments were performed with either no aerosol seed present, ammonium sulfate seed (AS), or ammonium sulfate plus sulfuric acid (AS + SA). The AS + SA produced a much more acidic aerosol seed. When applicable, seed particles were added to the chamber after the addition of the oxidant. Aerosol seed particles were generated by atomizing an aqueous solution of 15 mM  $(NH_4)_2SO_4$  (AS) or 15 mM  $(NH_4)_2SO_4$  and 15 mM  $H_2SO_4$  (AS + SA). Upon addition of an aerosol seed, the initial aerosol number concentration was  $\sim 1.8 \times 10^4 \text{ cm}^{-3}$ , with a mean diameter of  $\sim 60 \text{ nm}$ , resulting in the initial aerosol volume of  $10\text{--}15 \mu\text{m}^3 \text{ cm}^{-3}$ .

Once the aerosol seed was added and stable,  $\alpha$ -pinene was added to the chamber by transferring a known amount of  $\alpha$ -pinene from a small glass bulb to achieve a concentration of 20–50 ppb. The mixing ratio of  $\alpha$ -pinene was monitored with a gas chromatograph (Agilent 6890N) coupled with a flame ionization detector (GC-FID). The GC-FID was calibrated for  $\alpha$ -pinene using a standard prepared in a 551 Teflon bag. In photooxidation experiments where pinonaldehyde was the initial hydrocarbon, pinonaldehyde was introduced into the chamber by passing dry nitrogen over a liquid sample.

Gas-phase photooxidation products were monitored by a custom-modified Varian 1200 triple-quadrupole chemical ionization mass spectrometer (CIMS) (St. Clair et al., 2010). Details of the operation of the CIMS can be found in a number of previous reports (Crounse et al., 2006; Paulot et al., 2009a; St. Clair et al., 2010). The CIMS was operated in negative ion mode using  $CF_3O^-$  as the reagent ion, and in the positive ion mode using  $H_3O^+$  for proton transfer mass spectrometry (PTR-MS). In negative mode,  $CF_3O^-$  is sensitive to polar and acidic compounds by either clustering with the analyte (R) resulting in an ion with a mass-to-charge ratio ( $m/z$ )  $MW + 85$  ( $R \cdot CF_3O^-$ ) or via fluorine ion transfer resulting in  $m/z$   $MW + 19$  ( $HF \cdot R_{-H}^-$ ). The dominant ionization mechanism depends mostly on the acidity of the neutral species; highly acidic species such as nitric acid form only the fluorine transfer ion, while non-acidic species such as methyl hydrogen peroxide form only the cluster ion. This separation aids both in the determination of the structure of a molecule and in the identification of isomers. In negative mode, tandem mass spectrometry (MS/MS) was used to help identify functional groups of an analyte. In brief, a parent ion selected in the first quadrupole is exposed to an elevated pressure of  $N_2$  resulting in collision-induced dissociation (CID) in the second quadrupole, and the resulting fragmentation ions are detected in the third quadrupole. Molecules with different functional groups have been shown to fragment differently by CID. For example, fragmentation of hydroperoxides form a characteristic anion at  $m/z$  63 (Paulot et al., 2009b). Unfortunately, authentic standards for most compounds described here are not readily available, and thus the sensitivity of the CIMS cannot be experimentally determined. In the absence of such standards, we estimate that the sensitivity scales with

the thermal capture rate and the binding energy of the cluster ( $VOC \cdot CF_3O^-$ ). Details on calculating the sensitivity of the CIMS to a given analyte can be found in previous publications (Paulot et al., 2009a,b).

Duplicate Teflon filters (PALL Life Sciences, 47 mm diameter,  $1.0 \mu\text{m}$  pore size, Teflon membrane) were collected from each of the chamber experiments for off-line chemical analysis. Filter sampling was started when the aerosol volume reached a constant value. For the chemical analysis, each filter was extracted with methanol (LC-MS CHROMASOLV-grade, Sigma-Aldrich) under ultrasonication for 45 min. The extract was dried under ultra-pure nitrogen gas, and the residue was reconstituted with a 50 : 50 (*v/v*) solvent mixture of methanol with 0.1 % acetic acid (LC-MS CHROMASOLV-grade, Sigma-Aldrich) and water with 0.1 % acetic acid (LC-MS CHROMASOLV-grade, Sigma-Aldrich). Filter sample extracts were analyzed by ultra-performance liquid chromatography/electrospray ionization-time-of-flight mass spectrometry (UPLC/ESI-TOFMS) operated in negative ion mode. Further details of the filter collection, sample preparation procedures, and UPLC/ESI-TOFMS analysis can be found in a previous publications (Surratt et al., 2008; Chan et al., 2010).

Products having either a carboxylic acid group or that are organosulfates can be ionized via deprotonation and are detected in the negative ion mode as  $[M - H]^-$  ions. All accurate mass measurements were within  $\pm 5 \text{ mDa}$  of the theoretical mass associated with the proposed chemical formula. From repeated UPLC/ESI-TOFMS measurements, the variations in the chromatographic peak areas are about 5 % (Chan et al., 2011). The concentrations are not corrected for extraction efficiencies.

High-resolution time-of-flight aerosol mass spectrometry (HR-ToF-AMS) spectra were obtained for one low- $NO_x$  experiment with AS seed and one high- $NO_x$  experiment with AS seed. The analysis of the data has previously been reported (Chhabra et al., 2011). Both high-resolution W-mode and higher sensitivity V-mode were taken, switching between the two modes every minute. The V-mode data were analyzed using a fragmentation table that enables separation of sulfate, ammonium, and organic components and to time-trace specific mass-to-charge ratios ( $m/z$ ) (Allan et al., 2004). W-mode data were analyzed using the high-resolution spectra toolbox, PIKA, to determine the chemical formulas contributing to distinct  $m/z$  (DeCarlo et al., 2006).

### 3 Results and discussion

In Part 1 (Eddingsaas et al., 2012), the gas-phase composition of OH photooxidation of  $\alpha$ -pinene under low- $NO_x$ , high-NO (HONO as the OH source), and high- $NO_2$  (methyl nitrite as the OH source) conditions was discussed. Under low- $NO_x$  conditions, care was taken to ensure that reaction with  $HO_2$  dominated the loss of the peroxy radicals.  $O_3$  was suppressed



in all experiments so that the oxidation of  $\alpha$ -pinene was completely dominated by OH oxidation. Here, the results of the aerosol phase growth, yield, and composition from these controlled experiments are discussed.

### 3.1 Aerosol growth and yield

Table 1 lists the experimental conditions of the studies, the SOA yields, and a number of other variables of interest. The SOA density used to calculate SOA mass and SOA yield were taken from previous results:  $1.32 \text{ g cm}^{-3}$  under low- $\text{NO}_x$  conditions and  $1.33 \text{ g cm}^{-3}$  under high- $\text{NO}_x$  conditions (Ng et al., 2007a). SOA yield is calculated cumulatively throughout the experiments as the ratio of SOA mass to the mass of  $\alpha$ -pinene reacted. For this suite of experiments, we cannot directly relate the time-dependent aerosol growth curves (i.e. SOA mass as a function of experiment time) to yield because the OH concentration varied widely between the systems. For example, the initial OH concentration for the low- $\text{NO}_x$  experiments was  $\sim 2 \times 10^6 \text{ molecules cm}^{-3}$ , while in the high-NO experiments the initial OH was approximately 3 times larger, and under high- $\text{NO}_2$  conditions the initial OH was an order of magnitude larger, thereby resulting in much faster oxidation of  $\alpha$ -pinene and faster aerosol growth. In addition, under both high-NO and high- $\text{NO}_2$  conditions, the OH concentration declined significantly over time. The OH concentration through the experiments was determined by comparing the loss of  $\alpha$ -pinene to a kinetic model of  $\alpha$ -pinene OH oxidation under low- or high- $\text{NO}_x$  conditions. Details of the model and gas phase measurements can be found in Part 1 (Eddingsaas et al., 2012). By using OH exposure (as units of OH concentration multiplied by reaction time in hours) as the coordinate system, a more direct comparison between different photooxidation systems is, however, possible.

Figure 1 shows SOA yield as a function of OH exposure from all experiments in the presence of AS seed particles. The overall yield was consistent between runs with the same OH source, but there is a systematic difference in SOA yield between the systems, decreasing as the concentration of NO increases. SOA growth under high- $\text{NO}_2$  conditions resembles low- $\text{NO}_x$  SOA growth more than it does high-NO SOA growth, consistent with the hypothesis that reaction of the peroxy radicals with NO leads to reduced yields. Second, the SOA yield from high- $\text{NO}_2$  continued to increase after two  $\alpha$ -pinene lifetimes. This is in contrast to the high-NO experiments where most of the aerosol growth is complete after one  $\alpha$ -pinene lifetime. The SOA from low- $\text{NO}_x$  photooxidation also continued to increase after two  $\alpha$ -pinene lifetimes. This indicates that later generation oxidation products are important in determining the amount of SOA formed. As discussed in the gas-phase analysis (Eddingsaas et al., 2012), a distinct difference in the later generation oxidation products is the formation of carboxylic acids and peracids in the low- $\text{NO}_x$

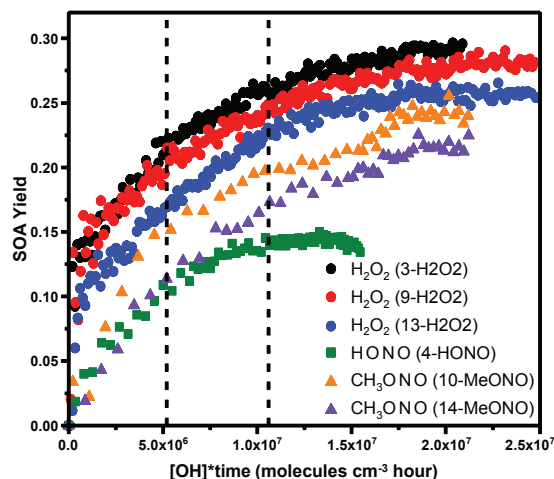


**Fig. 1.** SOA yield as a function of OH exposure of  $\alpha$ -pinene from low- $\text{NO}_x$ , high-NO, and high- $\text{NO}_2$  OH oxidation in the presence of ammonium sulfate seed particles. The vertical dashed lines represent one and two  $\alpha$ -pinene lifetimes with respect to reaction with OH. The OH source and sample ID for each experiment is shown in the figure.

photooxidation. In the high- $\text{NO}_2$  cases, more PANs and nitric acid are formed compared to high-NO.

Illustrating that later generation oxidation products are important to SOA growth, the gas-phase time traces of first- and second-generation oxidation products are shown along with the SOA growth under all three conditions in the presence of ammonium sulfate seed in Fig. 2. Under all conditions, aerosol growth continues through the production of second-generation oxidation products. Under low- $\text{NO}_x$  conditions, the signal for pinonaldehyde peracid and/or 10-hydroxypinonic acid is lost from the gas phase faster than pinonic acid. This is likely due to greater partitioning into the aerosol phase as a result of its lower vapor pressure. In the presence of high- $\text{NO}_2$ , pinonaldehyde PAN is observed to be lost from the gas phase faster than SOA growth as a result of thermal decomposition. Pinonaldehyde nitrate is lost at a faster rate when methyl nitrite is the OH source. This could be due to either higher OH exposure or aerosol uptake.

The effect of the acidity of the seed particle on SOA yield was investigated. Figure 3 shows the SOA yield as a function of OH exposure with no seed, and in the presence of either AS seed (mildly acidic) or AS+SA seed (highly acidic) in low- $\text{NO}_x$ , high-NO, and high- $\text{NO}_2$  OH oxidation. From low- $\text{NO}_x$  photooxidation with initial  $\alpha$ -pinene concentration of  $\sim 50 \text{ ppb}$ , there is no difference in the aerosol growth in the presence of no, AS, or AS+SA seed. This was expected as the only difference in the gas-phase composition is that  $\alpha$ -pinene oxide is in lower concentration in the presence of an

**Table 1.** SOA yields from low- and high-NO<sub>x</sub> photooxidation of  $\alpha$ -pinene.

Sample ID	Oxidant	Seed	Temp. (°C)	HC (ppb)	Initial Vol. ( $\mu\text{m}^3\text{cm}^{-3}$ )	$\Delta\text{HC}^a$ ( $\mu\text{g m}^{-3}$ )	$\Delta\text{M}_0^b$ ( $\mu\text{g m}^{-3}$ )	SOA Yield <sup>c</sup> (%)
1-H2O2	H <sub>2</sub> O <sub>2</sub>	no seed	20–23	45.0±1.0	0.9±0.3	250±6	66.8±6.0	26.7±2.5
2-HONO	HONO	no seed	20–23	50.1±1.1	0.3±.2	260±6	20.0±2.3	7.7±0.9
3-H2O2	H <sub>2</sub> O <sub>2</sub>	AS	20–25	48.5±1.1	11.0±0.4	265±6	76.6±6.7	28.9±2.6
4-HONO	HONO	AS	20–23	52.4±1.2	12.0±0.7	258±7	37.2±3.0	14.4±1.1
5-H2O2	H <sub>2</sub> O <sub>2</sub>	AS + SA	20–25	46.9±1.1	9.3±0.58	264±6	72.9±7.0	27.6±2.8
6-HONO	HONO	AS + SA	20–23	45.5±1.0	16.0±1.1	225±6	39.6±4.5	17.6±1.9
7-H2O2	H <sub>2</sub> O <sub>2</sub>	no seed	20–25	19.8±0.5	0.5±0.2	109±3	40.0±3.1	36.7±3.0
8-MeONO	CH <sub>3</sub> ONO	no seed	20–23	38.9±1.1	5.1±0.2	208±6	51.9±3.8	25.4±1.7
9-H2O2	H <sub>2</sub> O <sub>2</sub>	AS	20–25	46.8±1.1	9.4±0.4	254±6	71.6±6.2	28.2±2.5
10-MeONO	CH <sub>3</sub> ONO	AS	20–23	47.9±1.1	10.5±0.5	249±6	60.3±4.9	24.2±1.9
11-H2O2	H <sub>2</sub> O <sub>2</sub>	AS + SA	20–25	46.8±1.1	8.5±0.4	256±6	70.4±6.2	27.5±2.5
12-MeONO	CH <sub>3</sub> ONO	AS + SA	20–23	43.7	14	242	42.6	17.6
13-H2O2	H <sub>2</sub> O <sub>2</sub>	AS	20–25	45.0±1.0	13.7±0.6	247±6	63.5±5.6	25.7±2.3
14-MeONO	CH <sub>3</sub> ONO	AS	20–23	44.9±1	15.4±0.6	250±6	54.0±4.3	21.6±1.8

<sup>a</sup>  $\Delta\text{HC}$ : mass concentration of  $\alpha$ -pinene reacted.<sup>b</sup>  $\Delta\text{M}_0$ : mass concentration of SOA.<sup>c</sup> SOA yield is maximum mass concentration of SOA formed divided by the mass concentration of  $\alpha$ -pinene reacted.

acidic seed.  $\alpha$ -pinene oxide is a minor product. This indicates that there is almost no reactive uptake occurring due to acid-catalyzed reactions and that if there are any changes in the aerosol composition, they occur within the particle phase. SOA yield was different when the initial  $\alpha$ -pinene concentration was reduced to 20 ppb (37 % compared to 26–29 % when the initial concentration was 50 ppb). The cause of the increase in SOA yield with lower  $\alpha$ -pinene concentration is not known.

As with low-NO<sub>x</sub> photooxidation, there is no difference in aerosol growth under any seed conditions for high-NO<sub>2</sub> photooxidation. However, with high-NO, the yield does depend on seed conditions; yields increase from no seed to AS seed to AS + SA seed (increase of 22 % from AS to AS + SA seed). In the presence of AS+SA seed, the SOA yield was the same under high-NO and high-NO<sub>2</sub> conditions. This small increase with acidity is in contrast to low-NO<sub>x</sub> photooxidation of isoprene where the SOA increased markedly (1000 %) (Surratt et al., 2010).

Self-nucleation under high-NO conditions did not occur until nearly one  $\alpha$ -pinene lifetime. In contrast, nucleation occurred nearly immediately under both high-NO<sub>2</sub> and low-NO<sub>x</sub> conditions. One possible explanation for the difference in behavior is that for the aerosols in the higher NO<sub>2</sub> case, the self-nucleated and AS seeded aerosols are more acidic than in the low-NO<sub>2</sub> case due to increased partitioning of nitric acid and possibly the PANs. This would result in an acidic aerosol under all conditions for the higher NO<sub>2</sub> experiments. When AS + SA seed is used, the particles have the same level of acidity and partitioning should be more similar. Analysis of the particle-phase composition provides more insight into the differences between the systems.

### 3.2 Aerosol chemical composition

Tables 2 and 3 list the UPLC peak areas for each of the carboxylic acids associated with atmospheric photooxidation of  $\alpha$ -pinene under low-NO<sub>x</sub>, high-NO, and high-NO<sub>2</sub> conditions, in the presence of either AS or AS + SA seed. Figure 4 shows the structures of the identified SOA components. The peak areas are presented both as the raw peak areas (Table 2) as well as peak areas scaled to the SOA mass loading of the low-NO<sub>x</sub> AS seed run (Table 3), so that a weighted average of each component can be compared. Concentration calibrations were not performed and therefore the analysis is qualitative. Figure 5 shows the UPLC chromatograms from the filter samples from low-NO<sub>x</sub> OH oxidation in the presence of AS or AS + SA seed particles along with the chromatogram from pinonaldehyde low-NO<sub>x</sub> photooxidation, while Fig. 6 shows the UPLC chromatograms from high-NO and high-NO<sub>2</sub> OH oxidation in the presence of AS or AS + SA seed particles. The species of interest – pinonic acid, 10-hydroxy pinonic acid, pinic acid, terpenylic acid, 2-hydroxy terpenylic acid, diaterpenylic acid acetate, 3-MBTCA, the organosulfates and the nitrooxy organosulfates have previously been identified by UPLC/(-)ESI-TOFMS (Warnke et al., 2006; Szmigielski et al., 2007; Claeys et al., 2009), and it is these identifications that are being used to confirm the presence or absence of each species.

#### 3.2.1 Comparison of SOA composition between low-NO<sub>x</sub>, high-NO, and high-NO<sub>2</sub> OH oxidation in the presence of ammonium sulfate seed

Pinonic acid, pinic acid, and 10-hydroxy pinonic acid are only observed in substantial quantities in the aerosol phase

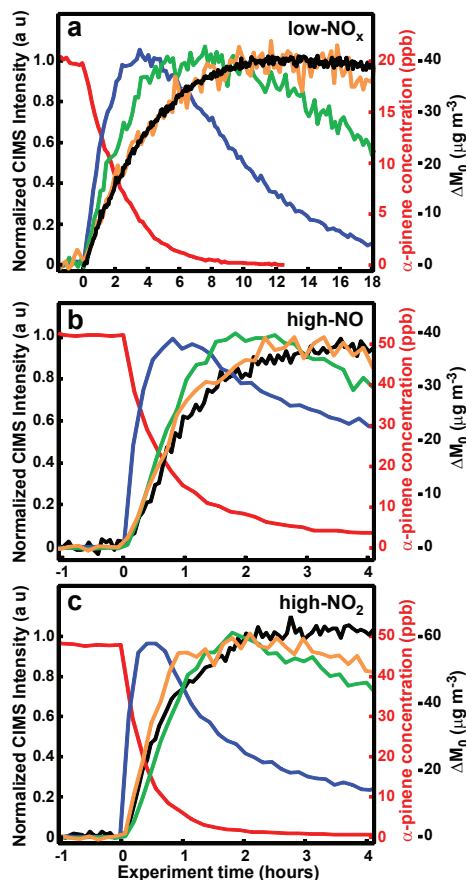


**Fig. 2.** Time evolution of SOA growth along with gas-phase time profile of first- and second-generation products of OH oxidation of  $\alpha$ -pinene under (a) low- $\text{NO}_x$  conditions (7-H $2\text{O}_2$ ), (b) high- $\text{NO}$  conditions (4-HONO), and (c) high- $\text{NO}_2$  conditions (10-MeONO). In all plots, the red line is  $\alpha$ -pinene, blue line is pinonaldehyde, and black line is SOA growth. In (a) green is 10-hydroxy pinonic/pinonic peracid and orange is pinonic acid, (b, c) green is pinonaldehyde-PAN, and orange is pinonaldehyde nitrate.

from the low- $\text{NO}_x$  photooxidation (Tables 2 and 3 and Fig. 5). This was expected as pinonic and 10-hydroxy pinonic acid were only observed in the gas-phase in the low- $\text{NO}_x$  photooxidation (Eddingsaas et al., 2012). These species originate from the oxidation of pinonaldehyde as confirmed by the gas-phase data (Eddingsaas et al., 2012) as well as the UPLC chromatogram of the low- $\text{NO}_x$  photooxidation of pinonaldehyde (Fig. 4c). Pinonic acid, pinic acid, and 10-hydroxy pinonic acid are also typical species found in SOA from the ozonolysis of  $\alpha$ -pinene (Hoffmann et al., 1997; Ma et al., 2008; Camredon et al., 2010). Thus, it is likely that previous observation of pinonic acid, pinic acid, and 10-hydroxy

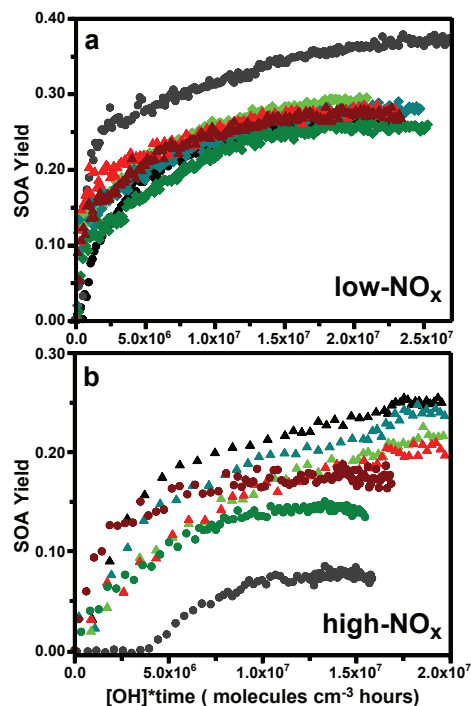


**Fig. 3.** SOA yield as a function of OH exposure of  $\alpha$ -pinene OH oxidation in the presence of no (black, gray), neutral (shades of green), or acidic (shades of red) seed particles under (a) low- $\text{NO}_x$  conditions and (b) high- $\text{NO}_x$  conditions where photolysis of HONO (dots) or methyl nitrite (triangles) is the OH source. The sample IDs for each experiment are (a) black dots (1-H $2\text{O}_2$ ), gray dots (7-H $2\text{O}_2$ ), light green diamonds (3-H $2\text{O}_2$ ), teal diamonds (9-H $2\text{O}_2$ ), green diamonds (13-H $2\text{O}_2$ ), red triangles (5-H $2\text{O}_2$ ), dark red triangles (11-H $2\text{O}_2$ ) (b) gray dots (2-HONO), black triangles (8-MeONO), green dots (4-HONO), light green triangles (10-MeONO), teal triangles (14-MeONO), dark red dots (6-HONO), and red triangles (12-MeONO). The low- $\text{NO}_x$  experiment that resulted in greater SOA yield (gray points in panel a (7-H $2\text{O}_2$ )) is from 20 ppb of  $\alpha$ -pinene, all other data is from the OH oxidation of  $\sim 50$  ppb of  $\alpha$ -pinene.

pinonic acid in studies of  $\alpha$ -pinene high- $\text{NO}_x$  photooxidation were a result of ozonolysis and not OH chemistry.

3-MBTCA is believed to be a tracer compound of  $\alpha$ -pinene derived SOA (Szmigielski et al., 2007; Kourtchev et al., 2009; Zhang et al., 2010) and indeed it was observed here under all conditions (as well as from the low- $\text{NO}_x$  photooxidation of pinonaldehyde). It has been proposed that 3-MBTCA is the result of further high- $\text{NO}_x$  oxidation of pinonic acid in the gas phase (Szmigielski et al., 2007; Müller et al., 2012). A recent study by Müller et al. (2012) shows evidence of gas-phase formation of 3-MBTCA from the photooxidation of pinonic acid in the presence of  $\text{NO}$ .

**Table 2.** Raw peak areas from UPLC chromatograms of carboxylic acids, organosulfates, and nitrooxy organosulfates from the photooxidation of  $\alpha$ -pinene.

SOA component ( $[M - H]^-$ )	H <sub>2</sub> O <sub>2</sub>		HONO		MeONO	
	AS	AS + SA	AS	AS + SA	AS	AS + SA
2-Hydroxyterpenylic acid (187)	–	–	1918	824	2285	1509
Terpenylic acid (171)	2097	2522	911	933	1152	1255
3-methyl-1,2,3-butanetricarboxylic acid (3-MBTCA) (203)	458	702	307	337	910	1231
Diaterpenylic acid acetate (231)	318	763	1984	401	1658	1728
10-Hydroxypinonic acid (199)	2229	1760	361	426	314	662
Pinic acid (185)	1552	1469	–	–	–	–
Pinonic acid (183)	1155	1297	–	–	–	–
Sulfate of 10-hydroxy pinonic acid (279)	–	723	–	1185	–	1343
$\alpha$ -pinene hydroxy sulfate (249)	–	1692	–	1904	–	933
Ring opened carbonyl nitrate sulfate (310)	–	–	–	1744	–	1075
<i>m/z</i> 247.07 (C <sub>10</sub> H <sub>15</sub> O <sub>5</sub> S)	–	–	–	3193	–	435
<i>m/z</i> 265.07 (C <sub>10</sub> H <sub>17</sub> O <sub>6</sub> S)	–	–	–	219	–	229
<i>m/z</i> 294.06 (C <sub>10</sub> H <sub>16</sub> NO <sub>7</sub> S)	–	–	–	1799	–	–
<i>m/z</i> 295.05 (C <sub>10</sub> H <sub>15</sub> O <sub>8</sub> S)	–	–	–	494	–	–
<i>m/z</i> 296.04 (C <sub>10</sub> H <sub>14</sub> NO <sub>8</sub> S)	–	–	–	108	–	–
<i>m/z</i> 328.07 (C <sub>10</sub> H <sub>18</sub> NO <sub>9</sub> S)	–	–	–	345	–	–
<i>m/z</i> 342.05 (C <sub>10</sub> H <sub>16</sub> NO <sub>10</sub> S)	–	–	–	110	–	–

**Table 3.** Peak areas scaled to low-NO<sub>x</sub> AS seed SOA loading from UPLC chromatograms of carboxylic acids, organosulfates, and nitrooxy organosulfates from the photooxidation of  $\alpha$ -pinene.

SOA component ( $[M - H]^-$ )	H <sub>2</sub> O <sub>2</sub>		HONO		MeONO	
	AS	AS + SA	AS	AS + SA	AS	AS + SA
2-Hydroxyterpenylic acid (187)	–	–	4480	1426	3167	2617
Terpenylic acid (171)	2097	2451	2128	1615	1597	2177
3-methyl-1,2,3-butanetricarboxylic acid (3-MBTCA) (203)	458	682	717	583	1261	2135
Diaterpenylic acid acetate (231)	318	742	4635	695	2298	2997
10-Hydroxypinonic acid (199)	2229	1711	843	737	435	1148
Pinic acid (185)	1552	1428	–	–	–	–
Pinonic acid (183)	1155	1261	–	–	–	–
Sulfate of 10-hydroxy pinonic acid (279)	–	703	–	2051	–	2329
$\alpha$ -pinene hydroxy sulfate (249)	–	1645	–	3296	–	1618
Ring opened carbonyl nitrate sulfate (310)	–	–	–	3019	–	1865
<i>m/z</i> 247.07 (C <sub>10</sub> H <sub>15</sub> O <sub>5</sub> S)	–	–	–	5527	–	755
<i>m/z</i> 265.07 (C <sub>10</sub> H <sub>17</sub> O <sub>6</sub> S)	–	–	–	379	–	397
<i>m/z</i> 294.06 (C <sub>10</sub> H <sub>16</sub> NO <sub>7</sub> S)	–	–	–	3114	–	–
<i>m/z</i> 295.05 (C <sub>10</sub> H <sub>15</sub> O <sub>8</sub> S)	–	–	–	855	–	–
<i>m/z</i> 296.04 (C <sub>10</sub> H <sub>14</sub> NO <sub>8</sub> S)	–	–	–	187	–	–
<i>m/z</i> 328.07 (C <sub>10</sub> H <sub>18</sub> NO <sub>9</sub> S)	–	–	–	597	–	–
<i>m/z</i> 342.05 (C <sub>10</sub> H <sub>16</sub> NO <sub>10</sub> S)	–	–	–	190	–	–

In the present study, however, 3-MBTCA is observed under high-NO and high-NO<sub>2</sub> conditions when pinonic acid is not observed and, in addition, 3-MBTCA is observed from low-NO<sub>x</sub> photooxidation where peroxy radical reactions are dominated by reactions with HO<sub>2</sub>. The ratio of 3-MBTCA to pinic acid in low-NO<sub>x</sub> oxidation of  $\alpha$ -pinene is substantially greater than from pinonaldehyde photooxidation. This is in contrast to the ratios of pinic acid, pinonic acid, and

10-hydroxypinonic acids which are very similar regardless of which initial hydrocarbon was used under low-NO<sub>x</sub> conditions.

Terpenylic acid and diaterpenylic acid were observed in filters from all  $\alpha$ -pinene photooxidation mechanisms, while 2-hydroxy terpenylic acid was observed only in the presence of NO<sub>x</sub>. Under low-NO<sub>x</sub> photooxidation, terpenylic acid is the dominant peak and is observed only as a dimer (*m/z*

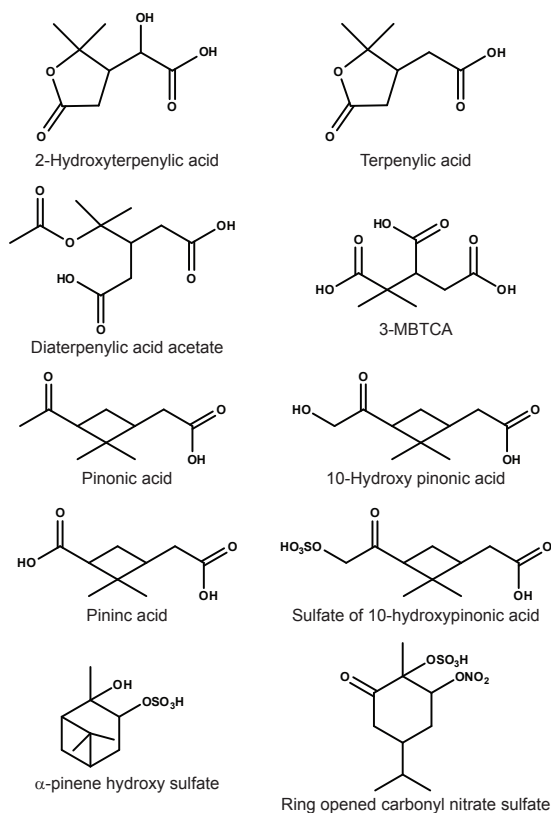


**Fig. 4.** Structures of identified SOA components detected by UPLC/(-)ESI-TOF.

343), while diaterpenylic acid is a minor peak. In the low- $\text{NO}_x$  photooxidation of pinonaldehyde, terpenylic acid was observed, but it is a small contributor to the aerosol mass; diaterpenylic acid was not observed at all. There is a peak in the chromatograms for low- $\text{NO}_x$  photooxidation of  $\alpha$ -pinene and pinonaldehyde with a molecular ion that corresponds to 2-hydroxy terpenylic acid ( $m/z = 187.06$ ), but it elutes much earlier than found in previous studies (Claeys et al., 2009) or in the high- $\text{NO}$  or high- $\text{NO}_2$  studies here. Under high- $\text{NO}$  and high- $\text{NO}_2$  photooxidation, diaterpenylic acid acetate is observed to be the dominant peak in the chromatograms. Terpenylic and 10-hydroxy terpenylic acids are also dominant peaks in the chromatograms, with their contribution to the total aerosol greater with higher  $\text{NO}_2$ . From this analysis, it appears that terpenylic acid arises from the photooxidation of pinonaldehyde while diaterpenylic acid acetate is from some other channel of  $\alpha$ -pinene photooxidation.

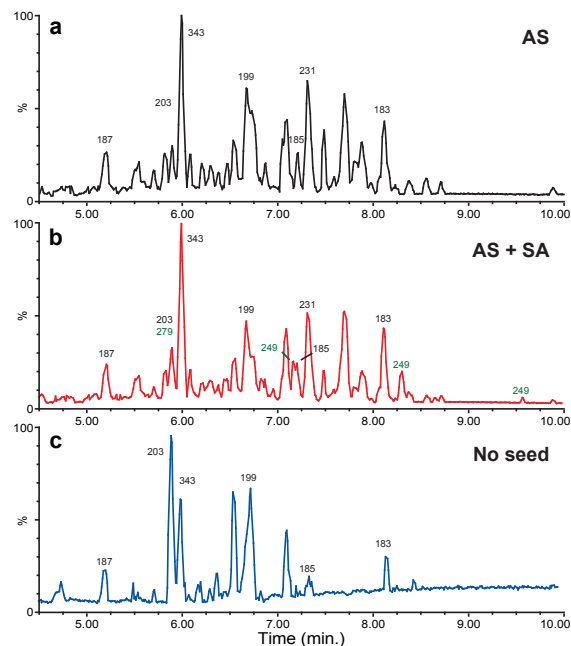


**Fig. 5.** UPLC/(-)ESI-TOF chromatograms from the filter samples of low- $\text{NO}_x$  photooxidation of  $\alpha$ -pinene or pinonaldehyde, (a)  $\alpha$ -pinene in the presence of AS seed particles (3- $\text{H}_2\text{O}_2$ ) (b)  $\alpha$ -pinene in the presence of AS + SA seed particles (5- $\text{H}_2\text{O}_2$ ) and (c) pinonaldehyde. Chromatographic peaks designated with black  $[\text{M} - \text{H}]^-$  ions are carboxylic acids and chromatographic peaks designated with green  $[\text{M} - \text{H}]^-$  ions are organosulfates. See Table 2 for compound names.

### 3.2.2 Change in SOA composition in the presence of highly acidic aerosol seed

The composition of the SOA in low- $\text{NO}_x$  photooxidation in the presence of AS or AS + SA seed is very similar (see Tables 2 and 3 and Fig. 5). This is consistent with the fact that the SOA yield and mass loading were almost identical between these experiments. In the presence of the acidic seed, four peaks were observed that correspond to organosulfates, one with  $m/z$  279 and three with  $m/z$  249. The organosulfate peak at  $m/z$  279 has been previously identified as the sulfate ester of 10-hydroxy pinonic acid and is thought to originate from the esterification of the hydroxyl group of 10-hydroxy pinonic acid (Surratt et al., 2008). Indeed, the signal for 10-hydroxy pinonic acid decreases in the presence of AS + SA seed (Table 3), while no change in peak area is observed from either pinonic or pinic acid, both of which lack a hydroxyl group. While it has been shown that for simple alcohols, sulfate esterification is too slow to be atmospherically relevant (Minerath et al., 2008), these data indicate that esterification may be sufficiently fast in more complex, acidic alcohols.

The three peaks with  $m/z$  249 are most likely from the reactive uptake of  $\alpha$ -pinene oxide, which was observed to be in lower concentration in the gas phase in the presence of an acidic seed. Iinuma et al. (2009) have shown that the uptake of  $\alpha$ -pinene oxide results in the formation of three different organosulfates: 2-pinanol-3-hydrogen sulfate, 3-pinanol-2-hydrogen sulfate, and campholenol hydrogen sulfate. The SOA yield is independent of aerosol seed acidity from low- $\text{NO}_x$  photooxidation indicating that the gas-phase yield of  $\alpha$ -pinene oxide and the resulting organosulfates are minor components.

The SOA composition (and yield) from high- $\text{NO}$  photooxidation is substantially different in the presence of AS + SA seed. In the presence of an acidic seed, diaterpenylic acid and 2-hydroxy terpenylic acid were greatly reduced in the aerosol while terpenylic acid was relatively unchanged (see Tables 2 and 3 and Fig. 6). A large number of organosulfates and nitrooxy organosulfates are observed. Both of the organosulfates observed in low- $\text{NO}_x$  photooxidation are observed. The source of the  $m/z$  249 is most likely the same,  $\alpha$ -pinene oxide. The mechanism for the formation of the sulfate ester of 10-hydroxy pinonic acid is less clear. 10-hydroxy pinonic acid is not observed in the gas phase, is a small fraction of the particle phase mass, and its aerosol concentration is relatively unchanged in the presence of an acidic seed. In addition, 10-hydroxy pinonic acid is more prominent in low- $\text{NO}_x$  photooxidation. However, the organosulfate associated with 10-hydroxy pinonic acid is of greater abundance in high- $\text{NO}$  and high- $\text{NO}_2$  conditions than in low- $\text{NO}_x$  conditions. The sulfate ester of 10-hydroxy pinonic acid coelutes with two other ions and therefore the peak area has greater error. However, even if the peak areas were similar, it would not be consistent with a source from 10-hydroxy pinonic acid under high- $\text{NO}$  and high- $\text{NO}_2$  conditions due to the low signal. The peak is observed at the same chromatographic time under all conditions; therefore, either the organosulfates at  $m/z$  279 are formed by different processes depending on  $\text{NO}$  concentration, or 10-hydroxy pinonic acid is not the source at all. We believe that there must be another mechanism that forms this organosulfate. The nitrooxy organosulfate ( $m/z = 310$ ) elutes as two peaks in the chromatogram. Under high- $\text{NO}$  and high- $\text{NO}_2$  conditions, two species are formed in the gas phase with molecular weight of 231 (CIMS  $m/z = 316$ ). One of the gas-phase species was assigned to  $\alpha$ -pinene dihydroxy nitrate as proposed in previous reports and upon sulfate esterification would produce a nitrooxy organosulfate that would produce the ion of interest ( $m/z$  310) (Aschmann et al., 2002; Surratt et al., 2008). Thus, there is once again evidence for particle-phase sulfate esterification of a hydroxyl group in a poly-functional molecule. The largest sulfate peak was also the dominant peak in the chromatogram corresponding to  $m/z$  247. The identification of the compound is unknown and its overall importance to the SOA yield is not known as no calibrations are available. Tables 2 and 3 list the most likely molecular formula for the ion at  $m/z$  247, along with

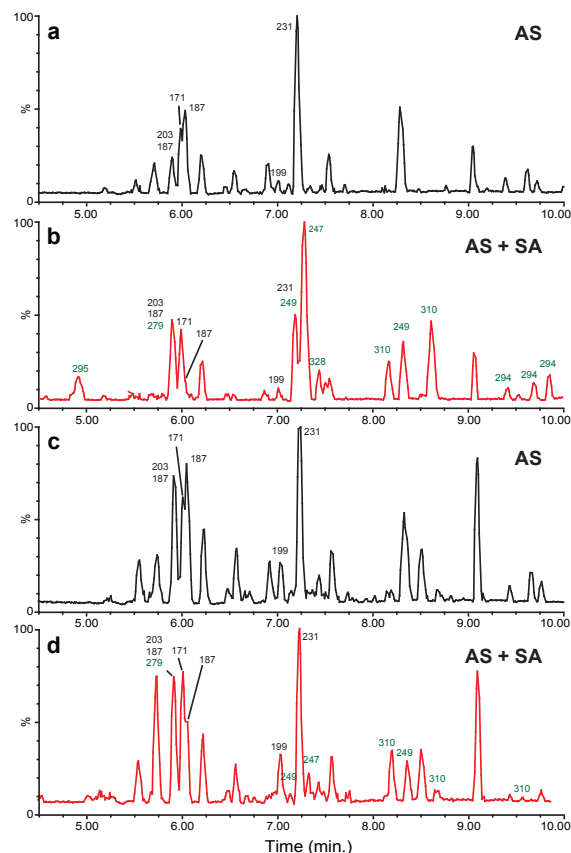


**Fig. 6.** UPLC/(-)ESI-TOF chromatograms from the filter samples of high- $\text{NO}_x$  photooxidation of  $\alpha$ -pinene. (a) HONO was the OH source, AS seed particles (4-HONO) (b) HONO was the OH source, AS + SA seed particles (6-HONO), (c)  $\text{CH}_3\text{ONO}$  was the OH source, AS seed particles (10-MeONO), and (d)  $\text{CH}_3\text{ONO}$  was the OH source, AS + SA seed particles (12-MeONO). Chromatographic peaks designated with black [M – H]<sup>–</sup> ions are carboxylic acids and chromatographic peaks designated with green [M – H]<sup>–</sup> ions are organosulfates and nitrooxy organosulfates. See Table 2 for compound names.

those from the other observed organosulfates and nitrooxy organosulfates.

Under high- $\text{NO}_2$  conditions, the addition of AS + SA rather than AS seed results in fewer new peaks in the UPLC chromatogram than under high- $\text{NO}$  conditions. As with low- $\text{NO}_x$ , this result is expected as the SOA yield is insensitive to aerosol acidity. As with high- $\text{NO}$ , 2-hydroxy terpenylic acid decreases in concentration in the presence of an acidic seed; however, the concentration of diaterpenylic acid acetate is insensitive to aerosol acidity. We have no explanation for this discrepancy. All of the organosulfates and nitrooxy

organosulfates observed in high- $\text{NO}_2$  photooxidation are observed in high- $\text{NO}$  photooxidation, but there are a few additional organosulfates and nitrooxy organosulfates that are unique to the high- $\text{NO}$  case (see Tables 2 and 3 and Fig. 6).

Given that the SOA yield and growth curves are so different, it is surprising that the UPLC/(-)ESI-TOFMS data from high- $\text{NO}$  or high- $\text{NO}_2$  photooxidation are remarkably similar in the presence of AS seed but substantially different with AS + SA seed (see Fig. 6). This suggests that there must be compositional differences which UPLC/(-)ESI-TOFMS is insensitive. The data also suggest that PANs may play a role in the SOA composition as the amount of PAN was the main difference observed in the gas phase.

### 3.2.3 Bulk SOA functionality determined by AMS

The aerosol composition in low- $\text{NO}_x$  and high- $\text{NO}_2$  OH oxidation of  $\alpha$ -pinene in the presence of AS seed particles was further analyzed by HR-ToF-AMS. A description of the results has previously been reported (Chhabra et al., 2011). In Chhabra et al. (2011) the H : C vs. O : C (Van Krevelen diagram) and the ratio of  $f_{44}$  (more oxidized species,  $\text{CO}_2^+$  likely from acids) to  $f_{43}$  (less oxidized species,  $\text{C}_2\text{H}_3\text{O}^+$ ) are compared over the course of the photooxidation experiments. The Van Krevelen diagram can be used to infer the bulk functionality of the organic species within the aerosol. Both the low- $\text{NO}_x$  and high- $\text{NO}_2$  photooxidation of  $\alpha$ -pinene fall along the  $-1$  slope of the H : C vs. O : C plot (see Fig. 2 of Chhabra et al., 2011), a value indicative of either carboxylic acids and/or hydroxy carbonyls (Heald et al., 2010; Ng et al., 2011; Chhabra et al., 2011). Under both low- $\text{NO}_x$  and high- $\text{NO}_2$  OH oxidation, the AMS data indicate the same bulk organic functionality while the gas-phase data show a greater quantity of carboxylic acids in the low- $\text{NO}_x$  oxidation. Consistent with the Van Krevelen diagram,  $f_{44}$  to  $f_{43}$  is very similar between the low- $\text{NO}_x$  and high- $\text{NO}_2$  experiments.  $f_{44}$  is assigned as an indicator of carboxylic acids and a higher degree of aerosol aging (Ng et al., 2011; Chhabra et al., 2011). Further analysis of AMS data indicates that carboxylic acids are a large fraction (30–40 % of the mass) of the aerosols in low- $\text{NO}_x$  and high- $\text{NO}_2$  OH oxidation of  $\alpha$ -pinene (see Table 2 of Chhabra et al., 2011).

### 3.3 Gas-phase composition with injection of inorganic seed after photooxidation

To study how different oxidation products interact with aerosol seed particles of different composition (acidity), experiments were performed in which  $\alpha$ -pinene was first photooxidized, followed by introduction of an aerosol seed after the lights had been off for two hours. This results in the exposure of gas-phase compounds, formed later on in the experiment, to fresh inorganic aerosol seed particles. This type of experiment has been used previously to study the SOA produced in the low- $\text{NO}_x$  photooxidation of isoprene (Sur-

ratt et al., 2010). Surratt et al. (2010) showed that epoxydiols formed from the photooxidation of isoprene preferentially partition to acidic aerosol by reactive uptake.

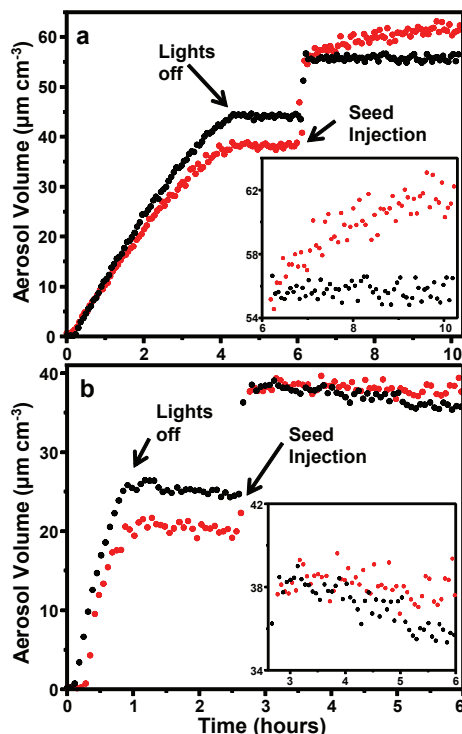
Two post-oxidation seed experiments were performed under low- $\text{NO}_x$  and two under high- $\text{NO}_2$  conditions. In all experiments, aerosol self-nucleation occurred as soon as the lights were turned on so a substantial amount of aerosol had already formed. Once the oxidation products were formed, the lights were extinguished and the chamber was left in the dark for two hours followed by injection of  $15\text{--}20\text{ }\mu\text{g m}^{-3}$  of aerosol seed. For low- $\text{NO}_x$ , this added about 50 % more aerosol volume into the chamber, while for high- $\text{NO}_2$  the aerosol concentration was doubled.

Figure 7 shows the aerosol growth from each of the photooxidation followed by aerosol injection experiments. Aerosol nucleation and growth occurs as soon as the lights are turned on in all experiments. The difference in SOA volume growth from self-nucleation from both low- and high- $\text{NO}_x$  experiments is due to greater gas-phase  $\alpha$ -pinene concentration at the beginning of each AS seed experiments compared to the AS + SA experiments. Once the lights are turned off, the aerosol mass remains constant until the addition of the inorganic seed. In the case of low- $\text{NO}_x$ , an additional growth of  $\sim 8\text{ }\mu\text{g m}^{-3}$  of SOA is observed after the addition of AS + SA seed; no growth is observed after the addition of the neutral seed. The difference in the aerosol growth is in contrast to the SOA behavior when the aerosol seed was added prior to photooxidation. Under high- $\text{NO}_2$  conditions, no additional SOA is formed after the addition of either neutral or acidic seed particles in the dark.

When ammonium sulfate seed was added in the dark after photooxidation under low- $\text{NO}_x$  or high- $\text{NO}_2$  conditions, no change in any of the gas-phase concentrations was observed. This indicates that the gas-phase molecules were not simply in equilibrium with the total aerosol concentration. It is possible that the gas-phase species were partitioning to the wall as well as to the particles, and were at equilibrium; since the surface area of the chamber walls is two orders of magnitude larger than that of the aerosol, no loss would be observed simply due to the greater surface area. Equilibrium partitioning to the walls does not, however, seem likely as the concentration of nearly all the species in the gas phase did not change when the lights were extinguished, decreasing temperature of  $\sim 5\text{ }^\circ\text{C}$ . If the gas-phase molecules were partitioning to the wall, it would be expected that their gas-phase concentration would drop as the temperature decreased.

The gas-phase concentration of a number of oxidation products formed under low- $\text{NO}_x$  conditions were noticeably reduced when AS + SA seed particles were introduced after photooxidation (Fig. 8).  $\alpha$ -pinene oxide is almost completely lost from the gas phase after introduction of the acidic seed (Fig. 8d). In addition, the highly oxidized products observed at  $m/z$  301 and 303 decrease by  $\sim 70\%$ . These two compounds probably contain either two hydroperoxy groups or one hydroperoxy group and one bridging peroxy group.





**Fig. 7.** Time traces of aerosol volume as a result of SOA growth from OH oxidation of  $\alpha$ -pinene followed by injection of ammonium sulfate seed (black) or ammonium sulfate and sulfuric acid seed (red) under (a) low- $\text{NO}_x$  and (b) high- $\text{NO}_x$  (methyl nitrite photolysis) conditions. The difference in the quantity of self-nucleated aerosol volume growth from both (a) low- and (b) high- $\text{NO}_x$  experiments is due to greater gas-phase  $\alpha$ -pinene concentration at the beginning of each of the AS seed experiments compared to the AS + SA experiments.

Upon addition of the AS + SA seed, the  $\alpha$ -pinene hydroxy hydroperoxides also decreased from the gas phase by  $\sim 75\%$  (Fig. 8a). This was unexpected, as it has been shown that the hydroxy hydroperoxides formed in the photooxidation of isoprene are not lost from the gas phase due to addition of either AS or AS + SA seed particles. (Surratt et al., 2010). In addition, it was unexpected because when aerosol seed was added prior to photooxidation, the only gas-phase product observed to be in lower concentration in the presence of AS + SA seed was  $\alpha$ -pinene oxide. It should be noted that the gas-phase mass loss was a factor of two greater than the SOA growth upon addition of AS + SA seed. It is not clear how to interpret the mass balance, as no species were observed to increase substantially in the gas phase after addition of the AS + SA seed.

The loss of additional organics upon addition of AS + SA seed after photooxidation compared to when the seed is in-

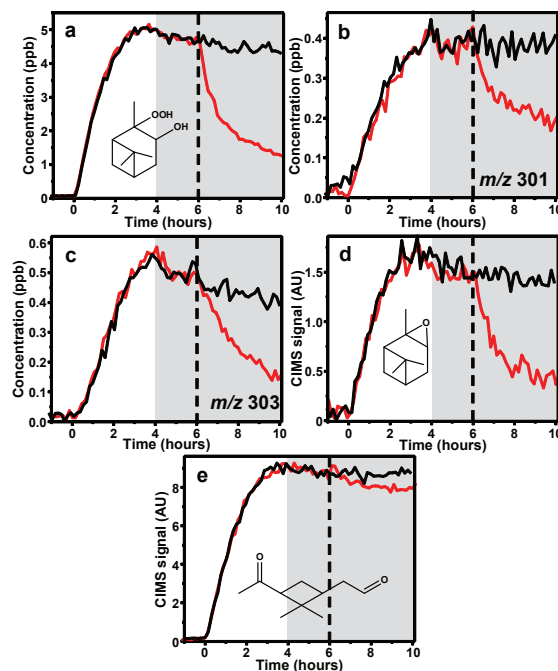


**Fig. 8.** CIMS traces of  $\alpha$ -pinene OH oxidation under low- $\text{NO}_x$  conditions, photooxidation for four hours, lights off and contents in the dark for two hours followed by injection of ammonium sulfate seed (black) or ammonium sulfate and sulfuric acid seed (red). Shaded gray area is when the chamber was dark and the dashed line indicates when aerosol seed was added.

jected prior to photooxidation may be related to the composition of the seed when exposed to a given organic. Specifically, perhaps products that are involved in self-nucleation and partition early on in the experiment coat the acidic seed resulting in a hydrocarbon surface rather than an acidic one. If this is the case, loss to the particle would be due to hydrocarbon partitioning rather than acid-catalyzed reactive uptake. Aerosol growth occurs as soon as the lights are turned on, and when a seed is present it takes only about 1.25 h before the aerosol volume has doubled. On the other hand, when the acidic seed is injected after photooxidation has occurred, the products are exposed to the acidic surface allowing reactive uptake to occur from the accumulated products.

Under high- $\text{NO}_2$  conditions,  $\alpha$ -pinene oxide is substantially lost from the gas phase when the acidic seed was added (Fig. 9). Besides  $\alpha$ -pinene oxide, there are minimal losses of other gas-phase species (Fig. 9). The observed losses include compounds that show up at  $m/z$  215, 301, and 316. The loss of each of these is less than 25 %, as opposed to the low- $\text{NO}_x$  case where losses were all greater than 50 %. As mentioned above, multiple species are observed at  $m/z$  316, a first-generation product from the oxidation of  $\alpha$ -pinene



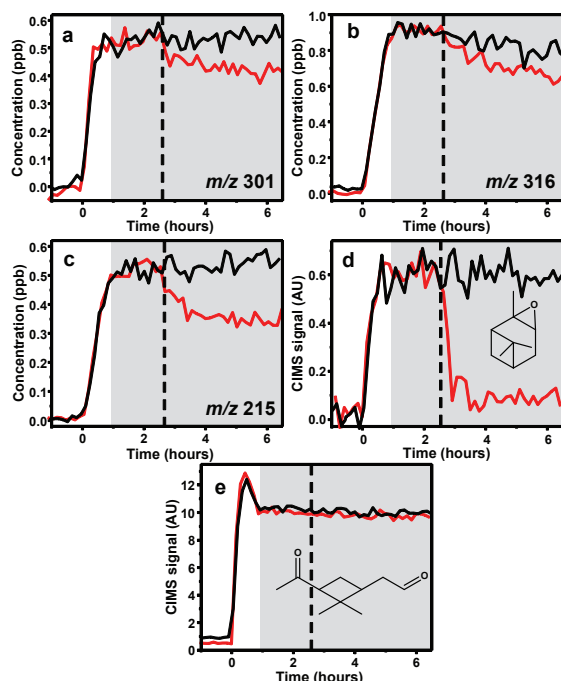


**Fig. 9.** CIMS traces of  $\alpha$ -pinene OH oxidation under high- $\text{NO}_x$  conditions, photooxidation for  $\sim 0.8$  h, lights off and contents in the dark for  $\sim 2$  h followed by injection of ammonium sulfate seed (black) or ammonium sulfate and sulfuric acid seed (red). Shaded gray area is when the chamber was dark and the dashed line indicates when aerosol seed was added.

( $\alpha$ -pinene dihydroxy nitrate) and norpinonaldehyde PAN. It is expected that if norpinonaldehyde PAN were to be lost from the gas phase upon addition of an acidic seed then pinonaldehyde PAN would as well. There is no loss of pinonaldehyde PAN from the gas phase, and therefore we conclude that the species lost from the gas phase is the  $\alpha$ -pinene oxidation product, which we believe to be  $\alpha$ -pinene dihydroxy nitrate. The structures of the molecules at  $m/z$  215 and 301 are not known. Due to the small losses, it appears that under high- $\text{NO}_2$  conditions, acidity will play only a small or negligible effect on SOA growth, as seen in Fig. 7 where no additional growth was observed upon addition of an acidic seed. Consistent with this result, Offenberger et al. (2009) saw only a modest increase in SOA yield with the increase of the aerosol acidity from high- $\text{NO}_2$  photooxidation of  $\alpha$ -pinene.

#### 4 Implications

In this study, the aerosol growth and composition from  $\alpha$ -pinene OH oxidation were compared in low- $\text{NO}$ , high- $\text{NO}$ , and high- $\text{NO}_2$  conditions. Aerosol growth from  $\alpha$ -pinene OH

oxidation under high- $\text{NO}_2$  conditions behaves more similarly to low- $\text{NO}_x$  than high- $\text{NO}$  aerosol growth. With low  $\text{NO}$ , aerosol growth continues well after two lifetime of  $\alpha$ -pinene with respect to OH oxidation. This indicates that later generation oxidation products are important for SOA growth, including the products of the oxidation of pinonaldehyde, a major product of both low- and high- $\text{NO}$  OH oxidation of  $\alpha$ -pinene.

In high- $\text{NO}$  conditions the SOA yield is dependent on aerosol acidity. The increase in SOA yield with acidic seed was, however, relatively small ( $\sim 22\%$  increase). The composition of the gas phase in high- $\text{NO}$  and high- $\text{NO}_2$  OH oxidation was identical with a few notable variations. In high- $\text{NO}_2$  experiments, 1.4 to 2 times greater concentrations of PANs and nitric acid were observed in the gas phase compared to the high- $\text{NO}$  experiments. One possible explanation for the difference in SOA growth is that the aerosols formed under high- $\text{NO}_2$  conditions are acidic enough in the presence of a neutral seed, due to the increased nitric acid and PANs, for the SOA yield to be the same in the presence of neutral or acidic particles. Further studies on the effect of  $\text{NO}_2$ , PANs, and nitric acid on SOA yield from high- $\text{NO}_x$  OH oxidation of  $\alpha$ -pinene would aid in elucidating the difference in behavior between using HONO and methyl nitrite as the OH source.

When an acidic seed was added after OH oxidation, the SOA yield under low- $\text{NO}_x$  conditions increased with a corresponding loss of species from the gas phase. This acid effect was not observed when the aerosol seed is added prior to oxidation, perhaps due to differences in the composition of the aerosol surface. The hypothesis is that when aerosol seed particles are added prior to oxidation, the surface is coated by organics, suppressing uptake of compounds that are catalyzed by acid. This has potential implications to any system that produces a high SOA yield or systems that start with a high organic VOC concentration. In systems where the seed particles become coated with organics relatively quickly, the acid effect and therefore the SOA yield under acidic conditions might be under represented.

Organic acids are a major component of SOA in both low- and high- $\text{NO}_x$  OH oxidation of  $\alpha$ -pinene. While AMS data indicate that the total concentration of organic acids in SOA from low- $\text{NO}_x$  and high- $\text{NO}_2$  is similar, the individual composition varies depending on the gas-phase conditions. Pinonic and pinic acid are observed in SOA only from low- $\text{NO}_x$  OH oxidation of  $\alpha$ -pinene. This is consistent with gas-phase data, where pinonic acid was only observed from low- $\text{NO}_x$  conditions. It is believed that 3-MBTCA is derived from high- $\text{NO}_x$  gas phase oxidation of pinonic acid; however, there must be other mechanism for its formation, as 3-MBTCA is observed in SOA from low- $\text{NO}_x$  OH oxidation of  $\alpha$ -pinene and high- $\text{NO}_x$  OH oxidation of  $\alpha$ -pinene where pinonic acid is not observed in the gas or aerosol phase.

**Acknowledgements.** This work was supported in part by Department of Energy grant DE-SC0006626 and National Science Foundation grant AGS-1057183. N. Eddingsaas was supported by the Camille and Henry Dreyfus Postdoctoral Program in Environmental Chemistry. C. Loza and L. Yee were supported by National Science Foundation Graduate Research Fellowships.

Edited by: R. McLaren

## References

- Allan, J. D., Delia, A. E., Coe, H., Bower, K. N., Alfarra, M. R., Jimenez, J. L., Middlebrook, A. M., Drewnick, F., Onasch, T. B., Canagaratna, M. R., Jayne, J. T., and Worsnop, D. R.: A generalised method for the extraction of chemically resolved mass spectra from aerodyne aerosol mass spectrometer data, *J. Aerosol Sci.*, 35, 909–922, doi:10.1016/j.jaerosci.2004.02.007, 2004.
- Anttila, P., Hyotylainen, T., Heikkilä, A., Jussila, M., Finell, J., Kulmala, M., and Riekkola, M. L.: Determination of organic acids in aerosol particles from a coniferous forest by liquid chromatography-mass spectrometry, *J. Sep. Sci.*, 28, 337–346, doi:10.1002/jssc.200401931, 2005.
- Aschmann, S. M., Atkinson, R., and Arey, J.: Products of reaction of OH radicals with alpha-pinene, *J. Geophys. Res.-Atmos.*, 107, 4191, doi:10.1029/2001jd001098, 2002.
- Camredon, M., Hamilton, J. F., Alam, M. S., Wyche, K. P., Carr, T., White, I. R., Monks, P. S., Rickard, A. R., and Bloss, W. J.: Distribution of gaseous and particulate organic composition during dark  $\alpha$ -pinene ozonolysis, *Atmos. Chem. Phys.*, 10, 2893–2917, doi:10.5194/acp-10-2893-2010, 2010.
- Capouet, M., Mueller, J. F., Ceulemans, K., Compennolle, S., Vereecken, L., and Peeters, J.: Modeling aerosol formation in alpha-pinene photo-oxidation experiments, *J. Geophys. Res.-Atmos.*, 113, D02308, doi:10.1029/2007JD008995, 2008.
- Chan, M. N., Surratt, J. D., Claeys, M., Edgerton, E. S., Tanner, R. L., Shaw, S. L., Zheng, M., Knipping, E. M., Eddingsaas, N. C., Wennberg, P. O., and Seinfeld, J. H.: Characterization and Quantification of Isoprene-Derived Epoxydiols in Ambient Aerosol in the Southeastern United States, *Environ. Sci. Technol.*, 44, 4590–4596, doi:10.1021/es100596b, 2010.
- Chan, M. N., Surratt, J. D., Chan, A. W. H., Schilling, K., Offenberg, J. H., Lewandowski, M., Edney, E. O., Kleindienst, T. E., Jaoui, M., Edgerton, E. S., Tanner, R. L., Shaw, S. L., Zheng, M., Knipping, E. M., and Seinfeld, J. H.: Influence of aerosol acidity on the chemical composition of secondary organic aerosol from  $\beta$ -caryophyllene, *Atmos. Chem. Phys.*, 11, 1735–1751, doi:10.5194/acp-11-1735-2011, 2011.
- Chhabra, P. S., Ng, N. L., Canagaratna, M. R., Corrigan, A. L., Russell, L. M., Worsnop, D. R., Flagan, R. C., and Seinfeld, J. H.: Elemental composition and oxidation of chamber organic aerosol, *Atmos. Chem. Phys.*, 11, 8827–8845, doi:10.5194/acp-11-8827-2011, 2011.
- Chung, S. H. and Seinfeld, J. H.: Global distribution and climate forcing of carbonaceous aerosols, *J. Geophys. Res.-Atmos.*, 107, 4407, doi:10.1029/2001JD001397, 2002.
- Claeys, M., Iinuma, Y., Szmigielski, R., Surratt, J. D., Blockhuys, F., Van Alsenoy, C., Boge, O., Sierau, B., Gomez-Gonzalez, Y., Vermeylen, R., Van der Veken, P., Shahgholi, M., Chan, A. W. H., Herrmann, H., Seinfeld, J. H., and Maenhaut, W.: Terpenylic Acid and Related Compounds from the Oxidation of alpha-Pinene: Implications for New Particle Formation and Growth above Forests, *Environ. Sci. Technol.*, 43, 6976–6982, doi:10.1021/es9007596, 2009.
- Cocker, David R., I., Flagan, R. C., and Seinfeld, J. H.: State-of-the-art chamber facility for studying atmospheric aerosol chemistry, *Environ. Sci. Technol.*, 35, 2594–2601, 2001.
- Crounse, J. D., McKinney, K. A., Kwan, A. J., and Wennberg, P. O.: Measurement of gas-phase hydroperoxides by chemical ionization mass spectrometry, *Anal. Chem.*, 78, 6726–6732, 2006.
- DeCarlo, P. F., Kimmel, J. R., Trimborn, A., Northway, M. J., Jayne, J. T., Aiken, A. C., Gonin, M., Fuhrer, K., Horvath, T., Docherty, K. S., Worsnop, D. R., and Jimenez, J. L.: Field-deployable, high-resolution, time-of-flight aerosol mass spectrometer, *Anal. Chem.*, 78, 8281–8289, doi:10.1021/ac061249n, 2006.
- Eddingsaas, N. C., Loza, C. L., Yee, L. D., Seinfeld, J. H., and Wennberg, P. O.:  $\alpha$ -pinene photooxidation under controlled chemical conditions – Part 1: Gas-phase composition in low- and high-NO<sub>x</sub> environments, *Atmos. Chem. Phys.*, 12, 6489–6504, doi:10.5194/acp-12-6489-2012, 2012.
- Glasius, M., Duane, M., and Larsen, B. R.: Determination of polar terpene oxidation products in aerosols by liquid chromatography-ion trap mass spectrometry, *J. Chromatogr. A*, 833, 121–135, 1999.
- Guenther, A., Hewitt, C. N., Erickson, D., Fall, R., Geron, C., Graedel, T., Harley, P., Klinger, L., Lerdau, M., McKay, W. A., Pierce, T., Scholes, B., Steinbrecher, R., Tallamraju, R., Taylor, J., and Zimmerman, P.: A global model of natural volatile organic compound emissions, *J. Geophys. Res.-Atmos.*, 100, 8873–8892, doi:10.1029/94JD02950, 1995.
- Heald, C. L., Kroll, J. H., Jimenez, J. L., Docherty, K. S., DeCarlo, P. F., Aiken, A. C., Chen, Q., Martin, S. T., Farmer, D. K., and Artaxo, P.: A simplified description of the evolution of organic aerosol composition in the atmosphere, *Geophys. Res. Lett.*, 37, L08803, doi:10.1029/2010gl042737, 2010.
- Hoffmann, T., Odum, J. R., Bowman, F., Collins, D., Klockow, D., Flagan, R. C., and Seinfeld, J. H.: Formation of organic aerosols from the oxidation of biogenic hydrocarbons, *J. Atmos. Chem.*, 26, 189–222, 1997.
- Iinuma, Y., Boge, O., Miao, Y., Sierau, B., Gnauk, T., and Herrmann, H.: Laboratory studies on secondary organic aerosol formation from terpenes, *Faraday Discuss.*, 130, 279–294, doi:10.1039/b502160j, 2005.
- Iinuma, Y., Boge, O., Kahnt, A., and Herrmann, H.: Laboratory chamber studies on the formation of organosulfates from reactive uptake of monoterpene oxides, *Phys. Chem. Chem. Phys.*, 11, 7985–97, doi: 10.1039/B904025K, 2009.
- Jaoui, M. and Kamens, R. M.: Mass balance of gaseous and particulate products analysis from alpha-pinene/NO<sub>x</sub>/air in the presence of natural sunlight, *J. Geophys. Res.-Atmos.*, 106, 12541–12558, 2001.
- Kavouras, I. G., Mihalopoulos, N., and Stephanou, E. G.: Formation of atmospheric particles from organic acids produced by forests, *Nature*, 395, 683–686, 1998.
- Kavouras, I. G., Mihalopoulos, N., and Stephanou, E. G.: Formation and gas/particle partitioning of monoterpenes photo-oxidation products over forests, *Geophys. Res. Lett.*, 26, 55–58, doi:10.1029/1998GL900251, 1999.

- Keyword, M. D., Varutbangkul, V., Bahreini, R., Flagan, R. C., and Seinfeld, J. H.: Secondary organic aerosol formation from the ozonolysis of cycloalkenes and related compounds, *Environ. Sci. Technol.*, 38, 4157–4164, 2004.
- Kourtchev, I., Copolovici, L., Claeys, M., and Maenhaut, W.: Characterization of Atmospheric Aerosols at a Forested Site in Central Europe, *Environ. Sci. Technol.*, 43, 4665–4671, doi:10.1021/es803055w, 2009.
- Laaksonen, A., Kulmala, M., O'Dowd, C. D., Joutsensaari, J., Vaatovaara, P., Mikkonen, S., Lehtinen, K. E. J., Sogacheva, L., Dal Maso, M., Aalto, P., Petäjä, T., Sogachev, A., Yoon, Y. J., Lihavainen, H., Nilsson, D., Facchini, M. C., Cavalli, F., Fuzzi, S., Hoffmann, T., Arnold, F., Hanke, M., Sellegri, K., Umann, B., Junkermann, W., Coe, H., Allan, J. D., Alfarra, M. R., Worsnop, D. R., Riekkola, M. -L., Hyötyläinen, T., and Viisanen, Y.: The role of VOC oxidation products in continental new particle formation, *Atmos. Chem. Phys.*, 8, 2657–2665, doi:10.5194/acp-8-2657-2008, 2008.
- Larsen, B. R., Di Bella, D., Glasius, M., Winterhalter, R., Jensen, N. R., and Hjorth, J.: Gas-phase OH oxidation of monoterpenes: Gaseous and particulate products, *J. Atmos. Chem.*, 38, 231–276, 2001.
- Librando, V. and Tringali, G.: Atmospheric fate of OH initiated oxidation of terpenes. Reaction mechanism of  $\alpha$ -pinene degradation and secondary organic aerosol formation, *J. Environ. Manag.*, 75, 275–282, doi:10.1016/j.jenvman.2005.01.001, 2005.
- Ma, Y., Russell, A. T., and Marston, G.: Mechanisms for the formation of secondary organic aerosol components from the gas-phase ozonolysis of  $\alpha$ -pinene, *Phys. Chem. Chem. Phys.*, 10, 4294–4312, doi:10.1039/b803283a, 2008.
- Minerath, E. C., Casale, M. T., and Elrod, M. J.: Kinetics Feasibility Study of Alcohol Sulfate Esterification Reactions in Tropospheric Aerosols, *Environ. Sci. Technol.*, 42, 4410–4415, 2008.
- Müller, L., Reinnig, M.-C., Naumann, K. H., Saathoff, H., Mentel, T. F., Donahue, N. M., and Hoffmann, T.: Formation of 3-methyl-1,2,3-butanetricarboxylic acid via gas phase oxidation of pinonic acid – a mass spectrometric study of SOA aging, *Atmos. Chem. Phys.*, 12, 1483–1496, doi:10.5194/acp-12-1483-2012, 2012.
- Ng, N. L., Chhabra, P. S., Chan, A. W. H., Surratt, J. D., Kroll, J. H., Kwan, A. J., McCabe, D. C., Wennberg, P. O., Sorooshian, A., Murphy, S. M., Dalleska, N. F., Flagan, R. C., and Seinfeld, J. H.: Effect of  $\text{NO}_x$  level on secondary organic aerosol (SOA) formation from the photooxidation of terpenes, *Atmos. Chem. Phys.*, 7, 5159–5174, doi:10.5194/acp-7-5159-2007, 2007a.
- Ng, N. L., Kroll, J. H., Chan, A. W. H., Chhabra, P. S., Flagan, R. C., and Seinfeld, J. H.: Secondary organic aerosol formation from m-xylene, toluene, and benzene, *Atmos. Chem. Phys.*, 7, 3909–3922, doi:10.5194/acp-7-3909-2007, 2007b.
- Ng, N. L., Canagaratna, M. R., Jimenez, J. L., Chhabra, P. S., Seinfeld, J. H., and Worsnop, D. R.: Changes in organic aerosol composition with aging inferred from aerosol mass spectra, *Atmos. Chem. Phys.*, 11, 6465–6474, doi:10.5194/acp-11-6465-2011, 2011.
- Nozière, B., Barnes, I., and Becker, K.-H.: Product study and mechanisms of the reactions of  $\alpha$ -pinene and of pinonaldehyde with OH radicals, *J. Geophys. Res.-Atmos.*, 104, 23645–23656, doi:10.1029/1999JD900778, 1999.
- Offenberg, J. H., Lewandowski, M., Edney, E. O., Kleindienst, T. E., and Jaoui, M.: Influence of Aerosol Acidity on the Formation of Secondary Organic Aerosol from Biogenic Precursor Hydrocarbons, *Environ. Sci. Technol.*, 43, 7742–7747, doi:10.1021/es901538e, 2009.
- Paulot, F., Crounse, J. D., Kjaergaard, H. G., Kroll, J. H., Seinfeld, J. H., and Wennberg, P. O.: Isoprene photooxidation: new insights into the production of acids and organic nitrates, *Atmos. Chem. Phys.*, 9, 1479–1501, doi:10.5194/acp-9-1479-2009, 2009a.
- Paulot, F., Crounse, J. D., Kjaergaard, H. G., Kurten, A., St. Clair, J. M., Seinfeld, J. H., and Wennberg, P. O.: Unexpected epoxide formation in the gas-phase photooxidation of isoprene, *Science*, 325, 730–733, doi:10.1126/science.1172910, 2009b.
- Presto, A. A., Hartz, K. E. H., and Donahue, N. M.: Secondary organic aerosol production from terpene ozonolysis. 2. Effect of  $\text{NO}_x$  concentration, *Environ. Sci. Technol.*, 39, 7046–7054, doi:10.1021/es050400s, 2005.
- Pye, H. O. T., Chan, A. W. H., Barkley, M. P., and Seinfeld, J. H.: Global modeling of organic aerosol: the importance of reactive nitrogen ( $\text{NO}_x$  and  $\text{NO}_3$ ), *Atmos. Chem. Phys.*, 10, 11261–11276, doi:10.5194/acp-10-11261-2010, 2010.
- Shilling, J. E., Chen, Q., King, S. M., Rosenoern, T., Kroll, J. H., Worsnop, D. R., DeCarlo, P. F., Aiken, A. C., Sueper, D., Jimenez, J. L., and Martin, S. T.: Loading-dependent elemental composition of  $\alpha$ -pinene SOA particles, *Atmos. Chem. Phys.*, 9, 771–782, doi:10.5194/acp-9-771-2009, 2009.
- Spittler, M., Barnes, I., Bejan, I., Brockmann, K. J., Benter, T., and Wirtz, K.: Reactions of  $\text{NO}_3$  radicals with limonene and  $\alpha$ -pinene: Product and SOA formation, *Atmos. Environ.*, 40, S116–S127, 2006.
- St. Clair, J. M., McCabe, D. C., Crounse, J. D., Steiner, U., and Wennberg, P. O.: Chemical ionization tandem mass spectrometer for the in situ measurement of methyl hydrogen peroxide, *Rev. Sci. Instrum.*, 81, 094102, doi:10.1063/1.3480552, 2010.
- Surratt, J. D., Kroll, J. H., Kleindienst, T. E., Edney, E. O., Claeys, M., Sorooshian, A., Ng, N. L., Offenberg, J. H., Lewandowski, M., Jaoui, M., Flagan, R. C., and Seinfeld, J. H.: Evidence for Organosulfates in Secondary Organic Aerosol, *Environ. Sci. Technol.*, 41, 517–527, 2007.
- Surratt, J. D., Gomez-Gonzalez, Y., Chan, A. W. H., Vermeylen, R., Shahgholi, M., Kleindienst, T. E., Edney, E. O., Offenberg, J. H., Lewandowski, M., Jaoui, M., Maenhaut, W., Claeys, M., Flagan, R. C., and Seinfeld, J. H.: Organosulfate formation in biogenic secondary organic aerosol, *J. Phys. Chem. A*, 112, 8345–8378, doi:10.1021/jp802310p, 2008.
- Surratt, J. D., Chan, A. W. H., Eddingsaas, N. C., Chan, M. N., Loza, C. L., Kwan, A. J., Hersey, S. P., Flagan, R. C., Wennberg, P. O., and Seinfeld, J. H.: Reactive intermediates revealed in secondary organic aerosol formation from isoprene, *P. Natl. Acad. Sci.*, 107, 6640–6645, doi:10.1073/pnas.0911114107, 2010.
- Szmigielski, R., Surratt, J. D., Gomez-Gonzalez, Y., Van der Veken, P., Kourtchev, I., Vermeylen, R., Blockhuys, F., Jaoui, M., Kleindienst, T. E., Lewandowski, M., Offenberg, J. H., Edney, E. O., Seinfeld, J. H., Maenhaut, W., and Claeys, M.: 3-methyl-1,2,3-butanetricarboxylic acid: an atmospheric tracer for terpene secondary organic aerosol, *Geophys. Res. Lett.*, 34, L24811, doi:10.1029/2007GL031338, 2007.
- Taylor, W. D., Allston, T. D., Moscato, M. J., Fazekas, G. B., Kozlowski, R., and Takacs, G. A.: Atmospheric photo-dissociation

- lifetimes for nitromethane, methyl nitrite, and methyl nitrate, *Int. J. Chem. Kinet.*, 12, 231–240, 1980.
- Warnke, J., Bandur, R., and Hoffmann, T.: Capillary-HPLC-ESI-MS/MS method for the determination of acidic products from the oxidation of monoterpenes in atmospheric aerosol samples, *Anal. Bioanal. Chem.*, 385, 34–45, doi:10.1007/s00216-006-0340-6, 2006.
- Yu, J., Cocker, David R., I., Griffin, R. J., Flagan, R. C., and Seinfeld, J. H.: Gas-phase ozone oxidation of monoterpenes: gaseous and particulate products, *J. Atmos. Chem.*, 34, 207–258, 1999a.
- Yu, J., Griffin, R. J., Cocker, David R., I., Flagan, R. C., Seinfeld, J. H., and Blanchard, P.: Observation of gaseous and particulate products of monoterpene oxidation in forest atmospheres, *Geophys. Res. Lett.*, 26, 1145–1148, doi:10.1029/1999GL900169, 1999b.
- Zhang, Y. Y., Müller, L., Winterhalter, R., Moortgat, G. K., Hoffmann, T., and Pöschl, U.: Seasonal cycle and temperature dependence of pinene oxidation products, dicarboxylic acids and nitrophenols in fine and coarse air particulate matter, *Atmos. Chem. Phys.*, 10, 7859–7873, doi:10.5194/acp-10-7859-2010, 2010.

## Appendix D

# Secondary Organic Aerosol Coating Formation and Evaporation: Chamber Studies Using Black Carbon Seed Aerosol and the Single-Particle Soot Photometer\*

---

\*Reproduced with permission from “Secondary Organic Aerosol Coating Formation and Evaporation: Chamber Studies Using Black Carbon Seed Aerosol and the Single-Particle Soot Photometer” by A. R. Metcalf, C. L. Loza, M. M. Coggon, J. S. Craven, H. H. Jonsson, R. C. Flagan, and J. H. Seinfeld, *Aero. Sci. Technol.*, 47, 326-347, doi:10.1080/2786826.2012.75072. Copyright 2013 by the American Association for Aerosol Research.



## Secondary Organic Aerosol Coating Formation and Evaporation: Chamber Studies Using Black Carbon Seed Aerosol and the Single-Particle Soot Photometer

Andrew R. Metcalf,<sup>1,2</sup> Christine L. Loza,<sup>3</sup> Matthew M. Coggon,<sup>3</sup> Jill S. Craven,<sup>3</sup> Haffidi H. Jonsson,<sup>4</sup> Richard C. Flagan,<sup>1,3</sup> and John H. Seinfeld<sup>1,3</sup>

<sup>1</sup>*Division of Engineering and Applied Science, California Institute of Technology, Pasadena, California, USA*

<sup>2</sup>*Combustion Research Facility, Sandia National Laboratories, Livermore, California, USA*

<sup>3</sup>*Division of Chemistry and Chemical Engineering, California Institute of Technology, Pasadena, California, USA*

<sup>4</sup>*Center for Interdisciplinary Remotely Piloted Aircraft Studies, Naval Postgraduate School, Monterey, California, USA*

We report a protocol for using black carbon (BC) aerosol as the seed for secondary organic aerosol (SOA) formation in an environmental chamber. We employ a single-particle soot photometer (SP2) to probe single-particle SOA coating growth dynamics and find that SOA growth on nonspherical BC aerosol is diffusion-limited. Aerosol composition measurements with an Aerodyne high resolution time-of-flight aerosol mass spectrometer (AMS) confirm that the presence of BC seed does not alter the composition of SOA as compared to self-nucleated SOA or condensed SOA on ammonium sulfate seed. We employ a 3-wavelength photoacoustic soot spectrometer (PASS-3) to measure optical properties of the systems studied, including fullerene soot as the surrogate BC seed, nucleated naphthalene SOA from high-NO<sub>x</sub> photooxidation, and nucleated  $\alpha$ -pinene SOA from low-NO<sub>x</sub> photooxidation. A core-and-shell Mie scattering model of the light absorption enhancement is in good agreement with measured enhancements for both the low- and high-NO<sub>x</sub>  $\alpha$ -pinene photooxidation systems, reinforcing the assumption of a core-shell morphology for coated BC particles. A discrepancy between measured and modeled absorption enhancement factors in the naphthalene photooxidation system is attributed to the wavelength-dependence of refractive index of the naphthalene SOA. The coating of high-NO<sub>x</sub>  $\alpha$ -pinene SOA decreases after reaching a peak thickness during irradiation, reflecting a volatility change in the aerosol, as confirmed by the relative magnitudes of  $f_{43}$  and  $f_{44}$  in the AMS spectra. The protocol described here provides a framework by which future studies of

SOA optical properties and single-particle growth dynamics may be explored in environmental chambers.

[Supplementary materials are available for this article. Go to the publisher's online edition of *Aerosol Science and Technology* to view the free supplementary files.]

### 1. INTRODUCTION

Refractory black carbon (rBC), alternately referred to as elemental carbon, is the dominant component of light-absorbing atmospheric aerosol. While rBC refers to the strongly light-absorbing component of soot, emission sources containing rBC, such as diesel exhaust, may contain other constituents such as polycyclic aromatic hydrocarbons (PAHs), aliphatic hydrocarbons, and other volatile compounds (Schauer et al. 1996; Kleeman et al. 2000; Fruin et al. 2004). These organic compounds co-emitted with rBC evaporate substantially upon dilution from the tailpipe to ambient conditions (Robinson et al. 2007).

The traditional understanding is that fresh, urban-emitted rBC is almost entirely composed of hydrophobic rBC and is unlikely to act as cloud condensation nuclei (CCN) (Weingartner et al. 1997). After emission, rBC particles can become coated by inorganic and organic non-light-absorbing components via coagulation with other particles and condensation of vapors (Abel et al. 2003; Pósfai et al. 2003; Riemer et al. 2004; Moffet and Prather 2009). Recent studies with a single-particle soot photometer (SP2) have revealed that fresh, urban-emitted rBC particles may be thinly coated with light-scattering material, while rBC in aged air masses tends to be more thickly coated (Moteki et al. 2007; Shiraiwa et al. 2007, 2008; Schwarz et al. 2008a; Subramanian et al. 2010; Metcalf et al. 2012). Timescales

Received 23 May 2012; accepted 21 October 2012.

This work was supported by the U.S. Department of Energy grant DE-SC0006626.

Address correspondence to John H. Seinfeld, Division of Chemistry and Chemical Engineering, California Institute of Technology, 1200 E. California Blvd., Mail Code: 210-41, Pasadena, CA 91125, USA. E-mail: seinfeld@caltech.edu

for the transition from a fresh to a more aged state have been estimated to range from 12 h to a day (Johnson et al. 2005; Moteki et al. 2007; Khalizov et al. 2009a; Park et al. 2012). Interactions with gas and aerosol species transform rBC into an internally mixed state, where it may eventually serve as a CCN (Zuberi et al. 2005). Hygroscopic coatings also enhance the wet deposition rate of these particles (Weingartner et al. 1997; Saathoff et al. 2003; Jacobson 2006; Stier et al. 2006). A coating of non-light-absorbing components onto rBC increases the light scattering and absorption cross sections of these particles (Fuller et al. 1999; Saathoff et al. 2003; Schnaiter et al. 2005; Bond et al. 2006; Mikhailov et al. 2006; Stier et al. 2006; Slowik et al. 2007a; Zhang et al. 2008; Wehner et al. 2009; Khalizov et al. 2009b; Cross et al. 2010; Lack and Cappa 2010; Shiraiwa et al. 2010). At least one ambient study, however, found no evidence of an enhancement of light absorption by condensation of secondary material (Chan et al. 2010b). A study of ambient rBC in Toronto showed no detectable change in absorption enhancement between fresh and aged aerosol but attributed this observation to the fact that the fresh rBC had a sufficient coating such that additional coatings did not further enhance absorption (Knox et al. 2009).

While ambient rBC measurements have revealed valuable insights into the aging process, namely coating thicknesses and growth timescales, important questions still remain. What mechanisms govern the transition from externally to internally mixed rBC aerosol? Does rBC, acting as a site for condensation of secondary organic aerosol (SOA), affect the composition of the SOA as compared to SOA condensed onto other aerosol types or nucleated homogeneous aerosol? To what extent are the coatings on rBC sufficiently volatile to evaporate upon dilution? Of what physical structure is the rBC and its "coating" and how might this affect interpretation of absorption enhancements seen (or not seen) in ambient data?

Controlled laboratory experiments of rBC aging can isolate some of the complexities of the aging process. The absorption enhancement that arises from coating nascent soot particles with a variety of non-light-absorbing materials is readily measured (Saathoff et al. 2003; Schnaiter et al. 2003, 2005; Mikhailov et al. 2006; Slowik et al. 2007a; Zhang et al. 2008; Khalizov et al. 2009b; Cross et al. 2010). Initially fractal soot agglomerates tend to compact substantially after a coating has formed (Saathoff et al. 2003; Slowik et al. 2007b; Zhang et al. 2008; Khalizov et al. 2009a,b; Cross et al. 2010; Bueno et al. 2011). In addition, rBC and polystyrene latex spheres (PSL) of the same mobility are observed to acquire sulfuric acid coatings at the same rate, indicating that the coating mechanism is independent of particle composition and shape (Khalizov et al. 2009a).

Limited laboratory chamber studies of SOA growth in the presence of soot seed particles exist. Studies at the University of North Carolina Ambient Air Research Facility have focused on how the presence of soot affects gas-particle partitioning and found that diffusional mass transfer is the limiting control on gas-particle partitioning (Strommen and Kamens 1997, 1999), and that the polarity of the seed particles, including diesel and

wood soot, and the gas-phase organic compounds can affect the gas-particle equilibrium partitioning (Leach et al. 1999). These studies have focused on the partitioning between gas and particle phases rather than any unique chemical or physical properties of either the gases or the soot. Studies at the Aerosols, Interactions and Dynamics in the Atmosphere (AIDA) chamber facility report the enhancement of light absorption by soot seed particles coated with  $\alpha$ -pinene ozonolysis SOA (Saathoff et al. 2003) and evaluate absorption enhancements by particle coagulation and growth of SOA (Schnaiter et al. 2003, 2005). These studies have focused primarily on the optical and morphological properties of the soot as growth of SOA or coagulation with other particles occurs in the chamber. Studies at the Carnegie Mellon University environmental chamber found that SOA formed by the photooxidation of evaporated diesel exhaust exceeded by a wide margin the SOA mass predicted by a model including the classified hydrocarbons (Weitkamp et al. 2007). A study at the Paul Scherrer Institute (PSI) smog chamber characterized the chemical composition and emission factors of primary and secondary organic aerosol from three diesel vehicles with various engine after-treatment systems (Chirico et al. 2010). These studies have focused on characterizing SOA from the many gas-phase precursors found in diesel exhaust or on the efforts to clean up the exhaust from diesel engines. Most of the studies listed above used fresh diesel or wood soot, which typically has a thin layer of nonrefractory material on the rBC or has soot co-emitted with many gas-phase species, such as PAHs. Uncoated spark-generated soot was also used and has been found to be chemically and optically different than diesel soot and is, therefore, not a good surrogate for atmospheric rBC (Kirchner et al. 2003; Schnaiter et al. 2003). Commercially available fullerene soot is a fractal, hydrophobic particle that most resembles ambient rBC in the SP2 instrument (Moteki and Kondo 2010; Laborde et al. 2012) and is structurally similar to diesel soot (Moteki et al. 2009), although chemical and optical comparisons to ambient soot have yet to be reported.

A principal goal of this study is to demonstrate the utility of chamber experiments that employ fullerene soot as a refractory black carbon seed aerosol in conjunction with the single-particle soot photometer, the photoacoustic soot spectrometer, and the aerosol mass spectrometer to probe the dynamics of secondary aerosol formation. Three SOA systems were studied to demonstrate the utility of this experimental protocol on a variety of chemical and optical properties. To distinguish this study from previous chamber studies with soot, the rBC surrogate used in this study is dry, uncoated fullerene soot to avoid artifacts from coatings and additional hydrocarbons that are present with, for example, diesel soot. Particle-by-particle measurements of the coating thickness of SOA on the rBC seed by the SP2 directly reveal dynamic growth and evaporation processes. Once SOA growth has reached a point at which the coating thickness is no longer changing appreciably, chamber dilution can be used to provide a driving force for SOA evaporation and an assessment of SOA volatility through decrease of coating thickness. Simultaneous particle optical property and coating

composition measurements provide data that can relate growth and evaporation behavior to SOA chemical composition. A fundamental chemical examination of the composition changes during SOA growth is beyond the scope of this study; however, demonstrating that composition changes occur coincidentally with changes in rBC coating thicknesses and aerosol optical properties provide a framework by which future mechanistic studies may be carried out.

## 2. METHODS

### 2.1. Experimental Protocols

Experiments (Table 1) were conducted in the Caltech dual 28-m<sup>3</sup> Teflon chambers. Details of the facilities are given

elsewhere (Cocker et al. 2001; Keywood et al. 2004). Before each experiment, the chambers were flushed with dried, purified air for >24 h, until the particle number concentration (<10 cm<sup>-3</sup>), mass concentration (<0.1 µg m<sup>-3</sup>), and hydrocarbon mixing ratios were below detection limits of the instruments. Seeded experiments were conducted with two types of seeds; fullerene soot (stock #40971, lot #L20W054, Alfa Aesar, Ward Hill, MA, USA) as a fractal, rBC surrogate and ammonium sulfate (AS) as a spherical inorganic particle alternative. Fullerene soot particles were generated by nebulizing a suspension of fullerene soot and milliQ water until the desired particle volume concentration in the chamber was reached. Prior to nebulizing, the fullerene soot suspension was sonicated for ~20 min to facilitate the mixing of the hydrophobic soot particles in water and to break up any large agglomerates. Ammonium sulfate

TABLE 1  
Summary of experiments

Experiment number	[HC] <sub>0</sub> [ppb]	OH source	Seed	Seed volume <sup>a</sup> [µm <sup>3</sup> cm <sup>-3</sup> ]	SOA mass [µg m <sup>-3</sup> ]	Description
Naphthalene						
1	16.6 ± 0.1	CH <sub>3</sub> ONO <sup>b</sup>	rBC <sup>c</sup>	10.1 ± 0.7	13.0 ± 0.20	SOA condensation followed by chamber dilution
2	10.7 ± 0.1	CH <sub>3</sub> ONO	AS <sup>d</sup> + rBC	34.4 ± 2.8	14.2 ± 0.14	SOA condensation with seed competition followed by chamber dilution
3	21.9 ± 0.1	CH <sub>3</sub> ONO	naph <sup>e</sup>	43.6 ± 0.5	—	SOA nucleation with rBC injection and coagulation
4	27.5 ± 0.1	CH <sub>3</sub> ONO	naph + rBC	62.3 ± 1.5	22.0 ± 0.34 <sup>f</sup>	SOA nucleation followed by rBC injection and SOA growth then chamber dilution
α-pinene						
5	27.0 ± 0.1	CH <sub>3</sub> ONO	rBC	14.4 ± 0.5	29.2 ± 0.70 <sup>g</sup>	SOA condensation followed by chamber dilution
6	24.1 ± 0.1	CH <sub>3</sub> ONO	AS + rBC	28.9 ± 1.1	9.4 ± 0.36	SOA condensation with seed competition followed by chamber dilution
7	10.8 ± 0.2	H <sub>2</sub> O <sub>2</sub> <sup>h</sup>	rBC	18.2 ± 1.0	23.0 ± 0.12	SOA condensation followed by chamber dilution
8	11.6 ± 0.2	H <sub>2</sub> O <sub>2</sub>	AS + rBC	32.6 ± 1.5	16.2 ± 0.14	SOA condensation with seed competition followed by chamber dilution
9	18.0 ± 0.1	H <sub>2</sub> O <sub>2</sub>	α-p <sup>i</sup> + rBC	28.2 ± 1.0	49.8 ± 0.16 <sup>f</sup>	SOA nucleation followed by rBC injection and SOA growth then chamber dilution

<sup>a</sup>Calculated from DMA data assuming spherical particles. <sup>b</sup>CH<sub>3</sub>ONO was used for high-NO<sub>x</sub> experiments, to which extra NO was added prior to irradiation to bring [NO]<sub>0</sub> to 369–416 ppb. <sup>c</sup>rBC = fullerene soot aerosol. <sup>d</sup>AS = ammonium sulfate aerosol. <sup>e</sup>naph = nucleated SOA from naphthalene-OH photooxidation prior to rBC injection. <sup>f</sup>SOA mass after the second growth period with SOA mass from the first period subtracted. <sup>g</sup>Measurement taken after some evaporation of SOA had occurred. <sup>h</sup>H<sub>2</sub>O<sub>2</sub> was used for low-NO<sub>x</sub> experiments, to which no extra NO was added prior to irradiation and [NO]<sub>0</sub> was 1.5–2.6 ppb prior to irradiation. <sup>i</sup>α-p = nucleated SOA from α-pinene-OH photooxidation prior to rBC injection.



(AS), a commonly used seed particle in environmental chambers, was injected into the chamber by atomizing a 0.015 M aqueous ammonium sulfate solution. In the “AS + rBC” experiments denoted in Table 1, ammonium sulfate was injected into the chamber and allowed to mix for  $\sim 30$  min while gas-phase species were loaded into the chamber before injection of the fullerene soot. Upon injection of rBC in these dual seed experiments, an attempt was made to match the calculated particle surface areas of the AS and rBC from online scanning mobility particle sizer measurements. The median mobility diameter of the AS seed was  $\sim 90$  nm while for the fullerene soot the median mobility diameter was  $\sim 140$  nm (Figure S1b).

Experiments were run under both low- and high- $\text{NO}_x$  conditions using hydrogen peroxide ( $\text{H}_2\text{O}_2$ ) and methyl nitrite ( $\text{CH}_3\text{ONO}$ ) as the OH sources, respectively.  $\text{H}_2\text{O}_2$  was injected into the chamber by evaporating 280  $\mu\text{L}$  of 50% wt aqueous solution into the chamber with 5  $\text{L min}^{-1}$  of purified air.  $\text{CH}_3\text{ONO}$  was vaporized into an evacuated 500 mL glass bulb and introduced into the chamber with 5  $\text{L min}^{-1}$  of purified air.  $\text{CH}_3\text{ONO}$  was synthesized following the method described by Taylor et al. (1980) and modified by Chan et al. (2010a).

Two SOA precursors were studied: naphthalene and  $\alpha$ -pinene. Naphthalene is an important polycyclic aromatic hydrocarbon (PAH) that, like rBC, is a product of incomplete combustion in diesel engines and biomass burning (Schauer et al. 1999, 2001; Ravindra et al. 2008). PAHs, in general, may account for as much as one-half of SOA from diesel emissions (Chan et al. 2009). Naphthalene (99%, Sigma-Aldrich, St. Louis, MO, USA) was introduced into the chamber by flowing 1  $\text{L min}^{-1}$  purified air through an FEP Teflon tube packed with solid naphthalene (Chan et al. 2009).  $\alpha$ -Pinene, the most abundantly emitted monoterpene, is an important biogenic volatile organic compound (VOC), with global emissions of 34–50  $\text{Tg C yr}^{-1}$  (Guenther et al. 1995; Chung and Seinfeld 2002; Pye et al. 2010).  $\alpha$ -Pinene was introduced into the chamber by injecting a volume of liquid into a glass bulb, and the vapor was carried into the chamber with 5  $\text{L min}^{-1}$  of purified air. All naphthalene experiments were conducted in the same chamber, while all but one  $\alpha$ -pinene experiment (Experiment 8 in Table 1) were conducted in the other chamber. In all experiments, the chamber contents, seed particles, parent hydrocarbon, and OH source, were allowed to mix for 1 h before beginning irradiation. In most experiments, after maximum particle growth was obtained, the UV lights were turned off and the chamber was diluted  $\sim 12$ – $18$  h while sampling continued. After irradiation was stopped and before chamber dilution began, cyclohexane, injected by a method similar to  $\alpha$ -pinene injection, was introduced to the chamber to be used as a tracer for dilution.

## 2.2. Instrumentation

A suite of instruments was used to study the evolution of the gas and particle phases. The parent hydrocarbons and dilution tracer were measured using a gas chromatograph with flame ionization detector (GC/FID, Model 6890N, Agilent Technologies,

Inc., Santa Clara, CA, USA), equipped with an HP-5 column ( $15 \text{ m} \times 0.53 \text{ mm ID} \times 1.5 \mu\text{m}$  thickness, Agilent). The GC/FID response to naphthalene was calibrated by dissolving a known mass of naphthalene in dichloromethane and vaporizing into a 55 L Teflon chamber. The GC/FID response to  $\alpha$ -pinene and cyclohexane was calibrated by vaporizing a small volume of liquid into a 50 L chamber and diluting aliquots of that sample into a 55 L chamber. NO and  $\text{NO}_x$  were measured with a chemiluminescence NO/ $\text{NO}_x$  analyzer (Model APNA 360, HORIBA Instruments Incorporated, Irvine, CA, USA). Relative humidity (RH), temperature (T), and  $\text{O}_3$  were continuously monitored. RH of the chamber was typically  $< 5\%$  during irradiation periods, rising to  $\sim 10\%$  during the overnight chamber dilution. The initial chamber temperature was typically  $\sim 20$ – $24^\circ\text{C}$ ; however, heating from the UV lights caused a rise in temperature of  $\sim 4$ – $6^\circ\text{C}$  during irradiation. Initial  $\text{O}_3$  concentration was typically  $< 5$  ppb. Varying amounts of NO were added from a gas cylinder (Scott-Marrin, Riverside, CA, USA) to ensure high  $\text{NO}_x$  conditions at the start of most experiments, except where noted in Table 1. Aerosol size distribution and number concentration were measured continuously using a custom-built scanning mobility particle sizer consisting of a differential mobility analyzer (DMA, Model 3081, TSI Incorporated, Shoreview, MN, USA) coupled to a condensation particle counter (CPC, Model 3010, TSI), henceforth referred to as the DMA.

Refractory black carbon (rBC) mass measurements were made with a Droplet Measurement Technologies (DMT, Boulder, CO, USA) Single Particle Soot Photometer (SP2). The SP2 affords measurements of both the particle-by-particle rBC mass as well as the thickness of non-rBC coating on each particle (Stephens et al. 2003; Baumgardner et al. 2004; Schwarz et al. 2006; Moteki and Kondo 2007; Slowik et al. 2007a). This particular SP2 was used in a previous study (Metcalfe et al. 2012) and the only difference in configuration was an increase in the gain setting on the narrowband incandescence channel to increase sensitivity to rBC mass. Calibrations, as detailed by Metcalfe et al. (2012), were repeated just prior to this set of chamber experiments. Aquadag (Aqueous Deflocculated Acheson Graphite, Acheson Colloids Company, Port Huron, MI, USA) was mobility-selected by a DMA and sampled by the SP2. Because the SP2 is known to be more sensitive to Aquadag than to other rBC standards (Laborde et al. 2012), a correction factor of 25% is used to relate the SP2 signals to fullerene soot mass (Baumgardner et al. 2012). Estimated uncertainty in single-particle mass determination is  $\sim 40\%$ , based largely on the uncertainty in Aquadag mass during calibration and the relationship to fullerene soot mass. To relate rBC mass to particle size, the volume-equivalent diameter (VED) is calculated assuming the rBC is a void-free sphere with an effective mobility density given by Gysel et al. (2011). Note that there is additional uncertainty in the fullerene mobility density because not all batches of fullerene soot have the same effective density (Laborde et al. 2012); the batch used in this study differs from that measured by Gysel et al. (2011). With propagation of

errors through the calculations, estimated uncertainty in VED is  $\sim 12\%$ .

Real-time particle mass spectra were collected continuously by an Aerodyne high resolution time-of-flight aerosol mass spectrometer (AMS) (Jayne et al. 2000; DeCarlo et al. 2006; Canagaratna et al. 2007). The AMS was operated predominantly in the lower resolution, higher sensitivity “V-mode,” but was manually switched periodically to the high resolution “W-mode.” “V-mode” data were analyzed using a fragmentation table to separate sulfate, ammonium, and organic spectra and to time-trace specific  $m/z$  ratios. “W-mode” data were analyzed in IGOR Pro (Wavemetrics, Inc., Lake Oswego, OR, USA) using the PIKA 1.10H module to determine the chemical formulas contributing to distinct  $m/z$  ratios (DeCarlo et al. 2006). The AMS ionization efficiency was calibrated at the beginning of the study using dried, 350 nm  $\text{NH}_4\text{NO}_3$  particles. AMS collection efficiency is assumed to be 0.5 to account for particle bounce off the heater inside the instrument (Huffman et al. 2005; Middlebrook et al. 2012); however, because the collection efficiency could not be explicitly determined for the systems studied, the mass-weighted optical properties calculated in this work use aerosol mass calculated from particle volume concentrations determined by the DMA measurements. Aerosol densities were determined by comparing DMA volume distributions with AMS particle time-of-flight mass distributions following the method described by DeCarlo et al. (2004). AMS mass loadings reported in the figures and in Table 1 have an overall uncertainty of  $\sim 30\%$  (Bahreini et al. 2009). AMS bulk masses are averaged over 3 min intervals.

Aerosol absorption and scattering coefficients ( $b_{\text{abs}}$  and  $b_{\text{sca}}$ ) were measured with a DMT 3- $\lambda$  photoacoustic soot spectrometer (PASS-3), which is an instrument based on several previous prototypes (Lewis et al. 2008, and references therein). Briefly, submicron aerosol scattering coefficient is determined by an integrating sphere/photodetector at each wavelength, 405 nm, 532 nm, and 781 nm. Aerosol absorption is determined by the photoacoustic method, which uses a microphone to measure sound/pressure waves emanating from heated gas around aerosols absorbing laser light. The PASS-3 scattering signal was calibrated with a concentrated stream of 220 nm polystyrene latex spheres (PSL) and the absorption signal with aerosol from a concentrated Nigrosin dye (product #198285 lot #MKBD9679V, Sigma-Aldrich) solution. Calibrations were performed at particle concentrations much higher than those used in the chamber experiments in order to make use of the laser power meter onboard the instrument and calculate extinction using Beer’s Law. The linear response of the PASS-3 is appropriately extrapolated to experiment-relevant values because of the linearity of the detectors (Cross et al. 2010, supplement). During this study, data from the  $\lambda = 532$  nm channel were deemed unreliable due to a hardware malfunction and have been omitted from the analysis. Lower detection limit is estimated by three times the standard deviation of signal noise during particle-free sampling. The lower detection limits for  $b_{\text{abs}}$  are  $24.62 \pm 0.36$

and  $3.89 \pm 0.65 \text{ Mm}^{-1}$  and for  $b_{\text{sca}}$  are  $10.40 \pm 1.42$  and  $8.20 \pm 1.64 \text{ Mm}^{-1}$  for  $\lambda = 405$  and 781 nm, respectively. Absolute accuracy at aerosol levels relevant to this study was not determined; however, other PASS-3 instruments have reported absolute accuracy well within 20% (Flowers et al. 2010, supplement). In this work, measured absorption enhancement,  $E_{\text{abs},\lambda}^m$ , is defined as

$$E_{\text{abs},\lambda}^m(t) = \frac{b_{\text{abs},\lambda}(t)}{b_{\text{abs},\lambda}(t_0)}, \quad [1]$$

where  $b_{\text{abs},\lambda}(t)$  is the measured aerosol absorption coefficient as a function of time,  $t$ , and  $b_{\text{abs},\lambda}(t_0)$  is the measured absorption coefficient of the (uncoated) fullerene soot seed particles prior to chamber irradiation. Because the mass of rBC in the chamber remains relatively constant during the irradiation periods of the experiments, this formulation is equivalent to defining enhancement using the mass absorption cross section (MAC).

A prototype instrument was used to detect particle sphericity by single-particle laser light scattering (see the online supplemental information). Briefly, single particles are brought into a circularly-polarized laser beam ( $\lambda = 532$  nm) and the angular pattern of light scattered off the particle is detected with a photomultiplier tube (PMT) assembly. Eight detectors positioned at a polar angle of  $50^\circ$  in the forward scattering direction measure light scattered onto lenses at one end of fiber optic cables, the other ends of which are mounted in front of a PMT assembly that has a single channel devoted to each cable.

According to Mie theory, homogeneous spherical particles scatter circularly polarized light uniformly around the azimuth of a given polar angle. Particle sphericity, the degree to which a given particle acts like a sphere when scattering light, has been measured and analyzed previously with instruments similar to that used here (Dick et al. 1994, 1998; Sachweh et al. 1995). Our analysis follows the same logic as that of previous authors, although our mathematical formulation of sphericity is different (see the online supplemental information). To determine the degree of sphericity, we quantify the deviation among eight sensors at a fixed polar angle, which we call “nonsphericity” ( $\Phi$ ). Little deviation and smaller nonsphericity values are indicative of a spherical particle, while a large deviation and larger nonsphericity values indicate a nonspherical particle. Because the optical fibers differ in length and in radii of curvature between the lenses and the PMT, these artifacts are accounted for in the nonsphericity calculation by quantifying the extent to which each channel has the same deviation from its respective median signal.

### 2.3. Mie Scattering Model

For determination of single-particle coating thicknesses from SP2 light-scattering measurements and for comparison to bulk optical properties measured by the PASS-3, the Mie scattering model is used to calculate scattering and absorption cross sections for single particles. The Mie scattering model in this study (used previously by Metcalf et al. 2012) was adapted from

a version of BHMIE (Bohren and Huffman 1998) to compute scattering coefficients for a stratified sphere (Toon and Ackerman 1981). For interpretation of SP2 scattering signals, the scattering function is integrated over the solid angles subtended by the SP2 detectors to compare the measured and modeled signals (scattering cross section) to derive an optical diameter, from which the coating thickness on the rBC core is determined. Note that coating thicknesses reported in this work are in terms of diameter and are, thus, the particle diameter increase as a result of the coating. Mean coating thicknesses are reported as a number-weighted mean over all detected coating thicknesses over all rBC core sizes. The measured peak scattering signal is derived from a leading edge-only (LEO) fit of the scattering signal in order to correct for evaporating coatings as particles traverse the laser in the SP2 (Gao et al. 2007). The rBC refractive index is assumed to be  $1.95 + 0.79i$  (Bond and Bergstrom 2006), and a coating refractive index of  $1.5 + 0.0i$  is used, matching previous studies (Schwarz et al. 2008a,b; Metcalf et al. 2012). Uncertainty in retrieved coating thickness from the SP2 scattering signal is  $\sim 40\%$  (Metcalf et al. 2012). The Mie scattering model of SP2 signals is also used to determine the size of purely scattering particles. Again, a refractive index of  $1.5 + 0.0i$  and the LEO fitting method on the measured scattering signal are used, and the optical size range of detection is 169–600 nm. Estimated uncertainty in retrieved optical diameter is  $\sim 5\%$  for purely scattering particles.

For comparison to the measured absorption enhancement factors, the Mie model is used to calculate a time-dependent absorption enhancement factor from the mean coating thicknesses retrieved from SP2 measurements. Because total scattering and absorption is considered, integration over the SP2 detection angles is not carried out in this calculation. At each time interval, rBC core sizes from SP2 incandescence signals are binned into 36 core size bins spanning 90–265 nm VED and into 37 coating thickness bins of  $\sim 60$ –300 nm diameter, based on the detected scattering cross sections. Note that negative coating thicknesses at a given rBC VED represent scattering cross sections smaller than what the core-shell Mie model calculates for a particle with zero coating thickness on those rBC cores. These values are necessary to include due to the uncertainties in assumed refractive index and in SP2 calibration. From these binned number of particles,  $N$ , a time- and rBC-core-size-dependent mean coating thickness,  $\bar{D}_{\text{coat}}$ , is calculated, from which the Mie model is used to calculate the absorption cross sections,  $\sigma_{\text{abs},\lambda}$ , at  $\lambda = 405$  and 781 nm. The rBC core-size-dependent enhancement factors,  $\bar{E}_{\text{abs},\lambda}^c$ , are calculated from these mean coating thicknesses by

$$\bar{E}_{\text{abs},\lambda}^c(t, \text{VED}) = \frac{\sigma_{\text{abs},\lambda}(\text{VED}, \bar{D}_{\text{coat}}(t, \text{VED}))}{\sigma_{\text{abs},\lambda}(\text{VED}, D_{\text{coat}} = 0)}. \quad [2]$$

The fraction,  $f_{\sigma_{\text{abs},\lambda}}$ , of total absorption cross section present at each rBC core size relative to the total absorption cross section

over all sizes is calculated by

$$f_{\sigma_{\text{abs},\lambda}}(t, \text{VED}) = \frac{\sum_{D_{\text{coat}}} N(t, \text{VED}, D_{\text{coat}}) \times \sigma_{\text{abs},\lambda}(\text{VED}, \bar{D}_{\text{coat}}(t, \text{VED}))}{\sum_{\text{VED}} \sum_{D_{\text{coat}}} N(t, \text{VED}, D_{\text{coat}}) \times \sigma_{\text{abs},\lambda}(\text{VED}, \bar{D}_{\text{coat}}(t, \text{VED}))}. \quad [3]$$

Finally, the calculated time-dependent absorption enhancement factor,  $E_{\text{abs},\lambda}^c$ , is calculated by weighting the rBC core-size-dependent enhancement factors by the fraction of absorption cross section at each rBC size bin,

$$E_{\text{abs},\lambda}^c(t) = \sum_{\text{VED}} f_{\sigma_{\text{abs},\lambda}}(t, \text{VED}) \times \bar{E}_{\text{abs},\lambda}^c(t, \text{VED}). \quad [4]$$

In the final calculation of size-dependent absorption enhancements, only rBC VED of 160–265 nm are considered in the equations above. At rBC VEDs smaller than 160 nm, the scattering cross section of uncoated rBC particles is below the optical detection limit of the SP2, and, therefore, mean coating thicknesses will be biased high at these rBC core sizes. Although the size range of detection of the SP2 is narrower than that of the PASS-3, the weighting done here should give proper importance to the fewer but larger and more optically active coated rBC particles that most influence the PASS-3 signal. Uncertainty in the calculations of absorption enhancements are likely dominated by the uncertainty in rBC VED.

### 3. RESULTS

#### 3.1. Fullerene Soot Characteristics

##### 3.1.1. Sphericity

Figure 1 presents distributions of nonsphericity values calculated for dry, uncoated fullerene soot (BC), ammonium sulfate (AS), and polystyrene latex spheres (PSL). Lognormal fits to each histogram were calculated to determine the mean nonsphericity values for these populations of particle types (Table 2). PSL exhibits the smallest mean nonsphericity value (0.070), while dry, uncoated rBC has the largest (0.353), indicating nonsphericity. The AS sample in Figure 1 was taken from a chamber wall-deposition experiment in which AS seed was injected into a dry ( $<10\%$  RH) chamber. AS mean nonsphericity is slightly larger than that for PSL, likely indicating that some AS particles do not retain water in the dry chamber. Calibrations with oxalic acid particles (data not shown in Figure 1, but statistics reported in Table 2) generated with a collision atomizer and sampled directly into the prototype instrument yield a mean nonsphericity similar to that of AS. Dried, cubic salt particles (statistics reported in Table 2), generated by atomizing a solution of NaCl and water and sampling through a nafion dryer directly into the instrument, yield a nonsphericity similar to that for rBC. Like the AS sample, the fullerene

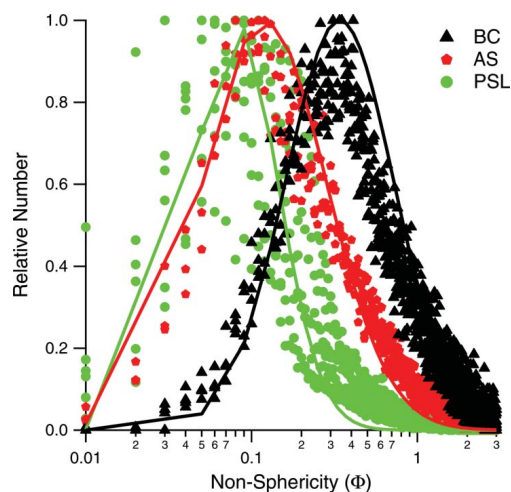


FIG. 1. Distributions of nonsphericity values for ammonium sulfate (AS), fullerene soot (BC) particles, and polystyrene latex spheres (PSL). Each distribution represents  $\sim 10,000$  particles sampled at various times throughout the respective experiments. "Relative number" is the number of particles in each bin divided by the maximum number in any bin for the given distribution. Solid lines denote a lognormal fit to a single distribution; only one fit per particle type is shown. Mean nonsphericity values corresponding to lognormal fits to all distributions are given in Table 2. (Color figure available online.)

soot sample was measured during wall-deposition experiments in which only rBC was present in the chamber. These measurements confirm that the fullerene soot, as we have prepared and loaded into the chamber as seed particles, is nonspherical.

### 3.1.2. Particle Wall Deposition

In environmental chamber studies, wall-deposition rates must be known in order to calculate SOA yields from a parent hydrocarbon (Keywood et al. 2004; Ng et al. 2007; Loza et al. 2012). Wall deposition processes have been well-described in the literature (Crump and Seinfeld 1981; McMurry and Rader 1985; Park et al. 2001; Pierce et al. 2008). Particles in the bulk of the chamber can diffuse or settle through a boundary layer near the chamber wall and deposit on the wall. Electrostatic effects can enhance deposition rates, especially for intermediate-sized particles (50–1000 nm diameter) (McMurry and Rader 1985).

TABLE 2  
Summary of nonsphericity values

Particle type	Mean nonsphericity ( $\pm 1\sigma$ )
BC	$0.353 \pm 0.042$
NaCl	$0.303 \pm 0.057$
AS	$0.173 \pm 0.091$
Oxalic acid	$0.150 \pm 0.030$
PSL	$0.070 \pm 0.029$

Typically, wall-deposition rates are determined by atomizing seed aerosol into a clean chamber and measuring the decay of particle concentration over  $\sim 24$  h. From these data, size-dependent, first-order loss coefficients,  $\beta$ , are obtained. Measured wall-deposition rates for both AS seed and fullerene soot seed exhibit differences, as shown in Figure 2. The wall-deposition rates presented in Figure 2, calculated from DMA size distribution data, are presented with respect to particle mass rather than mobility diameter in order to better relate the nearly spherical AS with the nonspherical rBC. The different range of masses for the two particle types in Figure 2 is the result

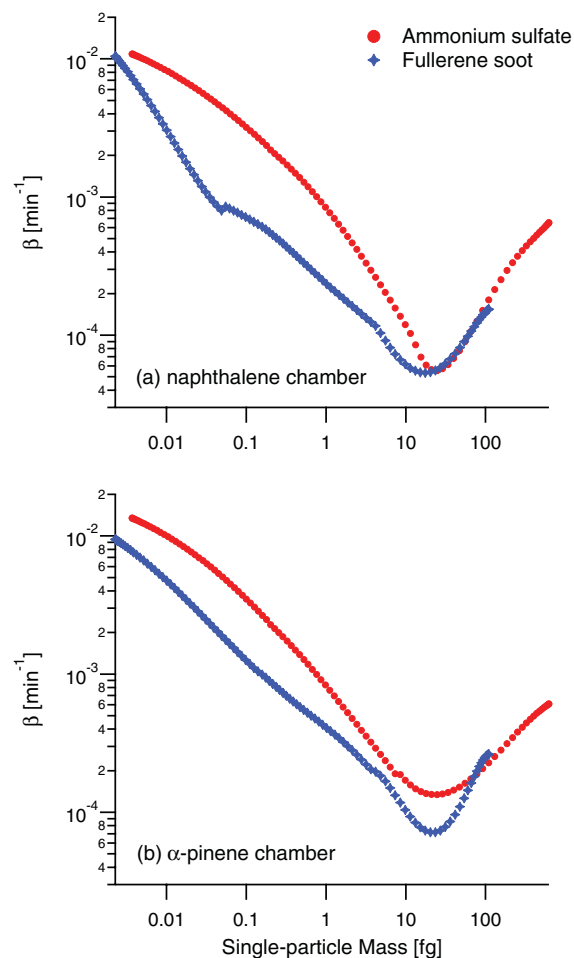


FIG. 2. Particle wall deposition rate coefficients,  $\beta$ , for the two chambers with ammonium sulfate and fullerene soot as the seed particles. Data are displayed by single-particle mass rather than mobility diameter to directly compare AS and BC. Ammonium sulfate mass is calculated from mobility diameter assuming a spherical particle and a density of  $1.77 \text{ g cm}^{-3}$ . Fullerene soot mass is calculated from mobility diameter using the relation reported by Gysel et al. (2011). (Color figure available online.)

of the smaller effective density ( $0.6\text{--}0.35\text{ g cm}^{-3}$  for mobility diameters  $300\text{--}800\text{ nm}$  [Gysel et al. 2011]) for fullerene soot than for AS ( $1.77\text{ g cm}^{-3}$ ) over all mobility diameters displayed.

The characteristic “V”-shape of the wall deposition rate curves in Figure 2 arises because of two competing processes: diffusion dominates wall deposition at smaller-size (and mass) particles and gravitational settling dominates wall deposition at larger-size (and mass) particles. The fact that the rBC deposition rate achieves a minimum at nearly the same single-particle mass as that for AS particles indicates a similar balance between these effects. At larger masses, where gravitational settling dominates, AS and rBC have similar values of  $\beta$ , indicating reduced effect of particle shape in this range. At smaller masses, however, the significant difference in  $\beta$  reflects differences in diffusion rates to the chamber walls or an invalid assumption of a first-order wall-deposition rate with unit sticking probability.

Because effective density measurements from a coupled DMA-SP2 system are used (Gysel et al. 2011), any artifacts in the DMA data used to calculate  $\beta$  in these experiments due to particle nonsphericity should be consistent during the entire wall-deposition experiment. Therefore, the differences in wall-deposition rates between AS and fullerene soot are likely not the product of measurement artifacts. The diffusion rate of the fullerene soot could be less than that for AS particles of the same mass owing to the larger size of the fullerene soot particles. Sticking probabilities may also be smaller for the dry fullerene soot than for the AS particles, which likely retain some water, even in a dry chamber. The implication for the current chamber experiments is that the rate of wall deposition can be expected to change over the course of an experiment as initially uncoated rBC particles become coated. For this reason, SOA yields are not calculated in this study.

### 3.2. General Experimental Results

Figure 3 shows the reaction profile during naphthalene photooxidation, Experiment 1 (Table 1), in the presence of rBC seed particles. The rapidly formed SOA deposits onto the fullerene soot, as indicated by the immediate increase in mean coating thickness. A modest amount ( $\sim 30\%$  by number in the SP2 detection range) of purely scattering particles, presumably from nucleation, are present after growth initiates, indicated by an increase in total number concentration just after the start of irradiation (Figure 3a). Despite the temperature increase that occurs once the UV lights are turned on (Figure 3b), the coating thickness rapidly increases early in the irradiation. Temperature decreases once the lights are turned off, accompanied by only a small increase in mean coating thickness. Single-particle mean coating thickness does not decrease at any point during Experiment 1, indicating that the decrease of aerosol mass during dilution of the chamber is the result of flushing the particles out of the chamber and wall deposition within the chamber and is not due to evaporation of the aerosol itself. The temperature decrease during dilution favors condensation and could influ-

ence mean coating thickness; however, the rate of temperature decrease varies during Experiment 1 while the rate of mean coating thickness increase does not vary in the same manner. Thus, it is unlikely that temperature alone is the dominant control of condensation of SOA in this system.

The evolution of coating thickness as a function of rBC core diameter is presented in Figure 4. About 30 min after the start of irradiation (Figure 4a), rBC particles of all core sizes already have an organic coating growing. As organic growth progresses (Figures 4b and c), the smaller rBC cores have markedly thicker coatings than the larger rBC cores. After  $\sim 7.5\text{ h}$  of chamber dilution (Figure 4d), there is no clear, systematic evidence of evaporation of these coatings.

In Figure 4, lines representing a diffusion-controlled growth law (Seinfeld and Pandis 2006) are shown,

$$\frac{dD_p}{dt} = \frac{A}{D_p}, \quad [5]$$

where  $D_p$  is the rBC VED. The parameter  $A$  varies with time and was determined by matching the value of  $\frac{dD_p}{dt}$  to the coating thickness of  $160\text{ nm}$  VED rBC cores (thicknesses of  $35$ ,  $120$ ,  $130$ , and  $150\text{ nm}$  for Figures 4a–d, respectively). The agreement between the model and measurement indicate that the coating thickness diameters follow a diffusion-controlled growth rate. During chamber dilution (Figure 4d), there is some deviation from the diffusion-controlled growth law for particles with rBC core VED  $< 100\text{ nm}$ , but this deviation is likely due to a faster wall deposition rate of larger particles (Figure 2). These rBC size-dependent results are consistent with ambient measurements by Moteki et al. (2007) over the western Pacific who also found that the rate of coating growth onto rBC particles follows a diffusion-controlled growth law. These results also support the findings of a recent modeling study that the aging of rBC by condensation of hygroscopic layers is rBC-size dependent (Park et al. 2012). That this simple, one-hydrocarbon system produces results that resemble ambient rBC aging by condensation of SOA supports this experimental protocol as a viable way to probe rBC aging dynamics in more detail with controlled environmental chambers.

Figure 5 presents results from Experiment 5 (Table 1), high- $\text{NO}_x$   $\alpha$ -pinene photooxidation in the presence of fullerene seed particles. Growth of SOA is rapid, indicated by immediate increase of organic mass (Figure 5a), coating thickness (Figure 5b), and change in optical properties (Figure 5c). What differentiates this experiment from the others is that mean coating thickness reaches a peak and then decreases during the irradiation period. Throughout the irradiation period, temperature in the chamber increases, but there is no distinct change in temperature near the peak in coating thickness that would indicate that the aerosol should suddenly start evaporating. Thus, it is likely that the evaporation of coating material is indicative of a chemical change causing particle-phase loss of higher-volatility species. During the irradiation period of Experiment 5, a greater

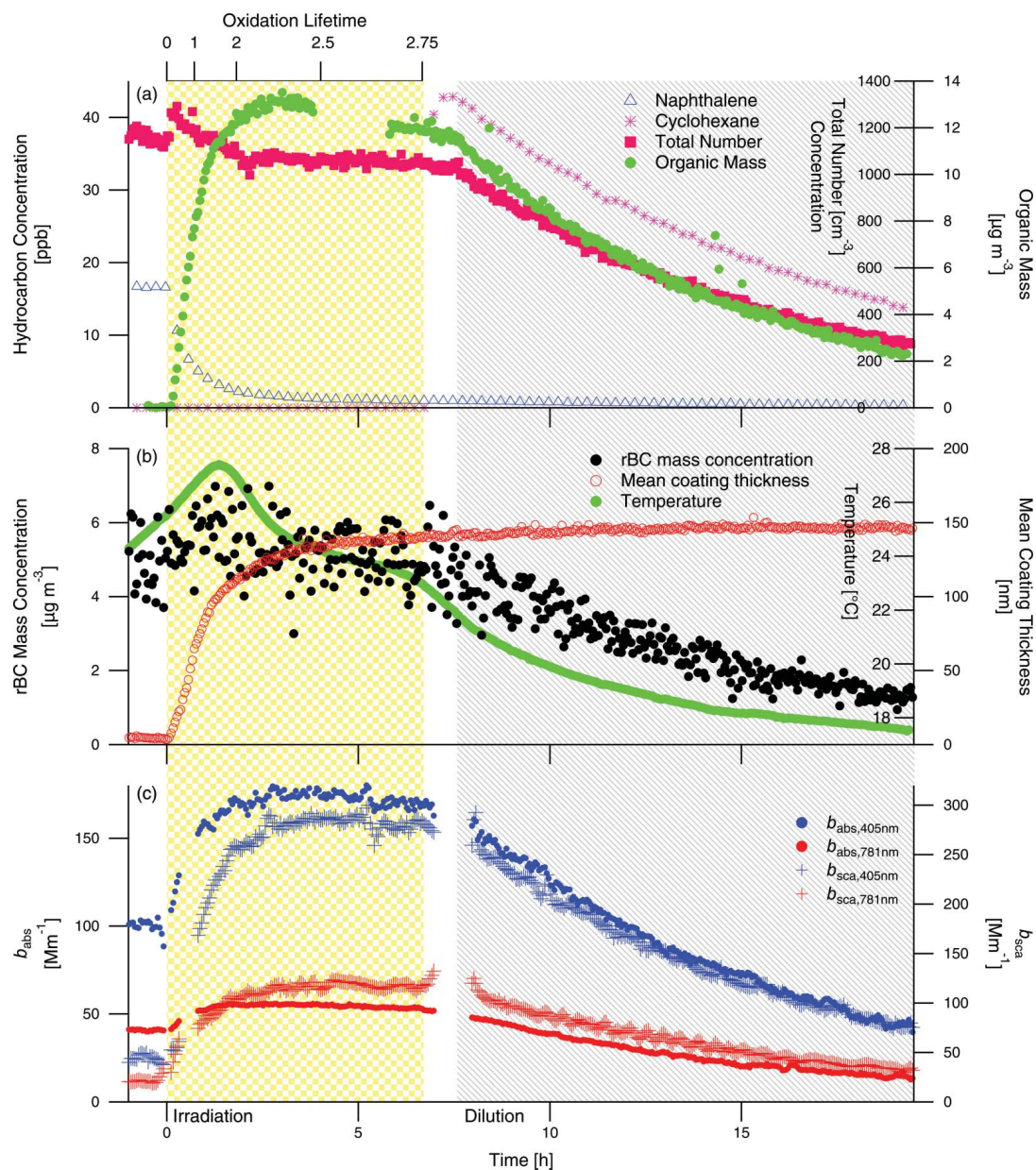


FIG. 3. Experiment 1, naphthalene photooxidation in the presence of rBC seed particles. The shaded regions denote periods of irradiation and dilution of the chamber. (Color figure available online.)

number of oxidation lifetimes (defined in Section 3.4.1) were reached, which may have provided the necessary conditions to allow more chemical aging than the other experiments. The coating evaporation continues after irradiation is stopped, and mean coating thickness does not level off until  $\sim 4.25$  h into the

dilution period. Examination of the evolution of coating thickness for this system (not shown) reveals that a diffusion-limited growth law continues to be valid, and all rBC core sizes exhibit evaporation of coatings. At the very end of the dilution period, a temperature increase of  $\sim 2^\circ\text{C}$  over the final 2 h of the



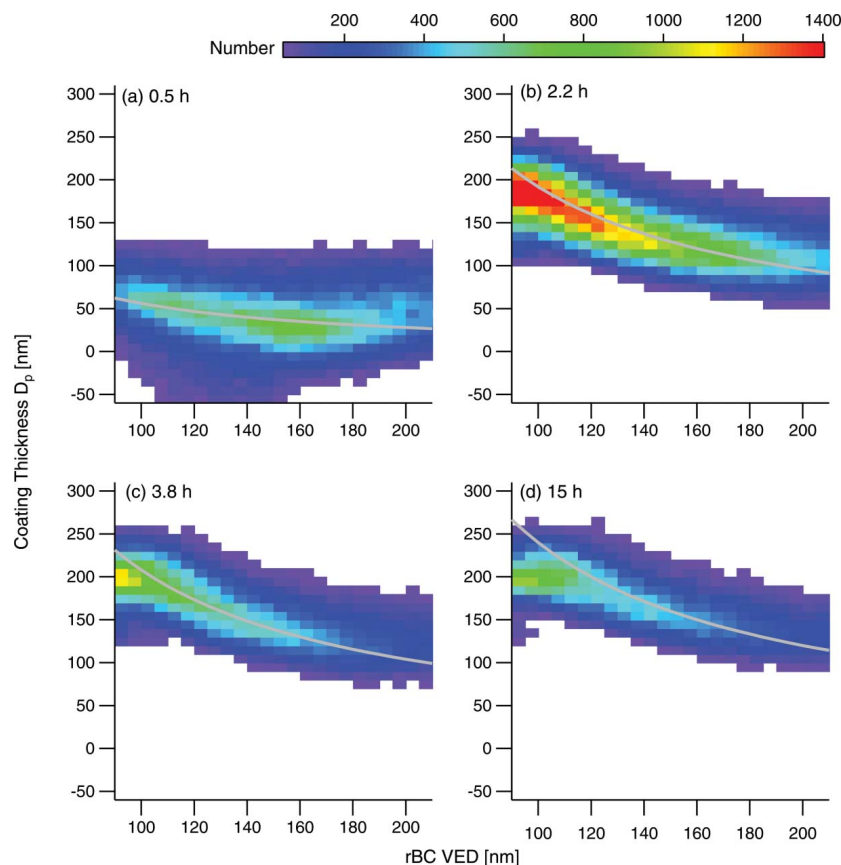


FIG. 4. Evolution of coating thickness in Experiment 1, presented as 2-D histograms of coating thickness determined by fitting the SP2 scattering signal to a core-and-shell Mie model binned versus rBC volume-equivalent diameter. The times are in hours after the onset of irradiation. The gray lines are diffusion-controlled growth laws matched to the coating thickness diameter at an rBC VED of 160 nm. (Color figure available online.)

experiment leads to a coating thickness decrease of  $\sim 5$  nm (calculated from 10-min averaged data, not shown), possibly highlighting the role of temperature in SOA volatility. SOA evaporation during chamber irradiation in this system will be further discussed in Section 3.4.2.

Figure 6 presents the results from Experiment 7 (Table 1), low- $\text{NO}_x$   $\alpha$ -pinene photooxidation in the presence of fullerene seed particles. In this system, SOA growth proceeds more slowly than in the high- $\text{NO}_x$  photooxidation systems as a result of a lower OH concentration produced by  $\text{H}_2\text{O}_2$  versus  $\text{CH}_3\text{ONO}$ . Total particle number concentration (Figure 6a) gives no evidence of SOA nucleation and shows a steady decline during irradiation, owing to wall-deposition and particle coagulation. Wall-deposition rates are slightly faster in the  $\alpha$ -pinene chamber versus the naphthalene chamber (Figure 2) and characteristic time for coagulation is shorter ( $\sim 1.8$  d versus  $\sim 3.4$  d, respectively) (Seinfeld and Pandis 2006) owing to higher initial par-

ticle number concentration. Despite a temperature decrease, which favors condensation of SOA (Figure 6b), there is a slight decrease in mean coating thickness during chamber dilution ( $\sim 8$  nm in  $\sim 10$  h). The flushing rate of the chamber does not change during dilution (see cyclohexane curve in Figure 6a), and the rate of decline in mean coating thickness remains constant as well (Figure 6b) despite the change in temperature trend from the first 5 h of flushing ( $-6.2^\circ\text{C}$ ) to the second 5 h of flushing ( $-0.2^\circ\text{C}$ ). A distinguishing feature of this SOA system is the change in SOA growth rate (see organic mass trace in Figure 6a) coincident with a change in optical properties (see the change in slope of the curves in Figure 6c)  $\sim 4$  h into the chamber irradiation. The change in particle composition during SOA growth in this system will be discussed in Section 3.4.3.

In this work, we focus on results from these three SOA systems in the presence of rBC seed aerosol. For completeness,

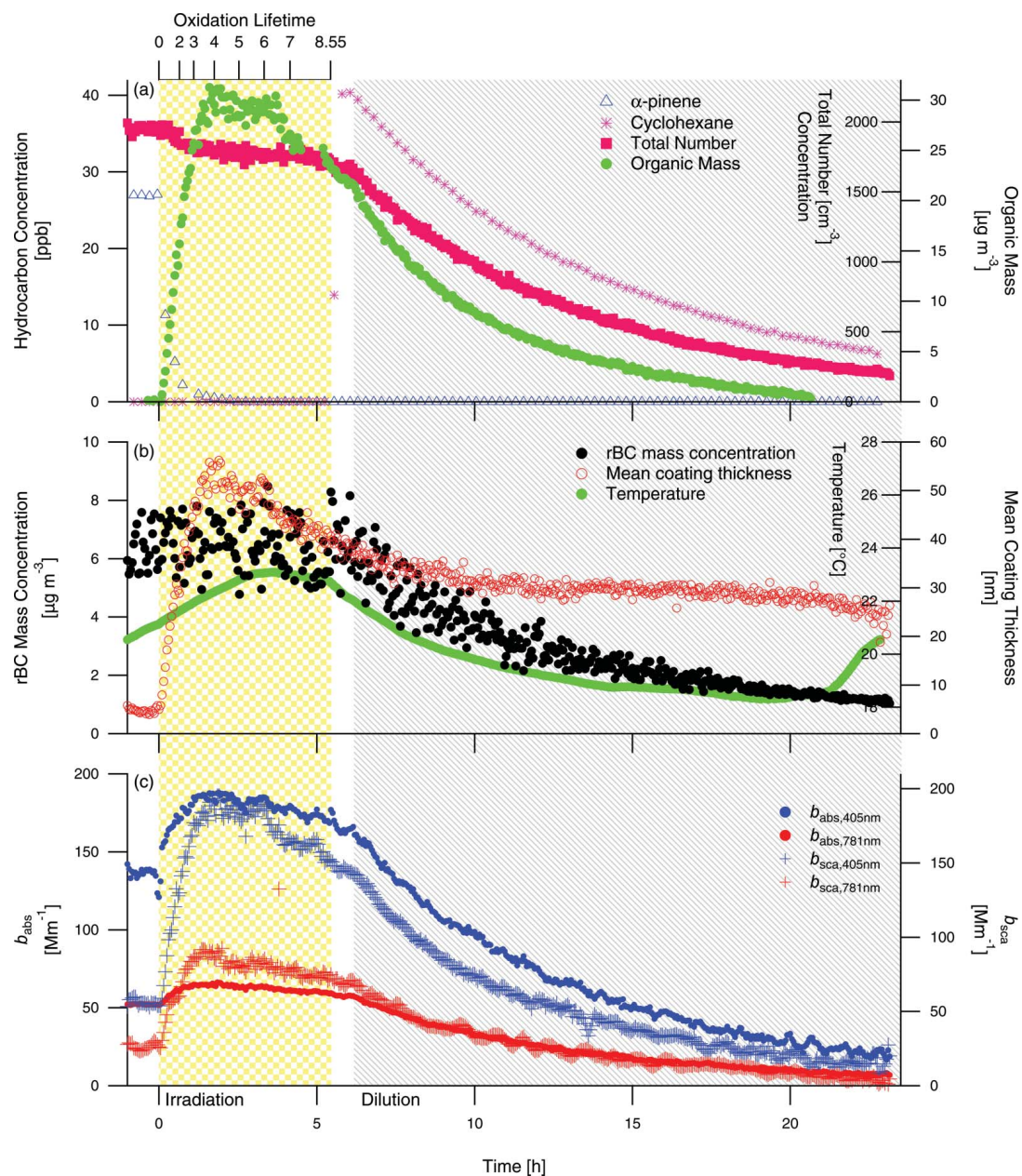


FIG. 5. Experiment 5, high- $\text{NO}_x$   $\alpha$ -pinene photooxidation in the presence of rBC seed particles. The shaded regions denote periods of irradiation and dilution of the chamber. (Color figure available online.)

Table 1 lists all experiments performed for this study. Although not shown in this work, each experiment in Table 1 was characterized by growth of organic layers on the rBC aerosol. In Experiment 3, the growth of coating by coagulation is estimated

to be small ( $\sim 20$  nm coating diameter in  $\sim 16$  h), owing to the modest particle number concentration ( $\sim 11,000 \text{ cm}^{-3}$ ) and coagulation timescale ( $\sim 1.3$  d). In the dual seed experiments with rBC and AS (Experiments 2, 6, and 8) and with rBC and



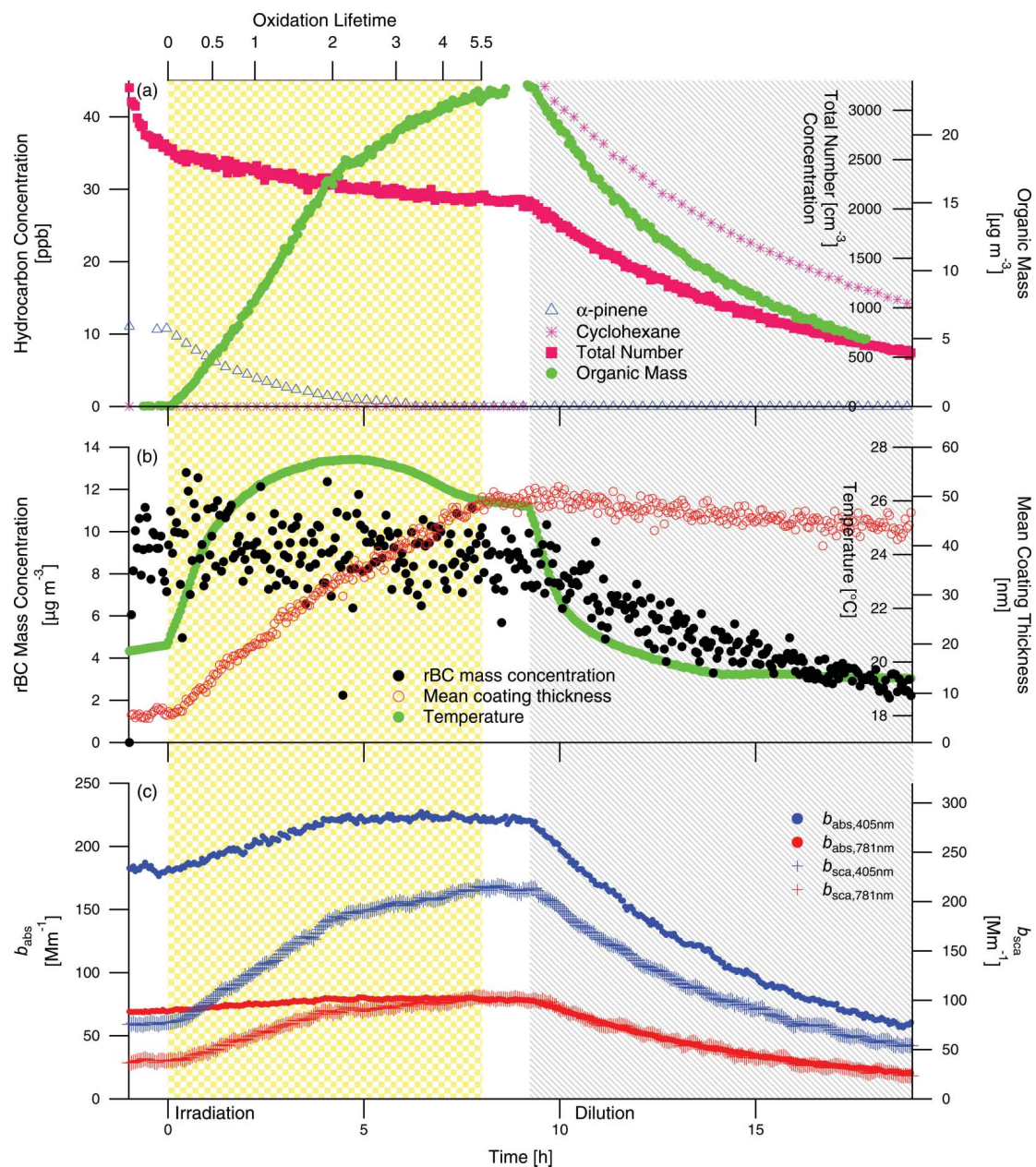


FIG. 6. Experiment 7, low- $\text{NO}_x$   $\alpha$ -pinene photooxidation in the presence of rBC seed particles. The shaded regions denote periods of irradiation and dilution of the chamber. (Color figure available online.)

nucleated SOA (Experiments 4 and 9), growth of coatings occurred during irradiation of the chamber at a faster rate than during the period of mixing prior to irradiation, indicative that growth by condensation of SOA was dominant.

### 3.3. Aerosol Optical Properties

Table 3 presents optical properties of the seed particles and nucleated SOA in this study, including the mass scattering cross section (MSC), mass absorption cross section (MAC),

TABLE 3  
Optical properties of particles in this study (mean  $\pm 1\sigma^a$ )

	$\lambda$	Fullerene soot	Ammonium sulfate	Naphthalene SOA	$\alpha$ -pinene SOA <sup>b</sup>
MSC <sup>c</sup> [ $m^2 g^{-1}$ ]	405 nm	8.39 $\pm$ 0.26	7.74 $\pm$ 0.35	10.93 $\pm$ 1.58	10.21 $\pm$ 0.21
	781 nm	4.28 $\pm$ 0.07	3.21 $\pm$ 0.20	1.30 $\pm$ 0.44	1.14 $\pm$ 0.19
MAC <sup>d</sup> [ $m^2 g^{-1}$ ]	405 nm	20.23 $\pm$ 1.08	<0.82 <sup>e</sup>	0.81 $\pm$ 0.32	<1.90 <sup>e</sup>
	781 nm	7.84 $\pm$ 0.26	<0.13 <sup>e</sup>	<0.08 <sup>e</sup>	<0.30 <sup>e</sup>
$\omega_0^f$	405 nm	0.29 $\pm$ 0.0041	1.00 $\pm$ 0.0065	0.91 $\pm$ 0.012	1.00 $\pm$ 0.012
	781 nm	0.35 $\pm$ 0.0087	0.99 $\pm$ 0.0018	0.99 $\pm$ 0.0018	0.94 $\pm$ 0.026
$\hat{A}_{sca}^g$		1.02	1.34 <sup>e</sup>	3.24	3.34 <sup>e</sup>
$\hat{A}_{abs}^h$		1.44		>3.53 <sup>e</sup>	

<sup>a</sup>Standard deviation during measurement period, not indicative of measurement uncertainty. <sup>b</sup>Low-NO<sub>x</sub> experiment only. <sup>c</sup>MSC = mass scattering cross section. <sup>d</sup>MAC = mass absorption cross section. <sup>e</sup>Absorption coefficient ( $b_{abs}$ ) measurements are at or below detection limit on the PASS-3. <sup>f</sup> $\omega_0$  = single-scatter albedo. <sup>g</sup> $\hat{A}_{sca}$  = scattering Ångström exponent. <sup>h</sup> $\hat{A}_{abs}$  = absorption Ångström exponent.

single-scatter albedo ( $\omega_0$ ), and scattering and absorption Ångström exponents ( $\hat{A}_{sca}$  and  $\hat{A}_{abs}$ , respectively), defined as

$$\hat{A}_{sca/abs} = -\frac{\ln \frac{b_{sca/abs,405nm}}{b_{sca/abs,781nm}}}{\ln \frac{405}{781}}, \quad [6]$$

where  $b_{sca/abs}$  is the observed scattering/absorption coefficient at the specified wavelengths. The fullerene soot and ammonium sulfate values are averages of measurements taken during the hour of chamber mixing prior to the start of irradiation on Experiments 1, 5, and 7 for fullerene soot and Experiments 2, 6, and 8 for ammonium sulfate (before injection of fullerene soot). The nucleated naphthalene and  $\alpha$ -pinene SOA values are taken before rBC was injected into the chamber on Experiments 3, 4, and 9. The mass absorption cross sections of uncoated fullerene soot (20.23  $\pm$  1.08 m<sup>2</sup> g<sup>-1</sup> and 7.84  $\pm$  0.26 m<sup>2</sup> g<sup>-1</sup> at  $\lambda$  = 405 nm and 781 nm, respectively) are higher than reported ensemble averages for uncoated ambient rBC (7.5  $\pm$  1.2 m<sup>2</sup> g<sup>-1</sup> at  $\lambda$  = 550 nm; Bond and Bergstrom 2006), but is certainly within the range of ambient measurements (Kirchstetter et al. 2004). In addition, the mass scattering cross section of ammonium sulfate is higher than previously reported ambient values of 2–4 m<sup>2</sup> g<sup>-1</sup> at  $\lambda$  = 530 nm (Malm et al. 2005a,b). Thus, it is possible that the PASS-3 measurements are biased high due to an offset, perhaps the result of calibrating at much higher aerosol concentrations than those used in the chamber experiments. This bias should not affect the calculations of absorption enhancement presented below.

The value of  $\hat{A}_{abs}$  for fullerene soot (1.44  $\pm$  0.03) is slightly higher than  $\hat{A}_{abs} = 1$  recommended for uncoated rBC (Bond and Bergstrom 2006) but lies within the range of modeled conditions (Lack and Cappa 2010) and ambient measurements of rBC (Gyawali et al. 2009).

Nucleated naphthalene SOA exhibits a small absorption signal at  $\lambda$  = 405 nm; these particles may be classified as “brown carbon,” a mildly absorbing carbonaceous aerosol that is distinct

from black carbon but has progressively stronger absorption at UV wavelengths as compared to visible wavelengths (Andreae and Gelencsér 2006; Wonaschütz et al. 2012). Nakayama et al. (2010) found a similar value for MAC at  $\lambda$  = 355 nm for SOA from the photooxidation of toluene, also an aromatic hydrocarbon. Some authors have detected absorption from gaseous PAH's (Weiner and Harris 1989; Schoemaeker Moreau et al. 2004), but in the present experiments the initial concentration of naphthalene gave no measurable absorption signal in the PASS-3. The measured value of the MAC of 0.81 m<sup>2</sup> g<sup>-1</sup> at  $\lambda$  = 405 nm for naphthalene SOA is within range of previously measured MAC values for brown carbon (Kirchstetter et al. 2004; Hoffer et al. 2006; Yang et al. 2009; Nakayama et al. 2010). For naphthalene SOA,  $\hat{A}_{abs}$  cannot be explicitly determined due to absorption at  $\lambda$  = 781 nm below PASS-3 detection limits, but it is estimated to be  $> \sim 3.5$ , which is indicative of brown carbon (Flowers et al. 2010).

### 3.3.1. Evolution of Aerosol Optical Properties During SOA Growth on rBC Seed

Figures 3c, 5c, and 6c show the absorption and scattering coefficients of the rBC-coated SOA during Experiments 1, 5, and 7, respectively. For all experiments, after UV lights are turned on, a clear increase in absorption coefficients at all wavelengths occurs, while rBC mass remains constant or slightly decreases due to wall deposition. Figure 7 displays absorption coefficient ( $b_{abs}$ ), measured absorption enhancement ( $E_{abs}^m$ ), and single-scatter albedo ( $\omega_0$ ) as a function of mean coating thickness for Experiments 1, 5, and 7, respectively. Time is shown by marker shading on each figure, generally increasing from left to right because the coating thickness grows during irradiation. For the  $\alpha$ -pinene systems (Figures 7b and c), the coating thickness eventually decreases, slightly during dilution of the low-NO<sub>x</sub> system (Figure 7c) and more dramatically during irradiation of the high-NO<sub>x</sub> system (Figure 7b).

As noted above, there is a small absorption signal from the naphthalene SOA at  $\lambda$  = 405 nm, but not at  $\lambda$  = 781 nm. We

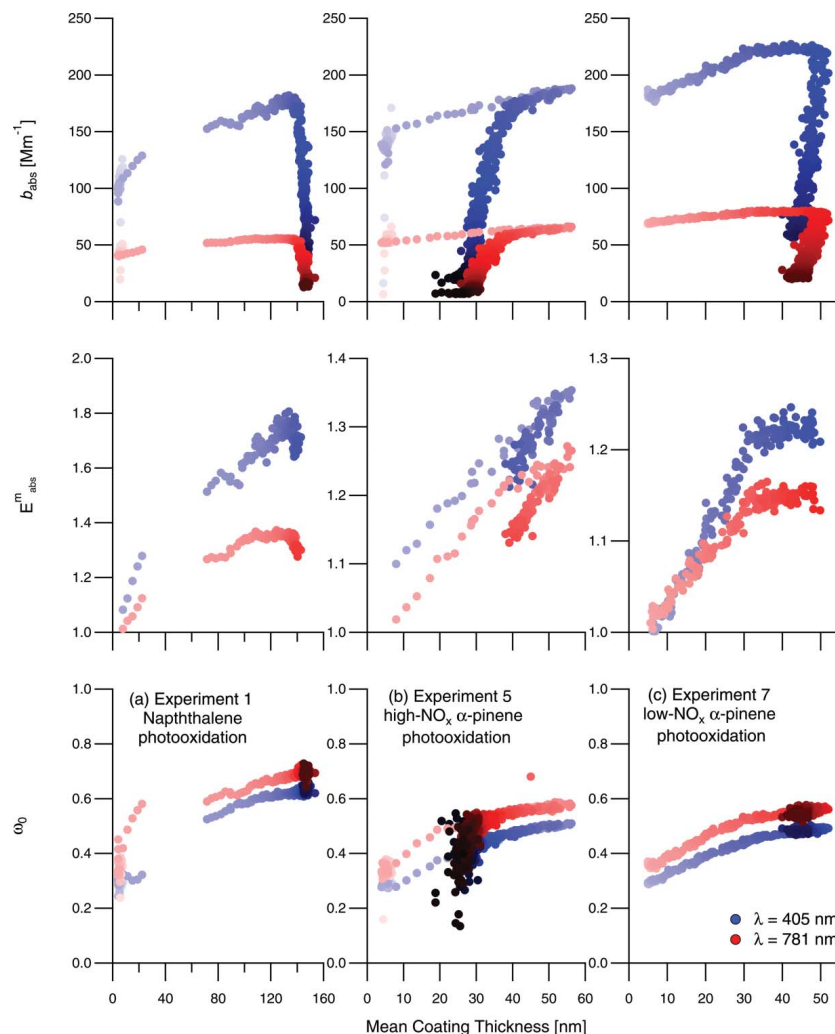


FIG. 7. Aerosol optical properties as a function of mean coating thickness on the fullerene soot seed during Experiment 1, naphthalene photooxidation (a), Experiment 5, high- $\text{NO}_x$   $\alpha$ -pinene photooxidation (b), and Experiment 7, low- $\text{NO}_x$   $\alpha$ -pinene photooxidation (c). Marker shading is a function of time after onset of irradiation, with later times indicated by darker colors. Measured absorption enhancement,  $E_{\text{abs}}^m$  (middle), is presented for the irradiation time period only. (Color figure available online.)

expect that naphthalene SOA condensed onto seed particles will exhibit optical properties similar to nucleated naphthalene SOA, and, therefore, that the absorption enhancement in Experiment 1 (Figure 7a, middle) at  $\lambda = 781$  nm is a result of the lensing effect of the coatings on the rBC seed particles, while at  $\lambda = 405$  nm there is additional absorption from the coating itself (Fuller et al. 1999; Lack and Cappa 2010). In Experiment 1,  $\bar{A}_{\text{abs}}$  increased from  $1.37 \pm 0.029$  to  $1.76 \pm 0.026$  during irradiation, indicating that the aerosol absorption at peak growth is more sensitive to wavelength than the uncoated fullerene soot seed. This is consistent with a small absorption coefficient at

$\lambda = 405$  nm of the condensed naphthalene SOA (Table 3) and exceeds the threshold (1.6) for which attribution of brown carbon to observed absorption can be made (Lack and Cappa 2010). The sharp decrease in  $b_{\text{abs}}$  (Figure 7a, top) occurs simultaneously with the start of chamber dilution. The apparent gap in data between  $\sim 25$  and  $75$  nm thickness is a result of the rapid growth of the coatings during irradiation and the timing of an automatic background signal correction on the PASS-3.

In Experiment 5 (high- $\text{NO}_x$   $\alpha$ -pinene photooxidation; Figure 5), absorption and scattering coefficients increase rapidly with formation of SOA, then decrease during irradiation as the

SOA evaporates. Figure 7b shows the rather dramatic decrease in coating thicknesses by the end of the experiment. Note that after reaching the peak in coating thicknesses,  $b_{\text{abs}}$  and  $\omega_0$  decrease along the same trajectory as the coatings evaporate. The sharp decreases in  $b_{\text{abs}}$  that deviate from this trajectory occur when dilution is initiated, because the decrease in total particle concentration has a larger influence on  $b_{\text{abs}}$  in this experiment than the evaporation of coatings. Single-scatter albedo continues its decline along the same trajectory because  $\omega_0$  is an intensive property whereas  $b_{\text{abs}}$  is an extensive property.

In Experiment 7 (low- $\text{NO}_x$   $\alpha$ -pinene photooxidation; Figure 6), absorption and scattering coefficients increase steadily with the slowly forming SOA. During irradiation, there is a clear change in the rate of increase of these properties, coincident with a change in rate of growth of organic mass (Figure 6a). This change in growth is not seen in the mean coating thickness of 160–180 nm VED rBC cores (Figure 6b). In the absorption coefficient and absorption enhancement especially (Figure 7c), this change indicates that additional absorption enhancement has nearly stopped despite continued growth of organic mass and coating thicknesses. Previous studies have speculated that absorption can be no further enhanced after an extremely thick (>300 nm) coating is present on an absorbing core because the shell may actually shield the core from receiving photons (Bond et al. 2006; Knox et al. 2009; Cross et al. 2010; Lack and Cappa 2010). Because the coatings in Experiment 7 are still relatively thin as compared to those in Experiment 1 (Figure 7a), it is unlikely that further absorption enhancement is being thwarted by an exceptionally thick scattering shell in this experiment.

In all experiments presented, coatings on the rBC cores enhance the light absorption of these particles. Single-scatter albedo increased in all systems as the organic coating thicknesses on the fullerene soot grew. In the naphthalene system, there is clear wavelength dependence of the absorption enhancements (Figure 7a, middle), owing to the wavelength dependence of refractive index of naphthalene SOA. In the  $\alpha$ -pinene systems, evaporation of the coatings leads to a decline of  $\omega_0$  from its peak value, indicating that the changes in optical properties can be considered reversible as the coating material is removed from the rBC cores. The absorption enhancements reported here provide further evidence that the mixing state of rBC in the atmosphere is an important consideration for the radiative forcing by these particles.

### 3.3.2. Comparison of Measured and Modeled Absorption Enhancements

Figure 8 presents a comparison of a core-and-shell Mie model of absorption enhancement, calculated from SP2 measurements as detailed in Section 2.3, to measured absorption enhancement, calculated from PASS-3 measurements, for Experiments 1 (Figure 8a), 5 (Figure 8b), and 7 (Figure 8c).

The rapid increase in absorption enhancement and large enhancement factor ( $\sim 1.8$ ) at  $\lambda = 405$  nm in Experiment 1 (Fig-

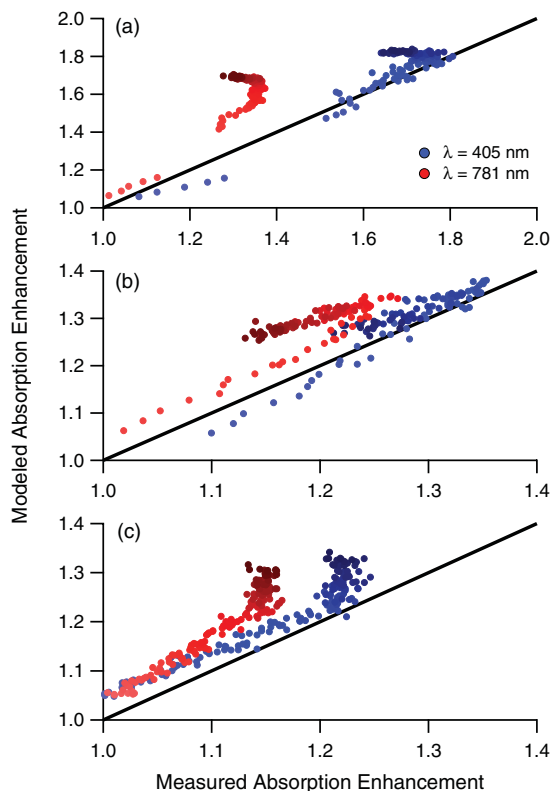


FIG. 8. Comparison of Mie-modeled absorption enhancement to measured absorption enhancement. The measurements are enhancements of  $b_{\text{abs}}$  at  $\lambda = 405$  nm and  $\lambda = 781$  nm measured by the PASS-3 relative to the values measured for the fullerene soot seed particles prior to irradiation. The Mie model enhancements are calculated by the increase in absorption cross section from uncoated rBC cores to rBC cores with the mean coating thickness measured by the SP2 (see text for details). Results for (a) Experiment 1, naphthalene photooxidation, (b) Experiment 5, high- $\text{NO}_x$   $\alpha$ -pinene photooxidation, and (c) Experiment 7, low- $\text{NO}_x$   $\alpha$ -pinene photooxidation are presented. Marker shading is a function of time after onset of irradiation, with later times indicated by darker colors. Data during chamber irradiation only are shown. The solid line is a 1-to-1 line. (Color figure available online.)

ure 8a) are represented by the Mie model, despite the known limitation that the refractive index used in the Mie scattering model does not include an absorbing (imaginary) part. Modeled absorption enhancement at  $\lambda = 781$  nm does not match the measured enhancement well. This discrepancy indicates a wavelength-dependence of the real part of the refractive index of the naphthalene SOA, which we have not captured with our assumed refractive index. If an absorbing refractive index is considered, then we would expect that the real part of refractive index would need to be smaller than 1.5 in order to keep good agreement at  $\lambda = 405$  nm. A further reduction in the real refractive index at  $\lambda = 781$  nm is also necessary to bring modeled and measured enhancement factors into better agreement.



The strong wavelength-dependence of the optical properties of naphthalene SOA is supported by the large  $\tilde{A}_{\text{abs}}$  in Table 3. In addition, Lack and Cappa (2010) found that coatings on rBC by mildly absorbing material reduces the absorption enhancement relative to rBC coated by non-absorbing material, which further explains why the measured absorption enhancements should be lower than modeled enhancements lacking an absorbing part of refractive index and suggests that any agreement between the model and measurements at  $\lambda = 405$  nm is by coincidence.

In Experiment 5 (Figure 8b), the measured increase and decrease in absorption enhancement due to the increase and decrease of coating thickness during irradiation are captured by the model. We expect fairly good agreement using a coating refractive index of  $1.5-0.0i$  based on a recent finding of no significant absorption for  $\alpha$ -pinene SOA (Nakayama et al. 2010) and on recent measurements of  $\alpha$ -pinene SOA refractive index in the range of  $1.42-1.56$  for  $\lambda = 450-700$  nm (Barkey et al. 2007; Yu et al. 2008). The small wavelength-dependence of refractive index (increasing refractive index with decreasing wavelength) reported by Yu et al. (2008) explains the small difference in the measured enhancement factors in this system.

In Experiment 7 (Figure 8c), there was a change in optical properties during the irradiation period (Figures 6c and 7c). This change, in which the measured absorption enhancement ceases to increase, is not reflected by the Mie model because organic coatings are continuing to grow (Figure 6b). To reconcile the differences between the measurements and model, a change in refractive index of the coating material at the time of this deviation needs to be considered. It is possible that a change in the physical properties of the aerosol is occurring as well; however, it is expected that as coatings deposit, the rBC core will collapse so that the aerosol will become more like a core-shell morphology, which should bring the model and measurements into better agreement rather than worse agreement as is observed.

The results presented here, of a core-and-shell Mie scattering model of absorption enhancement during these single-hydrocarbon SOA systems, suggest that a careful treatment of SOA refractive index is needed to fully model aerosol optical properties. SOA from the photooxidation of naphthalene under dry, high- $\text{NO}_x$  conditions has a refractive index with a strong wavelength-dependence which, if not included in the model, will lead to large discrepancies between modeled and measured absorption enhancements. In the  $\alpha$ -pinene system, for which measured refractive indices from previous studies exist, a change in optical properties during photooxidation causes discrepancies between the modeled and measured light absorption to arise during growth of coatings on rBC.

### 3.4. AMS Measurements

#### 3.4.1. Naphthalene SOA

Figure 9 presents normalized (signal at each  $m/z$  is divided by the total organic signal) unit-mass resolution AMS organic mass spectra of SOA formed by the photooxidation of naphthalene in the presence of rBC seed particles (Experiment 1; Figure

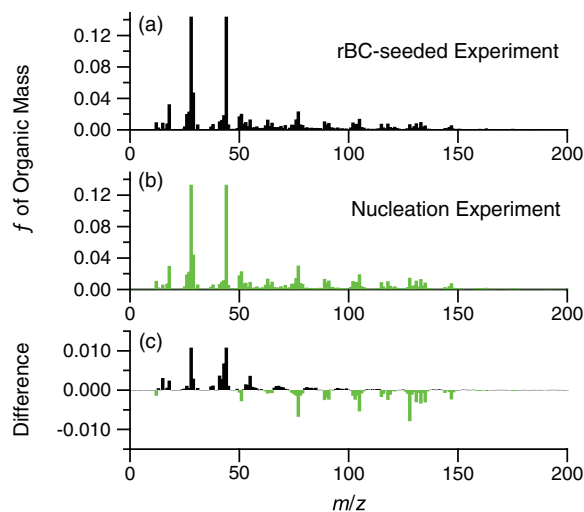


FIG. 9. Normalized unit-mass resolution AMS organic mass spectra at peak growth of (a) naphthalene SOA condensed on rBC seed (Experiment 1), (b) nucleated naphthalene SOA (Experiment 3), and (c) the difference spectrum, calculated relative to the mass spectrum from Experiment 1. On the difference spectrum, positive values denote  $m/z$ 's enriched in the rBC-seeded experiment and negative values denote  $m/z$ 's enriched in the nucleation experiment. (Color figure available online.)

9a), of nucleated naphthalene SOA (Experiment 3; Figure 9b), and the difference spectrum between the two (Figure 9c). The data are taken at the "peak growth" periods of each experiment, defined as the time after the parent hydrocarbon has either been consumed or has ceased to decrease (presumably due to OH being fully consumed) and when growth of suspended particle volume concentration has leveled off through reaching a balance with wall deposition. The number of oxidation lifetimes is defined as  $k_i[\text{OH}]\Delta t$ , where  $k_i$  is the second-order rate constant of species  $i$  reaction with OH,  $[\text{OH}]$  is the gas-phase concentration of OH, and  $\Delta t$  is the exposure time (Kroll et al. 2009). In Figure 9, the data were taken at an oxidation lifetime of about 2.5 in both cases, and there was about 1.3 (7.8% of initial) and 2.1 ppb (9.6% of initial) naphthalene remaining in the chamber at peak growth for Experiments 1 and 3, respectively.

Masses larger than about  $m/z$  275 from the nucleation experiment and masses larger than about  $m/z$  200 from the fullerene soot-seeded experiment are generally at or near the detection limit of the AMS for those individual masses. The detection limits at each  $m/z$  are calculated as three times the standard deviation of the measured signal during sampling with a particle filter in front of the inlet before the start of the experiment. For Experiment 1, a background spectrum, defined as the average mass spectrum during the hour of chamber mixing prior to irradiation, is subtracted from the raw spectra during the rest of the experiment. Thus, the small signal resulting from the fullerene soot seed is removed from the spectrum in Figure 9a.

There is a small difference between the SOA composition formed by nucleation and condensation onto fullerene soot for this system. The largest change in mass fraction at any given  $m/z$  is about  $\pm 1\%$  of total organic mass. This difference is most prominent at  $m/z$  44, which is the mass with the largest fraction in the organic spectra (Figures 9a and b). The discrepancies in the particular  $m/z$ 's between the two experiments may arise owing to a different organic loading at the times of interest (which could force the chemistry through a different pathway); for Experiment 1, organic mass was  $6.5 \pm 0.08 \mu\text{gm}^{-3}$ , while for Experiment 3, organic mass was  $18.2 \pm 0.22 \mu\text{gm}^{-3}$ . Because the spectra are reported at the same oxidation lifetime, it is expected that these are reported at the most comparable conditions possible. Due to the uncertainty of AMS measurements, a change of  $\pm 1\%$  should be viewed as small.

Although not shown in this work, similar AMS mass spectra comparisons were made at peak growth for the AS + rBC seeded experiment (Experiment 2 in Table 1) compared to the two experiments presented above. The largest difference in the mass spectra arises from interferences from sulfate at  $m/z$  48 and 64, which is remedied by properly adjusting the AMS fragmentation table. After adjustment, mass spectral differences are on the order of those shown in Figure 9d. These small differences in mass spectra may mean that the optical properties of the nucleated SOA reported in Table 3 may differ from the condensed SOA onto rBC seed. However, because the mass spectral differences are small among all experiments compared, one concludes that the fullerene soot seed does not affect the composition of the condensed naphthalene SOA more so than condensation on the more conventional AS seed as compared to nucleated SOA.

#### 3.4.2. High- $\text{NO}_x$ $\alpha$ -pinene SOA

During high- $\text{NO}_x$   $\alpha$ -pinene photooxidation (Experiment 5), the mean coating thickness initially increases rapidly, achieves a maximum, then decreases for the remainder of the irradiation period (Figure 5b). Figures 10a and b present normalized AMS mass spectra at two times during irradiation in Experiment 5, at oxidation lifetimes of 9, near the end of the irradiation period, and 1, during the early rapid growth of SOA, respectively. Figure 10c presents the difference between these two mass spectra, relative to the earlier mass spectra, where positive values denote mass fragments enriched at the end of irradiation. Typically, the dominant mass fragments in AMS organic mass spectra of ambient aerosol are at  $m/z$  44, which represents highly oxygenated organic species with low volatility, and at  $m/z$  43, which represents less oxygenated semivolatile species (Ng et al. 2010). The mass fractions of these  $m/z$ ,  $f_{44}$ , and  $f_{43}$ , are defined as the mass at  $m/z$  44 and  $m/z$  43, respectively, divided by the total organic mass, which is the sum of masses at all  $m/z$  in the AMS organic spectra.  $f_{43}$  is initially  $\sim 15\%$  of the total organic mass (Figure 10b) and decreases to  $\sim 13\%$  (Figure 10a) near the end of the irradiation period. Simultaneously,  $f_{44}$  increases from  $\sim 8\%$  (Figure 10b) to  $\sim 12\%$  (Figure 10a) of total organic mass during the irradiation period. These results indicate that the aerosol is

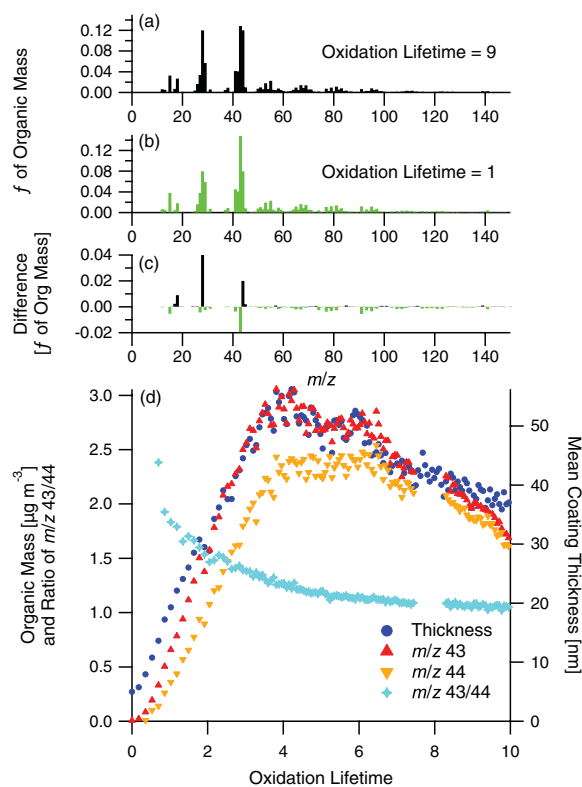


FIG. 10. Normalized unit-mass resolution AMS organic mass spectra from Experiment 5, high- $\text{NO}_x$   $\alpha$ -pinene photooxidation in the presence of fullerene soot, at (a) oxidation lifetime = 9 (after peak growth has been reached) and (b) oxidation lifetime = 1 (during rapid growth), (c) the difference spectrum, calculated relative to the earlier mass spectrum, and (d) comparison of AMS  $m/z$  43 and 44 and ratio of  $m/z$  43/44 with mean coating thickness measured by the SP2. On the difference spectrum, positive values denote  $m/z$ 's enriched in the later condensed SOA and negative values denote  $m/z$ 's enriched in the earliest condensed SOA. Note that dilution of the chamber began at an oxidation lifetime of approximately 9. (Color figure available online.)

transitioning from a semi-volatile to a lower volatility state, as is commonly observed during chemical aging of aerosol (Ng et al. 2010).

From the time series traces (Figure 10d) of AMS  $m/z$  43 and 44 and mean coating thickness on rBC as measured by the SP2, AMS  $m/z$  43 clearly traces the mean coating thickness ( $R^2 = 0.97$ ), capturing the decrease in thickness with time quite well, deviating only after chamber dilution has begun. AMS  $m/z$  44 lags behind  $m/z$  43 in formation, and, therefore, does not trace coating thickness as well ( $R^2 = 0.89$ ). Note that even though  $m/z$  44 decreases during the experiment,  $f_{44}$  is continuously increasing, as stated above, meaning that the other mass fragments in the AMS mass spectra are decreasing more rapidly than  $m/z$  44. This is shown in Figure 10d by the signals of  $m/z$  43 and 44 approaching a similar value towards the end of the irradiation

period. After the initial rapid growth, the  $m/z$  43/44 ratio continuously decreases due to  $f_{44}$  continuously increasing throughout the experiment. While chemical aging in such a way that converts species yielding high  $f_{43}$  to higher  $f_{44}$  in the AMS may explain these trends, the combination of single-particle coating thickness measured by the SP2 and the bulk organic mass spectra measured by the AMS suggest that the more semivolatile species are actually evaporating from the aerosol. The SP2 unambiguously shows changes in single particles, whereas AMS measurements of small decreases in organic mass alone may have been attributed to other processes, such as chamber wall deposition.

### 3.4.3. Low- $\text{NO}_x$ $\alpha$ -pinene SOA

In the evolution of various measured parameters during the low- $\text{NO}_x$   $\alpha$ -pinene photooxidation (Experiment 7), mean coating thickness steadily increased as SOA was formed (Figure 6b). About halfway through the irradiation period, a decrease in the rate of change of the absorption and scattering coefficients occurred (Figure 6c), coincident with a decrease in the growth rate of total organic mass concentration measured by the AMS (Figure 6a). This change during irradiation occurred at an oxidation lifetime of  $\sim 2$  ( $\sim 4$  h after the onset of irradiation).

Figures 11a and b present normalized AMS mass spectra at oxidation lifetimes of 3 and 1, respectively, on either side of the change in aerosol growth rate. Figure 11c presents the difference spectrum relative to the earlier spectrum and shows a decrease in  $f_{43}$ . Figure 11d shows the evolution of various AMS mass fractions with oxidation lifetime in addition to the absorption and scattering coefficients at  $\lambda = 405$  nm measured by the PASS-3. A shift in optical properties is evident at an oxidation lifetime of 2, while  $f_{43}$  and  $f_{44}$  continually change during the experiment and show no clear shift. The other mass fractions presented in Figure 11d also change continually throughout the experiment, although at different rates relative to each other. Some mass fractions, namely  $f_{1-50}$  and  $f_{50-100}$ , change much more rapidly during the early part of irradiation and then begin to approach a relatively constant value after an oxidation lifetime of 2. Throughout the entire period displayed in Figure 11d, organic mass is growing and the raw  $m/z$ 's are increasing; thus, the changes in mass fractions reflect the fact that different mass fragments are growing at different rates relative to each other, rather than by loss of certain fragments.

While  $m/z$  43 and 44 are important individual mass fragments in the AMS mass spectra, they fail to capture the change in aerosol behavior that occurs at an oxidation lifetime of 2 in this system. Examining a wider range of mass fragments in the AMS mass spectra reveals that the aerosol composition is continually evolving during the irradiation period. This change in composition is likely accompanied by a change in refractive index, explaining the shift in optical properties despite steady growth of rBC coating thicknesses. This experiment demonstrates that measurement of aerosol optical properties can help guide the analysis of data from other instruments, namely the AMS. In

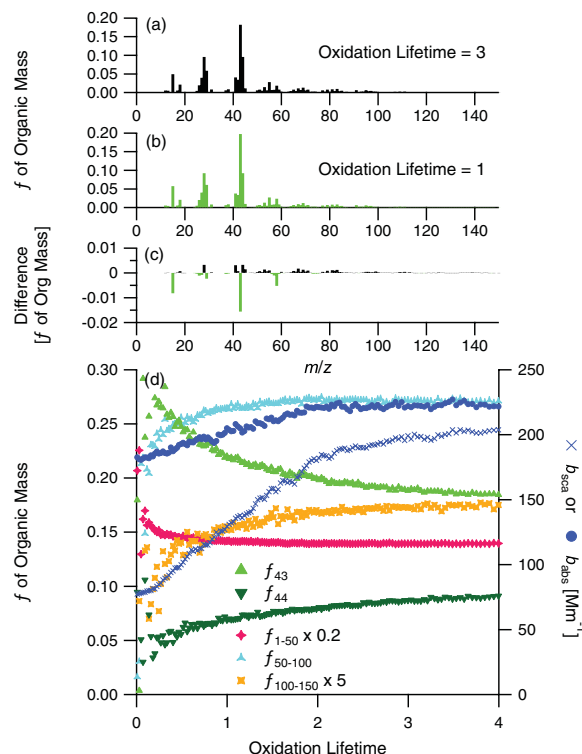


FIG. 11. Normalized unit-mass resolution AMS organic mass spectra from Experiment 7, low- $\text{NO}_x$   $\alpha$ -pinene photooxidation in the presence of fullerene soot, at (a) an oxidation lifetime = 3 (during the slower growth rate after the shift in optical properties) and (b) an oxidation lifetime = 1 (during the more rapid growth rate before the change in optical properties), (c) the difference spectrum, calculated relative to the earlier mass spectrum, and (d) comparison of  $f_{43}$ ,  $f_{44}$ ,  $f_{1-50}$  (scaled by 0.2),  $f_{50-100}$ , and  $f_{100-150}$  (scaled by 5) from the AMS with the scattering and absorption coefficients at  $\lambda = 405$  nm measured by the PASS-3. On the difference spectrum, positive values denote  $m/z$ 's enriched in the later condensed SOA and negative values denote  $m/z$ 's enriched in the earliest condensed SOA. (Color figure available online.)

the low- $\text{NO}_x$   $\alpha$ -pinene photooxidation system, the SOA optical properties change with time, and could be used as a model system to help understand the evolution of atmospheric SOA optical properties.

## 4. CONCLUSIONS

In this work, we demonstrate the utility of employing fullerene soot, a surrogate for refractory black carbon, as a seed aerosol in chamber studies of secondary organic aerosol formation, when done in conjunction with the single-particle soot photometer. Particle-by-particle measurement of the dynamics of the organic coating thickness on the rBC seed over the course of SOA formation allows evaluation of the rate of growth as a function of particle size. An experimental strategy is implemented in which a period of VOC oxidation and SOA growth is

followed by one in which growth is quenched while the chamber undergoes dilution. The dilution phase is used as a means to assess SOA volatility by measuring the possible evaporation of coatings on the rBC seed. In the experiments presented here, a 3- $\lambda$  photoacoustic soot spectrometer is used to measure the optical properties of the uncoated rBC seed, initially, and the coated rBC seed during the course of SOA formation. These measurements, coupled with the application of a core-and-shell Mie scattering model, allow one to infer the optical properties of the SOA. Application of a prototype single-particle angularly-resolved light scattering instrument confirms that the uncoated rBC particles are nonspherical. Important to understanding the effect rBC has on SOA formation is whether or not SOA condensed onto rBC seed is chemically and optically similar to nucleated SOA under dry conditions. High-resolution Aerodyne aerosol mass spectrometer measurements for the three systems considered here, naphthalene photooxidation and photooxidation of  $\alpha$ -pinene under both high- and low- $\text{NO}_x$  conditions, confirm that the composition of SOA coating rBC seed particles differs from homogeneously nucleated SOA by no more than condensing SOA on the more conventional ammonium sulfate seed used in many chamber experiments, so that the use of rBC as a seed is not expected to alter the basic chemistry of SOA formation under dry conditions. Both SP2 and PASS-3 measurements reveal a change in the SOA coating and particle optical properties during SOA growth in the high- $\text{NO}_x$   $\alpha$ -pinene system, which is mirrored by a corresponding change in the AMS mass spectra. The combination of SP2 and AMS measurements in this system suggest that semivolatile species are evaporating from the aerosol during chemical aging. A change in optical properties during SOA growth in the low- $\text{NO}_x$   $\alpha$ -pinene system is mirrored by a change in organic growth rate and AMS mass spectra, but not in single-particle coating thicknesses. Exploration of a fundamental explanation of the chemistry leading to these changes lies beyond the scope of the present work. We have provided a framework by which future studies of SOA optical properties and single-particle growth dynamics may be explored in environmental chambers.

## REFERENCES

- Abel, S. J., Haywood, J. M., Highwood, E. J., Li, J., and Buseck, P. R. (2003). Evolution of Biomass Burning Aerosol Properties from an Agricultural Fire in Southern Africa. *Geophys. Res. Lett.*, 30(15):1783, doi:10.1029/2003GL017342.
- Andreae, M. O., and Gelencsér, A. (2006). Black Carbon or Brown Carbon? The Nature of Light-Absorbing Carbonaceous Aerosols. *Atmos. Chem. Phys.*, 6:3131–3148, doi:10.5194/acp-6-3131-2006.
- Bahreini, R., Ervens, B., Middlebrook, A. M., Warneke, C., de Gouw, J. A., DeCarlo, P. F., Jimenez, J. L., Brock, C. A., Neuman, J. A., Ryerson, T. B., Stark, H., Atlas, E., Brioude, J., Fried, A., Holloway, J. S., Peischl, J., Richter, D., Walega, J., Weibring, P., Wollny, A. G., and Fehsenfeld, F. C. (2009). Organic Aerosol Formation in Urban and Industrial Plumes Near Houston and Dallas, Texas. *J. Geophys. Res.*, 114:D00F16, doi:10.1029/2008JD011493.
- Barkey, B., Paulson, S. E., and Chung, A. (2007). Genetic Algorithm Inversion of Dual Polarization Polar Nephelometer Data to Determine Aerosol Refractive Index. *Aerosol Sci. Technol.*, 41(8):751–760, doi:10.1080/02786820701432640.
- Baumgardner, D., Kok, G. L., and Raga, G. B. (2004). Warming of the Arctic Lower Stratosphere by Light Absorbing Particles. *Geophys. Res. Lett.*, 31:L06117, doi:10.1029/2003GL018883.
- Baumgardner, D., Popovicheva, O., Allan, J., Bernardoni, V., Cao, J., Cavalli, F., Cozic, J., Diapouli, E., Eleftheriadis, K., Genberg, P. J., Gonzalez, C., Gysel, M., John, A. T. W., Kirchstetter, T. A., Kuhlbusch, J., Laborde, M., Lack, D., Müller, T., Niessner, R., Petzold, A., Piazzalunga, A., Putaud, J. P., Schwarz, J., Sheridan, P., Subramanian, R., Swietlicki, E., Valli, G., Vecchi, R., and Viana, M. (2012). Soot Reference Materials for Instrument Calibration and Intercomparisons: A Workshop Summary with Recommendations. *Atmos. Meas. Tech.*, 5:1869–1887, doi:10.5194/amt-5-1869-2012.
- Böhren, C. F., and Huffman, D. R. (1998). *Absorption and Scattering of Light by Small Particles*. John Wiley & Sons, Inc., New York.
- Bond, T. C., and Bergstrom, R. W. (2006). Light Absorption by Carbonaceous Particles: An Investigative Review. *Aerosol Sci. Technol.*, 40(1):27–67, doi:10.1080/02786820500421521.
- Bond, T. C., Habib, G., and Bergstrom, R. W. (2006). Limitations in the Enhancement of Visible Light Absorption Due to Mixing State. *J. Geophys. Res.*, 111:D20211, doi:10.1029/2006JD007315.
- Bueno, P. A., Havey, D. K., Mulholland, G. W., Hodges, J. T., Gillis, K. A., Dickerson, R. R., and Zachariah, M. R. (2011). Photoacoustic Measurements of Amplification of the Absorption Cross Section for Coated Soot Aerosols. *Aerosol Sci. Technol.*, 45(10):1217–1230, doi:10.1080/02786826.2011.587477.
- Canagaratna, M. R., Jayne, J. T., Jimenez, J. L., Allan, J. D., Alfarra, M. R., Zhang, Q., Onasch, T. B., Drewnick, F., Coe, H., Middlebrook, A., Delia, A., Williams, L. R., Trimborn, A. M., Northway, M. J., DeCarlo, P. F., Kolb, C. E., Davidovits, P., and Worsnop, D. R. (2007). Chemical and Microphysical Characterization of Ambient Aerosols with the Aerodyne Aerosol Mass Spectrometer. *Mass Spectrom. Rev.*, 26(2):185–222, doi:10.1002/mas.20115.
- Chan, A. W. H., Kautzman, K. E., Chhabra, P. S., Surratt, J. D., Chan, M. N., Crounse, J. D., Kürten, A., Wennberg, P. O., Flagan, R. C., and Seinfeld, J. H. (2009). Secondary Organic Aerosol Formation from Photooxidation of Naphthalene and Alkyl-naphthalenes: Implications for Oxidation of Intermediate Volatility Organic Compounds (IVOCs). *Atmos. Chem. Phys.*, 9:3049–3060, doi:10.5194/acp-9-3049-2009.
- Chan, A. W. H., Chan, M. N., Surratt, J. D., Chhabra, P. S., Loza, C. L., Crounse, J. D., Yee, L. D., Flagan, R. C., Wennberg, P. O., and Seinfeld, J. H. (2010a). Role of Aldehyde Chemistry and  $\text{NO}_x$  Concentrations in Secondary Organic Aerosol Formation. *Atmos. Chem. Phys.*, 10:7169–7188, doi:10.5194/acp-10-7169-2010.
- Chan, T. W., et al. (2010b). Observations of OM/OC and Specific Attenuation Coefficients (SAC) in Ambient Fine PM at a Rural Site in Central Ontario, Canada. *Atmos. Chem. Phys.*, 10:2393–2411, doi:10.5194/acp-10-2393-2010.
- Chirico, R., DeCarlo, P. F., Heringa, M. F., Tritscher, T., Richter, R., Prévôt, A. S. H., Dommen, J., Weingartner, E., Wehrle, G., Gyse, M., Laborde, M., and Baltensperger, U. (2010). Impact of Aftertreatment Devices on Primary Emissions and Secondary Organic Aerosol Formation Potential from in-use Diesel Vehicles: Results from Smog Chamber Experiments. *Atmos. Chem. Phys.*, 10(11):545–11, 563, doi:10.5194/acp-10-11545-2010.
- Chung, S. H., and Seinfeld, J. H. (2002). Global Distribution and Climate Forcing of Carbonaceous Aerosols. *J. Geophys. Res.*, 107(D19):4407, doi:10.1029/2001JD001397.
- Cocker, D. R., Flagan, R. C., and Seinfeld, J. H. (2001). State-of-the-art Chamber Facility for Studying Atmospheric Aerosol Chemistry. *Environ. Sci. Technol.*, 35(12):2594–2601, doi:10.1021/es0019169.
- Crosso, E. S., Onasch, T. B., Ahern, A., Wrobel, W., Slowik, J. G., Olfert, J., Lack, D. A., Massoli, P., Cappaf, C. D., Schwarz, J. P., Spackman, J. R., Fahey, D. W., Sedlacek, A., Trimborn, A., Jayneb, J. T., Freedman, A., Williams, L. R., Ng, N. L., Mazzoleni, C., Dubey, M., Brem, B., Koki, G., Subramanian, R., Freitag, S., Clarke, A., Thornhill, D., Marrk,



- L. C., Kolb, C. E., Worsnop, D. R., and Davidovits, P. (2010). Soot Particle Studies—Instrument Inter-Comparison—Project Overview. *Aerosol Sci. Technol.*, 44(8):592–611, doi:10.1080/02786826.2010.482113.
- Crump, J. G., and Seinfeld, J. H. (1981). Turbulent Deposition and Gravitational Sedimentation of an Aerosol in a Vessel of Arbitrary Shape. *J. Aerosol Sci.*, 12(5):405–415, doi:10.1016/0021-8502(81)90036-7.
- DeCarlo, P. F., Slowik, J. G., Worsnop, D. R., Davidovits, P., and Jimenez, J. L. (2004). Particle Morphology and Density Characterization by Combined Mobility and Aerodynamic Diameter Measurements. Part I: Theory. *Aerosol Sci. Technol.*, 38:1185–1205, doi:10.1080/027868290903907.
- DeCarlo, P. F., Kimmel, J. R., Trimborn, A., Northway, M. J., Jayne, J. T., Aiken, A. C., Gonin, M., Fuhrer, K., Horvath, T., Docherty, K. S., Worsnop, D. R., and Jimenez, J. L. (2006). Field-Deployable, High-Resolution, Time-of-Flight Aerosol Mass Spectrometer. *Anal. Chem.*, 78(24):8281–8289, doi:10.1021/ac061249n.
- Dick, W. D., McMurry, P. H., and Bottiger, J. R. (1994). Size- and Composition-Dependent Response of the DAWN-A Multiangle Single-Particle Optical Detector. *Aerosol Sci. Technol.*, 20(4):345–362, doi:10.1080/02786829408959690.
- Dick, W. D., Ziemann, P. J., Huang, P.-F., and McMurry, P. H. (1998). Optical Shape Fraction Measurements of Submicrometre Laboratory and Atmospheric Aerosols. *Meas. Sci. Technol.*, 9(2):183–196, doi:10.1088/0957-0233/9/2/006.
- Flowers, B. A., Dubey, M. K., Mazzoleni, C., Stone, E. A., Schauer, J. J., Kim, S.-W., et al. (2010). Optical-Chemical-Microphysical Relationships and Closure Studies for Mixed Carbonaceous Aerosols Observed at Jeju Island: 3-Laser Photoacoustic Spectrometer, Particle Sizing, and Filter Analysis. *Atmos. Chem. Phys.*, 10(21):10, 387–10, 398, doi:10.5194/acp-10-10387-2010.
- Fruin, S. A., Winer, A. M., and Rodes, C. E. (2004). Black Carbon Concentrations in California Vehicles and Estimation of in-vehicle Diesel Exhaust Particulate Matter Exposures. *Atmos. Environ.*, 38(25):4123–4133, doi:10.1016/j.atmosenv.2004.04.026.
- Fuller, K. A., Malm, W. C., and Kreidenweis, S. M. (1999). Effects of Mixing on Extinction by Carbonaceous Particles. *J. Geophys. Res.*, 104(D13):15, 941–15, 954, doi:10.1029/1998JD100069.
- Gao, R. S., et al. (2007). A Novel Method for Estimating Light-Scattering Properties of Soot Aerosols Using a Modified Single-Particle Soot Photometer. *Aerosol Sci. Technol.*, 41(2):125–135, doi:10.1080/02786820601118398.
- Guenther, A., et al. (1995). A Global Model of Natural Volatile Organic Compound Emissions. *J. Geophys. Res.*, 100(D5):8873–8892.
- Gyawali, M., Arnott, W., Lewis, K., and Moosmüller, H. (2009). In Situ Aerosol Optics in Reno, NV, USA During and After the Summer 2008 California Wildfires and the Influence of Absorbing and Non-Absorbing Organic Coatings on Spectral Light Absorption. *Atmos. Chem. Phys.*, 9:8007–8015, doi:10.5194/acp-9-8007-2009.
- Gysel, M., Laborde, M., Olfert, J. S., Subramanian, R., and Gröhn, A. J. (2011). Effective Density of Aquadag and Fullerene Soot Black Carbon Reference Materials Used for SP2 Calibration. *Atmos. Meas. Tech.*, 4:2851–2858, doi:10.5194/amt-4-2851-2011.
- Hoffer, A., Gelencsér, A., Guyon, P., Kiss, G., Schmid, O., Frank, G. P., et al. (2006). Optical Properties of Humic-Like Substances (HULIS) in Biomass-Burning Aerosols. *Atmos. Chem. Phys.*, 6:3563–3570, doi:10.5194/acp-6-3563-2006.
- Huffman, J. A., Jayne, J. T., Drewnick, F., Aiken, A. C., Onasch, T., Worsnop, D. R., et al. (2005). Design, Modeling, Optimization, and Experimental Tests of a Particle Beam Width Probe for the Aerodyne Aerosol Mass Spectrometer. *Aerosol Sci. Technol.*, 39(12):1143–1163, doi:10.1080/02786820500423782.
- Jacobson, M. Z. (2006). Effects of Externally-Through-Internally-Mixed Soot Inclusions within Clouds and Precipitation on Global Climate. *J. Phys. Chem. A*, 110(21):6860–6873, doi:10.1021/jp056391r.
- Jayne, J. T., Leard, D. C., Zhang, X., Davidovits, P., Smith, K. A., Kolb, C. E., et al. (2000). Development of an Aerosol Mass Spectrometer for Size and Composition Analysis of Submicron Particles. *Aerosol Sci. Technol.*, 33(1–2):49–70, doi:10.1080/027868200410840.
- Johnson, K. S., Zuberi, B., Molina, L. T., Molina, M. J., Iedema, M. J., Cowin, J. P., et al. (2005). Processing of Soot in an Urban Environment: Case Study from the Mexico City Metropolitan Area. *Atmos. Chem. Phys.*, 5:3033–3043, doi:10.5194/acp-5-3033-2005.
- Keywood, M. D., Varutbangkul, V., Bahreini, R., Flagan, R. C., and Seinfeld, J. H. (2004). Secondary Organic Aerosol Formation from the Ozonolysis of Cycloalkenes and Related Compounds. *Environ. Sci. Technol.*, 38(15):4157–4164, doi:10.1021/es035363o.
- Khalizov, A. F., Xue, H., Wang, L., Zheng, J., and Zhang, R. (2009a). Enhanced Light Absorption and Scattering by Carbon Soot Aerosol Internally Mixed with Sulfuric Acid. *J. Phys. Chem. A*, 113(6):1066–1074, doi:10.1021/jp807531n.
- Khalizov, A. F., Zhang, R., Zhang, D., Xue, H., Pagels, J., and McMurry, P. H. (2009b). Formation of Highly Hygroscopic Soot Aerosols Upon Internal Mixing with Sulfuric Acid Vapor. *J. Geophys. Res.*, 114:D05208, doi:10.1029/2008JD010595.
- Kirchner, U., Vogt, R., Natzeck, C., and Goschnick, J. (2003). Single Particle MS, SNMS, SIMS, XPS, and FTIR Spectroscopic Analysis of Soot Particles During the AIDA Campaign. *J. Aerosol Sci.*, 34(10):1323–1346, doi:10.1016/S0021-8502(03)00362-8.
- Kirchstetter, T. W., Novakov, T., and Hobbs, P. V. (2004). Evidence that the Spectral Dependence of Light Absorption by Aerosols is Affected by Organic Carbon. *J. Geophys. Res.*, 109:D21208, doi:10.1029/2004JD004999.
- Kleeman, M. J., Schauer, J. J., and Cass, G. R. (2000). Size and Composition Distribution of Fine Particulate Matter Emitted from Motor Vehicles. *Environ. Sci. Technol.*, 34(7):1132–1142, doi:10.1021/es981276y.
- Knox, A., Evans, G. J., Brook, J. R., Yao, X., Jeong, C.-H., Godri, K. J., et al. (2009). Mass Absorption Cross-Section of Ambient Black Carbon Aerosol in Relation to Chemical Age. *Aerosol Sci. Technol.*, 43(6):522–532, doi:10.1080/02786820902777207.
- Kroll, J. H., Smith, J. D., Che, D. L., Kessler, S. H., Worsnop, D. R., and Wilson, K. R. (2009). Measurement of Fragmentation and Functionalization Pathways in the Heterogeneous Oxidation of Oxidized Organic Aerosol. *Phys. Chem. Chem. Phys.*, 11(36):8005–8014, doi:10.1039/b905289e.
- Laborde, M., Mertes, P., Zieger, P., Dommen, J., Baltensperger, U., and Gysel, M. (2012). Sensitivity of the Single Particle Soot Photometer to Different Black Carbon Types. *Atmos. Meas. Tech.*, 5:1031–1043, doi:10.5194/amt-5-1031-2012.
- Lack, D. A., and Cappa, C. D. (2010). Impact of Brown and Clear Carbon on Light Absorption Enhancement, Single Scatter Albedo and Absorption Wavelength Dependence of Black Carbon. *Atmos. Chem. Phys.*, 10:4207–4220, doi:10.5194/acp-10-4207-2010.
- Leach, K. B., Kamens, R. M., Strommen, M. R., and Jang, M. (1999). Partitioning of Semivolatile Organic Compounds in the Presence of a Secondary Organic Aerosol in a Controlled Atmosphere. *J. Atmos. Chem.*, 33(3):241–264, doi:10.1023/A:1006108430033.
- Lewis, K., Arnott, W. P., Moosmüller, H., and Wold, C. E. (2008). Strong Spectral Variation of Biomass Smoke Light Absorption and Single Scattering Albedo Observed with a Novel Dual-Wavelength Photoacoustic Instrument. *J. Geophys. Res.*, 113:D16203, doi:10.1029/2007JD009699.
- Loza, C. L., Chhabra, P. S., Yee, L. D., Craven, J. S., Flagan, R. C., and Seinfeld, J. H. (2012). Chemical Aging of m-xylene Secondary Organic Aerosol: Laboratory Chamber Study. *Atmos. Chem. Phys.*, 12:151–167, doi:10.5194/acp-12-151-2012.
- Malm, W. C., Day, D. E., Carrico, C., Kreidenweis, S. M., Collett Jr., J. L., McMeeking, G., Lee, T., Carrillo, J., and Schichtel, B. (2005a). Intercomparison and Closure Calculations Using Measurements of Aerosol Species and Optical Properties During the Yosemite Aerosol Characterization Study. *J. Geophys. Res.*, 110:D14302, doi:10.1029/2004JD005494.
- Malm, W. C., Day, D. E., Kreidenweis, S. M., Collett Jr., J. L., Carrico, C., McMeeking, G., and Lee, T. (2005b). Hygroscopic Properties

- of an Organic-Laden Aerosol. *Atmos. Environ.*, 39(27):4969–4982, doi:10.1016/j.atmosenv.2005.05.014.
- McMurry, P. H., and Rader, D. J. (1985). Aerosol Wall Losses in Electrically Charged Chambers. *Aerosol Sci. Technol.*, 4(3):249–268, doi:10.1080/02786828508959054.
- Metcalfe, A. R., Craven, J. S., Ensberg, J. J., Brioude, J., Angevine, W., Sorooshian, A., Duong, H. T., Jonsson, H. H., Flagan, R. C., and Seinfeld, J. H. (2012). Black Carbon Aerosol over the Los Angeles Basin During CalNex. *J. Geophys. Res.*, 117:D00V13, doi:10.1029/2011JD017255.
- Middlebrook, A. M., Bahreini, R., Jimenez, J. L., and Canagaratna, M. R. (2012). Evaluation of Composition-Dependent Collection Efficiencies for the Aerodyne Aerosol Mass Spectrometer Using Field Data. *Aerosol Sci. Technol.*, 46(3):258–271, doi:10.1080/02786826.2011.620041.
- Mikhailov, E. F., Vlasenko, S. S., Podgorny, I. A., Ramanathan, V., and Corrigan, C. E. (2006). Optical Properties of Soot–Water Drop Agglomerates: An Experimental Study. *J. Geophys. Res.*, 111:D07209, doi:10.1029/2005JD006389.
- Moffet, R. C., and Prather, K. A. (2009). In-Situ Measurements of the Mixing State and Optical Properties of Soot with Implications for Radiative Forcing Estimates. *Proc. Natl. Acad. Sci. USA*, 106(29):11872–11877, doi:10.1073/pnas.0900040106.
- Moteki, N., and Kondo, Y. (2007). Effects of Mixing State on Black Carbon Measurements by Laser-Induced Incandescence. *Aerosol Sci. Technol.*, 41(4):398–417, doi:10.1080/02786820701199728.
- Moteki, N., and Kondo, Y. (2010). Dependence of Laser-Induced Incandescence on Physical Properties of Black Carbon Aerosols: Measurements and Theoretical Interpretation. *Aerosol Sci. Technol.*, 44(8):663–675, doi:10.1080/02786826.2010.484450.
- Moteki, N., et al. (2007). Evolution of Mixing State of Black Carbon Particles: Aircraft Measurements Over the Western Pacific in March 2004. *Geophys. Res. Lett.*, 34:L11803, doi:10.1029/2006GL028943.
- Moteki, N., Kondo, Y., Takegawa, N., and Nakamura, S. (2009). Directional Dependence of Thermal Emission from Nonspherical Carbon Particles. *J. Aerosol Sci.*, 40(9):790–801, doi:10.1016/j.jaerosci.2009.05.003.
- Nakayama, T., Matsumi, Y., Sato, K., Imamura, T., Yamazaki, A., and Uchiyama, A. (2010). Laboratory Studies on Optical Properties of Secondary Organic Aerosols Generated During the Photooxidation of Toluene and the Ozonolysis of Alpha-Pinene. *J. Geophys. Res.*, 115:D24203, doi:10.1029/2010JD014387.
- Ng, N. L., Kroll, J. H., Chan, A. W. H., Chhabra, P. S., Flagan, R. C., and Seinfeld, J. H. (2007). Secondary Organic Aerosol Formation from m-xylene, Toluene, and Benzene. *Atmos. Chem. Phys.*, 7:3909–3922, doi:10.5194/acp-7-3909-2007.
- Ng, N. L., et al. (2010). Organic Aerosol Components Observed in Northern Hemispheric Datasets from Aerosol Mass Spectrometry. *Atmos. Chem. Phys.*, 10:4625–4641, doi:10.5194/acp-10-4625-2010.
- Park, S. H., Kim, H. O., Han, Y. T., Kwon, S. B., and Lee, K. W. (2001). Wall Loss Rate of Polydispersed Aerosols. *Aerosol Sci. Technol.*, 35(3):710–717, doi:10.1080/02786820152546752.
- Park, Y.-K., Park, S. H., and Bae, G.-N. (2012). Analytical Expression on Characteristic Time Scale of Black Carbon Aging Due to Condensation of Hygroscopic Species. *Aerosol Sci. Technol.*, 46(6):601–609, doi:10.1080/02786826.2011.647119.
- Pierce, J. R., Engelhart, G. J., Hildebrandt, L., Weitkamp, E. A., Pathak, R. K., Donahue, N. M., et al. (2008). Constraining Particle Evolution from Wall Losses, Coagulation, and Condensation-Evaporation in Smog-Chamber Experiments: Optimal Estimation Based on Size Distribution Measurements. *Aerosol Sci. Technol.*, 42(12):1001–1015, doi:10.1080/02786820802389251.
- Pósfai, M., Simonsics, R., Li, J., Hobbs, P. V., and Buseck, P. R. (2003). Individual Aerosol Particles from Biomass Burning in Southern Africa: 1. Compositions and Size Distributions of Carbonaceous Particles. *J. Geophys. Res.*, 108(D13):8483, doi:10.1029/2002JD002291.
- Pye, H. O. T., Chan, A. W. H., Barkley, M. P., and Seinfeld, J. H. (2010). Global Modeling of Organic Aerosol: The Importance of Reactive Nitrogen ( $\text{NO}_x$  and  $\text{NO}_3$ ). *Atmos. Chem. Phys.*, 10(11):261–11, 276, doi:10.5194/acp-10-11261-2010.
- Ravindra, K., Sokhi, R., and Van Grieken, R. (2008). Atmospheric Polycyclic Aromatic Hydrocarbons: Source Attribution, Emission Factors and Regulation. *Atmos. Environ.*, 42(13):2895–2921, doi:10.1016/j.atmosenv.2007.12.010.
- Riemer, N., Vogel, H., and Vogel, B. (2004). Soot Aging Time Scales in Polluted Regions During Day and Night. *Atmos. Chem. Phys.*, 4:1885–1893, doi:10.5194/acp-4-1885-2004.
- Robinson, A. L., Donahue, N. M., Shrivastava, M. K., Weitkamp, E. A., Sage, A. M., Grieshop, A. P., et al. (2007). Rethinking Organic Aerosols: Semivolatile Emissions and Photochemical Aging. *Science*, 315(5816):1259–1262, doi:10.1126/science.1133061.
- Saathoff, H., Naumann, K.-H., Schnaiter, M., Schöck, W., Möhler, O., Schurath, U., et al. (2003). Coating of Soot and  $(\text{NH}_4)_2\text{SO}_4$  Particles by Ozonolysis Products of  $\alpha$ -pinene. *J. Aerosol Sci.*, 34(10):1297–1321, doi:10.1016/S0021-8502(03)00364-1.
- Sachweh, B. A., Dick, W. D., and McMurry, P. H. (1995). Distinguishing between Spherical and Nonspherical Particles by Measuring the Variability in Azimuthal Light Scattering. *Aerosol Sci. Technol.*, 23(3):373–391, doi:10.1080/02786829508965321.
- Schauer, J. J., Kleeman, M. J., Cass, G. R., and Simoneit, B. R. T. (1999). Measurement of Emissions from Air Pollution Sources. 2. C1 Through C30 Organic Compounds from Medium Duty Diesel Trucks. *Environ. Sci. Technol.*, 33(10):1578–1587, doi:10.1021/es980081n.
- Schauer, J. J., Kleeman, M. J., Cass, G. R., and Simoneit, B. R. T. (2001). Measurement of Emissions from Air Pollution Sources. 3. C1–C29 Organic Compounds from Fireplace Combustion of Wood. *Environ. Sci. Technol.*, 35(9):1716–1728, doi:10.1021/es001331e.
- Schauer, J. J., Rogge, W. F., Hildemann, L. M., Mazurek, M. A., Cass, G. R., and Simoneit, B. R. T. (1996). Source Apportionment of Airborne Particulate Matter Using Organic Compounds as Tracers. *Atmos. Environ.*, 30(22):3837–3855, doi:10.1016/1352-2310(96)00085-4.
- Schnaiter, M., Horvath, H., Möhler, O., Naumann, K.-H., Saathoff, H., and Schöck, O. W. (2003). UV-VIS-NIR Spectral Optical Properties of Soot and Soot-Containing Aerosols. *J. Aerosol Sci.*, 34(10):1421–1444, doi:10.1016/S0021-8502(03)00361-6.
- Schnaiter, M., Linke, C., Möhler, O., Naumann, K.-H., Saathoff, H., Wagner, R., et al. (2005). Absorption Amplification of Black Carbon Internally Mixed with Secondary Organic Aerosol. *J. Geophys. Res.*, 110:D19204, doi:10.1029/2005JD006046.
- Schoemaeker Moreau, C., Therssen, E., Mercier, X., Pauwels, J. F., and Desgroux, P. (2004). Two-Color Laser-Induced Incandescence and Cavity Ring-Down Spectroscopy for Sensitive and Quantitative Imaging of Soot and PAHs in Flames. *Appl. Phys. B: Lasers Opt.*, 78(3–4):485–492, doi:10.1007/s00340-003-1370-9.
- Schwarz, J. P., Gao, R. S., Fahey, D. W., Thomson, D. S., Watts, L. A., Wilson, J. C., Reeves, J. M., Darbehesht, M., Baumgardner, D. G., Kok, G. L., Chung, S. H., Schulz, M., Hendricks, J., Lauer, A., Kärcher, B., Slowik, J. G., Rosenlof, K. H., Thompson, T. L., Langford, A. O., Loewenstein, M., and Aikin, K. C. (2006). Single-Particle Measurements of Mid-latitude Black Carbon and Light-Scattering Aerosols from the Boundary Layer to the Lower Stratosphere. *J. Geophys. Res.*, 111:D16207, doi:10.1029/2006JD007076.
- Schwarz, J. P., R. Gao, S., Spackman, J. R., Watts, L. A., Thomson, D. S., Fahey, D. W., Ryerson, T. B., Peischl, J., Holloway, J. S., Trainer, M., Frost, G. J., Baynard, T., Lack, D. A., de Gouw, J. A., Warneke, C., and Del Negro, L. A. (2008a). Measurement of the Mixing State, Mass, and Optical Size of Individual Black Carbon Particles in Urban and Biomass Burning Emissions. *Geophys. Res. Lett.*, 35:L13810, doi:10.1029/2008GL033968.
- Schwarz, J. P., Spackman, J. R., Fahey, D. W., R. Gao, S., Lohmann, U., Stier, P., Watts, L. A., Thomson, D. S., Lack, D. A., Pfister, L., Mahoney,

- M. J., Baumgardner, D., Wilson, J. C., and Reeves, J. M. (2008b). Coatings and Their Enhancement of Black Carbon Light Absorption in the Tropical Atmosphere. *J. Geophys. Res.*, 113:D03203, doi:10.1029/2007JD009042.
- Seinfeld, J. H., and Pandis, S. N. (2006). *Atmospheric Chemistry and Physics: From Air Pollution to Climate Change*, 2nd ed. John Wiley & Sons, Inc., New York.
- Shiraiwa, M., Kondo, Y., Iwamoto, T., and Kita, K. (2010). Amplification of Light Absorption of Black Carbon by Organic Coating. *Aerosol Sci. Technol.*, 44(1):46–54, doi:10.1080/02786820903357686.
- Shiraiwa, M., Kondo, Y., Moteki, N., Takegawa, N., Miyazaki, Y., and Blake, D. R. (2007). Evolution of Mixing State of Black Carbon in Polluted Air from Tokyo. *Geophys. Res. Lett.*, 34:L16803, doi:10.1029/2007GL029819.
- Shiraiwa, M., Kondo, Y., Moteki, N., Takegawa, N., Sahu, L. K., Takami, A., et al. (2008). Radiative Impact of Mixing State of Black Carbon Aerosol in Asian Outflow. *J. Geophys. Res.*, 113:D24210, doi:10.1029/2008JD010546.
- Slowik, J. G., Cross, E. S., Han, J.-H., Davidovits, P., Onasch, T. B., Jayne, J. T., Williams, L. R., Canagaratna, M. R., Worsnop, D. R., Chakrabarty, R. K., Moosmüller, H., Arnott, W. P., Schwarz, J. P., Gao, R.-S., Fahey, D. W., Kok, G. L., and Petzold, A. (2007a). An Inter-Comparison of Instruments Measuring Black Carbon Content of Soot Particles. *Aerosol Sci. Technol.*, 41(3):295–314, doi:10.1080/02786820701197078.
- Slowik, J. G., Cross, E. S., Han, J.-H., Kolucki, J., Davidovits, P., Williams, L. R., Onasch, T. B., Jayne, J. T., Kolb, C. E., and Worsnop, D. R. (2007b). Measurements of Morphology Changes of Fractal Soot Particles Using Coating and Denuding Experiments: Implications for Optical Absorption and Atmospheric Lifetime. *Aerosol Sci. Technol.*, 41(8):734–750, doi:10.1080/02786820701432632.
- Stephens, M., Turner, N., and Sandberg, J. (2003). Particle Identification by Laser-Induced Incandescence in a Solid-State Laser Cavity. *Appl. Opt.*, 42(19):3726–3736, doi:10.1364/AO.42.003726.
- Stier, P., Seinfeld, J. H., Kinne, S., Feichter, J., and Boucher, O. (2006). Impact of Nonabsorbing Anthropogenic Aerosols on Clear-Sky Atmospheric Absorption. *J. Geophys. Res.*, 111:D18201, doi:10.1029/2006JD007147.
- Strommen, M. R., and Kamens, R. M. (1997). Development and Application of a Dual-Impedance Radial Diffusion Model to Simulate the Partitioning of Semivolatile Organic Compounds in Combustion Aerosols. *Environ. Sci. Technol.*, 31(10):2983–2990, doi:10.1021/es970079g.
- Strommen, M. R., and Kamens, R. M. (1999). Simulation of Semivolatile Organic Compound Microtransport at Different Time Scales in Airborne Diesel Soot Particles. *Environ. Sci. Technol.*, 33(10):1738–1746, doi:10.1021/es981035q.
- Subramanian, R., et al. (2010). Black Carbon over Mexico: The Effect of Atmospheric Transport on Mixing State, Mass Absorption Cross-Section, and BC/CO Ratios. *Atmos. Chem. Phys.*, 10:219–237, doi:10.5194/acp-10-219-2010.
- Taylor, W. D., Allston, T. D., Moscato, M. J., Fazekas, G. B., Kozlowski, R., and Takacs, G. A. (1980). Atmospheric Photodissociation Lifetimes for Nitromethane, Methyl Nitrite, and Methyl Nitrate. *Int. J. Chem. Kinet.*, 12(4):231–240, doi:10.1002/kin.550120404.
- Toon, O. B., and Ackerman, T. P. (1981). Algorithms for the Calculation of Scattering by Stratified Spheres. *Appl. Opt.*, 20(20):3657–3660, doi:10.1364/AO.20.003657.
- Wehner, B., et al. (2009). Mixing state of Nonvolatile Aerosol Particle Fractions and Comparison with Light Absorption in the Polluted Beijing Region. *J. Geophys. Res.*, 114:D00G17, doi:10.1029/2008JD010923.
- Weiner, A. M., and Harris, S. J. (1989). Optical Detection of Large Soot Precursors. *Combust. Flame*, 77(3–4):261–266, doi:10.1016/0010-2180(89)90133-8.
- Weingartner, E., Burtscher, H., and Baltensperger, U. (1997). Hygroscopic Properties of Carbon and Diesel Soot Particles. *Atmos. Environ.*, 31(15):2311–2327, doi:10.1016/S1352-2310(97)00023-X.
- Weitkamp, E. A., Sage, A. M., Pierce, J. R., Donahue, N. M., and Robinson, A. L. (2007). Organic Aerosol Formation from Photochemical Oxidation of Diesel Exhaust in a Smog Chamber. *Environ. Sci. Technol.*, 41(20):6969–6975, doi:10.1021/es070193r.
- Wonaschütz, A., Hitznerberger, R., Bauer, H., Pouresmaeil, P., Klatzer, B., Caseiro, A., et al. (2012). Application of the Integrating Sphere Method to Separate the Contributions of Brown and Black Carbon in Atmospheric Aerosols. *Environ. Sci. Technol.*, 43(4):1141–1146, doi:10.1021/es8008503.
- Yang, M., Howell, S. G., Zhuang, J., and Huebert, B. J. (2009). Attribution of Aerosol Light Absorption to Black Carbon, Brown Carbon, and Dust in China—Interpretations of Atmospheric Measurements During EAST-AIRE. *Atmos. Chem. Phys.*, 9:2035–2050, doi:10.5194/acp-9-2035-2009.
- Yu, Y., Ezella, M. J., Zelenyuk, A., Imre, D., Alexander, L., Ortega, J., D’Anna, B., Harmon, C. W., Johnson, S. N., and Finlayson-Pitts, B. J. (2008). Photooxidation of  $\alpha$ -pinene at High Relative Humidity in the Presence of Increasing Concentrations of NO<sub>x</sub>. *Atmos. Environ.*, 42(20):5044–5060, doi:10.1016/j.atmosenv.2008.02.026.
- Zhang, R., Khalizov, A. F., Pagels, J., Zhang, D., Xue, H., and McMurry, P. H. (2008). Variability in Morphology, Hygroscopicity, and Optical Properties of Soot Aerosols During Atmospheric Processing. *Proc. Natl. Acad. Sci. USA*, 105(30):10291–10296, doi:10.1073/pnas.0804860105.
- Zuberi, B., Johnson, K. S., Aleks, G. K., Molina, L. T., and Molina, M. J. (2005). Hydrophilic Properties of Aged Soot. *Geophys. Res. Lett.*, 32:L01807, doi:10.1029/2004GL021496.